Spectroscopic Techniques for Photodynamic Therapy Dosimetry

Ann Johansson

Doctoral Thesis
2007

Lund University

Spectroscopic Techniques for Photodynamic Therapy Dosimetry

Printed in Sweden by Media-Tryck, Lund, 2007

Division of Atomic Physics
Department of Physics
Faculty of Engineering, LTH
Lund University
P.O. Box 118
SE–221 00 Lund
Sweden

http://www.atom.fysik.lth.se

ISSN 0281-2762
Lund Reports on Atomic Physics, LRAP-387

ISBN: 978-91-628-7281-6

To my beloved family

Abstract

Photodynamic therapy (PDT) as a cancer treatment modality relies on the simultaneous presence of three components; light, photosensitiser and oxygen. Once excited by the light, the photosensitiser can interact with oxygen, leading to the formation of toxic oxygen species. These reactive substances induce cellular damage within the irradiated tissue volume. PDT has been investigated for treating malignancies in numerous organs and is nowadays an approved treatment modality for certain types of malignancies of, for example, the skin, lungs, bladder and oesophagus.

However, PDT still suffers from several drawbacks. For example, many photosensitisers accumulate also in non-malignant tissue, introducing the risk of damaging surrounding, sensitive tissue. Another drawback is the large intra- and inter-patient variation in treatment response despite utilising standardised light and photosensitiser doses.

In this thesis, two approaches have been investigated with the aim to overcome on the one hand, the sub-optimal tumour-selective uptake of the photosensitiser, and on the other, the variable treatment effects. For both tasks, spectroscopic techniques were employed to monitor parameters relevant to the PDT effect.

The first project involved pharmacokinetic studies of a novel, liposomal photosensitiser formulation for both topical and intravenous administration. The topical application route led to good tumour-selective uptake both in an animal skin tumour model and in human skin malignancies. However, the clinical treatment conditions, such as photosensitiser application time, light and photosensitiser doses, need to be further optimised. Furthermore, following systemic administration in a murine tumour model, the pharmacokinetics of this novel formulation led to a rapid biodistribution and clearance from the blood stream. The tumour-to-skin and tumour-to-muscle selectivity at two to eight hours after photosensitiser administration were higher than reported for the free mTHPC formulation.

The second approach aimed at implementing realtime treatment feedback for interstitial PDT. The first in a series of instru-

ments incorporated six optical fibres for light delivery and monitoring of light transmission and photosensitiser fluorescence in the target tissue. Post-treatment data analysis indicated significant differences between the intended and actual light dose distributions. Hence, we concluded there is a need for treatment monitoring and feedback in order to ascertain delivery of a prescribed light dose to the entire target tissue. More recently, the hardware has been adapted to interstitial PDT on the human prostate. The number of source fibres has been increased to 18 and realtime feedback based on a light dose threshold model has been implemented. We can now present a clinical instrument for interstitial PDT on prostate tissue incorporating modules for pre-treatment planning, monitoring of the optical properties of the target tissue and updating irradiation times in realtime. This realtime feedback scheme has been evaluated for simulated treatment scenarios for which it was concluded that the realtime dosimetry module makes it possible to deliver a certain light dose to the target tissue despite spatial and temporal variations of the optical properties of the target tissue.

Populärvetenskaplig sammanfattning

Denna avhandling handlar till stora delar om fotodynamisk tumörterapi (PDT). PDT har sedan början av förra århundradet undersökts som ett tänkbart alternativ till strålningsbehandling, kirurgi och kemoterapi för behandling av cancertumörer i kroppen.

Precis som namnet antyder involverar metoden en fotodynamisk reaktion. För att denna reaktion skall ske behövs tre komponenter; ljus, sensibiliserare och syre. Ljuset exciterar sensibiliserarmolekylerna som i sin tur överför en del av energin till bland annat syremolekyler. Syret, som förekommer naturligt i biologisk vävnad, bildar därvid den giftiga molekyl som är den egentliga celldödande substansen. Vävnadsdöd induceras endast då alla tre komponenterna är närvarande; var och en för sig är varken ljuset, sensibiliseraren eller syret skadligt. Likaså beror den totala behandlingsvolymen på mängden ljus och koncentrationen av sensibiliserare och syre. Till exempel gäller att vid obegränsad syretillgång ökar nekrosvolymen med mängden ljus och sensibiliserare. Det är därför av stor vikt att kunna mäta och/eller modellera mängden ljus, sensibiliserare och syre inom den vävnadsvolym man vill behandla.

Tursamt nog besitter många sensibiliserare förmågan att fluorescera, vilket underlättar för minimalt invasiva koncentrationsmätningar. Fluorescens är ett fenomen där inkommande ljus absorberas av molekylen för att strax därpå skickas ut med en annan energi och därmed med en annan färg. Detta kan åskådliggöras genom att belysa till exempel en hudtumör, på vilken sedan tidigare någon sensibiliserare administrerats, med blått ljus. De sensibiliserare som använts inom detta avhandlingsarbete fluorescerar därvid i rött. Fluorescensljuset är ofta så starkt att det mänskliga ögat uppfattar ett rött skimmer från tumören. Med hjälp av teknisk utrustning, såsom laser, spektrometer och CDD, är det möjligt att använda fluorescensspektroskopi för att mäta sensibiliserarkoncentration i biologisk vävnad.

Vidare kan mängden ljus inom den intressanta vävnadsvolymen

beräknas genom att kombinera ett fåtal stickprov, dvs mätningar av ljustransmission i några olika punkter på eller i vävnaden, med en lämplig teoretisk modell för ljusutbredning. På så vis kan man skaffa sig en uppfattning om hur pass långt ljuset utbreder sig och därmed inom hur stora volymer man kan förvänta sig fullgod behandling. Transmissionsmätningar vid flera våglängder, dvs för flera olika färger, kan dessutom relateras till vävnadens syresättning och därmed till syretillgången inom behandlingsområdet.

Inom ramen för detta avhandlingsarbete har två frågeställningar undersökts i syfte att förbättra PDT som cancerbehandlingsmetod. Dessa frågeställningar berörs nedan.

Många sensibiliserare som används i klinik idag besitter inte optimala tumörlokaliseringsegenskaper. Tyvärr ackumuleras dessa substanser även inom normal, kringliggande vävnad, vilken därmed löper risk att skadas under behandling. Som den första frågeställningen har vi undersökt distributionsmönstret av en ny sensibiliserarformulering för både topisk och intravenös administrering. Dessa försök, som genomförts i två djurmodeller, visade på god förmåga hos sensibiliseraren att lokalisera inom tumörer. Även för patienter med avancerade hudtumörer ledde topisk applicering av den nya substansen till god selektivitet mellan tumör och kringliggande vävnad.

Vi, liksom många andra forskargrupper, har uppmärksammat att vävnadens respons på behandling skiljer sig åt mellan patienter. Dessutom varierar sensibiliserarkoncentrationen och ljusgenomsläppligheten lokalt inom tumörvävnaden. Inom avhandlingsarbetets andra huvudspår har vi utvecklat hårdvara och mjukvara för övervakning och kontroll av PDT-behandling. Vår förhoppning är, att genom att anpassa behandlingen till varje individuell patient, kan behandlingsresultatet förbättras. Nuvarande instrument och tillhörande programvara gör det möjligt att anpassa mängden ljus till lokala variationer i vävnadens ljustransmission under behandling av prostatacancer.

List of Publications

This thesis is based on the following papers, which will be referred to by their Roman numerals in the text.

I **Fluorescence and absorption assessment of a lipid mTHPC formulation following topical application in a non-melanotic skin tumor model**
A. Johansson, J. Svensson, N. Bendsoe, K. Svanberg, E. Alexandratou, M. Kyriazi, D. Yova, S. Gräfe, T. Trebst, S. Andersson-Engels.
Journal of Biomedical Optics **12(3)**, 034026 (2007).

II **Fluorescence monitoring of a topically applied liposomal Temoporfin formulation and photodynamic therapy of non-pigmented skin malignancies**
N. Bendsoe, L. Persson, A. Johansson, J. Svensson, J. Axelsson, S. Andersson-Engels, S. Svanberg, K. Svanberg.
Journal of Environmental Pathology, Toxicology and Oncology **26(2)**, 117-226 (2007).

III **Tumor selectivity at short times following systemic administration of a liposomal Temoporfin formulation in a murine tumor model**
J. Svensson, A. Johansson, S. Gräfe, B. Gitter, T. Trebst, N. Bendsoe, S. Andersson-Engels, K. Svanberg.
Photochemistry and Photobiology, in press (2007).

IV **Clinical system for interstitial photodynamic therapy with combined on-line dosimetry measurements**
M. Soto Thompson, A. Johansson, T. Johansson, S. Andersson-Engels, S. Svanberg, N. Bendsoe, K. Svanberg.
Applied Optics **44(19)**, 4023-4031 (2005).

V **In vivo measurement of parameters of dosimetric importance during interstitial photodynamic therapy of thick skin tumors**
A. Johansson, T. Johansson, M. Soto Thompson, N. Bendsoe, K. Svanberg, S. Svanberg, S. Andersson-Engels.
Journal of Biomedical Optics **11(3)**, 034029 (2006).

VI **Influence of treatment-induced changes in tissue absorption on treatment volume during interstitial photodynamic therapy of thick skin tumors**
A. Johansson, N. Bendsoe, K. Svanberg, S. Svanberg, S. Andersson-Engels.
Medical Laser Applications **21**, 261-270 (2006).

VII **Pre-treatment dosimetry for interstitial photodynamic therapy**
A. Johansson, J. Hjelm, A. Eriksson, S. Andersson-Engels.
Therapeutic Laser Applications and Laser-Tissue Interactions II, Ed. H. van den Bergh, A. Vogel, Proc. SPIE **5863**, 58630S (2005).

VIII **Realtime light dosimetry software tools for interstitial photodynamic therapy of the human prostate**
A. Johansson, J. Axelsson, J. Swartling, S. Andersson-Engels.
Medical Physics, in press (2007).

Other related publications by the author:

Tissue temperature monitoring during interstitial photodynamic therapy
J. Svensson, A. Johansson, K. Svanberg,
S. Andersson-Engels.
Proc. SPIE **5698**, 126-136 (2005).

A comparison of diagnostic fluorescence point and hyperspectral imaging spectroscopy - geometry effects
J. Svensson, G. Somesfalean, A Johansson,
S. Andersson-Engels.
2004 *Proc. OSA*.

System for integrated interstitial photodynamic therapy and dosimetric monitoring
A. Johansson, M. Soto Thompson, T. Johansson,
N. Bendsoe, K. Svanberg, S. Svanberg,
S. Andersson-Engels.
Proc. SPIE **5689**, 130-140 (2005).

Interstitial photodynamic therapy for primary prostate cancer incorporating realtime treatment dosimetry
A. Johansson, J. Axelsson, J. Swartling, T. Johansson,
S. Pålsson, J. Stensson, M. Einarsdóttír, K. Svanberg,
N. Bendsoe, K.M. Kälkner, S. Nilsson, S. Svanberg,
S. Andersson-Engels.
Proc. SPIE **6427**, 64270O (2007).

Remote multicolor excitation laser-induced fluorescence imaging
R. Grönlund, J. Hällström, A. Johansson, K. Barup,
S. Svanberg.
Laser Chemistry **2006**, Article ID 57934 (2006).

Documentation of soiled and biodeteriorated façades: A case study on the Coliseum, Rome, using hyperspectral imaging fluorescence Lidars
J. Hällström, K. Barup, R. Grönlund, A. Johansson,
S. Svanberg, L. Palombi, D. Lognoli, V. Raimondi,
G. Cecchi, and C. Conti.
Submitted, 2007.

Hyperspectral fluorescence Lidar imaging at the Coliseum, Rome: Elucidating past conservation interventions
L. Palombi, D. Lognoli, V. Raimondi, G. Cecchi, J. Hällström, K. Barup, C. Conti, R. Grönlund, A. Johansson, and S. Svanberg.
Manuscript in preparation, 2007.

Laser-induced fluorescence for assessment of cultural heritage
R. Grönlund, J. Hällström, A. Johansson, L. Palombi, D. Lognoli, V. Raimondi, G. Cecchi, K. Barup, C. Conti, O. Brandt, B. Santillo Frizell, and S. Svanberg.
Proc. of the 23rd International Laser Radar Conference, Nara, Japan, 723–726 (2006).

Abbreviations

AK	actinic keratosis
ALA	amino-laevulinic acid
AlS_xPc	aluminium sulphonated phthalocyanine
AMD	age-related macular degeneration
BCC	basal cell carcinoma
BD	Bowen's disease
BPD	benzoporphyrin derivative
BPD-MA	benzoporphyrin derivative monoacid ring A
CD	cell death
CNV	choroidal neovascularisation
CR	cure rate
CW	continuous-wave
DLI	drug-light interval
DPPC	dipalmitoylphosphatidylcholine
DPS	differential path length spectroscopy
DVH	dose-volume histogram
DW-MRI	diffusion-weighted MRI
EBC	extrapolated-boundary condition
EIS	electrical impedance spectroscopy
FEM	finite element method
FR	frequency-resolved
HGD	high grade dysplasia
HpD	haematoporphyrin derivative
HPLC	high performance liquid chromatography
IPDT	interstitial photodynamic therapy
LDL	low-density lipoprotein
m-ALA	methyl-esterified ALA, also MAL, ME-ALA
MLu	mutexafin lutetium

mTHPC	meso-tetrahydroxyphenylchlorin
MRI	magnetic resonance imaging
NIR	near-infrared
NMSC	non-melanoma skin cancer
OAR	organs at risk
OCT	optical coherence tomography
PBGD	porphobilinogen deaminase
PCBC	partial-current boundary condition
PDT	photodynamic therapy
PpIX	protoporphyrin IX
PS	photosensitiser
PSA	prostate-specific antigen
ROS	reactive oxygen species
RTE	radiative transport equation
SCC	squamous cell carcinoma
SD	standard deviation
SNR	signal-to-noise ratio
SOLD	singlet-oxygen luminescence dosimetry
SR	spatially-resolved
SVD	singular value decomposition
TR	time-resolved
UV	ultraviolet
WST09	Pd-bacteriopheoporbide
ZBC	zero boundary condition

Nomenclature

A	internal reflection parameter or absorbance
b	scattering slope
c	speed of light (cms^{-1}) or concentration (M or %)
D	diffusion coefficient (cm)
D_L	light dose ($\mathrm{J/cm}^2$)
D_{PDT}	PDT dose
DPF	differential path length factor
E	energy (J)
$\mathbf{F}(\mathbf{r}, \mathbf{t})$	photon flux (Wcm^{-2})
F	fluorescence signal (a.u.)
g	anisotropy factor
h	Planck's constant (Js)
Hb	deoxygenated haemoglobin
HbO_2	oxygenated haemoglobin
$\mathrm{Hb}_{\mathrm{tot}}$	total haemoglobin
I	detected light power (W)
I_0	incident light power (W)
$L(\mathbf{r}, \mathbf{s}, t)$	radiance ($\mathrm{Wcm}^{-2}\mathrm{sr}^{-1}$)
L_{eff}	effective path length (cm)
n	refractive index
$\hat{\mathbf{n}}$	normal unit vector
${}^1O_2$	excited singlet state oxygen
${}^3O_2$	ground state oxygen
$p(\mathbf{s} \cdot \mathbf{s}')$	scattering phase function
$q(\mathbf{r}, t)$	source term (Wcm^{-3})
$Q(\mathbf{r}, t)$	source term ($\mathrm{Wcm}^{-3}\mathrm{sr}^{-1}$)
$\mathbf{r}, r$	position or source-detector distance (cm)
$R(\rho)$	reflectance (Wcm^{-2})

$\mathbf{s}, \mathbf{s}'$	direction unit vectors
S_0	isotropic source term or photosensitiser ground state
S_1	excited photosensitiser state
S_{O2}	tissue oxygen saturation
t	time (s)
T	transmittance (Wcm^{-2})
T_1	excited photosensitiser triplet state
$[x]$	concentration of substance x (M or %)
z_b	extrapolation distance (cm)
δ	penetration depth (cm)
ϵ	extinction coefficient ($\mathrm{M}^{-1}\mathrm{cm}^{-1}$)
ζ	uniformly distributed random number
Θ	deflection angle (sr)
λ	wavelength (nm)
μ_a	absorption coefficient (cm^{-1})
μ_{eff}	effective attenuation coefficient (cm^{-1})
μ_s	scattering coefficient (cm^{-1})
μ_s'	reduced scattering coefficient (cm^{-1})
μ_t'	transfer attenuation coefficient (cm^{-1})
ν	frequency (Hz)
ρ	radial distance (cm)
$\Phi(r,t)$	fluence rate (Wcm^{-2})
Φ_Δ	singlet-oxygen yield
Φ_{fl}	fluorescence yield
Φ_t	triplet-state yield
Ψ	azimuthal angle or random number
ω, Ω	solid angle (sr)

Contents

Papers

Chapter 1

Introduction

1.1 PDT in a historical perspective

Photodynamic therapy (PDT) is emerging as a promising treatment modality for cancer in various organs. PDT relies on the simultaneous presence of three components; light, photosensitiser and oxygen. Cellular damage is caused by various reactive oxygen species, induced by the light-activated photosensitiser.

The phrase "photodynamic therapy" was first introduced by von Tappeiner and Jodlbauer in 1907 [1]. Preceding this work, a student of von Tappeiner, Oscar Raab, had by coincidence observed peculiar effects of acridine on *in vitro* paramecium [2]. Performing two experiments, only one resulted in the death of all paramecia, whereas the other showed no toxic effects of the acridine. As the only difference was the occurrence of a thunderstorm during one of the experiments, Raab concluded that the transfer of energy from the light, i.e. the lightning, to the chemical was of importance for inducing toxicity. In collaboration with a dermatologist, von Tappeiner treated skin malignancies utilising eosin and white light [3]. Some years later he also observed that oxygen was necessary for the reaction to take place [4].

The porphyrins constitute one class of compounds that have been used extensively for photodiagnostic as well as phototherapeutic purposes. Friedrich Meyer-Betz was the first to demonstrate human photosensitisation utilising this group of photosensitisers. After injecting himself with 200 mg of haematoporphyrin he experienced pain and swelling in skin areas exposed to ambient light and he remained photosensitive for more than two months [5]. This generalised photosensitivity, evident in Figure 1.1, is associated with systemic administration of many photosensitisers of today and constitutes one of the major drawbacks of this treatment modality.

During the 1950s, the fluorescence properties of haematopor-

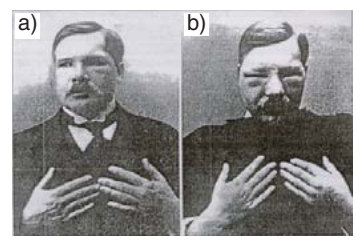

Figure 1.1. *Friedrich Meyer-Betz* ***a)*** *before and* ***b)*** *after injecting himself with 200 mg haematoporphyrin.*

phyrin together with its ability to sometimes accumulate selectively in malignant tissue was investigated as a tool for tumour detection in both animal and human tissues [6]. In 1955, Schwartz demonstrated that haematoporphyrin did in fact consist of many different substances of which the pure haematoporphyrin exhibited only very poor tumour-selective uptake [7]. After isolating another of these substances, haematoporphyrin derivative (HpD), Schwartz and Lipson found evidence of improved phototoxicity [7] and tumour localisation [8] as compared to pure haematoporphyrin.

Despite the many and extensive studies on the localising properties of HpD, it was not until 1966 that Lipson utilised the substance for cancer treatment; PDT on a single patient with a recurrent breast carcinoma [9]. Despite repeated treatments the lesion recurred. Hence Dougherty *et al.* were the first to demonstrate complete tumour clearance following HpD injection and irradiation with red light in animal tumour models [10]. In 1976, Kelly and Snell utilised HpD and a quartz rod for coupling light into the bladder of a patient with a recurrent bladder carcinoma [11]. This work was followed by the first large-scale clinical trial in which Dougherty *et al.* were able to achieve an 87% cure rate (CR) of the 113 skin tumours included in the study [12]. HpD is now one of the most common photosensitisers in clinical and experimental use. For further information on tumour detection and treatment using HpD, the reader is referred to Refs. [6, 13]. Numerous clinical trials have shown PDT to be a safe and successful treatment option, also where conventional therapies fail. In particular, PDT holds great potential for the treatment of superficial and easily accessible lesions, such as malignancies of the skin and hollow organs. For example, more than 2 500 skin malignancies have been treated at the Departments of Oncology and Dermatology, Lund University, Sweden, since 1987 [14, 15] and PDT is nowadays performed on a weekly schedule.

Since the first clinical trials in the 1970s, extensive research has been devoted to improving PDT as a cancer treatment modality. For example, the search for the ideal photosensitiser is ongoing, scientists are still investigating the basic mechanisms behind the photodynamic effect and different dosimetry models are being developed and tested. Interstitial PDT (IPDT), relying on light delivery via thin optical fibres implanted in the tumour, has been developed in order to target also deep-lying and massive tumours.

1.2 Aim and outline of this thesis

Chapters 2-5 are intended to provide an introduction to the work presented in Papers I-VIII as well as to summarise the work of others that is relevant to the understanding of PDT and light propagation in biological media. Hence, Chapter 2 gives an overview

of PDT, its basic principles and the present status of some clinical work. Chapter 3 describes important aspects of commonly used photosensitisers and Chapter 4 introduces the theory of light propagation in scattering and absorbing media. Finally, Chapter 5 presents some PDT dosimetry models.

The papers upon which this thesis is based summarise some of the work performed at the Department of Physics, Lund University, with the aim to improve PDT as a cancer treatment modality for skin and prostate malignancies. Two main objectives, having the use of spectroscopic techniques as the common link, have been pursued; first, the use of a novel liposomal photosensitiser formulation, and second, the development of a system for IPDT with realtime feedback for treatment of prostate malignancies.

For the first task, the pharmacokinetics of the novel photosensitiser formulation were investigated in a murine skin tumour model following topical application. Due to the good selectivity observed in that study, the substance was for the first time evaluated for clinical PDT of various human skin malignancies. The results of these studies are presented in Papers **I** and **II**. Furthermore, the pharmacokinetics of the liposomal photosensitiser formulation were also studied following systemic photosensitiser administration in a murine colon carcinoma model and are presented in Paper **III**. The conclusions from these studies are discussed in the perspective of photosensitiser pharmacokinetics in general in Chapter 3. In particular, the liposomal photosensitiser formulation is compared to its non-liposomal counterpart and to another photosensitiser conventionally used for topical PDT in Sections 3.2.2 and 3.4, respectively.

For the second task, an instrument for IPDT with realtime monitoring of treatment-related parameters was developed and used in a clinical setting. This instrument utilised six optical fibres for both therapeutic light delivery and monitoring of the light transmission, the photosensitiser fluorescence level and the tissue near-infrared (NIR) absorbance. These measurements were included to track the light distribution, the photosensitiser concentration and tissue oxygenation in realtime during a treatment session. A total of ten treatment sessions were performed, mostly of thick non-melanoma skin lesions, at the Departments of Oncology and Dermatology at the Lund University Hospital, Lund, Sweden. Paper **IV** describes the instrumentation and Papers **V** and **VI** focus on analysing the spectroscopic data obtained during the treatment sessions. The hardware was then further adapted to allow for PDT in the prostate gland. In close cooperation with a spin-off company, SpectraCure AB, Lund, Sweden, a novel instrument, incorporating 18 optical fibres, was developed. Furthermore, the software was extended to include pre-treatment dosimetry, as exemplified in Paper **VII**, as well as realtime treatment feedback based on the measured light transmission and a light dose thresh-

old model. This dosimetry model is presented and evaluated in Paper **VIII**. Chapter 5 discusses our realtime IPDT dosimetry module with reference to existing PDT dose models and also provides some initial results on instrument performance.

In addition to discussing the two main objectives, some of the experience gained while working with fluorescence and absorption spectroscopy is incorporated into Sections 3.5, 4.6.2 and 5.5 of this thesis.

Chapter 2

Photodynamic therapy

This chapter provides an introduction to PDT. In Section 2.1 the underlying chemical reactions are discussed and in Section 2.2 the effects these photodynamic reactions induce in *in vivo* biological tissue are described. Finally, the clinical status of PDT is summarised in Section 2.3. Here, emphasis is on PDT for the treatment of skin and prostate malignancies. Besides highlighting its clinical use for these two indications, some of the remaining issues are described. This discussion thus introduces and motivates the work presented in Papers **I** to **VIII**.

2.1 The photodynamic reactions

Photodynamic therapy (PDT) relies on the light-induced activation of a photosensitiser and the subsequent formation of different reactive species, which in turn cause cellular damage. Light with a wavelength tuned to match an absorption band of the photosensitiser excites it from the ground state, S_0, into a higher lying singlet state, S_1; see Figure 2.1. From here, the photosensitiser molecules either relax back down to the ground state or cross into a triplet state, T_1. From the triplet state, the transition back to the ground state is spin-forbidden and hence the lifetime of the excited state is long, allowing the molecule to interact with its surroundings. The two processes that constitute the photodynamic reactions are referred to as Type I and II reactions. Type I reactions, involving electron or hydrogen atom transfer from the triplet state of the photosensitiser to substrates other than oxygen molecules, lead to the formation of highly reactive radicals or radical ions [16]. These radicals most often react with oxygen to form different reactive oxygen species (ROS), followed by the formation of oxygenated products. On the other hand, Type II reactions involve an electron spin exchange between T_1 and ground

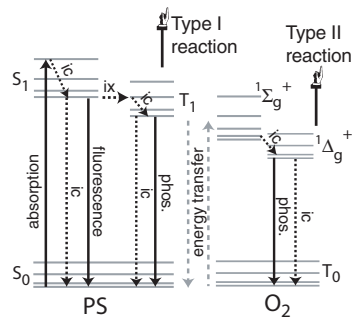

Figure 2.1. *Jablonski diagram illustrating transition processes following absorption of light. PS, photosensitiser; phos, phosphorescence; ic, internal conversion; ix, intersystem crossing.*

state oxygen molecules $^3O_2$, leading to the formation of highly reactive singlet oxygen,$^1O_2$ ($^1\Delta_g^+$) [17]. Both processes, illustrated in Figure 2.1, occur simultaneously and are critically dependent on the presence of oxygen [18, 19]. Because the photosensitiser returns to the ground state, one single photosensitiser molecule can generate manifold reactive species. The relative involvement of either Type I or II processes in the PDT action is influenced by factors such as the biological condition of the target, the type of photosensitiser used and its binding site within the tissue [20]. For example, it has been suggested that hypoxic conditions and/or high photosensitiser concentrations might favour Type I reactions, whereas high oxygen concentrations lead to domination of Type II reactions [16, 21].

Most cellular structures constitute potential targets for the photo-induced oxygen species. For example, in proteins certain amino acids are targeted and in lipids the unsaturated bonds are photo-oxidisable, leading to protein dysfunction, loss of enzymatic activity and membrane damage [16, 22]. Eventually, the PDT-induced functional and structural changes lead to cell death. Due to the extremely high reactivity and short lifetime of the ROS, their site of production, as determined by the localisation of the photosensitiser, primarily dictates which cellular structures are targeted. For example, it has been generally believed that within biological media the diffusion distance of singlet oxygen is of the order of $\sim$10 nm [23]. However, recent results have indicated that in intact cells the $^1O_2$ is not as effectively quenched as one might infer from bulk studies and thus the lifetime of singlet oxygen is much longer than previously believed [24]. This also means that radius of activity of the singlet-oxygen molecule is significantly larger than stated above. The diffusion distance of $^1O_2$ can be compared to the size of a typical living cell, $\sim$10 μm, or the thickness of the cell membrane, $\sim$10 nm, clearly emphasising the importance of localisation of the photosensitiser on the targeted structure. The cellular compartments in which the photosensitiser localise depend on the chemical properties of the photosensitiser, such as its hydrophobicity and charge, as well as on the cell line [25]. For example, lipophilic photosensitisers accumulate in membrane structures such as the mitochondrial, nuclear and plasma membranes as well as the endoplasmic reticulum, whereas hydrophilic photosensitisers mostly accumulate in lysosomes [26].

2.2 Mechanisms behind tissue damage

The tissue damage caused by PDT is usually described in terms of three interdependent mechanisms; direct cell kill, vascular damage and activation of the anti-tumour immune system. These pathways are illustrated in Figure 2.2. The relative importance of

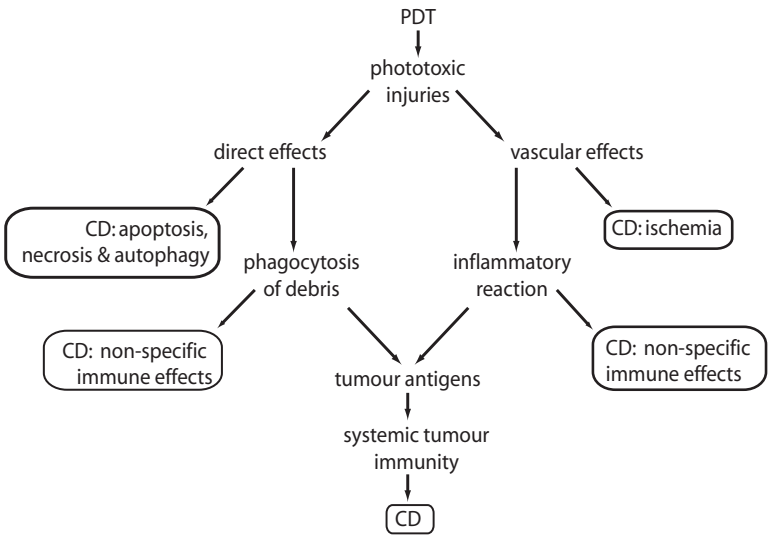

Figure 2.2. *A flow chart illustrating the mechanisms behind PDT-induced tissue damage. Direct effects represent direct tumour cell damage and vascular effects denote damage to epithelial cells in the vascular system. CD: cell death.*

each mechanism depends on the intra-tumoural localisation of the photosensitiser, which is dictated by the mode of drug delivery, the time between photosensitiser and light administration, also referred to as the drug-light interval (DLI), the chemical character of the photosensitiser, the tissue vascularisation and the rate of light delivery. This complex interplay is not yet fully understood but one has observed that the long-term treatment effect is dependent on all three effects [20, 27, 28].

2.2.1 Direct effects

Direct PDT effects on cells most often comprise a combination of apoptosis and necrosis [29, 30]. Usually, apoptosis precedes necrosis but the exact time course, the tissue volume affected and the relation of apoptotic versus necrotic volume depend on the photosensitiser [31], cell type and light dose [32]. Apoptosis can be described as programmed cellular suicide and is a natural process carefully controlled by intra- and extracellular signals. It is considered a "clean" death path since any residual cell components are incorporated into apoptotic bodies which are thereafter engulfed by macrophages. This process, most often initiated following minor cell damage, prevents tissue inflammation. On the other hand, necrosis results from higher levels of cell damage and leads to a pronounced inflammatory response [31, 33]. Typical

features of apoptosis are nuclear condensation, plasma membrane blebbing and appearance of apoptotic bodies, whereas necrosis is characterised by cell swelling, rupture of membranes and loss of chromatin [34]. Following PDT, the zone of necrosis is sharply delineated, a fact that has led to the development of a threshold dose model; see further Section 5.2. On the other hand, apoptosis can be observed beyond this necrotic boundary [31]. These peripheral regions have been exposed to lower light doses and thus it appears that the more acute the damage, the more the path towards cell death is shifted in favour of necrosis [30–32]. An interesting feature of PDT-induced apoptosis is that it appears able to overcome the resistance to radiation and chemotherapy expressed by some cells [32]. In general, apoptosis is initiated and controlled via four main components; the mitochondria, a family of proteases called caspases, activation of certain cell surface receptors and the Bcl-2 family proteins. The overall biological response to PDT probably involves all these components to varying degrees, but it has been shown that photosensitisers that bind to mitochondria are especially effective in inducing apoptosis [32]. Conversely, photosensitisers that accumulate within lysosomes and plasma membranes cause less damage and usually by non-apoptotic pathways [32, 35]. It is also known that PDT initiates a highly complex series of signalling events out of which some contribute to the cell death, whereas others antagonise this process. The possibilities of modulating the treatment outcome at the molecular level are attracting increasing attention [36, 37].

Autophagy is a third process in which cells are directly damaged by PDT [38]. Autophagy, which was initially considered a survival response following nutrient deprivation, is similar to apoptosis in that it can also be considered a type of programmed cell death. This process involves encasing cell organelles in vacuoles that fuse with lysosomes in order for their content to be digested and recycled. It appears that autophagy can act either as a survival or a death route following PDT [38].

2.2.2 Vascular damage

In 1911, Hausmann was one of the first to observe PDT-induced vessel damage [39]. Furthermore, in 1985 Henderson *et al.* established the significant role of vascular damage for the total PDT effect by comparing the treatment volumes of tumours remaining in the host to those being excised and explanted following irradiation [40]. The latter group was nearly unaffected by the treatment and this led to the conclusion that damage to circulation in the tumour is an important aspect of PDT. This observation was soon confirmed by others and the importance of also targeting vessels within a certain margin of normal, surrounding tissue was highlighted [41].

The vascular photosensitivity is related to the level of circulating photosensitiser [42]. Thus, a short DLI results in pronounced vascular damage whereas a longer DLI allows the photosensitiser to diffuse further away from the blood vessels, thereby increasing the relative importance of direct effects as described in Section 2.2.1 [43–45]. Furthermore, hydrophilic photosensitisers mostly accumulate in the vascular stroma [46, 47] and hence cause more vascular damage than do lipophilic photosensitisers [48, 49]. The endothelial cells are believed to be important to the vascular effect [27, 50, 51]. Following the light-induced oxidation, the cytoskeleton of these cells is rearranged, leading to an altered cell shape. As the tight junctions between the endothelial cells are lost the base membrane is exposed, which induces platelet binding and aggregation. This process further promotes release of, for example, thromboxane, an eicosanoid that is known to cause vessel constriction, further platelet aggregation and thrombus formation. The blood flow is thus stopped and the ensuing hypoxia and nutrient deprivation induce local tissue damage.

The hypoxia resulting from the vascular collapse and the oxygen consumption of the photodynamic reaction itself might render cells resistant to further PDT damage [52]. Such hypoxic conditions have been observed experimentally [53, 54] and much work has therefore focused on monitoring tissue oxygenation and blood flow during the PDT treatment; see Sections 5.2 and 5.4.

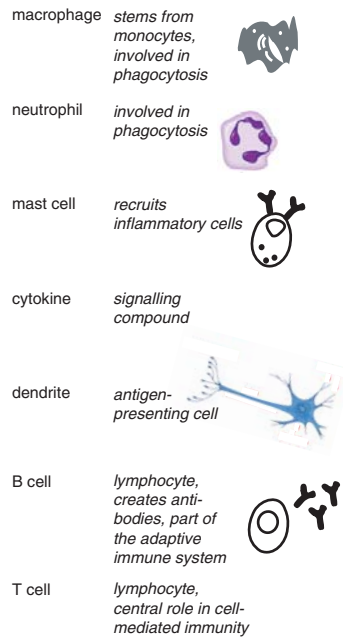

Figure 2.3. *Selected components of the innate and adaptive immune system and their respective roles.*

2.2.3 The immune response

Many commonly used cancer treatment modalities display pronounced immunosuppressive effects. Although some components of the host immune system are known to be sensitive to PDT, the PDT-induced systemic anti-tumour immune response is believed important for the long-term tumour control [55, 56]. PDT causes acute inflammation that triggers activation of tumour-specific components of the immune system. This two-step process is similar to the sequence of events following microbial invasion of healthy tissue. In the early inflammatory phase, which is induced primarily by the vascular PDT-effects as described in Section 2.2.2, the treatment site is rapidly invaded by neutrophils [57], cytokines, mast cells, monocytes and macrophages [55, 56, 58]. Figure 2.3 illustrates these components of the host immune system. One of the roles of the macrophages is to remove cells damaged via the direct PDT effects; see Section 2.2.1. The macrophages, together with antigen-presenting cells such as dendritic cells and B cells, will process and present tumour-specific antigens, a process that further promotes the production of tumour-specific, cytotoxic T lymphocytes [58]. This process constitutes one path towards the development of a systemic tumour immunity. Evidence for such systemic tumour immunity has been published by, among others,

Korbelik *et al.*, who demonstrated that tumour-sensitised immune cells could be recovered from lymph nodes distant from the treated lesion at varying times post PDT [59]. Furthermore, the tumour response to PDT was compared between normal and immunocompromised mice with poor long-term tumour control reported for the latter group [60]. However, this effect could be reversed by bone-marrow transplants from immunocompetent animals, further emphasising the importance of the immune response is important for eliminating those cancer cells surviving the more imminent effects of PDT. This conclusion is also supported by the observation that distant, untreated metastases can regress following the PDT treatment of the primary lesion [61].

An interesting approach to cancer treatment suggests producing cancer vaccines by performing *in vitro* PDT of cell cultures. It has been shown that by injecting mice with a tumour-cell lysate isolated from such cell cultures treated with PDT, these animals became resistant to developing multiple tumours [62]. This effect was more pronounced for the PDT-produced vaccine than lysates resulting from ultraviolet (UV) or ionising radiation. Another promising concept is to combine PDT with immunotherapy in order to improve overall tumour cures. Strategies that are being investigated involve intra-tumoural injection of an agent that stimulates the innate immunity, i.e. the non-specific defence against pathogens, or systemic administration of substances, such as cytokines and regulatory T cells, that alter or augment different parts of the immune system on the molecular or cellular level [55]. However, more research is needed before PDT-produced vaccines or combination therapies can be benefitted from clinically.

2.3 Clinical use

Since first coining the term "photodynamic therapy" more than 100 years ago, PDT has acquired clinical approvals for treatment or palliation of some malignant and non-malignant indications and many more trials have investigated its use for numerous other indications. This section will give a brief introduction to the clinical use of PDT. Far from all contributions in bringing PDT into the clinic are included, instead approved indications and promising clinical trials for some advanced cancers are taken up. The clinical work in this thesis is related to skin and prostate cancer and hence Sections 2.3.1 and 2.3.2 describe PDT for these two indications in more detail.

In contrast to radiation therapy, PDT can be repeated without cumulative toxicity. PDT might thus play an important role for tumours recurring after radiotherapy or surgery as these patients are often not eligible for further radiation or surgery [43]. PDT also has the potential of being a truly local treatment as the simul-

Table 2.1: Approved PDT agents, corresponding indications and countries of approval.

Photosensitiser	Indication	Country
Photofrin	lung cancer	Canada, Denmark, Finland, France, Germany, Ireland, Japan, The Netherlands, UK, U.S.
	gastric cancer	Japan
	cervical cancer	Japan
	bladder cancer	Canada
	oesophageal cancer	Canada, Denmark, Finland, France, Ireland, Japan, The Netherlands, UK, U.S.
	Barrett's HGD	Canada, EU, U.S.
mTHPC	head & neck cancer	EU, Norway, Iceland
ALA	AK	U.S.
m-ALA	AK, BD	EU
	BCC	EU
BPD	AMD	Canada, U.S.

taneous presence of light, photosensitiser and oxygen is required. Appropriate light delivery systems can be utilised to tailor the light distribution to the target tissue [63, 64] and the use of green light as the activating radiation can limit the treatment depth in the case of thin, superficial lesions [65]. Furthermore, some photosensitisers display tumour-selective uptake, as will be discussed in Section 3.1.2, further promoting treatment selectivity. Additional advantages of PDT include preservation of the tissue structure [43], good cosmetic outcome [66, 67] and cost-effectiveness [65]. In contrast to radiotherapy and many cytotoxic drugs used for cancer treatment, PDT induces only a limited effect on DNA and therefore is not considered cancerogenic. This has been explained by the fact that most photosensitisers accumulate outside the cell nucleus and do not readily bind to DNA [21, 68].

Since the early days of PDT, it has attracted particular interest for the treatment of superficial malignancies, since for lesions of the skin or within hollow organs PDT can be applied non-invasively. PDT utilising the photosensitiser Photofrin was first approved for the treatment of bladder cancer in 1993. This approval was soon followed by others, such as Photofrin-mediated PDT for lung, cervical and oesophageal cancer. Table 2.1 lists approved PDT photosensitisers together with their corresponding indications. For hollow organs, illumination is provided utilising flexible cylindrical diffusers inserted through an endoscope. As PDT preserves the mechanical integrity of connective tissue structures it is characterised by much improved long-term functional and cosmetic outcomes [65].

Table 2.2: Selected clinical PDT trials on advanced cancers.

Indication	Photosensitiser	Ref.
liver	HpD	[73, 74]
pancreas	mTHPC	[75]
brain	HpD, Photofrin	[76–78]
	ALA	[79, 80]
mesothelioma	mTHPC	[81]
peritoneum	HpD	[82]

Although not a malignant indication, the use of PDT for the treatment of age-related macular degeneration (AMD) and other eye diseases related to choroidal neovascularisation (CNV) should be mentioned due to its widespread use. In CNV, blood vessels start to grow in the retina, leading to irreversible loss of the central vision field. PDT, often relying on the use of benzoporphyrin derivative (BPD, trade name: Verteporfin), aims at permanently destroying these abnormal blood vessels. Recently published results from European and North American multi-centre trials have led to recommendations of BPD-PDT for the treatment of subfoveal lesions with certain CNV growth patterns [69, 70].

Table 2.2 presents a few selected clinical PDT trials for some additional advanced cancerous indications. Due to the advantages already discussed, PDT constitutes a treatment option that might become valuable for these indications. For reviews on clinical PDT, the reader is referred to Refs. [65, 71, 72].

2.3.1 PDT for skin disorders

Non-melanoma skin cancer (NMSC) is the most common malignancy in the Caucasian population and displays increasing incidence rates. For NMSC, including basal cell carcinomas (BCC), squamous cell carcinomas (SCC) and Bowen's disease (BD), as well as for non-cancerous indications such as actinic keratosis (AK) the cosmetic outcome, patient preference and ease of treatment are important factors in selecting the appropriate treatment. Conventional therapies include surgical resection, ionising radiation, cryosurgery, Mohs' micrographic surgery, curettage and electrodesiccation and are associated with different degrees of scarring, fibrosis, altered pigmentation and extended healing times.

PDT has been used successfully in the treatment of NMSC and its use is widespread due to the good or even excellent cosmetic outcomes. Furthermore, this treatment method is non-invasive, easy to use and applicable for lesions covering large areas. Although the limited penetration depth of the activating light might increase the risk of recurrences within deeper lying tissue regions, for some applications it leads to a natural protection of the normal tissue below the tumour. The general photosensitivity remain-

Table 2.3: Recently published recommendations for the use of ALA-PDT in the treatment of skin diseases [67].

Indication	Typical CR	Recommendation
sBCC	80-97%	AI
nBCC	70-91%	AI
SCC	40%	CIIiii
AK	69-100%	AI
BD	83-100%	AI

ing after systemic administration of many photosensitisers can be avoided by utilising topical application of the photosensitiser precursor amino-laevulinic acid (ALA). As a part of the heme biosynthesis, ALA is converted into the actual photosensitiser protoporphyrin IX (PpIX) [83]; see further Section 3.3. Different ALA ester derivatives have been developed to improve biological availability and skin permeability. One of these, methyl amino-laevulinate (m-ALA), is marketed as Metvix and Levulan in Europe and the U.S, respectively. ALA or m-ALA is often applied as a cream for three to 18 hours [67] leading to good tumour-selective uptake of PpIX [83, 84]. Drawbacks of ALA- or m-ALA-PDT include the treatment-related pain [66, 85] and limited treatment depths [83, 86, 87].

Topical ALA-PDT for BCC, SCC and AK was first performed in a clinical setting in 1990 [88]. Today, it is widespread and offered as a standard procedure at numerous hospitals including the Lund University Hospital. This section will try to reflect the great progress ALA-PDT has made in becoming an accepted treatment option for NMSC by quoting a recently published recommendation [67] from a meeting of the International Society for Photodynamic Therapy in Dermatology[1]. Table 2.3 lists some common indications, typical CR following PDT and the evidence-based recommendations. The scoring system for strength of recommendations is illustrated in Figure 2.4. BCCs rarely metastasise and are classified as either superficial (sBCC) or nodular (nBCC). Large phase III trials have proved ALA- or m-ALA-PDT to be a good treatment option for sBCC with 80 to 97% CR [67, 83]. nBCCs are typically thicker than sBCC and result in slightly lower CR. PDT for BCCs is given the highest recommendation as it results in good cosmetic outcome and long-term treatment efficacy. In contrast to BCCs, SCCs are potentially metastatic. Initial CR following PDT are usually high (54 to 100%) but so are recurrence rates. For this indication, PDT does not display any advantage over conventional treatment options and is therefore given a much lower rating. Also for AK, constituting the most common premalignant skin lesion, and BD, presenting as SCC *in situ*, PDT receives the highest rec-

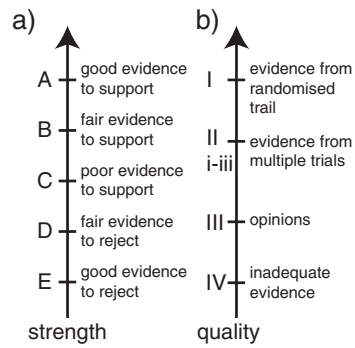

Figure 2.4. ***a)*** *Strength of recommendations together with* ***b)*** *quality of evidence [67].*

[1]The society homepage at http://www.euro-pdt.com/index.html.

ommendation, a great extent due to good cosmetic outcome and high CR.

However, for nodular and thicker skin malignancies, ALA-PDT is associated with lower treatment efficacy [83]. Numerous factors contribute to the limited CR. First, the longest possible wavelength used for activating the photosensitiser falls within the spectral region where blood absorption is relatively strong and thus the penetration depth of the therapeutic irradiation is restricted [86]. Also, the absorption coefficient of the photosensitiser at this wavelength is relatively low [89]. The importance of these two effects will be further discussed in Section 3.1.1. Furthermore, the penetration depth of the ALA molecule itself might also limit treatment depths [87]. Other photosensitisers have therefore been evaluated for the treatment of skin malignancies; HpD [90], BPD [91] and meso-tetra(hydroxyphenyl)chlorin) (mTHPC) [92]. However, the systemic administration route used in these studies led to high levels of generalised photosensitivity as well as poor tumour-selective uptake. Section 3.4 will discuss further efforts towards improving PDT for topically applied photosensitisers.

2.3.2 PDT for prostate cancer

In contrast to PDT for skin malignancies, prostate-PDT has not been as thoroughly studied and has not yet reached the same clinical status. The feasibility of utilising PDT for the treatment of prostate cancer was first investigated in pre-clinical, canine studies. The pharmacokinetics of photosensitisers such as mTHPC [93], ALA-induced PpIX [94] and Pd-bacteriopheoporbide (WST09) [95] as well as the respective treatment-induced areas of necrosis were investigated. It was concluded that PDT was capable of inducing significant necrotic volumes within the prostate while maintaining the glandular volume and shape. Furthermore, these studies reported on only transient or minor urethral complications, giving some evidence that the urethra is not a very sensitive organ with regard to PDT.

Conventional therapies for prostate cancer include radical treatments such as surgery, external and internal beam radiation therapy (also referred to as brachytherapy) as well as hormonal therapy, cryotherapy and thermotherapy [96]. For these methods, the CR is usually high but side-effects such as incontinence and erectile dysfunction are common due to the destruction of many surrounding organs during the treatment. PDT is thus being investigated as a treatment alternative for which one hopes for equally high treatment efficacy but better discrimination between target tissue and organs at risk (OAR). Today, prostate-PDT most often relies on light delivery via transperitoneally inserted cut-end optical fibres or cylindrical diffusers. As for brachytherapy, the positioning of the sources is facilitated by hollow steel catheters,

trochars, an external positioning grid and a transrectal ultrasound probe as illustrated in Figure 2.5.

Utilising the photosensitiser mTHPC and light delivery via cut-end fibres, Bown *et al.* [97–99] have performed PDT in secondary and primary prostate cancer. Figure 2.6 shows contrast enhanced magnetic resonance images (MRI) for a patient with primary prostate cancer prior to and at four days and two months after light delivery. mTHPC-PDT proved capable of inducing significant volumes of necrosis and decreasing prostate-specific antigen (PSA) levels. Treatment-related complications consisted of transitory irritative voiding symptoms, stress incontinence and slight deterioration of (however, impaired already pre-PDT) sexual function. For both secondary and primary cases, PSA levels eventually started to increase again and evidence of viable cancer tissue post-PDT could be observed in all patients. ALA-PDT has been investigated by Sroka *et al.* [94] for primary prostate cancer patients, resulting in decreasing PSA levels (20-80%) without any evidence of incontinence or dysuria after PDT. Furthermore, at the University of Toronto the vascular-targeted photosensitiser WST09 is being investigated for recurrent prostate cancer [100, 101]. Phase I/II clinical trials have investigated escalated light and drug doses. In a recent publication by Haider *et al.* [102] MRI post-PDT indicated treatment-induced necrosis and sparing of the neurovascular bundles in all 25 patients. On the other hand, the PSA levels assessed at four and twelve weeks after therapy showed poor correlation to the intra-prostatic necrotic volume. Finally, at the University of Pennsylvania it has been concluded that PDT utilising motexafin lutetium (MLu) is an attractive and safe treatment option associated with only mild and transient toxicity [103].

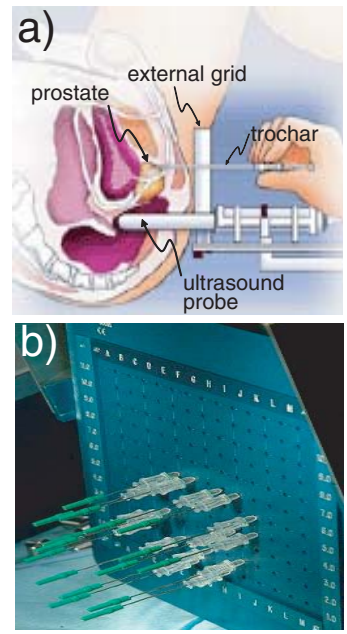

Figure 2.5. ***a)*** *Illustration of source fibre insertion aided by trochars, a transrectal ultrasound probe and an external grid.* ***b)*** *Photograph of the external grid.*

The clinical prostate-PDT studies cited above give evidence of significant intra- and inter-patient variations of the light-induced tissue necrosis. A possible explanation lies in the observation of varying light levels, photosensitiser and oxygen concentrations and the heterogeneous optical properties of the tissue [103]. The development of instrumentation and dosimetry models that include realtime monitoring of parameters important to the treatment outcome has recently received increasing attention [100, 104]. Furthermore, a more detailed photosensitiser and light dosimetry might lead to better discrimination between target tissue and surrounding sensitive organs. The concept of individualised realtime treatment feedback is along the lines described in Papers **VII** and **VIII** as will be discussed in greater detail in Section 5.5.3.

To summarise the referenced prostate studies, PDT seems to be a safe treatment modality capable of inducing significant tissue necrosis in the prostate with only minor and transient complications. The drawback of the prolonged generalised photosensitivity can be avoided by utilising WST09 and ALA-induced PpIX due to the rapid clearance of these PDT agents as compared to for ex-

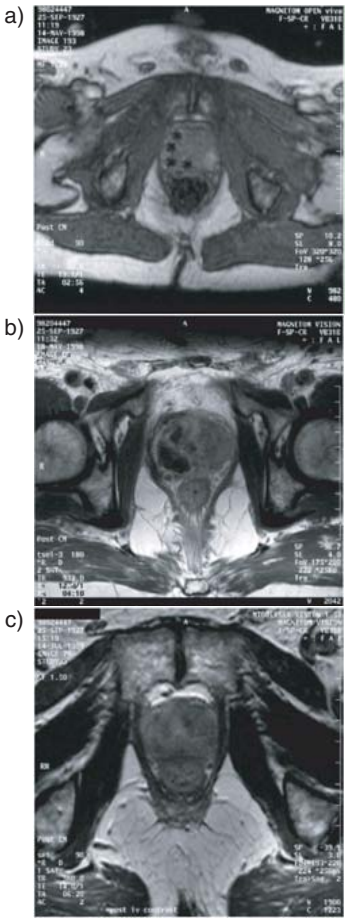

Figure 2.6. *Contrast enhanced MRI of a primary prostate cancer* ***a)*** *prior to,* ***b)*** *four days and* ***c)*** *two months after PDT. In* ***a)*** *the four optical fibres used for light delivery can be seen. In* ***c)*** *the enhancement pattern indicates progressed healing with resolved necrosis and little effect on connective tissue. The figure has been adapted from Ref. [97].*

ample mTHPC and MLu. Utilising WST09, the photosensitiser is actually administered intravenously in parallel with the delivery of the therapeutic irradiation [100]. However, such short drug-light intervals might negatively influence the tumour-selective photosensitiser distribution as will be discussed in Section 3.1.2. At the moment, clinical work is in the process of evaluating the long-term effects of prostate-PDT, the feasibility of targeting either the full gland or only the cancerous sites and the possibility of introducing individualised dosimetry.

Chapter 3

Photosensitisers

Over the decades it has become increasingly obvious that the concept of the "optimal" photosensitiser is quite controversial. Often different indications and treatment situations require conflicting photosensitiser characteristics. Some of these properties are discussed and put in relation to existing photosensitisers in Section 3.1. In Sections 3.2 and 3.3 the photosensitisers used in this thesis, i.e. mTHPC and ALA-induced PpIX, are discussed in greater detail. In particular, the pharmacokinetics of a liposomal mTHPC formulation, presented in Paper **III**, are discussed and compared to that of the conventional mTHPC formulations in Section 3.2.2. Alternatives for improving PDT with topically administered photosensitisers are discussed in Section 3.4 in which the conclusions from Papers **I** and **II** are also summarised. Finally, in Section 3.5 fluorescence in general, and mTHPC and PpIX fluorescence in particular, is presented as a tool for concentration measurements, tissue diagnosis and PDT dosimetry.

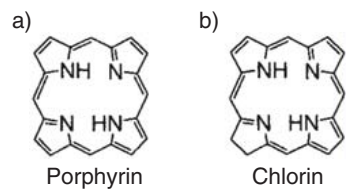

Figure 3.1. *The basic chemical structures of* ***a)*** *porphyrin and* ***b)*** *chlorin.*

3.1 Optimal versus existing photosensitisers

This section presents some photophysical, chemical and pharmacological properties of an ideal photosensitiser [49, 105–108] and relates these characteristics to a few selected photosensitiser families. These photosensitiser groups, presented in Table 3.1, are all based on multiple planar-aromatic molecules containing several conjugated, i.e. alternating single and double, bonds. The basic chemical structures of porphyrin and chlorin, to which PpIX and mTHPC belong, respectively, are shown in Figure 3.1. By varying the chemical composition of sidechains and introducing metallation with different metal atoms, the photophysical, chemical and pharmacological properties of the compound are affected.

Table 3.1: Photophysical properties of a few selected photosensitisers, PS. λ: longest absorption wavelength, ε: extinction coefficient, Φ_t: triplet state yield, Φ_Δ: singlet-oxygen yield, Φ_{fl}: fluorescence yield.

PS	λ (nm)	ε ($M^{-1}cm^{-1}$)	Φ_t	Φ_Δ	Φ_{fl}
Porphyrins:					
PpIX	633	5000	0.6		
Photofrin	630	1170	0.2-0.3	0.89	<0.1
Chlorins:					
mTHPC	652	22400	0.3-0.43	0.89	
BPD	690	35000	0.68	0.84	0.1
Bacteriochlorins:					
WST09:	740	32000		0.99	≤0.01
Phthalocyanines:					
AlS_2Pc	680	110000	0.2-0.6	0.3-0.6	0.08-0.35
AlS_4Pc	680	110000	0.2-0.6	0.38	0.3-0.5
Texapyrins:					
MLu	734	42000			

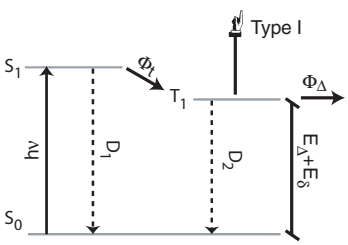

Figure 3.2. *A simplified Jablonski diagram illustrating possible transitions following light absorption. Dashed lines (D_1 and D_2) collectively indicate processes that quench the induction of ROS. h is Planck's constant, c is the speed of light and the other symbols have been explained in relation to Table 3.1.*

3.1.1 Photophysical characteristics

The photophysical properties of a photosensitiser influence its production efficiency of singlet oxygen. Following absorption of light, a series of energy transitions need to take place in order to induce $^1O_2$; see Section 2.1. Some of the processes are repeated in the simplified Jablonski diagram in Figure 3.2.

Firstly, the extinction coefficient, ε, at the therapeutic wavelength, controlling the transition $S_0 + h\nu \rightarrow T_1$, needs to be high to efficiently excite the photosensitiser and decrease the light and drug doses required. Photosensitiser absorption at long wavelengths increases treatment depth due to the lower light attenuation in the red and NIR wavelength regions. Typical absorption spectra are illustrated in Figure 3.3 for two different tissue types. The dependence of the light transmission on wavelength will be further discussed in Section 4.5. However, for Type II reactions the therapeutic wavelength should correspond to an energy exceeding that of the singlet-oxygen state, i.e. E_Δ=0.97 eV, plus the energy gap between the excited photosensitiser S_1 and T_1 states, E_δ=0.5-0.6 eV [106]. Thus, the excitation wavelength should not exceed approximately 850 nm to efficiently induce the production of $^1O_2$. Furthermore, absorption bands between 400 and 600 nm should be avoided to minimise the risks associated with generalised photosensitivity and sunlight. On the other hand, when treating superficial malignancies in the oesophagus, for example, green light is desirable in order to limit the penetration depth and avoid perforation of mucosal membranes [109].

Due to the reduction of one or two double bonds, the chlorins

and bacteriochlorins have 20 and 18 delocalised π electrons in the aromatic ring, respectively, as compared to 22 for porphyrins. In analogy to the square-well potential, the Schrödinger equation can be used to describe the energy levels of these systems [21];

$$E_l = \frac{h^2(l+1)^2}{8mW^2} + E(l,N) \quad l = 1,2,\ldots \quad N = 1,2,\ldots \tag{3.1}$$

Here, l is the energy state, m is the electron mass and W is the width of the square well, assumed to be constant for the different photosensitiser ring systems. The term $E(l,N)$ denotes the electron-electron interaction which acts to decrease the binding energy of the excited energy levels within the well. Figure 3.4 is an oversimplified energy level diagram for two systems to illustrate the higher energy required for the excitation from the ground state in systems with an increasing number of delocalised electrons. Thus, the blue-shifted absorption bands of porphyrins as compared to chlorins and bacteriochlorins, see Table 3.1, can be explained. Metallation of the chlorin or bacteriochlorin molecules also acts to red-shift and strengthen their absorption within the red [108].

The triplet state yield, Φ_t, controlling the conversion $S_1 \rightarrow T_1$, the lifetime of the triplet state, τ_t, as well as the yield of singlet oxygen, Φ_Δ, influencing the pathway $T_1 + {}^3O_2 \rightarrow {}^1O_2 + S_0$, should be high. In general, metallation influences these conversion efficiencies as well as the lifetime of the triplet state. For example, adding aluminium or another diamagnetic cation improves the Φ_t and τ_t of the phthalocyanines, whereas the compound ZnPc has essentially zero yield of singlet oxygen [108].

The dashed arrows in Figure 3.2 indicate various decay processes that act to lower Φ_t and Φ_Δ. In particular, the transition $S_1 \rightarrow S_0$ might give rise to fluorescent light with a quantum efficiency of Φ_{fl}. Despite the fact that this process decreases the triplet state yield, it constitutes an attractive feature as the fluorescence can be utilised as a tool for tissue diagnosis, photosensitiser pharmacokinetics and PDT dosimetry as will be described in Section 3.5. For optimal fluorescence studies, the photosensitiser should exhibit tumour-selective uptake, little dependence of the fluorescence yield on the chemical environment and a characteristic fluorescence spectrum that is easily resolved from the tissue autofluorescence, i.e. the fluorescence originating from naturally occurring chromophores. In addition, the photosensitiser should fluoresce at >650 nm to minimise the influence of absorption by haemoglobin. Finally, photosensitiser absorption bands at both short and long wavelengths provide the possibility to probe either very superficial or deeper lying tissue regions. The term photobleaching refers to the oxidation of ground state photosensitiser molecules by the light-induced ROS [108, 112], leading to a consumption of the photosensitiser during the therapeutic irradiation.

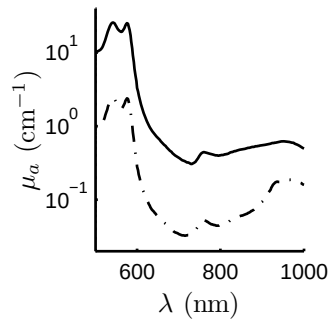

Figure 3.3. *Typical absorption spectra, μ_a, of prostate (solid line) and breast (dashed line) tissue. The following data were used for deriving μ_a; Prostate:* [Hb] = 65 μM, [HbO] = 150 μM, $\mu_s'(660\,nm) = 9\ cm^{-1}$ *[110],* [water] = 30% *and* [lipids] = 5%. *Breast:* [Hb] = 5 μM, [HbO] = 15 μM, $\mu_s'(660\,nm) = 8\ cm^{-1}$ *[111],* [water] = 30% *and* [lipids] = 50%.

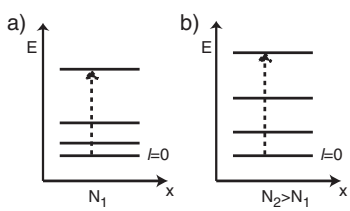

Figure 3.4. *Energy level diagram for* ***a)*** *N_1 and* ***b)*** *N_2 delocalised π electrons.*

The ability to photobleach has been suggested to promote tumour-selective treatment, provided that the photosensitiser concentration is higher in the tumour than in normal tissue. In this case, the photosensitiser might be photodegraded before a sufficient amount of ROS has been created, thus protecting tissues characterised by low photosensitiser concentrations [106, 112].

3.1.2 Biological distribution

A high tumour-selective uptake with low levels of systemic toxicity is perhaps the most essential characteristic of a good photosensitiser. Furthermore, a fast distribution and rapid clearance would limit the treatment to one single hospital visit and avoid the risk of prolonged general photosensitivity. Finally, the photosensitiser should be stable, chemically pure and exhibit no dark toxicity. All these properties, some of which are discussed below, are influenced by the chemical composition of the photosensitiser, its hydrophobicity, charge, polarity and molecular size.

Opposing photosensitiser characteristics may present different advantages from the perspective of achieving good PDT efficacy. For example, the choice between a hydrophilic and lipophilic photosensitiser is not obvious. Photosensitisers belonging to the former group are easily dissolved and do not aggregate, i.e. form dimeric or oligomeric compounds, in aqueous media. Aggregation effectively shortens the triplet state lifetime, decreases the yield of singlet oxygen, alters the absorption properties and influences the distribution within biological media. An aggregated substance often constitutes a less efficient photosensitiser. On the other hand, lipophilic photosensitisers are known to localise intracellularly, thus reaching biological structures that constitute more effective targets for the photodynamic action [26, 28, 46, 47], and they generally exhibit a higher quantum yield of singlet oxygen [26, 28]. Amphiphilic photosensitisers, i.e. photosensitisers that possess both hydrophilic and lipophilic properties, have been suggested to constitute near-optimal photosensitisers [21]. These substances are less prone to aggregate than are lipophilic photosensitisers and they are able to efficiently bind to important PDT targets, such as proteins at the interface between hydrophobic and hydrophilic regions of membranes [113]. Amphiphilic photosensitisers have been shown to be more photodynamically active than photosensitisers exhibiting either hydrophilic or lipophilic characteristics [114].

Most photosensitisers induce general photosensitivity that remains for hours to months following systemic administration. When supplied via the blood, photosensitisers accumulate in organs rich in reticulo-endothelial components, i.e. phagocytic cells. The highest photosensitiser levels are thus found in the liver, spleen and kidneys followed by the lungs and heart, skin and muscle and

finally brain tissue [115–117]. The fibrous tissue matrix, consisting of collagen, elastin and reticular fibres, also displays photosensitiser accumulation. The high uptake in skin constitutes a major drawback of many existing photosensitisers, leading to limited tumour-to-skin concentration ratios ($\leq$1:1 to 2:1 [116]).

Although largely dependent on photosensitiser and tissue type, photosensitiser retention and treatment-induced tissue damage are thus far from tumour-selective [118]. The sometimes observed selectivity is most likely not due to any particular property of the tumour cells as compared to normal cells but rather due to certain physiological prerequisites that promote photosensitiser accumulation within tumour tissue [119]. For example, tumours are often characterised by decreased pH, a condition that renders a photosensitiser more water soluble and increases retention [120]. A leaky vasculature [121] and poor lymphatic drainage [121] further promote accumulation and retention in tumour tissue. Furthermore, tumour-associated macrophages are capable of accumulating large amounts of aggregated photosensitiser [122]. Increased selectivity can also be achieved for photosensitisers that bind to low-density lipoproteins (LDL) [49, 123, 124]. LDL are serum lipoproteins that transport cholesterol and triglycerides to cells. Due to their rapid proliferation, cancer cells present an increased number of LDL receptors. Lipophilic photosensitisers bind more readily to LDL than do hydrophobic dyes, thus promoting tumour-selective uptake via LDL receptor-mediated endocytosis. By pre-associating the photosensitiser with LDL [123, 125] or incorporating it into liposomes [126–129], which interact with serum lipoproteins, an improved tumour-selective uptake has been observed. Section 3.2.2 will focus on the pharmacokinetics of liposome-encapsulated mTHPC. Other strategies for improving tumour-selective localisation are based on active targeting, realised for example by linking either the photosensitiser [127] or the liposome encapsulating the photosensitiser [126] with antigen-specific monoclonal antibodies. Finally, the time interval between photosensitiser and light delivery also affects the treatment selectivity. As already mentioned in Section 2.2.2, a longer DLI allows the photosensitiser more time to diffuse out of the blood vessels and into the surrounding tissue, thus increasing tumour selectivity. However, some uncertainties remain as to whether longer DLI actually improves treatment response. Tissue regions at larger distances from the oxygen-supplying blood vessels might quickly become hypoxic during therapeutic irradiation, thus effectively halting further PDT action [49, 130].

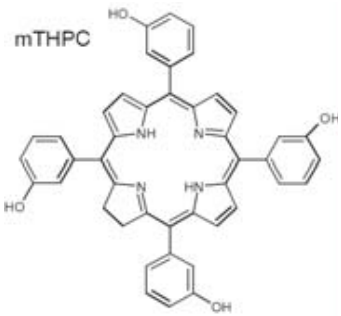

Figure 3.5. *The mTHPC molecule.*

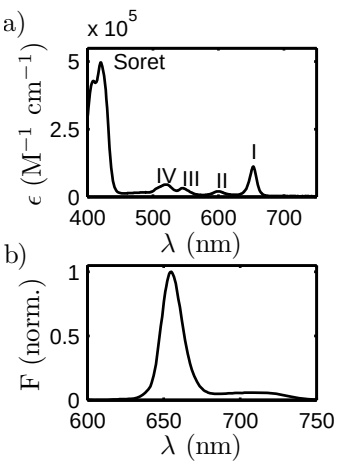

Figure 3.6. ***a)*** *$\epsilon_{\mathrm{mTHPC}}$ with the absorption bands indicated.* ***b)*** *mTHPC fluorescence following excitation at 405 nm.*

3.2 Temoporfin

The molecular structure of mTHPC is illustrated in Figure 3.5. The extinction coefficient and fluorescence spectrum following excitation at 405 nm are shown in Figure 3.6 for mTHPC dissolved in ethanol[1]. mTHPC is one of the most potent photosensitisers in clinical use today and displays phototoxicity exceeding that of HpD by a factor of 100-200 [131]. This can be partly attributed the higher extinction coefficient, the longer treatment wavelength, the slightly higher triplet and singlet state yields and a remarkably tight intracellular binding [131, 132]. In addition, mTHPC results in shorter periods of generalised photosensitivity than does HpD [92, 133]

3.2.1 Pharmacokinetics

mTHPC localises at intracellular sites that are typical for hydrophobic and amphiphilic [114] photosensitisers, i.e. within membranes of mitochondria [134], endoplasmic reticulum and the Golgi apparatus [135]. Recently, localisation in the nuclear envelope has also been observed [136].

Animal models, such as mice, rats, hamsters, dogs and rabbits, are extensively used to study photosensitiser pharmacokinetics with the aim to optimise clinical drug and light delivery conditions. Although it is often impossible to directly extrapolate accumulation and elimination rates from animal to man [138], much knowledge is gained on the general distribution pattern of the photosensitiser. For example, pharmacokinetic studies following systemic administration of mTHPC in mice indicate rapid clearance from the plasma and high levels in organs of the reticuloendothelial system (RES), such as the liver, spleen and lungs, for short times after photosensitiser administration [117, 137, 139, 140]. Maximum concentration in the tumour, skin and muscle is usually achieved later, i.e. one to two days after photosensitiser administration [139, 140]. At these relatively long DLI the selectivity between tumour and surrounding skin/muscle peaks. Figure 3.7 shows typical mTHPC levels in different organs following systemic photosensitiser administration in a murine tumour model [137].

Quite surprisingly, the correlation between the intra-tumoural mTHPC levels and the resulting PDT efficacy is poor [137, 141]. Instead, maximum PDT effect is observed for short DLI, when the photosensitiser concentration within the blood stream is high [141, 142]. PDT performed shortly after drug administration results in pronounced overtreatment of normal, surrounding tissues and little true treatment selectivity whereas irradiating at the later time point generates better selectivity [143]. These observations

[1]Data were provided by biolitec AG, Jena, Germany. http://www.biolitec.com

indicate that mTHPC-mediated PDT is capable of inducing both vascular damage, which is pronounced at early times post injection, and direct cell kill, as evident at longer DLI when the photosensitiser has diffused out of the blood vessels into the surrounding tumour tissue [144, 145]. More recent reports have confirmed these observations in clinical treatment situations [92, 146].

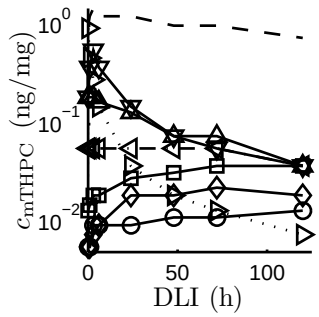

Figure 3.7. *mTHPC concentration following systemic administration of 0.3 mg/kg b.w. [137]. ◇: tumour, ○: muscle, □: skin, ▽: liver, △: lung, –: kidney, ◁: heart, ▷: blood.*

3.2.2 Liposomal delivery

The biodistribution of hydrophobic photosensitisers depends on the delivery vehicle, as it influences how the compound will be distributed among the serum proteins [114, 147]. As was discussed in Section 3.1.2, association with LDL favours a tumour-selective uptake and liposomes have been proposed to constitute a delivery system that orientates the systemically administered photosensitiser towards lipoproteins [123]. In Paper **III** we investigated the mTHPC pharmacokinetics in a murine tumour model following systemic administration of this photosensitiser incorporated into the lipophilic bilayer of liposomes based on dipalmitoylphosphatidylcholine (DPPC). This compound is referred to as Foslip. Following injection, the mTHPC molecules are believed to exist in a more monomeric form than if administered in the conventional ethanol, polyethylene glycol and water solution. In Figure 3.8 the mTHPC concentration in various organs following Foslip administration is compared with the levels reported following injection of mTHPC dissolved in ethanol, polyethylene glycol and water. Our main finding was an unusually high tumour-selective uptake as compared to muscle (6.6:1) for DLI of two to eight hours. Combined with the very low mTHPC levels observed in blood plasma, this indicates a more rapid biodistribution as compared to mTHPC in the ethanol-based solution. In agreement with our observations, improved selectivity and bioavailability have also been observed by incorporating other hydrophobic photosensitisers, such as benzoporphyrin derivative monoacid ring A (BPD-MA) [128], bacteriochlorin a [148], SIM01 [149] and hypocrellin A [129], in liposomes as compared to the corresponding free formulation.

The improved tumour-selective uptake following Foslip administration might be explained by an increased association with LDL. The structure of the DPPC-based liposomes lets them be quickly disintegrated by plasma lipoproteins, which releases the mTHPC molecules into the blood stream. Here, the photosensitiser is associated with different plasma lipoproteins and proteins [126]. In contrast to highly aggregated molecules, which are mostly taken up by albumin and globulin, the still partly monomeric mTHPC molecules might be associated with LDL to a higher degree than if not administered via liposomes [123, 150]. The final distribution pattern in the different tissues as well as the photosensitiser elimination rate is likely to depend on the animal tumour model and

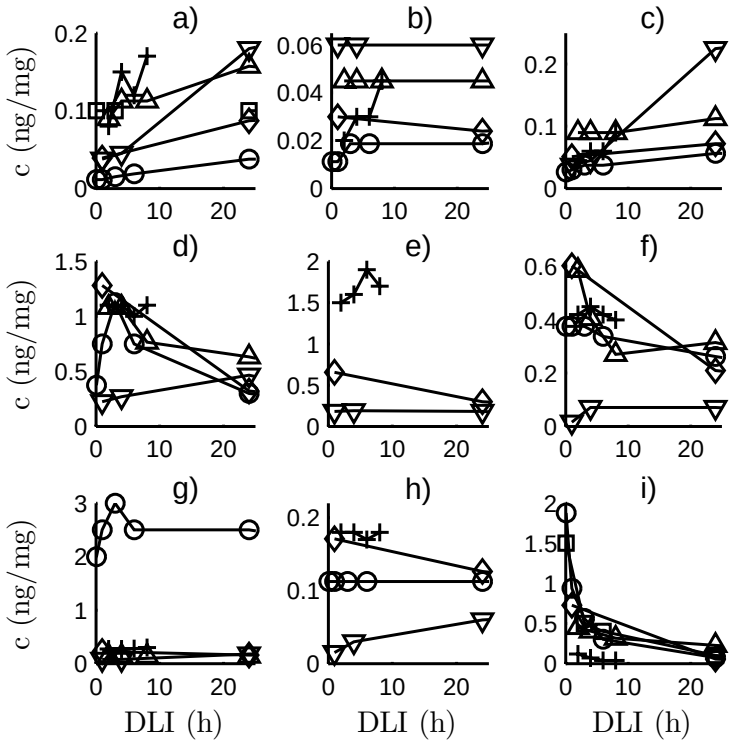

Figure 3.8. *Published mTHPC concentration following systemic administration. a) tumour, b) muscle, c) skin, d) liver, e) spleen, f) lung, g) kidney, h) heart, i) blood. ♢: Ref. [139], □: Ref. [142], ▽: Ref. [144], ○: Ref. [137], △: Ref. [151], + Paper* ***III****.*

the photosensitiser itself.

Conventional liposomes, such as DPPC, are rapidly phagocytised and transported to organs with a rich mononuclear phagocyte system [126]. This process supports our observation of high mTHPC concentration in the liver, spleen and lungs. Although association with the phagocyte system could possibly contribute to the good tumour selectivity due to the presence of macrophages, phagocytes and leucocytes close to the outer boundary of the tumour, the heavy load on the liver and spleen is an undesirable factor. An alternative might be to use pegylated liposomes, also known as sterically stabilised liposomes, characterised by prolonged circulation times [126]. Finally, further improvements of tumour selectivity and bioavailability might be possible by incorporating cholesterol in the lipid layers [126]. In other words, the use of DPPC is by no means optimal from the pharmacokinetic and phototherapeutic perspectives.

Two further observations might be of relevance when comparing the pharmacokinetics of the liposomal formulation to mTHPC in the ethanol, polyethylene glycol and water solution. First, with the ethanol-based solvent, clinical *in vivo* data indicate two concentration peaks in blood plasma, one immediately following injection and the other at ten hours [152], and second, compared to many other substances mTHPC follows a very slow distribution process [153]. This unique biodistribution pattern, observed in man but not in mouse, has been ascribed to either accumulation in some primary compartment, such as the liver [154], or aggregation of mTHPC in plasma [155] followed by slow release of monomeric photosensitiser molecules. Thus, any modification of the photosensitiser formulation that leads a more rapid biodistribution is attractive as the DLI and time periods of generalised photosensitivity could then be decreased.

The work presented in Paper **III** has not yet been extended to a comparison between the PDT effects of Foslip and mTHPC in the ethanol-based solvent. Improved PDT efficacy has been reported for liposome-encapsulated bacteriochlorin *a* in a cell culture medium [148] and for BPD-MA *in vivo* [128] as compared to the free photosensitiser. One might speculate that apart from a higher photosensitiser concentration caused by association to LDL, the improved treatment effect is caused by a different microlocalisation within the cell [123] and a higher fraction of the photosensitiser existing in its monomeric form. While albumin primarily delivers the drug to the vascular stroma, lipoproteins internalise the photosensitiser in malignant cells [150]. Furthermore, the importance of avoiding aggregation has been observed in a cell culture medium, in which encapsulation of the hydrophobic photosensitiser bacteriochlorin *a* in liposomes, thereby promoting monomerisation, was shown to increase oxygen consumption during PDT and decrease cell survival as compared to its partly aggregated original formulation [148]. However, conflicting reports exist on whether monomeric or aggregated mTHPC molecules possess the greatest phototoxicity [156, 157].

In summary, systemic administration of Foslip resulted in rapid biodistribution and improved selectivity for short DLI, which has not been observed for mTHPC administered in the conventional ethanol-based solvent. Whether the liposomal mTHPC formulation would lead to faster pharmacokinetics, increased tumour-selective uptake and improved PDT efficacy in man remains to be elucidated.

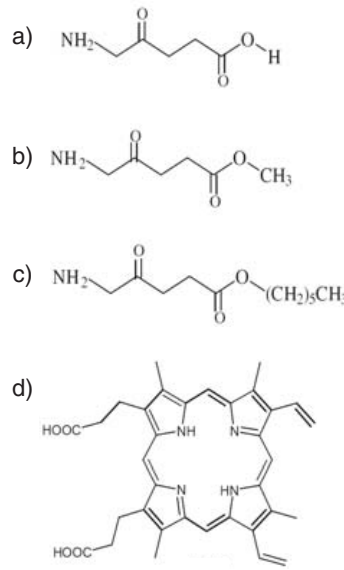

Figure 3.9. *The molecular structures of* ***a)*** *ALA [158],* ***b)*** *m-ALA [158],* ***c)*** *h-ALA [158] and* ***d)*** *PpIX [159].*

3.3 Protoporphyrin IX

ALA and PpIX, whose molecular structures are shown in Figure 3.9, are endogenous substances that occur naturally as a part

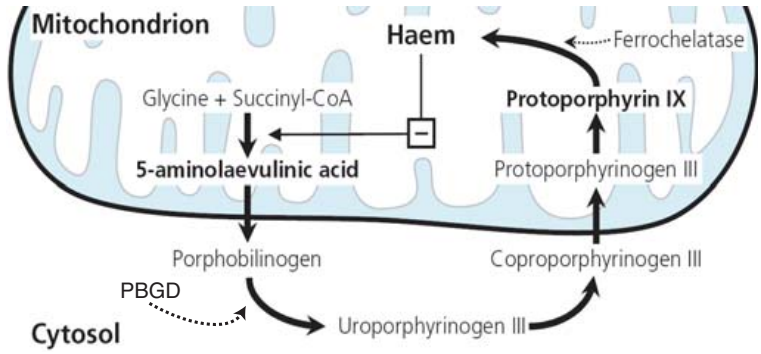

Figure 3.10. *The haem biosynthetic pathway. The enzymes PBGD and ferrochelatase are also indicated.*

of the haem biosynthesis. Despite the phrase ALA-PDT, PpIX and not ALA constitutes the actual photosensitising compound. The haem biosynthetic pathway, outlined in Figure 3.10 and in Ref. [84], is initiated by the production of ALA from glycine and succinyl coenzyme A (CoA). Several enzyme-regulated conversions, both within the cytosol and the mitochondria, lead to the formation of PpIX. The final step, during which iron is incorporated into the porphyrin molecule, is catalysed by the enzyme ferrochelatase, which is localised in the inner mitochondrial membrane. Upon administration of exogenous ALA, two biological effects promote tumour-selective PpIX accumulation; first, the ferrochelatase activity is decreased in certain malignancies [160–162] and second, the enzyme porphobilinogen deaminase (PBGD) expresses an increased activity in cancer cells [162, 163]. In the case of topical ALA administration, the damaged keratin layer of the skin lesions further promotes tumour-selective PpIX accumulation [83].

Systemic administration, such as oral intake, intravenous and intraperitoneal injection, leads to peak PpIX levels in the tumour after one to six hours but also result relatively limited tumour-to-skin selectivity [84]. Muscle, cartilage, heart and lungs show only very low PpIX levels [164].

Topical application of ALA has widespread clinical use, resulting in maximum tumour PpIX levels after four to 14 hours [83, 165]. For this time window and application route, photosensitiser levels have been observed to increase with application time in normal, remote skin, plasma, the liver, intestines and lungs in a murine tumour model [166]. Most normal tissues do not show any trace of PpIX after 24-48 hours irrespective of the administration route of ALA [83, 84].

The short DLI and relatively rapid clearance of PpIX consti-

tute attractive features of ALA-PDT. Another advantage is the tumour-selective PpIX accumulation [161, 167, 168], facilitating treatment selectivity and/or tissue diagnosis via the characteristic fluorescence of PpIX [15, 169–171] also shown in Figure 3.11.

3.4 Improving topical PDT

As already mentioned in Section 2.3.1, topical ALA-application results in relatively poor PDT efficacy for thicker skin lesions. Two factors partially responsible for this shortcoming can be deduced from the PpIX extinction coefficient shown in Figure 3.12; first, the therapeutic wavelength most often used clinically, i.e. tuned to the absorption peak at 635 nm, is relatively short, thus limiting treatment depths, and second, the extinction coefficient at this wavelength is weaker than for many other second generation photosensitisers. These effects limit light penetration, and thus treatment depth, and increase the irradiation times necessary. Although the matter has not been settled yet [174], another limiting factor in achieving sufficient treatment depths with topical ALA delivery is the hydrophilic character of the ALA molecule, restricting its diffusion through the upper skin layers [83, 87].

The lipophilicity can be increased by attaching alcohols of varying carbon chain lengths to the ALA molecule [175]; see Figure 3.9**b** and **c**. The substances thus formed have been shown to increase PpIX production levels in cell cultures [175–178], cell spheroids [179] and in normal mouse [166, 176, 180–182] or rat [183] skin following topical application. In addition, the esters seem to induce less generalised photosensitivity [166, 181–183]. The extensive use of one ALA ester, m-ALA, for PDT on human skin malignancies was already discussed in Section 2.3.1.

The low systemic PpIX levels caused by the ALA esters and the poor penetration through intact, *in vitro* skin [184] could perhaps be explained by a tight binding to biological membranes of these highly lipophilic substances. ALA incorporated into liposomes has also been observed to induce lower PpIX concentration in a murine subcutaneous tumour model [185] and increased retention in and decreased permeation through epidermis and dermis in an *in vitro* skin model [186]. Increased treatment depths might thus require photosensitisers or photosensitiser precursors with intermediate lipophilic properties [183].

Topical administration of mTHPC was reported by Gupta *et al.* [187] for the treatment of Bowen's disease and BCCs. In that study, utilising 2% mTHPC in a gel formulation and application times of 24 hours, the pathological tumour CR at the two-month follow-up was only 32%. The authors suggested that the method of topical photosensitiser application and the specific mTHPC formulation used were the primary limiting factors.

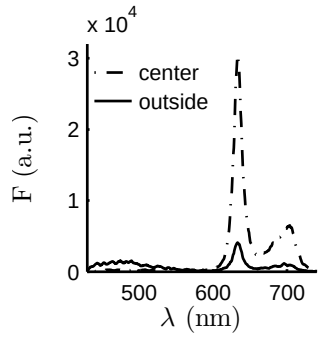

Figure 3.11. *In vivo PpIX fluorescence and tissue autofluorescence following excitation at 405 nm [172]. The data were acquired during the clinical study described in Paper* **V**.

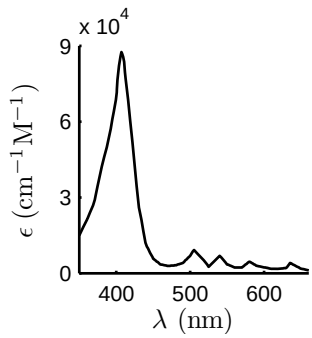

Figure 3.12. *The extinction coefficient of PpIX in water. Adapted from Ref. [173]*

In Papers **I** and **II**, topical administration of the liposomal mTHPC formulation, Foslip, was investigated. For the animal skin tumour model utilised in Paper **I**, low levels of generalised photosensitivity, a good tumour-selective uptake and an optimal drug application time of four hours were observed. For those tumours in which the photosensitiser depth distribution was investigated, an mTHPC concentration in the range of μM was observed down to three or four millimetres. Similar photosensitiser levels have been shown to induce pronounced PDT effects upon irradiation [137]. As a comparison, Peng *et al.* observed a good selectivity and homogeneous photosensitiser distribution down to two millimetres in human BCCs after topical application of m-ALA [188].

The four-hour DLI was used also in the clinical setting as described in Paper **II**. The Foslip-mediated PDT resulted in a preliminary CR of 35% which is comparable to the results reported by Gupta *et al.* [187]. However, it should be noted that the photosensitiser formulation, the DLI and light irradiation conditions were by no means optimised in this study. The patients included presented advanced and massive lesions, thus contributing to the high fraction of partial and non-responders. In this patient group, two lesions were biopsied and the depth penetration of Foslip was studied in these samples by means of fluorescence microscopy. The tissue samples were frozen immediately following excision and later sliced to five μm thick slices and fixated in formalin. The output from a mercury arc lamp was filtered to provide excitation light at 405 nm and fluorescence was detected above 575 nm. In contrast to the results in the animal skin tumour model, no photosensitiser fluorescence could be detected at depths exceeding a few hundred μm. A notable difference between the two trials was the "spongy" and slightly more porous composition of the lesions in the murine model. We have good reason to believe that the slightly more intact uppermost skin layers generally observed in the clinical trial efficiently hindered the photosensitiser from diffusing very deep. The same argument could also help explain the good tumour-selective uptake observed both in animal and human skin lesions; for lesions, the damaged and/or absent stratum corneum caused increased Foslip penetration and accumulation as compared to normal tissue. The disappointingly poor penetration depth of Foslip for human skin malignancies might also reflect a too pronounced lipophilicity of the delivery vehicle. As for the lipophilic, long-chained ALA esters, the liposomes perhaps get stuck to the upper-most tissue layers. We conclude that more detailed studies of the liposome pharmacokinetics and its penetration through skin are needed to optimise the clinical treatment protocol for this photosensitiser formulation.

3.5 Photosensitiser fluorescence

This section provides a short introduction to the use of photosensitiser fluorescence as a tool for concentration measurements, tissue diagnosis and PDT dosimetry. In parallel with this general discussion, some of our results and conclusions on PpIX and mTHPC fluorescence studies will be commented upon.

3.5.1 Fluorescence for concentration measurements

Ideally, the photosensitiser fluorescence signal is proportional to its concentration and thus constitutes a tool for minimally invasive pharmacokinetic studies. In contrast to extraction methods, such as high performance liquid chromatography (HPLC), no tissue excision is required and pharmacokinetics studies incorporating multiple time points can therefore be carried out in a single animal. However, photosensitiser aggregation and spatially heterogeneous optical properties of the tissue make interpretation of the absolute fluorescence signal less straight-forward. Aggregation of a hydrophobic photosensitiser is known to quench its fluorescence [134, 150, 157] and variations in tissue haemoglobin content can induce artificial peaks in the fluorescence spectrum as shown in Figure 3.13. Ultimately, these effects tend to decrease the overall correlation between the true photosensitiser concentration, assessed by means of HPLC, and the absolute fluorescence signal as shown in Figure 3.14. These plots, adapted from Paper **III**, illustrate the lack of overall agreement between HPLC and fluorescence, either imaging (R) or point-monitoring (A_{mTHPC}), data. For example, the high absorbance in the liver and spleen, caused by a high blood content, attenuates both excitation and fluorescent light. This effect helps to explain the lower slope of the correlation curves in Figure 3.14 for these organs as compared to those for tumour, muscle and skin.

A more robust, albeit less sensitive, method of assessing *in vivo* photosensitiser concentration was presented in Paper **I**. This method, which will be further described in Section 4.6.2, is based on measuring the tissue reflectance at a source-detector distance for which the effective path length of the detected photons does not depend on the scattering coefficient. The total tissue absorbance is then resolved into absorption caused by the different tissue chromophores, such as deoxy- and oxyhaemoglobin and water. Thus, the absorption caused by an exogenous photosensitiser can be disentangled from the absorbance of the bulk tissue, resulting in a more accurate concentration estimate.

An excellent review of the subject of different correction techniques for tissue fluorescence spectroscopy has been published by Bradley and Thorniley [189]. Here, the methods are categorised

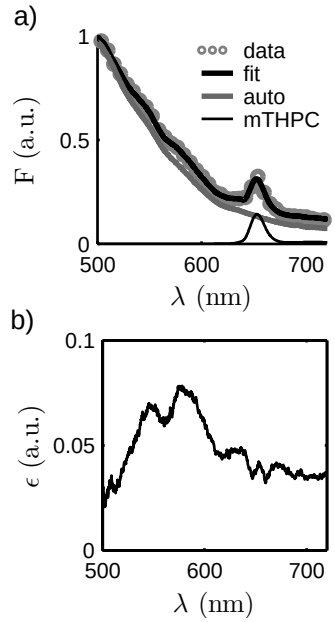

Figure 3.13. ***a)*** *Ex vivo tissue autofluorescence and mTHPC fluorescence from tumour tissue four hours after systemic Foslip administration. The fit component corresponding to tissue autofluorescence (**auto**) was assessed as the average fluorescence signal from the tumours in three unsensitised animals. The instrumentation, photosensitiser formulation and data analysis described in Paper **III** were utilised.* ***b)*** *The residual, ϵ, between the detected fluorescence and the fit components corresponding to the autofluorescence and mTHPC fluorescence. The influence of a varying blood volume and/or oxygenation is evident from the peaks at 540 and 580 nm.*

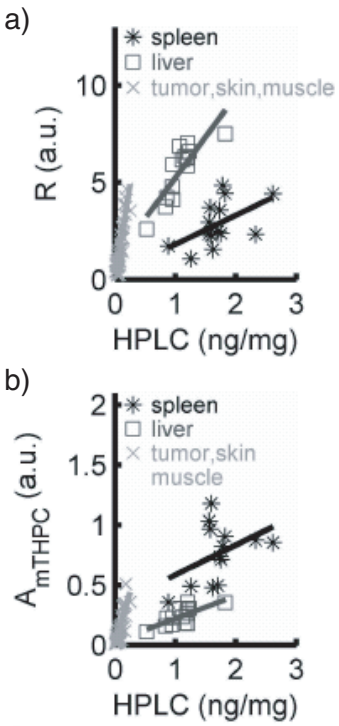

Figure 3.14. *Plots showing the poor overall correlation between HPLC and fluorescence* **a)** *imaging as well as* **b)** *point-monitoring data used for quantifying the mTHPC concentration. The figure has been adapted from Paper* ***III****.*

into techniques based on empirical results, measurements, theory or Monte Carlo simulations. The second group includes various fibre-optic probe designs that have been shown to decrease the influence of tissue absorption and/or scattering on the absolute fluorescence level [190, 191]. By utilising small source-detector separations, or even a single small-diameter fibre for both excitation light delivery and fluorescence detection, the number of elastic scattering events experienced by the detected fluorescence photons is limited, thus rendering the fluorescence signal less sensitive to variations in tissue absorbance. The theory-based techniques include methods based on forming a ratio between the fluorescence signals at two wavelengths that are equally attenuated by haemoglobin. Either a single [192] or a double [193] ratio technique can be used. For the latter method, the double ratio is formed between the ratios of the same two fluorescence spectral bands following excitation at two different wavelengths. Furthermore, methods based on photon migration theory have been utilised for modeling fluorescence propagation [194]. By combining fluorescence and white-light reflectance data, Müller *et al.* have proposed a closed form expression relating the measured to the intrinsic, i.e. the undistorted, fluorescence spectrum [195]. Also combining fluorescence and reflectance data, Foster *et al.* have utilised both light propagation theory, based on the P3-approximation [196], and Monte Carlo simulations to assess the intrinsic fluorescence signal [197]. In their work, either the optical properties of the tissue could be extracted from the reflectance signal and then used to assess the intrinsic fluorescence or both the optical properties and the intrinsic fluorescence could be extracted directly from the detected fluorescence signal.

3.5.2 Fluorescence for tissue diagnosis

A fluorescence investigation aims at providing a minimally invasive optical biopsy tool. When utilising exogenous tumour-markers for lesion delineation one relies on their tumour-selective uptake as well as on the possibility to easily discriminate their fluorescence signal from the tissue autofluorescence. Fluorescence imaging of PpIX distribution has been used for surface visualisation of epithelial lesions, for example in the skin [199, 200], the mucosa of the cervix [201] and the bladder [202]. Furthermore, PpIX fluorescence imaging has been used as a valuable tool for fluorescence-guided resection of malignant brain tumours [80].

However, tissue diagnosis can also rely on differences in tissue autofluorescence between normal and malignant tissue. The prolonged photosensitivity associated with systemic administration of some photosensitisers can thereby be avoided. When utilising tissue autofluorescence, discrimination between normal and malignant tissue is based on variations in elastin, collagen, carotene,

tryptophan, reduced nicotinamide adenine dinucleotide (NADH) and flavin adenine dinucleotide (FAD) content [203–205]. Furthermore, tumours sometimes display an increased blood flow which tends to reduce the overall light penetration within the tissue. These differences between malignant and normal tissue obviously also affect the detected fluorescence spectrum of the photosensitiser as discussed in the previous section and makes interpretation of the raw fluorescence signal less intuitive.

The instrumentation used for fluorescence investigations includes point-monitoring as well as imaging setups [206, 207], and excitation and detection can be performed both in continuous-wave (CW) [203, 208, 209], time-resolved (TR) [203, 208–210] and frequency-resolved (FR) [211] mode. Although the surface excitation-detection geometry is of greater value for diagnostic purposes, a point-monitoring setup can more easily provide detailed spectral information. Such information can then be used to guide the choice of spectral detection bands for the imaging setup. By imaging the fluorescence within several wavelength bands, also referred to as multi-spectral imaging, a contrast function can be constructed [207]. Such a contrast function should exhibit good sensitivity and specificity in discriminating cancerous from normal tissue. Furthermore, when utilising a simple ratio between two fluorescence wavelengths a dimensionless quantity is formed which is less sensitive to variations in light source output, angle of incidence of the excitation light and detection system efficiency. Figure 3.15 gives an example of improved lesion demarcation and suppression of non-uniform irradiance effects by forming a ratio between the fluorescence emission at 635 and 470 nm.

In Paper **II** *in vivo* mTHPC fluorescence measurements, both in point-monitoring and imaging mode, were performed. The point-monitoring system relied on pulsed irradiation and detection and thus measurements could be performed without interference from the room lighting. Furthermore, the point-monitoring instrument was more sensitive than the imaging setup, partly due to the poor transmission of the liquid crystal tunable filter (LCTF) used in the imaging instrument. In that work, however, the analysis of the point-monitoring data did not take advantage of the entire fluorescence spectrum as only three wavelength bands were utilised for constructing the contrast function. A better approach is offered by the singular value decomposition (SVD) scheme [212, 213], for example, as used in Paper **III**. This scheme provides the possibility to resolve individual tissue fluorophores and PDT-induced photoproducts. For the imaging setup, its primary advantage is its ability to monitor large surface areas, providing information on the tumour extension and/or the spatial distribution of the photosensitiser. From the data presented in Paper **II** it was also observed that fluorescence images acquired following excitation at 405 nm were notably less blurred than those obtained for 652 nm excita-

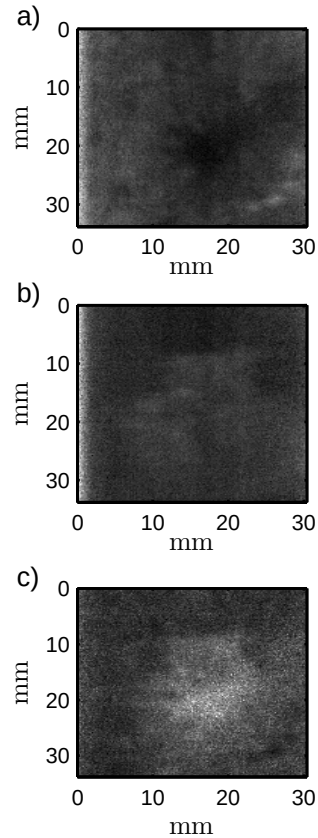

Figure 3.15. *Fluorescence at* **a)** *470 and* **b)** *635 nm following excitation at 365 nm. The lesion is not easily resolved in any of the images and the non-uniform irradiance of the excitation light is evident by the bright vertical stripe to the left.* **c)** *The ratio between the two fluorescence wavelengths shows improved lesion demarcation. All images have been scaled to their maximum respective pixel value and thus share the same colorbar. The instrument described in Ref. [198] was used for data acquisition. m-ALA was applied four hours prior to the fluorescence investigation of this BCC.*

tion. This we attributed to the higher tissue attenuation and thus more shallow probing depth of the shorter wavelength; see further Section 4.5.

3.5.3 Fluorescence for PDT dosimetry

The concept of PDT-induced photosensitiser photobleaching was already introduced in Section 3.1.1. The main idea behind utilising the amount of photosensitiser photobleaching as a tool for PDT dosimetry is that this process is believed to be partly caused by the same substances that induce damage to the target tissue [214–216]. Thus, a PDT treatment performed under stable oxygen supply leads to pronounced tissue damage as well as efficient photosensitiser photobleaching. A good correlation has been observed between the PDT treatment efficacy and the amount of photobleaching, as quantified by the treatment-induced decrease of the photosensitiser fluorescence level [217–219]. Photosensitiser bleaching as a measure of the PDT dose will be further discussed in Section 5.3.

Chapter 4

Light propagation

Photons interact with biological tissue primarily via two processes; scattering (elastic or inelastic) and absorption. In this thesis, the term scattering will refer only to the elastic scattering component as it is several orders of magnitude stronger than the inelastic part. Figure 4.1 is an illustration of the events following light incident on a tissue surface. Scattering arises due to refractive index variations within the medium, caused for example by cell nuclei, mitochondria and other organelles. Absorption induces heat, photodynamic processes and fluorescence. Any absorbing structure, either the entire or only part of a molecule, is referred to as a chromophore.

In Section 4.1 the radiative transport equation (RTE) is introduced as a tool for describing light propagation in scattering and absorbing media. A summary of the derivation of the diffusion approximation from the RTE is provided in Section 4.2. Sections 4.3 and 4.4 and describe the Beer-Lambert law and the use of statistical methods such as Monte Carlo simulations or non-sequential ray-tracing, respectively. The origins of tissue absorption and scattering are presented in Section 4.5. Finally, in Section 4.6 different methods to asses *in vivo* optical properties are discussed. Here, emphasis is on continuous-wave (CW) techniques. Somewhat arbitrarily, this presentation distinguishes between techniques that rely on multiple source-detector distances combined with the diffusion approximation model, as used in Papers **VI** and **VIII**, and techniques that utilise a single source-detector configuration, as presented in Paper **I**.

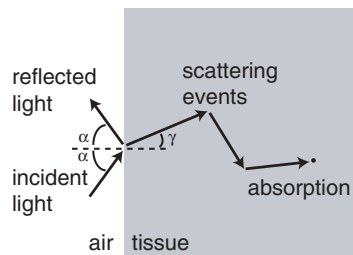

Figure 4.1. *Light incident on an air-tissue interface might be either reflected or transmitted into the medium. Reflection, α, and transmission, γ, angles are related by Snell's law. Photons inside the tissue experience scattering and absorption events. The latter might induced heat, fluorescence and photodynamic processes.*

4.1 The radiative transport equation

Transport theory forms the basis for the description of light propagation in scattering media. Most often the phase and polarisation of the electromagnetic radiation are ignored. Thus, the radiative

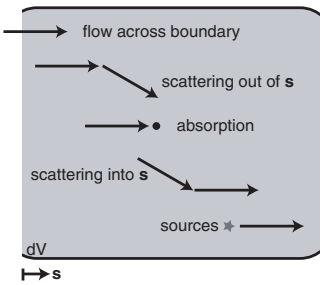

Figure 4.2. *The light propagation events according to radiative transport theory are illustrated in the order they appear on the right hand side of Equation (4.1). All terms relate to the direction given by the unit vector* **s**.

transport equation (RTE) is given by;

$$\frac{1}{c}\frac{\partial L(\mathbf{r},\mathbf{s},t)}{\partial t} = -\mathbf{s}\cdot\nabla L(\mathbf{r},\mathbf{s},t) - (\mu_s+\mu_a)L(\mathbf{r},\mathbf{s},t) + \mu_s\int_{4\pi} p(\mathbf{s},\mathbf{s}')L(\mathbf{r},\mathbf{s}',t)d\omega' + q(\mathbf{r},\mathbf{s},t) \qquad (4.1)$$

.

Here, $L(\mathbf{r},\mathbf{s},t)$ ($\mathrm{Wcm^{-2}sr^{-1}}$) denotes the radiance of light at position $\mathbf{r}$ travelling in the direction $\mathbf{s}$, c ($\mathrm{cms^{-1}}$) is the speed of light in the medium, $d\omega$ is the differential solid angle and $q(\mathbf{r},\mathbf{s},t)$ represents the source. μ_a and μ_s ($\mathrm{cm^{-1}}$) are the absorption and scattering coefficients, respectively. Furthermore, $p(\mathbf{s},\mathbf{s}')$ is the scattering phase function determining the probability of scattering from a direction $\mathbf{s}'$ into $\mathbf{s}$. The RTE essentially describes conservation of the radiance in a certain direction $\mathbf{s}$ within a volume element dV as illustrated in Figure 4.2. The terms on the right hand side reflect losses due to photons escaping over the volume boundaries, photons being scattered away from direction $\mathbf{s}$ and photons being absorbed, as well as gains due to photons being scattered from direction $\mathbf{s}'$ into $\mathbf{s}$ and possible sources within dV.

The scattering phase function describes the probability distribution of the scattering angle and is most often assumed to depend only on the deflection angle Θ between $\mathbf{s}'$ and $\mathbf{s}$ and not on the azimuthal angle Ψ; see Figure 4.3**a**. For example, the scattering phase function associated with an isolated microscopic sphere becomes increasingly forward directed the larger the diameter of the sphere but also displays smaller lobes in other directions due to interference effects. These phenomena can be described by Mie theory. In tissue, the situation is much more complex due to the high particle density and polydispersity. An approximation extensively used for $p(\mathbf{s},\mathbf{s}')$ is given by the Henyey-Greenstein phase function in Equation (4.2).

$$p_{\mathrm{HG}}(\mathbf{s},\mathbf{s}') = p(\mathbf{s}\cdot\mathbf{s}') = p(\cos\Theta) = \frac{(1-g^2)}{4\pi(1+g^2-2g\cos\Theta)} \qquad (4.2)$$

Here $g = \langle\cos\Theta\rangle$ and is referred to as the scattering anisotropy factor. This coefficient reflects the asymmetry of scattering events, where -1, 0 and 1 correspond to backward, isotropic and forward scattering, respectively. Figure 4.3**b** illustrates $p_{\mathrm{HG}}(\mathbf{s},\mathbf{s}')$ for different g-values.

No analytical solution exists for the RTE for arbitrary three-dimensional geometries, i.e. without symmetries to reduce the dimensionality of the problem, and unlimited range of optical properties. Instead, numerical methods combined with discretisation of the radiance can be employed. The discrete ordinates method [220], Kubelka-Munk [221] and adding-doubling [222] constitute three such approaches of varying complexity. In addition,

Monte Carlo simulations of photon trajectories and non-sequential ray-tracing constitute statistical methods that can be used for arbitrary geometries. Another approach is to simplify the problem by introducing various approximations. Perhaps the most common method is the diffusion approximation which will be presented in the following section. More details on the RTE and the derivation of the diffusion equation can be found in Refs. [223, 224].

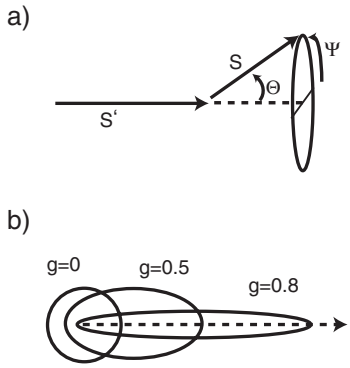

Figure 4.3. ***a)*** *Deflection, Θ, and azimuthal, Ψ, angles associated with scattering from direction* $\mathbf{s}'$ *into* $\mathbf{s}$. ***b)*** *The Henyey-Greenstein phase function for different values of* g.

4.2 The diffusion approximation

The diffusion approximation relies on an expansion of the quantities in Equation (4.1) in terms of spherical harmonics. For example, the radiance is expressed as;

$$L(\mathbf{r},\mathbf{s},t) = \sum_{l=0}^{\infty}\sum_{m=-l}^{l}\sqrt{\frac{2l+1}{4\pi}}\Psi_{lm}(\mathbf{r},t)Y_{lm}(\mathbf{s}) \tag{4.3}$$

The P_1-approximation is based on retaining only the terms corresponding to $l = 0, 1$. The radiance can thus be expressed in terms of the fluence rate, $\Phi(r)$, and the radiant flux, $\mathbf{F}(\mathbf{r})$, as shown in Equation (4.4).

$$L(\mathbf{r},\mathbf{s},t) = \frac{1}{4\pi}\Phi(\mathbf{r},t) + \frac{3}{4\pi}\mathbf{F}(\mathbf{r},t)\cdot\mathbf{s} \tag{4.4}$$

The fluence rate is defined as the power incident on an infinitesimal sphere divided by the cross-sectional area of that sphere; see Equation (4.5). The radiant flux describes the power transferred per unit area and is given in Equation (4.6).

$$\Phi(\mathbf{r},t) = \int_{4\pi} L(\mathbf{r},\mathbf{s},t)d\omega \tag{4.5}$$

$$\mathbf{F}(\mathbf{r},t) = \int_{4\pi} L(\mathbf{r},\mathbf{s},t)\mathbf{s}d\omega \tag{4.6}$$

The time-dependent diffusion equation, Equation (4.7), results from assuming an isotropic light source and a time-invariant radiant flux are assumed [224].

$$\frac{1}{c}\frac{\partial\Phi(\mathbf{r},t)}{\partial t} - \nabla\cdot(D(\mathbf{r})\nabla\Phi(\mathbf{r},t)) + \mu_a\Phi(\mathbf{r},t) = S_0(\mathbf{r},t) \tag{4.7}$$

The validity of Equation (4.7) is restricted to situations in which the reduced scattering by far exceeds the absorption coefficient and to regions far from any light sources. The diffusion coefficient is given by Equation (4.8).

$$D = \frac{1}{3(\alpha\mu_a + \mu_s')} \tag{4.8}$$

Here, the reduced scattering coefficient is given by $\mu_s' = (1-g)\mu_s$. This definition can be interpreted as equating $1/(1-g)$ anisotropic scattering events with one fully isotropic event. For the time-invariant flux; α=1. If one instead assumes a flux vector that decays exponentially with time, the diffusion coefficient becomes independent of μ_a, i.e. α=0 [225]. Improved accuracy and extended range of validity for Equation (4.7) have been reported by setting $0 \leq \alpha < 1$ [225–227] or even letting α depend on both μ_a and μ_s [228, 229]. In Papers **IV**, **V**, **VI**, **VII** and **VIII**, α was set to unity.

An analytical Green's solution to Equation (4.7) exists, for example, for the case of an isotropic point source within an infinitely large and homogeneous medium; see Equation (4.9).

$$\Phi(r,t) = \frac{c}{4\pi Dct}\exp(-\mu_a ct)\exp(-\frac{r^2}{4Dct}) \tag{4.9}$$

The corresponding solution to the time-independent diffusion equation is given by Equation (4.10). Here, $\mu_{\text{eff}} = [3\mu_a(\mu_a + \mu_s')]^{1/2}$.

$$\Phi(r) = \frac{1}{4\pi Dr}\exp(-\mu_{\text{eff}} r) \tag{4.10}$$

Equations (4.9) and (4.10) are very often used to predict the light distribution from an interstitial optical fibre and they can also aid in formulating an analytical expression approximately describing the fluence rate distribution within a semi-infinite medium of either an isotropic point-source or a pencil beam incident on the air-tissue interface; see Sections 4.2.1 and 4.2.2. Analytical expressions for $\Phi(r)$ have also been obtained for geometries including layered structures [230–232], embedded spheres [233] and parallelepipeds [234].

For more complex geometries one often has to rely on numerical methods, such as the finite element method (FEM) [235]. In the FEM, the entire geometry is divided into smaller subelements in which the fluence rate is assumed to vary according to a low order degree polynomial [236]. In Papers **IV**, **V**, **VI**, **VII** and **VIII** Comsol's[1] software packages (FEMLab® or Multiphysics®) have been extensively used. The "Near Infrared Frequency Domain Optical Absorption and Scatter Tomography" (NIRFAST)[2] platform is an alternative software package based on FEM simulations for solving the forward light propagation as well as the inverse problem of image reconstruction [237, 238].

4.2.1 Boundary conditions

The exact boundary condition at the interface between a non-scattering and a scattering medium cannot be implemented in the

[1] The reader is referred to http://www.comsol.com

[2] See further http://newton.ex.ac.uk/research/biomedical/hd/NIRFAST.html

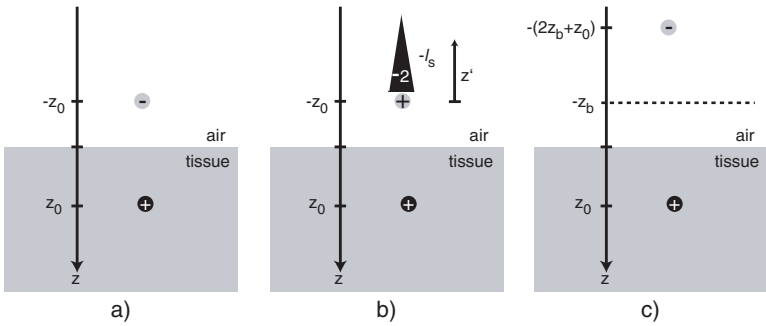

Figure 4.4. *Source configuration used for the* **a)** *ZBC,* **b)** *PCBC and* **c)** *EBC.*

diffusion approximation regime [230, 239]. In this section three approximate boundary conditions will be discussed with respect to the diffusion equation and an isotropic point source at a depth z_0 within the scattering medium.

A mathematically simple approximation is the zero boundary condition (ZBC) in which the fluence rate is set to zero at the physical boundary [240, 241]. This can be realised by introducing an imaginary negative point source above the physical surface as illustrated in Figure 4.4**a**. The ZBC is clearly unphysical but can be used when restricting the analysis to regions far away for any sources or boundaries.

Instead, it is often assumed that at the boundary the total diffuse flux directed into the medium equals the part of the outward propagating flux as prescribed by the Fresnel coefficients [242]. Refractive index matching thus predicts zero photon current back into the scattering medium whereas index mismatching introduces considerable internal reflection at the surface. The boundary condition, Equation (4.11), resulting when taking into account Fresnel reflection is referred to as the partial-current boundary condition (PCBC) [242];

$$\Phi(r) - 2AD\,\hat{\mathbf{n}} \cdot \nabla\Phi(r) = 0 \tag{4.11}$$

The internal reflection parameter, A, can be derived from an approximation of the Fresnel reflection coefficient for unpolarised light [242, 243] and an empirically obtained expression has also been used to relate A to the refractive index ratio between the scattering and non-scattering media n_{rel} [244, 245]; see Equation (4.12). Either approach yields A=1 for index matching.

$$A = \frac{1 + r_d}{1 - r_d} \tag{4.12}$$

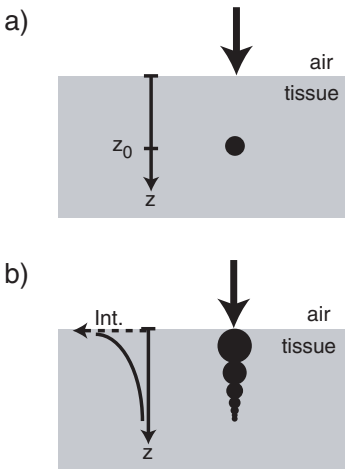

Figure 4.5. ***a)*** *Single or* ***b)*** *multiple source representation of a pencil beam incident on an air-tissue interface.*

Here, $r_d = -1.440n_{\text{rel}}^{-2} + 0.710n_{\text{rel}}^{-1} + 0.668 + 0.0636n_{\text{rel}}$. For the case of an isotropic point source at depth z_0 the PCBC can be fulfilled by introducing imaginary sources as illustrated in Figure 4.4**b**. Here, the negative source stretches from $z{=}{-}z_0$ to $z{=}{-}\infty$ and is attenuated according to $\exp(-z'/l_s)$ where $l_s = 2AD$ [243].

A mathematically simpler boundary condition is the extrapolated-boundary condition (EBC) [243, 244]. Here, the fluence rate is forced to zero at an imaginary boundary a distance z_b above the physical boundary. For an isotropic point source at a depth z_0 this is accomplished by introducing a negative image source at $z = -(2z_b + z_0)$ as shown in Figure 4.4**c**. The extrapolation distance is given by Equation (4.13) [243, 244].

$$z_b = 2AD \tag{4.13}$$

The fluence rate distributions with the PCBC and the EBC have been compared to each other, resulting in only minor or non-significant differences [243, 244, 246]. One reason might be that the source configurations used for the two boundary conditions share the same dipole and quadrupole moments.

The EBC was utilised when modeling the diffuse light distribution for Papers **IV**, **V** and **VI**. In Paper **VIII**, Equation (4.11) was implemented directly to solve for $\Phi(r)$ by the FEM and the internal reflection parameter, A, was calculated from Equation (4.12).

4.2.2 Source representation

The simplicity of the closed form expression for the fluence rate from an isotropic point source within an infinite, homogeneous medium, Equation (4.10), makes representation of any light source by one or a distribution of isotropic pointsources attractive.

A commonly employed measurement geometry, especially for non-invasive *in vivo* applications, involves a collimated laser beam normally incident on the tissue surface. This pencil beam can be approximated by an isotropic point source at a depth $z_0{=}1/\mu_s'$ [244]. Alternatively, the source term can be described as a distribution of isotropic point-sources with strengths proportional to $\exp[-z(\mu_a + \mu_s')]$. Both situations are illustrated in Figure 4.5 [245]. According to the EBC, negative mirror sources need to be introduced at the same distance above the extrapolated boundary in order to incorporate the correct boundary condition. Thus, for the single source representation the Green's solution for the fluence rate at depth z and radial position ρ is given by;

$$\Phi(\rho, z) = \frac{1}{4\pi D}\left[\frac{\exp(-\mu_{\text{eff}} r_1)}{r_1} - \frac{\exp(-\mu_{\text{eff}} r_2)}{r_2}\right] \tag{4.14}$$

where $r_1 = \sqrt{(z - z_0)^2 + \rho^2}$ and $r_2 = \sqrt{(z + 2z_b + z_0)^2 + \rho^2}$.

Along the same lines, the interstitially positioned, cut-end optical fibres used in Papers **IV**, **V**, **VI**, **VII** and **VIII** were modelled

as isotropic point sources located a distance $1/\mu_s'$ in front of the actual fibre tips.

4.3 The Beer-Lambert law

The Beer-Lambert law as stated in Equation (4.15) can be derived from the discretised RTE when including only the forward angular component of the radiance.

$$I = I_0 \exp\left[-(\mu_a + \mu_s')L\right] \tag{4.15}$$

Here, L is the path length and I_0 and I are the incident and detected intensities, respectively. The Beer-Lambert law is illustrated in Figure 4.6 for an absorbing but non-scattering medium. For a scattering medium, the parameter L in Equation (4.15) generally exceeds the physical distance between source and detector. Hence, one often introduces a differential path length factor (DPF) which relates the source-detector distance r to the (usually unknown) average path length $\langle L \rangle$ of the detected photons;

$$\langle L \rangle = r\,\mathrm{DPF} \tag{4.16}$$

DPF>1 due to light scattering in the tissue and it also depends on the specific geometry as well as on μ_a, μ_s and $p(\mathbf{s}, \mathbf{s}')$ [247, 248]. However, a measurement configuration for which the dependence on the scattering coefficient is minimised will be discussed in Section 4.6.2.

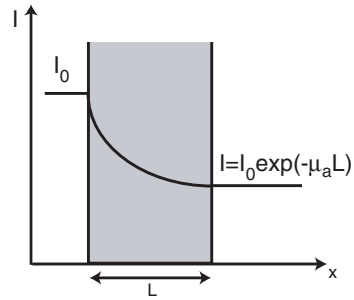

Figure 4.6. *Within an absorbing medium the transmitted signal is exponentially attenuated with respect to the sample thickness L and the absorption coefficient μ_a. Refractive index matching is assumed.*

4.4 Statistical methods

The Monte Carlo method is a statistical method by which the trajectories of individual photons or photon packages are determined in a random fashion. Uniformly distributed random numbers, ζ, are transformed via appropriate distribution functions to attain certain probability density functions, $p(\zeta)$. Thus, the step size s of a photon is given by $s = -\ln(\zeta)/(\mu_a + \mu_s)$, the deflection angle Θ is determined from the Henyey-Greenstein distribution and the azimuthal angle Ψ is uniformly distributed in the interval $[0, 2\pi[$. In contrast to the diffusion approximation, the light distribution can be accurately modelled close to boundaries and sources and any range of optical properties can be used. In 1989 the general principles for Monte Carlo simulations of light propagation in scattering media were published [249]. With the computer program "Monte Carlo simulation for multilayered tissues" (MCML)[3] [250], made available in 1995, parameters such as the fluence rate distribution, time-of-flight, absorption, reflection and transmission can be obtained within a specified layered geometry for some set of μ_a, μ_s

[3] http://omlc.ogi.edu/software/mc/index.html#MCML

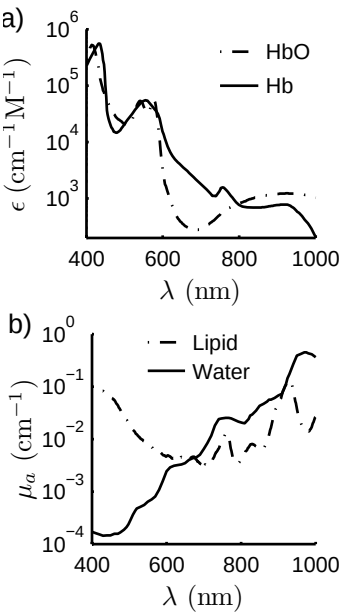

Figure 4.7. ***a)*** *Extinction spectra of deoxy- and oxyhaemoglobin [256].* ***b)*** *Absorption spectra of pure lipid [258, 259] and water [257].*

and g. Monte Carlo simulations are used extensively as a gold standard for light propagation calculations. More recent implementations include arbitrary geometries [251] and time-resolved fluorescence Monte Carlo simulations [252, 253]. The main drawbacks of the Monte Carlo method are the long simulation times required, especially for large geometries and high absorption and scattering levels, and the lack of an analytical expression for the simulated parameter.

In Paper **I** we used non-sequential ray-tracing offered by the software "Advanced Systems Analysis Program" (ASAP®) developed by Breault Research[4]. This method of non-sequential ray-tracing has the advantage over conventional ray-tracing that it also handles scattering within bulk media, and over MCML that arbitrary three-dimensional geometries are easily implemented.

4.5 *In vivo* optical properties

In this section some common tissue absorbers and scatterers will be presented. The reader is referred to Refs. [254, 255] for compiled data on *in vivo* optical properties of tissue.

4.5.1 Tissue chromophores

The total absorption coefficient is given by Equation (4.17) where the summation includes any chromophore that contributes to the overall absorption.

$$\mu_a(\lambda) = \ln(10) \sum_i \epsilon_i(\lambda)[x_i] \tag{4.17}$$

Here, ϵ (cm^{-1}M^{-1}) denotes the extinction coefficient, which is wavelength dependent, and $[x_i]$ (M) is the chromophore concentration. The factor ln(10) is included depending on whether the absorption and extinction coefficients are defined using the natural logarithm or $\log_{10}$. Figure 4.7 illustrates the extinction coefficients (using $\log_{10}$) of deoxy- (Hb) and oxyhaemoglobin (HbO_2) [256] and the absorption spectra (using the natural logarithm) of pure water [257] and pig fat [258, 259]. Due to the lower overall absorption between 650 and 1000 nm this spectral region is often denoted the "optical window". Red and NIR wavelengths can thus be used to probe deeper lying tissue volumes.

Besides the chromophores presented in Figure 4.7, other absorbing tissue constituents include melanin, myoglobin and different cytochromes. Melanin is a dark pigment consisting of different polymers and can be found in human skin and hair. Although the compound is present only within a thin layer its high absorption [260] severely limits light penetration in dark-skinned people

[4]The reader is referred to http://www.breault.com

as well as in malignant melanomas. Myoglobin transports and stores oxygen but in contrast to haemoglobin it is present only in muscle tissue. Here, its concentration often exceeds that of haemoglobin [261] and thus absorption by myoglobin constitutes a significant fraction of the overall absorption. For red and NIR wavelengths the extinction spectra of myoglobin and haemoglobin are almost identical and thus it is virtually impossible to distinguish between the two chromophores [262]. Cytochromes are proteins found in the membranes of mitochondria and the endoplasmic reticulum of most cells. The spectral shape of the different cytochromes differ slightly but they typically display maximum absorption between 500 and 620 nm, which gradually decreases at longer wavelengths [263]. For UV wavelengths DNA and certain amino acids add to the already strong absorption by water, haemoglobin, myoglobin and cytochrome *c* [223].

With the aid of Equation (4.17) and appropriate data analysis, the total wavelength-dependent absorption coefficient can be resolved into components corresponding to each specific absorber. In principle, measurements at only i wavelengths are required to determine the concentration of i chromophores. Equation (4.18) exemplifies the situation for i=2 and the wavelengths employed in Paper **IV**.

$$\begin{bmatrix} \mu_a(760\text{ nm}) \\ \mu_a(800\text{ nm}) \end{bmatrix} = \begin{bmatrix} \epsilon_{\text{Hb}}(760\text{ nm}) & \epsilon_{\text{HbO}_2}(760\text{ nm}) \\ \epsilon_{\text{Hb}}(800\text{ nm}) & \epsilon_{\text{HbO}_2}(800\text{ nm}) \end{bmatrix} \begin{bmatrix} [\text{Hb}] \\ [\text{HbO}_2] \end{bmatrix} \tag{4.18}$$

However, by including a larger number of wavelengths, thus resulting in an over-determined system of equations, the data analysis becomes more robust. In Paper **V**, the data analysis was expanded to include all data points, for that particular spectrometer the number of data points being 200, within the spectral range 760 to 810 nm to obtain the least squares solution for $\Delta[\text{Hb}]$ and $\Delta[\text{HbO}_2]$. The simple method of matrix inversion did not work for the spectrally overlapping fit components used in Paper **I** despite relying on a broad fit interval. Instead, an SVD algorithm was utilised to solve for individual chromophore concentrations from the overall absorption coefficient. In general, the SVD algorithm is useful for singular, or numerically close to singular, problems [212] and has been successfully used for assessing the concentration of absorbing [264] and fluorescing [213] substances from experimental data.

The accuracy of these methods also depends on fitting the correct extinction spectra. As for a fluorescence spectrum, ϵ might display spectral shifts, broadening and attenuation of some absorption bands depending on the chemical environment. For example, we introduced a wavelength shift, empirically determined to +2 nm, of the mTHPC extinction coefficient when analysing mTHPC levels in biological tissue as compared to in liquid phantoms con-

Table 4.1: The refractive index for some selected human tissues [223, 265].

Tissue	n
Stratum corneum	1.55
Muscle	1.37-1.410
Liver	1.368-1.38
Fat	1.44-1.46
Cytoplasm	1.350-1.367
Blood	1.400

taining water, TiO_2 and polyethylene glycol.

Beside chromophore concentrations, physiological parameters, such as the total blood content, Equation (4.19), and the level of oxygen saturation in the tissue, Equation (4.20), can also be assessed [110, 266].

$$[\mathrm{Hb_{tot}}] = [\mathrm{HbO_2}] + [\mathrm{Hb}] \tag{4.19}$$

$$S_{\mathrm{O2}} = \frac{[\mathrm{HbO_2}]}{[\mathrm{HbO_2}] + [\mathrm{Hb}]} \cdot 100\% \tag{4.20}$$

4.5.2 Tissue scattering

Cell components such as the cell nuclei, mitochondria, lysosomes, membranes within the endoplasmic reticulum and the Golgi apparatus introduce refractive index changes and thus cause scattering, refraction and reflection. Furthermore, red blood cells, melaninosomes and the fibrous structure of collagen and elastin also constitute important scatterers. The volume-averaged refractive index, n, for most tissues and biofluids is in the range 1.335 to 1.65 for visible wavelengths [223]. A few selected values are listed in Table 4.1.

The phase function, and hence the g-factor, is influenced by the microscopic properties, such as the size and shape, of the scattering structure. The anisotropy factor is in the range 0.4-0.99 in biological tissue, reflecting its forward scattering character [223]. As a rule of thumb, the smaller the scatterer the more isotropic the phase function. For example, in the Rayleigh limit, i.e. scattering particles being very much smaller than the wavelength, the volume-averaged scattering is totally isotropic. However, due the size distribution of scattering centres in biological tissues ($\sim$100 Å to $\sim$10 μm) scattering of visible light cannot be appropriately described by Rayleigh scattering.

Mie, or Lorenz-Mie, theory can be used to predict scattering from homogeneous, dielectric and arbitrary-sized spheres following incidence of a plane electromagnetic wave. According to this theory, both μ_s and $p(\mathbf{s}, \mathbf{s}')$ exhibit oscillations as a function of deflection angle and wavelength. For polydisperse ensembles of particles,

such as biological tissue, these oscillations are damped out [267]. With increasing average particle size, the wavelength dependence of the reduced scattering coefficient changes from λ^{-4}, i.e. the Rayleigh limit, to $\lambda^{-0.37}$ [268]. Although scattering centra are typically non-spherical, Mie theory has been successfully employed to predict the principal spectral characteristics of the reduced scattering coefficient and to assess the average size of scattering components related to the parameter b in Equation (4.21) [268, 269].

$$\mu_s' = a\lambda^{-b} \tag{4.21}$$

Values for b have been published, e.g for the human arm (1.11) [266] and *ex vivo* rat liver tissue (0.87) [269]. The data analysis of Papers **IV** and **V** utilised the former value. Also, Intralipid-10%, a fat emulsion extensively used in our laboratory as the scattering component in liquid tissue phantoms, is characterised by $\mu_s \propto \lambda^{-2.4}$ [270]. In Figure 4.8, experimental data, assessed by means of time-resolved spectroscopy [110], on the reduced scattering coefficient of this substance is compared to Rayleigh theory, large-sized particle Mie scattering [268] and the λ^{-2}-behaviour proposed in Ref. [267].

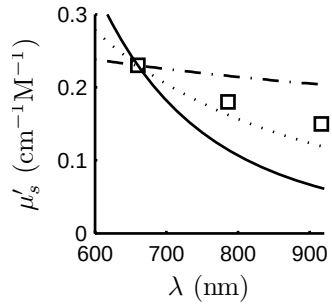

Figure 4.8. *The reduced scattering coefficient of Intralipid-10% assessed by the instrument described in Ref. [110] (□). As a comparison, μ_s' as predicted by Rayleigh theory (solid line), Mie (dash-dotted line) theory and the fit proposed by Mourant et al. [267], i.e. $\mu_s' \propto \lambda^{-2}$ (dotted line), are included. The theoretical data has been normalised to the experimental data at 660 nm.*

4.6 Assessing optical properties

The need to assess the optical properties of tissue arises from attempts to solve either the forward problem of predicting the diffuse light distribution or the inverse problem of finding the concentration of various endogenous chromophores, such as deoxy- and oxyhaemoglobin, or exogenous chromophores, for example photosensitiser, from some set of measurement data. All parameters mentioned are of importance to PDT dosimetry as will be discussed in Chapter 5.

The methods presented in this section can be referred to as two-parameter techniques as they provide only μ_s' and μ_a but cannot resolve μ_s' into μ_s and g. In order to probe deeper than the very superficial tissue structures one often relies on wavelengths within the "optical window" as discussed in Section 4.5.1. In this spectral region, where the scattering dominates absorption, the light distribution is fairly diffuse and thus many techniques have made use of the diffusion approximation for predicting the optical properties of tissue.

In this section some time- and spatially-resolved techniques for assessing optical properties of tissue will be presented. These techniques can employ multiple wavelengths and thus all parameters in this section may be wavelength-dependent although this is not explicitly indicated. Other methods, such as photothermal techniques [271], elastic scattering spectroscopy [272], optical coherence tomography (OCT) [273], diffuse optical tomogra-

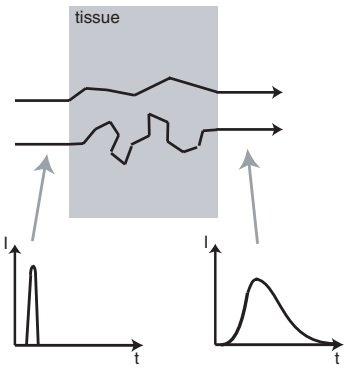

Figure 4.9. *A short light pulse is attenuated and temporally broadened upon transmission through a scattering and absorbing medium.*

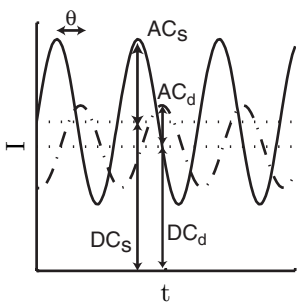

Figure 4.10. *Light from a sinusoidally modulated source (solid) is delayed and demodulated as it propagates through an absorbing and scattering medium (dashed).*

phy (DOT) [274] and techniques applicable only to *ex vivo* samples [275] will not be discussed.

4.6.1 Time- and frequency-resolved techniques

The principle behind time-resolved (TR) spectroscopy as illustrated in Figure 4.9 is that a short light pulse is attenuated and temporally broadened after propagating through an absorbing and scattering medium. Utilising Equation (4.9) both the absorption and reduced scattering coefficient can be determined from the temporal shape of the fluence rate (with extensions to transmission and reflectance signals) and thus no absolute measurements are required. More details on experimental techniques and data analysis can be found in Refs. [110, 276, 277].

Frequency-resolved (FR) spectroscopy relies on a sinusoidally modulated light source with modulation frequencies typically in the range ∼100 MHz to ∼1 GHz [278–280]. After propagating through tissue, the detected signal displays a phase-shift, θ, and a demodulation, $M = (AC_d/DC_d)\,(AC_s/DC_s)^{-1}$, relative to the source or some other reference signal as illustrated in Figure 4.10. These two parameters are related to the absorption and reduced scattering coefficient of the tissue. Compared to TR spectroscopy, FR techniques often rely on simpler and cheaper equipment.

4.6.2 Continuous-wave techniques

The CW techniques that have been utilised in this thesis are based on either spatially-resolved (SR) spectroscopy of the diffuse light distribution, combining multiple source-detector distances and diffusion theory, or a single source-detector distance for which the Beer-Lambert law can be used to assess the absorption coefficient. These two approaches will be discussed in the following sections. The incorporation of a broadbanded light source and a spectrometer on the detection side is more straightforward and cheaper than for TR-instruments and has the potential to improve robustness of data analysis algorithms.

Multiple source-detector pairs

SR techniques rely on monitoring the fluence rate, the reflectance or the transmittance at several detector positions; see Figure 4.11, and fitting data to the appropriate expression in order to assess the absorption and reduced scattering coefficients.

For the case of isotropic, interstitial light delivery and collection, Equation (4.10) can be utilised to solve for these parameters. The effective attenuation coefficient is related to the decay rate of the fluence rate at large source-detector distances, r, via $r\,\Phi(r) \propto \exp(-\mu_{\text{eff}}\, r)$. The diffuse fluence rate is plotted as a func-

tion of source-detector distance in Figure 4.12**a** for two sets of μ_a and μ_s' that yield the same μ_{eff}. From this example it is clear that in order to separately assess the absorption and reduced scattering coefficients one needs to either include small source-detector distances, for which the validity of the diffusion approximation is debatable, or perform absolute measurements, thereby relying on accurate calibration of the detection unit.

For the case of non-invasive measurements, one often relies on the reflected light. The reflectance has been described in terms of either the flux at the boundary, Equation (4.22) [281], or as a combination of the flux and the fluence rate, Equation (4.23) [282].

$$R_f(\rho) = -D\nabla\Phi(\rho, z)\cdot(-\mathbf{z})|_{z=0} \tag{4.22}$$

$$\begin{aligned} R(\rho) = \int_{2\pi} d\Omega(1 - R_{\text{fres}}(\Theta))\frac{1}{4\pi}\Big[\Phi(\rho, z=0) + \\ 3D\frac{\partial\Phi(\rho, z=0)}{\partial z}\cos\Theta\Big]\cos\Theta = \\ C_1\Phi(\rho, z=0) + C_2 R_f(\rho) \end{aligned} \tag{4.23}$$

Here, the C_i are related to the refractive indices of the tissue and detection fibre as well as to the numerical aperture (NA) of the optical fibre used. Utilising the EBC and $\Phi(\rho, z)$ according to Equation (4.14), the resulting R_f is given by Equation (4.24).

$$\begin{aligned} R_f(\rho) = \frac{1}{4\pi\mu_t'}\Big[\Big(\mu_{\text{eff}} + \frac{1}{r_1}\Big)\frac{\exp(-\mu_{\text{eff}} r_1)}{r_1^2} + \\ \Big(\frac{1}{\mu_t'} + 2z_b\Big)\Big(\mu_{\text{eff}} + \frac{1}{r_2}\Big)\frac{\exp(-\mu_{\text{eff}} r_2)}{r_2^2}\Big] \end{aligned} \tag{4.24}$$

Here $\mu_t' = \mu_a + \mu_s'$ and the remaining variables have been defined previously. The reflectance according to Equation (4.23) is exemplified in Figure 4.12**b**. As for the fluence rate, it is necessary to include either small source-detector distances or absolute measurements to separately assess μ_a and μ_s'. Alternatively, it is possible to add another independent measurement, such as the total diffuse reflectance [283], to discriminate between μ_{eff}-isovalues with different absorption and scattering levels.

The SR technique typically predicts the absorption and reduced scattering coefficients of homogeneous tissue phantoms with an accuracy limited to ±10% [244, 264, 283, 284]. However, reports also exist on poor results when relying on diffusion theory for assessing the optical properties from the reflectance or transmittance [285, 286]. The contradictory conclusions probably reflect the importance of implementing the correct boundary conditions and restricting the measurement geometry to a situation where diffusion theory constitutes a valid approximation.

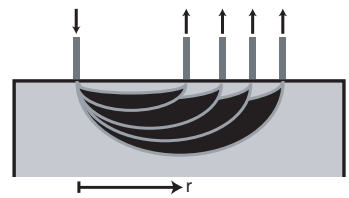

Figure 4.11. *SR spectroscopy is illustrated for the reflectance geometry.*

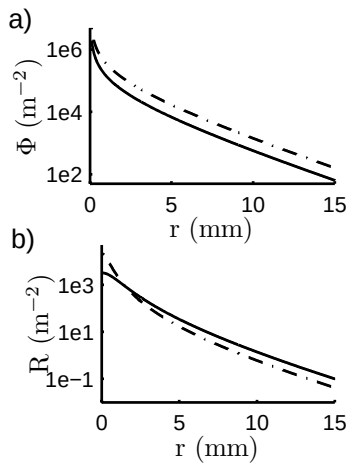

Figure 4.12. ***a)*** *$\Phi(r)$ due to an interstitial isotropic point source.* ***b)*** *$R(r)$ due to an incident pencil beam. μ_{eff}=3.57 cm^{-1} for all curves but (μ_a, μ_s')=(0.5,8) (solid) and (μ_a, μ_s')=(0.2,21) (dashed). Refractive index matching and the EBC were employed with n=1.4.*

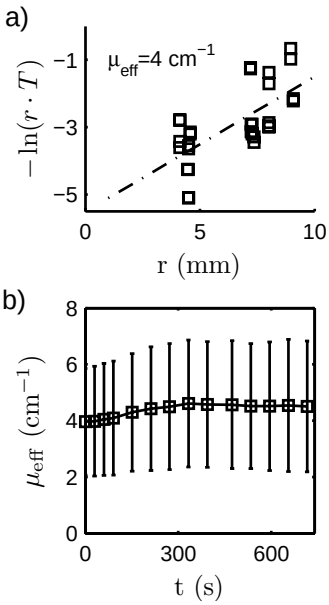

Figure 4.13. ***a)*** *The negative logarithm of the in vivo transmission signal multiplied by the source-detector distance, r, as a function of r. Transmission signals (□) were assessed between all six treatment fibres prior to PDT treatment of this nBCC. The linear fit (dashed line) and the evaluated μ_{eff} are indicated.* ***b)*** *Average μ_{eff} as a function of treatment time. The error bars represent ±1SD.*

The interstitial approach, based on monitoring the absolute fluence rate via calibrated isotropic detectors, has been employed in canine [287, 288] and human [289, 290] prostate tissue. For the instruments developed for IPDT in massive skin tumours, Papers **IV**, **V** and **VI**, and in prostate tissue, Paper **VIII**, the light transmitted between the optical fibres used for therapeutic light delivery is utilised to assess the effective attenuation coefficient as well as any changes thereof induced by the treatment. In the clinical setting, the source-detector distances are relatively large and we also do not attempt to detect the absolute fluence rate with the cut-end fibres. The realtime monitoring of light transmission levels implemented by our IPDT instruments is therefore not capable of separating μ_a from μ_s'. Instead, we aim at evaluating the effective attenuation coefficient from the decay rate of the fluence rate at large r, i.e. from the slope of the expression

$$-\ln(r\,\Phi(r)) = C - \mu_{\text{eff}} r \tag{4.25}$$

Figure 4.13 illustrates some data points together with the evaluated μ_{eff} as a function of the treatment time for one of the patients treated with the six-fibre IPDT instrument described in Paper **IV**.

In connection with the discussion of interstitial light transmission measurements it is worthwhile to comment on which parameter is actually being detected by an anisotropic detector, such as a cut-end optical fibre. The collection efficiency of such a fibre has been shown to depend on the optical properties of the tissue [291, 292]. Considering the measurement configuration in Figure 4.14, the detected signal $T(r)$ equals the radiance integrated over the fibre surface area S_f and the acceptance angle Ω_f. As for the surface reflectance in Equation (4.23), $T(r)$ contains both a fluence rate and a flux term [243, 292]; $T(r) = C_1\Phi(r) + C_2\, D\nabla\Phi(r)\cdot\mathbf{z}$. In the case of no vertical offset and large distance between source and detector fibres one can assume that $\partial\Phi/\partial z = 0$. Thus, the detected light transmission, $T(r)$, is proportional to the fluence rate at the fibre tip and the parameter $T(r)$ replaces $\Phi(r)$ in Equation (4.25) [254]. This approximation was employed for the data analysis in Papers **IV**, **V** and **VI**.

The scattered appearance of the data points and the relatively large standard deviations (SD) in Figure 4.13 probably result from a heterogeneous medium with possible blood pooling at the front surface of the fibres. The sensitivity to heterogeneous tissue structures, especially those present close to either the source or the detection fibre, constitutes one of the major drawbacks of SR spectroscopy. The presence of a layered medium and the finite spatial dimensions of the tissue under investigation have been shown to cause erroneous results as discussed in Refs. [293–296] and in Paper **VIII**. However, by utilising multiple source-detector distances, thereby probing different tissue depths as indicated in Figure 4.11, it is possible to gain information on layered tissue struc-

tures and to assess the depth distribution of a fluorescent inclusion [297, 298]. Furthermore, when employing a broadbanded light source the spectral shape of the reflected or transmitted light also contains information related to the depth distribution of a chromophore or fluorophore [299, 300]. In comparison with the TR and FR techniques, the instrumentation for SR spectroscopy is often simple, cheap and robust.

By utilising smaller source-detector distances the probed tissue volume is spatially confined but usually the diffusion approximation breaks down. Instead, the data analysis used to assess absorption and scattering levels need to rely on calibration via, for example, Monte Carlo databases [301–303] or P3-theory [196]. In the latter approach, more terms are included in the expansion of the radiance, i.e. N=3 instead of 1 as used for the diffusion approximation, and thus the requirement of diffuse light propagation is somewhat relaxed. Yet another approach has been investigated by Amelink *et al.* for which the backscattered light is detected both via the source fibre and via a second fibre in close contact with the source fibre [304]. By subtracting the two reflection signals, the differential path length of the photons in this residual signal is independent of the optical properties of the tissue. The method, referred to as differential path length spectroscopy (DPS), can be used to extract the concentration of various chromophores, such as haemoglobin and β-carotene, the average blood vessel diameter and the scattering slope b in Equation (4.21). DPS has been employed for optical diagnosis [305, 306] and for tracking PDT-induced changes of the optical properties of the target tissue [307].

Non-contact imaging systems have been investigated as a means to avoid the disturbing effects of contact-based surface probes. A CCD [283, 285, 308] or a Fourier transform interferometric imaging system [309, 310] can be utilised to image $R(\rho)$ for a narrow beam incident on the planar surface of the scattering and absorbing medium. By using data analysis based on diffusion theory, neural network or partial least squares (PLS), the absorption and/or scattering coefficients can be assessed with an accuracy of ±5-15%. Finally, the diffuse reflectance following spatially modulated illumination has been utilised for optical property mapping and depth-resolved imaging of heterogeneities in tissue phantoms [311].

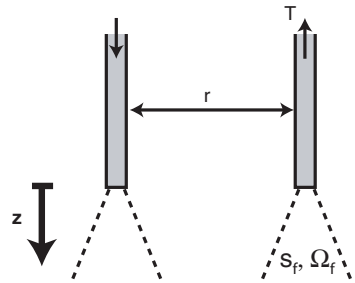

Figure 4.14. *Illustration of interstitial light delivery and detection utilising cut-end fibres.*

Single source-detector pair

Instrumentation relying on a single source-detector pair often incorporates broadbanded light sources. The total absorption spectrum is resolved into the components caused by individual absorbers, thereby assessing the concentration of the different tissue chromophores. This section will discuss the use of the Beer-Lambert law for monitoring chromophore concentration.

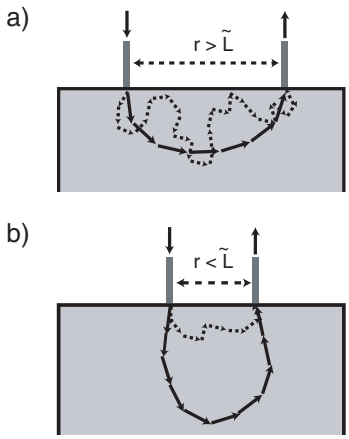

Figure 4.15. ***a)*** *For a relatively large source-detector fibre distance, L, the path lengths of the detected photons are longer for higher (dashed) than for lower (solid) scattering levels.* ***b)*** *For a small fibre separation the situation is reversed with respect to the scattering level.*

From Equation (4.15) the modified Beer-Lambert law can be derived;

$$A = \ln\left[\frac{I_0}{I}\right] = \mu_a \mathrm{DPF}\, r + G \tag{4.26}$$

Here, A is the absorbance defined using the natural logarithm and G is a geometry-dependent factor representing scattering losses. As in Section 4.3, r is the source-detector distance and DPF denotes the differential path length factor. In general, G is unknown and hence the absolute absorption coefficient cannot be solved for in a scattering medium. An alternative approach is to monitor the absorbance change between two measurement time points as presented in Equation (4.27).

$$\Delta A = \ln\left[\frac{I(t_2)}{I(t_1)}\right] = \Delta\mu_a \mathrm{DPF}\, r + \Delta G \tag{4.27}$$

Time-of-flight and frequency-modulated studies have been utilised to assess the DPF for some common measurement configurations [312–314]. In utilising Equation (4.27) two brave and sometimes erroneous assumptions are often made; first the scattering is assumed to remain constant between measurements, thereby eliminating ΔG, and second, the DPF is assumed to be independent of scattering level [247]. Inter- and intra-patient variations of the optical properties might thus result in significant error in the predicted changes in chromophore concentration. The modified Beer-Lambert law has been utilised to assess tissue oxygenation and cytochrome aa_3 concentration in adult and neonatal brain [315, 316]. Commercial systems are now offered by, among others, Hamamatsu Photonics (Hamamatsu City, Japan[5]).

A different approach to the modified Beer-Lambert law has been presented by Mourant *et al.* [317, 318]. Here, the source and detector fibres are separated a certain distance $\widetilde{L}$ that minimises the dependence of the path length on the scattering coefficient. For scattering levels typically found in tissue, i.e. μ_s'=5-15 cm^{-1}, $\widetilde{L}$ is in the range 1.5-2.6 mm. Figure 4.15 exemplifies the underlying idea; for relatively large source-detector distances the average path length of the detected photons is longer the higher the scattering coefficient, whereas a very small r combined with low μ_s requires the photons to penetrate relatively deep into the tissue before being able to complete a full 180° turn. For some intermediate source-detector distance, $\widetilde{L}$, the path length, and hence the DPF, are quite insensitive to variations in the scattering coefficient. Others have proposed $r \approx$3-3.5 mm as the "optimal" fibre separation [303, 319]. However, at this source-detector distance it is the reflectance, $R(r)$, and not the path length that displays minimal dependence on the scattering level.

[5] http://sales.hamamatsu.com/en/products/system-division/medical-instruments.php

In Refs. [317, 318] and in Paper **I** the effective path length, L_{eff}, replaces the term DPF r in Equation (4.27). L_{eff} is derived via Equation (4.28) and can be seen as representing some weighted average path length of the detected photons. Here, the incident light intensity I_0 is considered to consist of n photons or photon packages with individual weight I'.

$$L_{\text{eff}} = \frac{1}{\mu_a} \ln\left[\frac{I_0}{I}\right] = \frac{1}{\mu_a} \frac{\ln(\sum_{i=1}^{n} I')}{\sum_{i=1}^{n} I' \exp(-\mu_a L_i)} = \frac{1}{\mu_a} \frac{n}{\sum_{i=1}^{n} \exp(-\mu_a L_i)} = -\frac{1}{\mu_a} \ln\langle \exp(-\mu_a L_i) \rangle \tag{4.28}$$

As discussed above, L_{eff} displays minimal dependence on the scattering level within the probed tissue. However, as detailed in Ref. [318] it does depend on the total absorption coefficient μ_a^{tot}. Here, $\mu_a^{\text{tot}} = \Delta\mu_a + \mu_a^0$ where μ_a^0 is the absorption coefficient at the first measurement, t_1, and $\Delta\mu_a$ denotes the absorption change occurring between t_1 and t_2. As the source-detector distance utilised in Paper **I** was slightly larger than in the original work (2.0 instead of 1.7 mm) non-sequential ray-tracing software was employed to elucidate the exact dependence for our setup; see Figure 4.16.

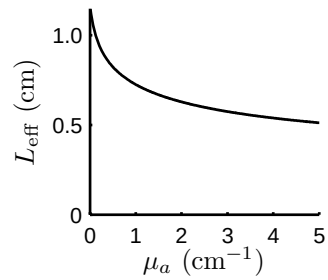

Figure 4.16. *Ray-tracing software, ASAP 8.0.3, Breault Research Organization, Tucson, Arizona, was utilised to assess the absorption dependence of the effective path length for a source-detector distance of 2.0 mm. The plot illustrates the average $L_{\text{eff}}(\mu_a)$ for a reduced scattering coefficient and anisotropy of 10 cm^{-1} and 0.9, respectively.*

In their original paper, Mourant *et al.* used data outside the wavelength range of the dye absorption to fit a wavelength-dependent background, representing the term ΔG in Equation (4.27). Furthermore, a certain assumption on the absorption level at t_1 must be made as the effective path length requires knowledge of μ_a^0. In Ref. [318] it was assumed that tissue absorption in the wavelength range 750 to 800 nm equals zero. To avoid the unknown factor ΔG and include the possibility of tissue absorption in the NIR wavelength range, we instead analysed each individual transmission signal without reference to any time-zero measurement. First, we assumed that at 900 nm, absorption is caused only by water at 60% concentration (w/w) and $I(t_1) = I_0 \exp[-\mu_a(60\%\,\text{water}) L_{\text{eff}}(60\%\,\text{water})]$. Next, the actual, detected signal, $I(t_2)$, should also include the absorption caused by any other tissue chromophores, $\Delta\mu_a$, such as deoxy- and oxyhaemoglobin and photosensitiser, and would thereby be related to $I(t_1)$ via Equation (4.29). Note that ΔG has been eliminated.

$$\Delta A = -\ln\left[\frac{I(t_2)}{I(t_1)}\right] = \Delta\mu_a L_{\text{eff}}(\Delta\mu_a + \mu_a(60\%\,\text{water})) \tag{4.29}$$

In Paper **I** we employed this particular probe for studying the pharmacokinetics of mTHPC following topical application in a murine skin tumour model. In contrast to the fluorescence imaging results, the absorption spectroscopy data displayed an overall good agreement with the chemical extraction data. We proposed two main explanations for these observations; first, in contrast to

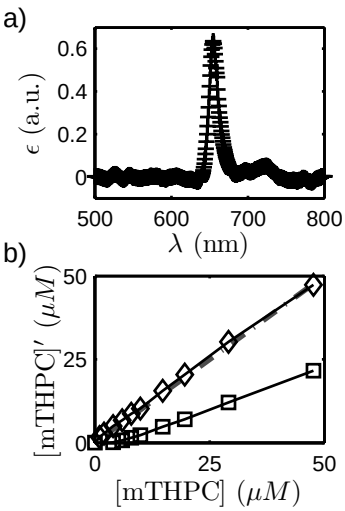

Figure 4.17. ***a)*** *The residual, ϵ, between absorbance data and fit shows a remarkable resemblance with the mTHPC fluorescence spectrum. The fit was performed between 500 and 650 nm and did not include the photosensitiser fluorescence component. Here, $\mu_s' = 10$ cm^{-1} and the mTHPC concentration was 4 μM.* ***b)*** *The calculated mTHPC concentration versus the true concentration with ($\diamond$) and without ($\square$) the mTHPC fluorescence component included in the fitting procedure. The spectral fitting interval was 500 to 750 nm and the same scattering level as in* ***a*** *was used.*

the absolute fluorescence signal; see Section 3.5.1, the absorbance-based probe takes into account the varying absorption coefficient within the probed tissue volume, and second, the average probing depth [317] for the absorption spectroscopy setup matched that of the skin lesions, whereas the violet excitation light used for the fluorescence studies makes this method sensitive to only very superficial tissue regions. However, fluorescence spectroscopy is more sensitive than the absorption-based method. For example, from experimental data of liquid tissue phantoms, containing 2.8-3.7%(v/v) Intralipid and 0.35-1.05%(v/v) Pelikan Fount India ink to give μ_s'=7-9 cm^{-1} and μ_a=0.2-0.6 cm^{-1}, the measured mTHPC lower detection limit was 5 nM and 0.5 μM for the fluorescence and absorbance-probe setups, respectively.

In Paper **I**, the $\Delta\mu_a$ in Equation (4.29) included concentration changes of mTHPC, deoxy- and oxyhaemoglobin as well as a component corresponding to the mTHPC fluorescence. Figure 4.17**a** illustrates a typical residual between the raw ΔA and the fit when the mTHPC fluorescence component was not included. This residual shows a remarkable resemblance with the photosensitiser fluorescence spectrum in Figure 3.6**b**. These data were acquired in liquid tissue phantoms containing titanium oxide (TiO_2) as scatterer and the fit, relying on SVD analysis, was performed between 500 and 650 nm. Most likely, the fluorescence arises due to the relatively strong emission in the violet-blue-green wavelength regions of the pulsed xenon lamp used in the setup. The mTHPC fluorescence thus overlaps the absorption Q-band at 652 nm, thereby causing an apparent decrease in absorbance at this wavelength and a risk of under-predicting the true concentration. In the data analysis, the fluorescent component was therefore implemented as a "negative" chromophore with an extinction coefficient corresponding to the mTHPC fluorescence spectrum. Figure 4.17**b** shows the resulting underestimation of the mTHPC concentration when the fluorescence component of the photosensitiser was excluded from the data analysis. The degree of underestimation was dependent on the spectral fitting range and when only including 500 to 620 nm, thereby avoiding wavelengths at which mTHPC fluoresce, the effect was minimal. However, due to the strong absorption by blood we found it necessary to include the red and NIR wavelengths in the analysis of *in vivo* data. In Figure 4.17**b** the calculated mTHPC concentration with the photosensitiser fluorescence component included in the analysis shows excellent agreement with the true photosensitiser concentration. Similarly good results were achieved for μ_s' in the range 5 to 15 cm^{-1}. As discussed in Paper **I**, excluding the fluorescent component from the analysis of *in vivo* data led to an underestimation of the mTHPC concentration by a factor of two as compared to the extraction results.

Chapter 5

PDT dosimetry

This chapter introduces different PDT dosimetry models which have been categorised according to Wilson *et al.* [215, 320];

(i) Direct dosimetry; Section 5.1: The dose metric is based on the amount of singlet oxygen produced during the treatment.

(ii) Explicit dosimetry; Section 5.2: The dose metric is defined based on multiple parameters relevant to the photodynamic reaction. Such parameters might be light, photosensitiser and oxygen levels.

(iii) Implicit dosimetry; Section 5.3: The dose metric is based on a single parameter, for example the photobleaching kinetics of the photosensitiser.

(iv) Dosimetry via biological response; Section 5.4: The dose metric is related to the immediate biological response of the tissue to the treatment. For example, changes in blood flow has been correlated to the PDT treatment response.

These models are more or less complex, but still only represent crude simplifications of the biological processes involved in PDT. The models do, for instance, not consider the micro-localisation of the parameters included in the model, other stress conditions affecting the individual cells in the treated tissue volume, treatment-induced re-localisation of the photosensitiser etc.

Following this introduction, Section 5.5 discusses the need for individualised PDT. This section also summarises our research towards implementing an instrument with realtime treatment feedback for IPDT in prostate tissue. Many of the conclusions presented in Papers **IV**, **V**, **VI**, **VII** and **VIII** will be discussed.

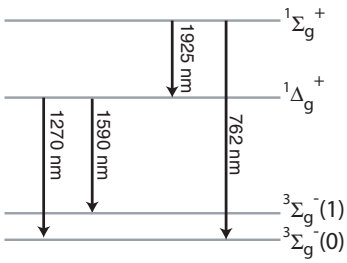

Figure 5.1. *Energy level diagram of molecular oxygen illustrating different radiative decay processes together with the corresponding emission wavelength. For SOLD, the luminescence at 1270 nm is utilised. The other transitions are characterised by even lower transition probabilities within biological media.*

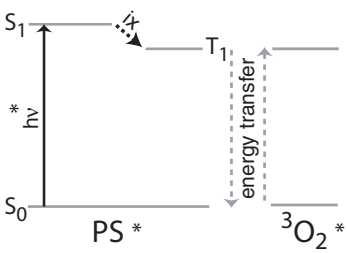

Figure 5.2. *This energy level diagram has been simplified from Figure 2.1 to only illustrate processes leading to production of singlet oxygen. The asterisks indicate variables that can be monitored in connection to explicit PDT dosimetry.*

5.1 Direct PDT dosimetry

Singlet-oxygen luminescence dosimetry (SOLD) has been investigated as a tool for direct PDT dosimetry. The technique relies on the assumption that the PDT effect is mainly exerted via the Type II pathway as discussed in Section 2.1. SOLD quantifies the amount of singlet oxygen by detecting the $^1O_2$ luminescence at 1270 nm; see Figure 5.1. The short lifetime of $^1O_2$ in biological media and the low probability for the transition $^1\Delta_g^+ \rightarrow^3 \Sigma_g^-(0)$ makes it extremely difficult to detect this NIR luminescence signal and to discriminate it from background light and/or background fluorescence. For some time conflicting reports existed regarding the feasibility of *in vivo* detection of singlet-oxygen luminescence [321, 322]. However, a great deal due to improved NIR-sensitive photomultiplier tubes and time-gated detection it has been possible to monitor singlet-oxygen production in parallel to PDT both in *in vitro* and *in vivo* systems [323]. Furthermore, despite varying treatment conditions, such as different light delivery rates, photosensitiser and light doses, a strong correlation between cell survival and the cumulative $^1O_2$ luminescent count has been demonstrated both in cell suspensions [324] and *in vivo* [325, 326]. These observations thus support both the notion of singlet oxygen as the main cytotoxic agent and the use of the total amount of singlet oxygen as a direct and predictive PDT dose metric [320]. As will be discussed in Section 5.2, most explicit dosimetry models rely on the concept of a dose threshold that must be exceeded in order to irreversibly induce tissue damage. However, often no threshold is obvious from "cell-survival versus cumulative $^1O_2$ production" curves. Instead the number of singlet-oxygen molecules required to induce a surviving fraction of $1/e$ per cell is used to quantify the sensitivity to PDT [324]. For cell suspensions sensitised with PpIX, $\sim 10^7$ $^1O_2$ molecules per cell were needed to induce a $1/e$ surviving fraction [324]. At the moment, work is in progress trying to bring SOLD into clinical use, to correctly interpret the luminescence signals by also taking into account tissue heterogeneity, to implement the ultimate goal of realtime treatment feedback [320] and to further investigate the diffusion distance of singlet-oxygen molecules in biological tissues [24].

5.2 Explicit PDT dosimetry

The explicit PDT dosimetry model takes into account the entire pathway starting at the absorption of light and ending at the production of singlet oxygen. Thus, it is necessary to monitor the activating light, Φ, the photosensitiser concentration, $[S_0]$, and the oxygen level, $[^3O_2]$, as illustrated in Figure 5.2. The photosensitiser concentration can be quantified via its fluorescence or

absorption signal as outlined in Sections 3.5.1 and 4.5.1, respectively. The partial oxygen pressure of the tissue, p_{O_2}, can be measured by polarographic microelectrode probes [327], fluorescence- and phosphorescence-based techniques [327], electron paramagnetic resonance oximetry [328] or hypoxia markers [329]. Furthermore, the oxygen saturation of tissue, defined in Equation (4.20), can also be monitored via optical techniques and put in relation to the partial pressure of oxygen via Equation (5.1). This so called Hill curve, shown in Figure 5.3, describes the dissociation of oxygen from haemoglobin in the tissue on a macroscopic scale. p_{50} equals the partial pressure of oxygen at which half of the haemoglobin binding sites are bound to oxygen and n is the Hill coefficient.

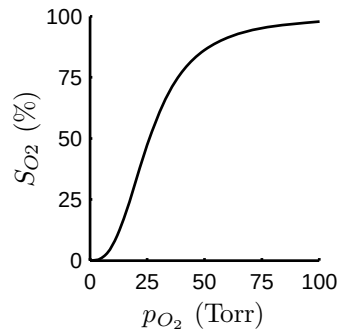

Figure 5.3. *The Hill curve relating the partial pressure of oxygen to the tissue oxygenation. Here, p_{50}=26 Torr and n=2.8.*

$$S_{\mathrm{O2}} = \frac{(p_{O_2})^n}{(p_{O_2})^n + (p_{50})^n} \tag{5.1}$$

Utilising an explicit dosimetry model, the measured parameters need to be incorporated into some dose metric, D_{PDT}, that preferentially correlates with and is predictive of the PDT effect [215]. Following PDT, damaged regions often display a distinct border to unaffected tissue [330], an observation that has coined the threshold dose concept. This hypothesis states that only tissue regions exposed to a PDT dose exceeding some threshold value, i.e. $D_{\mathrm{PDT}} > D_{\mathrm{threshold}}$, experience irreversible damage.

Explicit dose metrics with different degrees of sophistication have been investigated. For example, in a clinical setting, where it is easiest to control parameters such as the total light dose, the light delivery rate, the administered photosensitiser dose and the DLI, dose metrics are often based on only the light and photosensitiser doses according to Equation (5.2).

$$D_{\mathrm{PDT}} = \alpha \int \epsilon[S_0(t)]\Phi(t)dt \tag{5.2}$$

Here, ϵ denotes the extinction coefficient of the photosensitiser and α is a constant that can be included to reflect the varying sensitivity of different cell lines or tissue types to the treatment. Reciprocity of light and drug doses has been observed [331, 332], meaning that similar PDT effects can be achieved if varying the light and photosensitiser doses in such a way as to keep the product of the two invariant. However, photosensitiser photobleaching and the oxygen-dependence of PDT lead to failure of reciprocity and emphasise the importance of including the time-dependence in Equation (5.2) [333, 334].

An even cruder PDT dose metric incorporates only the total light dose, Equation (5.3), thus disregarding the effects a varying, subject-specific photosensitiser concentration [335, 336]. The use of this simplified model is particularly tempting due to the relative ease of manipulating the light dose and the extensive theory for

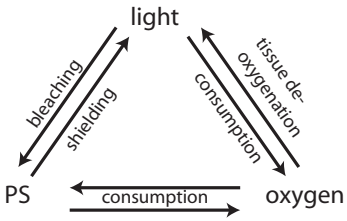

Figure 5.4. *Illustration of some of the interdependencies between the light, photosensitiser, PS, and oxygen. Light induces photosensitiser photobleaching and oxygen consumption. On the other hand, high photosensitiser concentration increases light absorption and limits/shields light penetration. Tissue de-oxygenation induced by the photodynamic reaction further increases tissue absorbance. Finally, the excited photosensitiser consumes oxygen via the photodynamic reaction.*

describing light propagation in biological tissue [337].

$$D_{\mathrm{PDT}} = \alpha \int \Phi(t)dt \tag{5.3}$$

Although the two dose metrics proposed in Equations (5.2) and (5.3) might be valid over limited dose ranges, for certain photosensitisers and treatment conditions, they are obviously quite crude as they ignore the effects of oxygen on the resulting PDT effect. As already mentioned in Section 2.2.2, the oxygen consumption and the vascular effects associated with PDT are capable of rendering the target tissue hypoxic, thus preventing further direct PDT damage [19, 338–341]. Different light irradiation schemes have been employed with the purpose to limit light-induced oxygen depletion and to allow tissue re-oxygenation. For example, utilising lower light delivery rates, thereby decreasing the instantaneous oxygen consumption of the photodynamic reaction, higher oxygen levels and improved treatment outcome have been observed in various animal models following Photofrin- [342], AlS_2Pc- [343], BPD-MA- [344], ALA- [217, 344, 345] and mTHPC-mediated [340, 346–348] PDT. On the extreme end, metronomic PDT (mPDT), during which both photosensitiser and light are delivered at low rates for extended time periods, i.e. several days, has been investigated in order to increase the tumour-selectivity of the treatment [349]. Furthermore, irradiation fractionation, i.e. splitting the therapeutic light delivery into multiple fractions separated by dark periods, has been proposed to improve the PDT outcome by allowing tissue re-oxygenation during the dark intervals [350, 351]. Improved PDT efficacy has indeed been observed when comparing CW to fractionated irradiation, with dark intervals in the range of seconds to minutes, following ALA [217, 344, 352] and mTHPC [346, 348] administration.

Thus, from the above cited results it is clear that an explicit PDT dose metric must take into account not only the light and photosensitiser doses but also the oxygenation level within the target tissue. Furthermore, the use of explicit dosimetry is complicated by the interdependencies of all variables involved in the PDT process as illustrated in Figure 5.4. For example, the therapeutic irradiation photobleaches the photosensitiser and consumes oxygen. On the other hand, the increased light absorption caused by high photosensitiser concentration [215] and light-induced de-oxygenation of the tissue limits light propagation [86]. Finally, photosensitiser consumption caused by ROS, in particular singlet oxygen, introduces a strong connection between the oxygen and photosensitiser concentrations. A dose model that implicitly takes into account these interdependencies will be presented in the following section.

5.3 Implicit PDT dosimetry

Numerous studies have observed a strong correlation between the PDT effect and the degree and/or rate of ALA [217, 353, 354] or mTHPC [219, 355] photobleaching. The explanation to this phenomenon, motivating the use of the kinetics of photosensitiser photobleaching as an implicit dose metric, is that tissue damage and photosensitiser bleaching are both induced by the same process(es). Separate assessment of fluence rate, photosensitiser and oxygen are thus unnecessary since one single variable yields information related to the amount of toxic substance induced by the treatment. High ROS levels induce pronounced and rapid photosensitiser bleaching as well as extensive tissue damage and hence the use of an implicit dose model actually invokes a relationship between the PDT effect and the photosensitiser concentration in direct conflict with in Equation (5.2). Whereas this equation implies a greater treatment effect for the case of no photobleaching, i.e. when $[S_0(t)]$ remains high throughout the entire treatment, the implicit approach predicts the opposite behaviour. Although attractive due to its simplicity, the validity of the implicit PDT dose model is greatly influenced by the mechanism of photosensitiser photobleaching [356].

5.3.1 Photobleaching mechanisms

The reactions that cause irreversible photosensitiser destruction are summarised in Equations (5.4)-(5.6). These equations explicitly account for reactions between photosensitiser ground state and singlet oxygen, Equation (5.4), substrate and excited singlet state of the photosensitiser, Equation (5.5), and substrate and excited triplet state of the photosensitiser, Equation (5.6). Table 5.1 lists symbols used throughout this chapter. Unless otherwise stated, all parameters are time-dependent.

$$S_0 + {}^1O_2 \rightarrow_{k_{os}} PP + SO \tag{5.4}$$
$$S_1 + A \rightarrow_{k_{sa}} PP + SA \tag{5.5}$$
$$T_1 + A \rightarrow_{k_{ta}} PP + SA \tag{5.6}$$

Furthermore, singlet oxygen is consumed as described by the following reactions;

$${}^1O_2 + S_0 \rightarrow_{k_{os}} PP + SO \tag{5.7}$$
$${}^1O_2 + A \rightarrow_{k_{oa}} AO \tag{5.8}$$

The corresponding rate equations are given by Equations (5.9)-(5.13).

Table 5.1: The notation pertaining to this chapter. Remaining parameters have been defined in the "Nomenclature" on pages *xv-xvi*.

Symbol	Explanation	Unit
A	cellular target	
SO, SA, AO	oxidative products	
PP	photoproduct	
σ_{S0}	S_0 absorption cross section	cm^2
	Rate constants:	
k_f	$S_1 \rightarrow S_0$	s^{-1}
k_p	$T_1 \rightarrow S_0$	s^{-1}
k_{isc}	$S_1 \rightarrow T_1$	s^{-1}
k_d	${}^1O_2 \rightarrow {}^3O_2$	s^{-1}
k_{ot}	$T_1 + {}^3O_2$	$\mathrm{M}^{-1}\,\mathrm{s}^{-1}$
k_{os}	${}^1O_2 + S_0$	$\mathrm{M}^{-1}\,\mathrm{s}^{-1}$
k_{oa}	${}^1O_2 + A$	$\mathrm{M}^{-1}\,\mathrm{s}^{-1}$
k_{sa}	$S_1 + A$	$\mathrm{M}^{-1}\,\mathrm{s}^{-1}$
k_{ta}	$T_1 + A$	$\mathrm{M}^{-1}\,\mathrm{s}^{-1}$

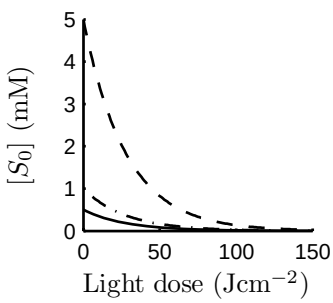

Figure 5.5. *The concentration of ground state photosensitiser assuming bleaching kinetics according to Equation (5.14) for different $[S_O(t_0)]$. Here, the decay rate, $\beta = -\sigma_{SO}/(h\nu)$, was set to 0.036 $J^{-1}cm^2$. Different fluence rates would yield overlapping curves.*

$$\frac{d[S_0]}{dt} = -[S_0]\frac{\sigma_{SO}\Phi}{h\nu} + k_f[S_1] + k_p[T_1] + k_{ot}[T_1][{}^3O_2] - k_{os}[S_0][{}^1O_2] \tag{5.9}$$

$$\frac{d[S_1]}{dt} = [S_0]\frac{\sigma_{SO}\Phi}{h\nu} - k_f[S_1] - k_{isc}[S_1] - k_{sa}[A][S_1] \tag{5.10}$$

$$\frac{d[T_1]}{dt} = k_{isc}[S_1] - k_p[T_1] - k_{ot}[T_1][{}^3O_2] - k_{ta}[A][T_1] \tag{5.11}$$

$$\frac{d[{}^3O_2]}{dt} = -\Phi_\Delta k_{ot}[T_1][{}^3O_2] + k_d[{}^1O_2] \tag{5.12}$$

$$\frac{d[{}^1O_2]}{dt} = \Phi_\Delta k_{ot}[T_1][{}^3O_2] - k_d[{}^1O_2] - k_{oa}[A][{}^1O_2] - k_{os}[S_0][{}^1O_2] \tag{5.13}$$

Within a commonly used model, the analysis is restricted to Equation (5.9) and furthermore includes only the first term on the right hand side of this rate equation. The solution to this rate equation, as given by Equation (5.14), predicts photosensitiser bleaching that depends only on the fluence and the photosensitiser concentration according to first-order kinetics [333, 334, 357]. As shown in Figure 5.5, this model predicts an exponential decay of the photosensitiser concentration with respect to the light dose, $\Phi\, t$, a behaviour that is seldom observed in practise [358] and that fails to correctly account for the oxygen and fluence rate dependency of the bleaching kinetics [359]. In Paper **V** it was also observed that the *in vivo* PpIX fluorescence signal could not be

described by Equation (5.14).

$$[S_0(t)] = [S_0(t_0)] \exp(-\frac{\sigma_{SO}\Phi\, t}{h\nu}) \tag{5.14}$$

A second-order model has been proposed by Forrer *et al.* [360] and is given in Equation (5.15) [345]. Here, the time derivatives in Equations (5.10)-(5.13) have been set to zero, the $[^3O_2]$ is assumed non-limiting and only singlet oxygen-mediated photosensitiser bleaching is taken into account.

$$[S_0(t)] = [S_0(t_0)]\Big[1 + \frac{[S_0(t_0)]\Phi_\Delta\Phi_t\sigma_{SO}k_{os}}{k_d + k_{oa}[A]}\Phi t\Big]^{-1} \tag{5.15}$$

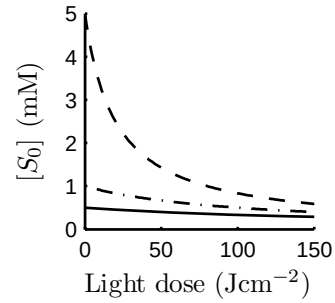

Figure 5.6. *Photosensitiser photobleaching for different $[S_0(t_0)]$ according to Equation (5.15). Here, the term $\frac{\Phi_\Delta\Phi_t\sigma_{S0}k_{os}}{k_d+k_{oa}[A]}$ was set to 10. Different fluence rates yield overlapping curves.*

Figure 5.6 illustrates some bleaching curves for varying initial photosensitiser concentrations. However, this model fails to take into account the influence of varying oxygen concentration and it also predicts a photobleaching rate independent of the fluence rate, clearly deviating from experimental results [345].

Foster *et al.* have devoted extensive work on evaluating Equations (5.9)-(5.13) for PDT employing various photosensitisers on multicell spheroids [131, 359, 361] and *in vivo* [362]. First, restricting the analysis to singlet oxygen-mediated photobleaching, the photosensitiser concentration is given by Equation (5.16).

$$[S_0(t)] = [S_0(t_0)] \exp\big(-k_{os}\int[^1O_2(t')]dt'\big) \tag{5.16}$$

where

$$[^1O_2] = \Phi_\Delta\Phi_t\frac{\sigma_{S0}\Phi}{h\nu}\frac{k_{ot}[^3O_2]}{k_{ot}[^3O_2] + k_p}\frac{1}{k_d + k_{oa}[A]} \tag{5.17}$$

This model has been shown to appropriately describe Photofrin and PpIX fluorescence levels in multicell spheroids for varying fluence rates, light doses and oxygenation conditions [359, 361]. Furthermore, solving the rate equations after incorporating a model for the oxygen diffusion kinetics within the cell spheroids, the theoretically calculated $[^3O_2]$ was in good agreement with measured data [359, 361]. By putting the resulting PDT effect in relation to the calculated cumulative $^1O_2$ production, the threshold dose of singlet oxygen was determined to 12.1±1.2 mM for EMT6 cell spheroids [361].

Despite the good agreement obtained between theory and experimental results for the $^1O_2$-mediated photobleaching model as described by Equation (5.16), a mixed bleaching mechanism, including both $^1O_2$- and T_1-mediated bleaching has been investigated [362]. This mixed model was prompted by the observation of slightly increased photobleaching rates of Photofrin at higher irradiances, thus possibly contradicting the notion of lower bleaching

efficiency during hypoxic conditions. The rate equation for this mixed photobleaching model is given in Equation (5.18). After simplifying the analysis by assuming a constant oxygen level, the photosensitiser concentration can be expressed by Equation (5.19).

$$\frac{d[S_0]}{dt} = -k_{ta}[A][T_1] - k_{os}[^1O_2] \tag{5.18}$$

$$[S_0] = \left[\left(\frac{1}{[S_0(t_0)]} + c_1\right)\exp(c_2 t) - c_1\right]^{-1} \tag{5.19}$$

Here, c_1 and c_2 can be expressed in terms of the parameters in Table 5.1; see Ref. [362] for details. According to this model, the Photofrin bleaching is predominantly mediated via $^1O_2$ at high photosensitiser levels, whereas at low Photofrin concentrations the triplet-mediated reaction is more efficient. This effect, as well as theoretical predictions of the photoproduct kinetics, were indeed confirmed by *in vivo* observations and in cell spheroids [362]. However, experimental $[^3O_2]$ measurements agreed equally well with both the purely $^1O_2$- and the T_1-mediated bleaching model.

Although the different models of photobleaching kinetics, i.e. Equations (5.14), (5.15), (5.16) and (5.19), have been confirmed experimentally for certain treatment conditions, it is likely that *in vivo* photobleaching is a highly complex process. A general expression relating photosensitiser distribution to fluence rate, oxygen concentration and type of biological target must take into account both singlet oxygen- and excited state photosensitiser-mediated bleaching, light-induced re-localisation of the photosensitiser, affecting the microenvironment and thus the triplet, singlet and fluorescence yields, and the influence of the optical properties on the fluorescence signal. It remains to be verified whether an implicit dose model is capable of incorporating these effects.

5.4 Dosimetry via biological response

As discussed in Section 2.2.2, PDT exerts some of its action by damage to endothelial cells within the vasculature. The degree of these vascular effects depends on the photosensitiser, DLI and tissue type. By monitoring the local blood flow, several treatment-induced physiological alterations have been observed. For example, utilising diffuse correlation spectroscopy (DCS) during Photofrin-mediated PDT, an initial increase followed by a decrease in local blood flow has been observed [363]. The decrease displayed significant correlation with the resulting PDT effect. Laser Doppler [364–366], interstitial Doppler OCT [367], Doppler ultrasound [368] and fluorescein angiography [369] have also been utilised to monitor blood flow during PDT.

Electrical impedance spectroscopy (EIS) has been employed to study the permittivity during *in vitro* and *in vivo* PDT [370].

It has been observed that treatment-induced changes of the permittivity were dose-dependent and could be correlated to tissue oedema, cell necrosis and vascular damage. Furthermore, the apoptotic and necrotic cell damage was shown to result in different EIS signals.

As cell damage is associated with changes in water diffusion, diffusion-weighted magnetic resonance imaging (DW-MRI) is useful for detecting treatment response following for example chemo- and radiation therapy. Recently, DW-MRI was employed to detect early changes, i.e occurring within seven hours following treatment, of the water diffusion coefficient [371]. Although this method is not a realtime dosimetry tool, it might prove useful in early response monitoring.

5.5 Towards interactive IPDT

5.5.1 Is there a need for realtime individualised dosimetry?

In the clinical setting it is common to specify only standardised light and drug doses. By defining the PDT dose, D_{PDT}, in terms of the total, delivered light energy (in J/cm^2 for topical irradiation, in J/cm for cylindrical diffusing light sources and in J for point sources, such as cut-end or isotropic fibre tips) and the administered bolus dose of photosensitiser (in mg/kg b.w.) inter- and intra-patient variations in optical properties, photosensitiser distribution and tissue vasculature are obviously ignored. Furthermore, the geometry of the target tissue, such as the thickness of a skin lesion, the total prostate volume or the location of nearby OAR, is often highly patient-specific. Finally, any treatment-induced changes of the tissue composition may also affect the PDT dose being deposited.

The clinical data presented in Papers **IV**, **V** and **VI** provide evidence for intra- and inter-patient variations of many parameters relevant to the treatment outcome. For example, the heterogeneous structure of the treated skin lesions caused spatial variations of μ_{eff}; see for example Figure 4.13**b** in Section 4.6.2. Furthermore, Figure 5.7 displays the varying *in vivo* PpIX concentration at and slightly below the tissue surface. In addition, treatment-induced changes of light transmission, degree and rate of PpIX photobleaching and variations of total haemoglobin content differed among patients as shown in Figure 5.8.

For observations in *in vivo* prostate tissue, the extensive studies performed by the research groups in Toronto and Pennsylvania serve as excellent references.

At the University of Toronto, SR spectroscopy, relying on cylindrical diffusing light sources and isotropic detectors, has been

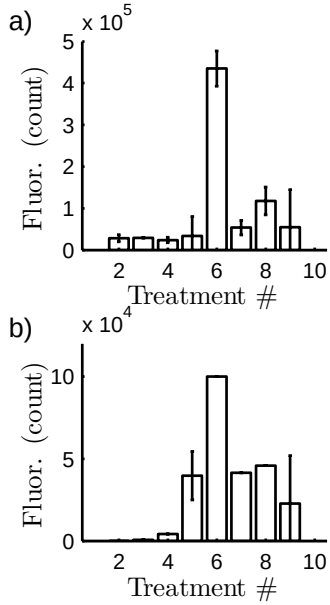

Figure 5.7. *The PpIX fluorescence intensity (at 635 nm) pre-PDT at* **a)** *the tissue surface and at* **b)** *1 mm depth. m-ALA was applied topically four hours prior to the fluorescence investigation. Intra-tumoural m-ALA administration was also utilised for treatments 4, 6 and 8. Error bars represent ±1SD in case of multiple measurement sites. Data were collected using the instrument described in Ref. [172].*

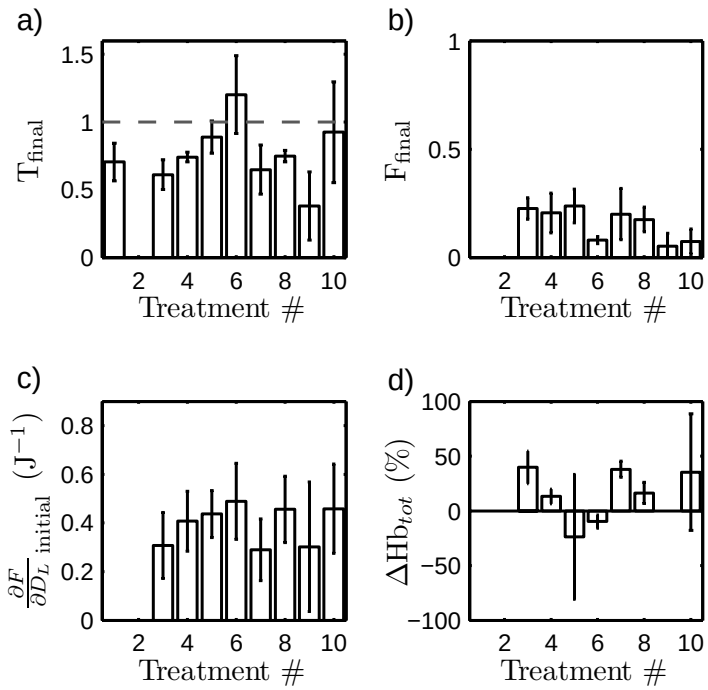

Figure 5.8. ***a)*** *The light transmission at the therapeutic wavelength and* ***b)*** *the PpIX fluorescence level remaining at the end of each treatment session. For each treatment, the data have been normalised to their respective initial level.* ***c)*** *The treatment-specific initial PpIX photobleaching rate (with respect to the delivered light dose).* ***d)*** *The relative change in total haemoglobin content for each treatment session. Error bars represent ±1SD.*

employed to assess the patient-specific μ_a and μ_s' [100]. Inter-patient variations in light distribution as well as fluctuations of the fluence rate occurring during the treatment have been reported. Supporting their observations of heterogeneous tissue structure, the PDT response, following delivery of a standardised light dose, exhibited large variations ([101], Weersink, personal communication).

At the University of Pennsylvania, an integrated system is being developed that is capable of monitoring the fluence rate during MLu-mediated PDT, the absorption and reduced scattering coefficients of the target tissue, the photosensitiser concentration and the tissue oxygenation [104, 372, 373]. The optical properties are assessed by SR spectroscopy but in contrast to the Toronto group, both source and detector fibres consist small isotropically

emitting/receiving spherical diffusors. Step-motors are utilised to acquire the fluence rate distribution for several source depths and hundreds of detector positions [372]. Significant intra- and inter-patient variations in μ_a (range: 0.07-1.62 cm^{-1}) and μ_s' (range: 1.1-44 cm^{-1}) have been observed and for some measurement locations the fluence rate have been shown to vary also during the treatment session. Similarly, a heterogeneous MLu concentration, as assessed by both fluorescence and absorption spectroscopy, has been observed [373]. Although the irradiation times were determined by *in situ* fluence measurements at a few selected sites, a variable the PDT response was reported [103].

Due to the observed intra- and inter-patient variations in fluence rate, photosensitiser distribution and tissue oxygenation, these groups are now developing instrumentation that integrates therapeutic light delivery with realtime monitoring of these parameters. The ultimate aim of such online treatment monitoring is to introduce treatment feedback and optimisation. Investigations along these lines have also been discussed in the treatment of bladder cancer [374] and Barrett's eosophagus [375], for which *in situ* dosimetry guarantees delivery of a prescribed light dose. Bringing the concept of realtime dosimetry one step further, Hasan and Pogue *et al.* have included subject-specific light and photosensitiser levels in the dose metric and studied its correlation to treatment outcome. For example, by compensating the total light dose for variations in pre-treatment photosensitiser uptake, the differences in PDT response were decreased in an animal tumour model [376]. Improved treatment control was also reported by letting the PDT dose metric equal the product of measured fluence rate and photosensitiser concentration integrated only over time periods of rapid photosensitiser bleaching [377]. Adopting the idea of $^1O_2$-mediated tissue destruction and photosensitiser bleaching as discussed in Section 5.3, this dose metric (implicitly) incorporates also the oxygen concentration. It was shown that for fractionated irradiation, each dark period was followed by a time interval of increased rate of photobleaching. A realtime treatment control might thus aim at pausing light delivery when photosensitiser bleaching rates are low, thus allowing for re-oxygenation of the target tissue.

In this section, some experimental data have been presented that highlight the need for individualised dosimetry for IPDT in massive skin tumours and in prostate tissue and that provide evidence that for some animal tumour models and photosensitisers the incorporation of intra- and inter-patient variations in the PDT dose model results in improved treatment control. However, the feasibility of online PDT dosimetry still remains to be elucidated in the clinical situation. The next two sections will describe hardware and software developments towards such an interactive system for IPDT in prostate tissue.

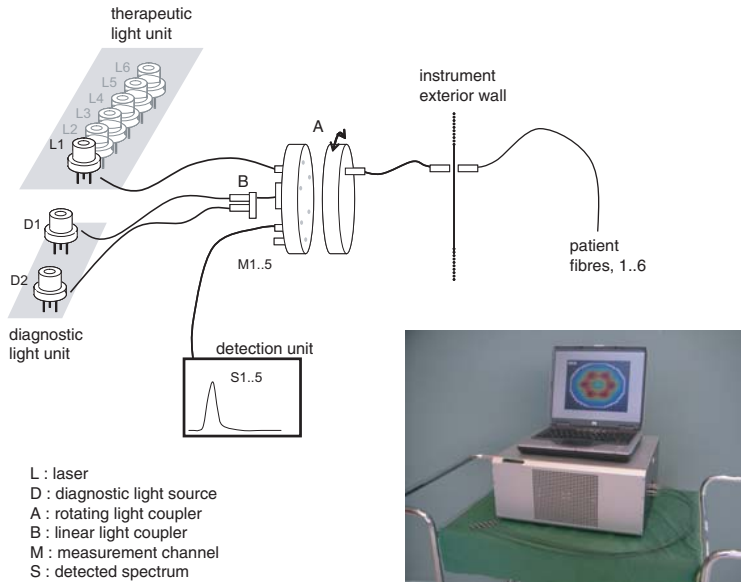

Figure 5.9. *A schematic of the prototype instrumentation described in Paper* ***IV****. Also shown is a digital photo of the instrument.*

5.5.2 The Lund setup

The work described in Paper **IV** aimed at developing hardware allowing for realtime PDT monitoring according to an explicit dose model. Figure 5.9 is a sketch of our prototype instrument developed in 2004. The light coupler A is used to control the operating mode of the instrument; either treatment or measurement mode. While in treatment mode, the output from six diode lasers, L1..6, is transmitted via A into six 400 μm-diameter patient fibres. As this instrument was developed for PDT utilising PpIX, the therapeutic wavelength is 635 nm. The maximum output power per fibre is approximately 200 mW. In measurement mode, the light coupler B sequentially transmits light from the two diagnostic light sources $D1$ and $D2$ into each of the patient fibres. The diagnostic light sources consist of a 635 nm-diode laser ($D1$, similar to the therapeutic light sources) and an LED ($D2$) covering the wavelength interval between 750 and 800 nm. The light transmission signals detected by the remaining five fibres are guided into the detection unit. This unit allows for spectrally resolved detection between 620 and 810 nm. Further hardware details can be found in Paper **IV**. The system (excluding the computer) is enclosed in a clinically compatible case measuring 30 cm x 43 cm x 21 cm (length x width x height) and weighing 12 kg. Prior to each treatment session, the patient fibers are calibrated to emit equal output

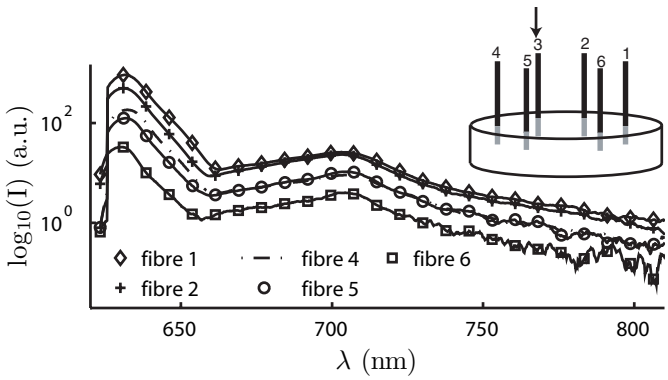

Figure 5.10. *The detected transmission spectra following excitation at 635 nm via patient fibre 3. The inset illustrates the fibre configuration. Data were acquired during treatment session 6 as described in Paper* **V**.

powers while in therapeutic mode. Experimental validation have shown output power stability within ±5% and detection efficiency stability of ±10% over single treatment sessions.

The two diagnostic light sources are utilised to assess three parameters; 1) the light transmission at 635 nm, 2) the PpIX fluorescence at 705 nm and 3) the tissue absorbance in the NIR wavelength region.

Utilising $D1$, the transmission signals are employed to assess $\mu_{\text{eff}}(635\,\text{nm})$ via SR spectroscopy as described in Section 4.6.2. The possibility to track the patient-specific $\mu_{\text{eff}}(r,t)$ is of importance in delivering a prescribed light dose to the entire target geometry as discussed in Paper **VI**. The heterogeneous tissue structure, the limited range of source-detector distances and the presence of bleeding at the front surfaces of the patient fibres complicate the data analysis. As described in Papers **V** and **VI**, we observed an increase in light absorption during the majority of the PDT sessions. Furthermore, the almost complete loss of transmission signal for a some source-detector pairs could possibly be attributed to pronounced blood accumulation at the front surface of a few patient fibres.

The PpIX concentration is monitored via its fluorescence, F, at 705 nm following excitation by $D1$. Thus, the 635 nm-transmission and the PpIX fluorescence are contained in the same transmission spectrum and can be monitored simultaneously; see Figure 5.10. A Schott long-pass filter is necessary to reduce the dynamic range of the detected spectrum. Another advantage of using the therapeutic instead if a less penetrating UV wavelength for inducing photosensitiser fluorescence is that the probed tissue volume better matches the treated tissue region.

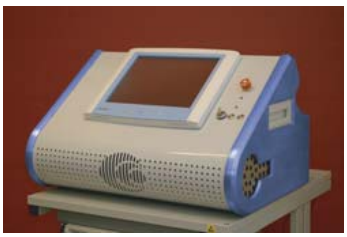

Figure 5.11. *Photograph of the P18 system developed in 2007. A touch-screen allows the user to operate the instrument. Connectors for the patient fibres (missing on the photo) are situated on the right side.*

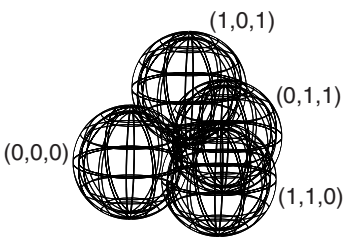

Figure 5.12. *Isodose spheres are assumed to localise with their centres at the corners of equally sized and homogeneously distributed tetrahedrons. A tetrahedron with corners at the displayed coordinates has its centre located at* $(1/2, 1/2, 1/2)$. *The spheres need to overlap in order to target tissue regions at the centre of each tetrahedron, hence* $\delta = \frac{\sqrt{1/4+1/4+1/4}}{1/\sqrt{2}} = 1.225$.

Utilising the second diagnostic light source, $D2$, changes in the tissue absorbance in the NIR wavelength range are assessed. The absorbance spectra can then be related to the optical properties of the tissue, and the absorption coefficient in particular, in order to yield information on variations of the oxygen saturation and total blood volume of the tissue; see Section 4.5.1.

Of importance to the development of explicit PDT dose models, three observations reported in Paper **V** are repeated here;

(i) The light transmission changes, ΔT, at 635 nm and between 750 and 800 nm were consistent if assuming any $\Delta\mu_a$ was due to varying [Hb] and [HbO_2].

(ii) $\Delta \mathrm{Hb}_{\mathrm{tot}} \propto -T_{\mathrm{final}}$, i.e. increases in blood volume decreases the final light transmission and vice versa.

(iii) $T_{\mathrm{final}} \propto \left(\frac{\partial F}{\partial D_L}_{\mathrm{initial}}\right)^{-1}$, i.e. final transmission levels are higher for treatment session displaying an initially rapid PpIX photobleaching.

One might speculate on the interpretation of observation *iii*; due to the higher absorption of Hb as compared to HbO_2, tissue deoxygenation would lead to increased light absorption as well as lower photobleaching rates. However, our analysis of the NIR transmission data did not reveal any significant treatment-induced hypoxia. More detailed studies are needed to elucidate any relation between photosensitiser bleaching kinetics and light transmission levels at the therapeutic and NIR wavelengths. It is worth emphasising that explicit monitoring of light, photosensitiser and tissue oxygenation is relevant both for increasing the understanding of the *in vivo* PDT effects and in developing implicit dose metrics.

5.5.3 Prostate-PDT instrumentation and dosimetry

Aided by the knowledge gained from the clinical trial described in the previous section, we have developed an instrument, referred to as P18 and shown in Figure 5.11, for IPDT in prostate tissue. This instrument incorporates realtime treatment feedback based on a light dose threshold model. In this section, necessary hardware updates are discussed, followed by a description of the realtime dosimetry module. Finally, some initial experimental results related to system performance are given.

Adapting the instrumentation

The most prominent hardware adjustment enforced when aiming at irradiating the entire prostate gland is the increase from six to 18 patient fibres (hence the name P18). However, the working

principle of the internal beamsplitter has not been modified. The number 18 was decided upon somewhat arbitrarily but simplified calculations can aid in illustrating the dependence of irradiation times on number of patient fibres;

(i) Prostate volume: V_{tot} =40 cm^3

(ii) Maximum targeted radius per fibre: $R_{\max} = \delta\left(\frac{3V_{\text{tot}}}{4\pi\,\#\text{fibres}}\right)^{1/3}$

(iii) Threshold light dose: D_L =5 J/cm^2

(iv) Φ at maximum radius: $\Phi(R_{\max}) = \frac{P\mu_{\text{eff}}^2}{4\pi\mu_a R_{\max}} \exp(-\mu_{\text{eff}} R_{\max})$

(v) Irradiation time per fibre: $t_i = \frac{D_L}{\Phi(R_{\max})}$

Several simplifications have been employed in this chain of calculations. First, it is assumed that the isodose surfaces of the fluence rate originating from each source fibre are spherically shaped. Thus, the target volume needs to be filled with these equally sized spheres. The factor δ in item *ii* has been included in order to ascertain overlapping isodose surfaces leaving no untargeted tissue regions in between spheres. δ depends on sphere packing configuration. Here, $\delta = 1.225$ as can be determined from geometrical considerations for the packing configuration shown in Figure 5.12. Furthermore, the threshold light dose value, item *iii*, has been estimated from the results presented by Bown *et al.* ([97], personal communication). From their results, a maximum treatment radius of 10 mm for each source fibre was found reasonable. The use of the maximum, instead of the average, obtainable treatment radius can be justified if assuming the smaller treatment volumes were due to obstructed light propagation, for example caused by blood pooling at the fibre tips. Ideally, such effects are monitored and adjusted for by the realtime treatment monitoring scheme and hence should not be incorporated into the set of baseline optical properties. Utilising the average optical properties published in Ref. [110], $D_L = \Phi\, t$ at the transition zone between treated and untreated tissue regions could be calculated. In calculating Φ we assume diffuse light distribution, isotropic point sources and homogeneous medium. The resulting irradiation time for each patient fibre is plotted in Figure 5.13 for varying μ_{eff} and number of light delivering fibres. Here, the requirement on total irradiation time not to exceed 45 minutes results in 12 as the minimum number of necessary patient fibres. As several factors act to increase the demand on irradiation times, for example that D_L>5 J/cm^2, that the source fibres cannot be distributed uniformly throughout the gland and that the target tissue absorption might exceed previously reported levels, the inclusion of 18 patient fibres provides a safety margin.

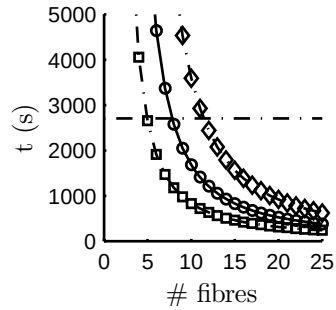

Figure 5.13. *Approximate irradiation times for a 40 cm^3-sized target tissue. μ_{eff} levels were set to represent the mean and mean±1SD values reported in Ref. [110]. μ_{eff}=3.0 (□), 3.8 (○) and 4.6 cm^{-1} (◇). The dashed line indicates the 45-minute limit.*

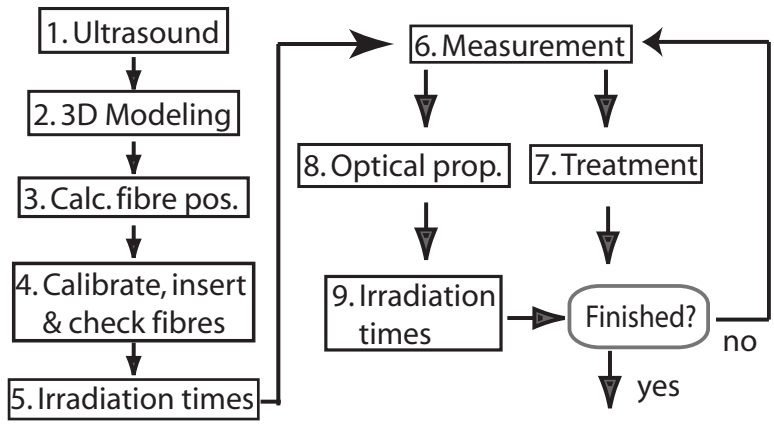

Figure 5.14. *Flow chart illustrating the entire treatment procedure. A transrectal ultrasound investigation, step (1), provides data utilised to create a three-dimensional voxel representation of the target geometry, step (2). Source fibre positions are calculated, step (3), fibres are inserted, step (4), and their individual irradiation times are predicted, step (5). During the treatment session, dosimetric measurements, step (6), and calculations, steps (8) and (9), repeatedly interrupt the therapeutic irradiation, step (7). Thus, steps (6) and (8) track the fibre-specific effective attenuation coefficients, $\mu_{\mathrm{eff(i)}}$. These coefficients are then used to re-calculate the irradiation times of individual fibres, t_i, thus updating the dose plan. The treatment session finishes once the remaining irradiation times as predicted by step (9) equal zero.*

Other hardware modifications include setting the output wavelength of the treatment and first diagnostic light source ($D1$) to 652 nm in order to match the photosensitiser mTHPC. The second diagnostic light source, i.e. the NIR-LED ($D2$), has been broadened spectrally in order to achieve a more robust fit of ϵ_{Hb} and $\epsilon_{\mathrm{HbO_2}}$ to measurement data. Finally, an added feature is a blue LED for single-fibre fluorescence spectroscopy prior to therapeutic light delivery.

Realtime prostate-IPDT dosimetry

Here, the intended treatment procedure as shown in Figure 5.14 will be discussed, some of the conclusions presented in Paper **VIII** will be summarised and the assumptions inherent in our dose model will be commented upon. Paper **VIII** provides a more detailed description of the realtime dosimetry module, also referred to as the Interactive DOsimetry by Sequential Evaluation (IDOSE) module.

Via the built-in touch-screen and a graphical user interface, the physician is guided through the pre-treatment and treatment procedures shown in Figure 5.14. A transrectal ultrasound inves-

tigation is performed to assess the geometry of the target tissue, i.e. the prostate gland, as well as nearby OAR, consisting of the urethra, rectum, cavernous nerve bundles, upper and lower sphincters. In step (3), an optimisation algorithm is employed to calculate the source fibre positions for each patient-specific geometry. Patient fibres are then calibrated, to guarantee 0.15 W output power, guided into position by transperineally inserted hollow steel needles and their actual positions are either confirmed or updated depending on the deviations from the calculated set of fibre positions. The geometry model, the actual fibre positions and a set of default optical properties are used as input for a Block-Cimmino optimization algorithm [378–380] to predict required irradiation times for all source fibers, step (5). Steps (3) and (5) employ a set of "default" optical properties that equals the average μ_a and μ_s' reported in Ref. [110].

During the treatment session, measurements, step (6), and treatment, step (7), sequences are iterated. Immediately following a measurement sequence, delivery of therapeutic irradiation, step (7), runs in parallel to evaluating the measurement data, step (8). This evaluation aims at assessing the effective attenuation coefficients of the tissue, which are then utilised by the Block-Cimmino algorithm, step (9), for updating the irradiation times of individual fibres. Steps (6)-(9) are iterated until the remaining treatment time as predicted by the Block-Cimmino algorithm equals zero. This scheme, in which steps (6), (8) and (9) constitute the real-time IDOSE module, aims at making it possible to deliver a certain light dose to the entire target tissue despite spatial and temporal variations of the optical properties at the therapeutic wavelength.

Step (3): Both a random-search and a generic algorithm have been investigated for optimising source fibre positions within arbitrary three-dimensional geometries. The latter method is described in Paper **VII**. However, it was noted that for similar execution times, the random-search algorithm generally produced more stable results irrespective of tissue geometry. This algorithm, described in Ref. [381], was thus implemented in the P18 system. Briefly, for every iteration each patient fibre is moved a limited length in a random direction and a fitness function value is computed according to Equation (5.20).

$$\widetilde{F} = \sum_{j=1}^{M} w_j^{\text{target}} \phi_{\text{ij}} + \sum_{j=1}^{N} w_j^{\text{OAR}} \phi_{\text{ij}} \tag{5.20}$$

Here, M and N are chosen so that the first summation includes 25% of the prostate voxels with the lowest fluence rate and the second summation includes 25% of the voxels within the OAR with the highest fluence rate. The new set of fibre positions is accepted only if the fibre movement leads to a higher fitness function value. In Equation (5.20), target tissue weights, w_j^{target}, are

positive, whereas $w_j^{\mathrm{OAR}}<0$. ϕ_{ij} denotes the fluence rate in voxel j due to an isotropic point source in voxel i. Here, the analytical solution to the diffusion equation for an isotropic point source in a homogeneous medium, Equation (4.10), is employed. The algorithm thus seeks to maximise the fluence rate within the prostate while minimising the light dose delivered to the OAR. The execution time determines the maximum number of iterations. For a typical prostate geometry, no improvement of the resulting $\widetilde{F}$-values could be observed for execution times exceeding 45 minutes, which is the time slot reserved for the optimisation procedure in the clinical setting.

Steps (6 & 8): In step (6), the light transmission levels between patient fibres are monitored just as described in Section 5.5.2. Although it is technically feasible, not all possible source-detector configurations are utilised. Instead, only the light transmission signals between each patient fibre and its six closest neighbours are measured, thus restricting the probed tissue volume to regions closer to the source fiber. Equation (4.25) in Section 4.6.2 is employed to fit data for these six source-detector distances to a fibre-specific $\mu_{\mathrm{eff(i)}}$.

Steps (5 & 9): Just as for the fibre positioning problem, determining the irradiation times of individual fibres can be expressed as the requirement to deliver a light dose exceeding a pre-determined threshold dose to the target tissue while minimising the dose in the OAR. Here, the PDT dose is based on the fluence, i.e. the fluence rate, Φ, multiplied by the irradiation time, t. In Equation (5.21) the optimisation problem is stated as a system of inequalities for the fluence.

$$L_{\mathrm{j}} \leq \langle \Phi_{\mathrm{j}}, t \rangle = \sum_i \Phi_{\mathrm{ij}} t_{\mathrm{i}} \leq U_{\mathrm{j}} \quad j = 1, 2, .., J$$
$$t_{\mathrm{i}} \geq 0 \quad i = 1, 2, .., 18 \tag{5.21}$$

Here, J is the number of tissue voxels and L_{j} and U_{j} represent the tissue-specific lower and upper threshold doses, respectively. For the OAR, L_{j}=0 and U_{j}=5 J/cm^2, whereas for the target tissue L_{j}=5 J/cm^2 and $U_{\mathrm{j}} = \infty$. In the Block-Cimmino optimisation algorithm, each tissue type is given a certain weight, α_{j}, which reflects the punishment associated with delivering a light dose outside the allowed interval. These importance weights were empirically adjusted to reflect the sensitivity of the different OAR and to discriminate these organs from the target tissue. For the clinical trial, we aim at delivering a light dose exceeding our pre-defined threshold to at least 90% of the target tissue, whereas a maximum of 25% of the voxels representing the rectum is allowed this light dose. No dose restrictions are imposed on the normal tissue surrounding the gland or on the urethra due to the transient periods of catheterisation reported by others[97].

Table 5.2: Details of phantom set used for evaluating P18 performance. The total phantom volume was 800 ml and optical properties were evaluated by the TR setup described in Ref. [110]. IL (20% Intralipid, Fresenius Kabi, Uppsala, Sweden) and ink (Pelikan Fount India Ink, Hannover, Germany) were used. The optical properties are given in cm^{-1}.

Phantom#	μ_a	μ_s'	μ_{eff}
1	0.58	8.0	3.9
2	3.6	7.7	4.0
3	3.6	7.7	4.2
4	2.8	7.4	3.2
5	4.3	10.3	3.7
6	3.6	9.2	4.0
7	2.8	7.9	4.1
8	4.3	10.7	4.6

The PDT dose: As literature on mTHPC distribution and tissue oxygenation in *in vivo* prostate tissue during IPDT is sparse, the development of our dose metric will proceed in a stepwise manner. At present, the PDT dose equals the fluence only. This simplification effectively means that we ignore the effects of heterogeneous photosensitiser distribution and photobleaching as well as varying oxygen concentration and treatment-induced tissue hypoxia. However, the clinical trial will provide data on mTHPC fluorescence and NIR absorbance that will aid in developing an extended dose model, also taking into account the conclusions presented in Sections 5.2, 5.3 and 5.4.

Hardware performance

The performance of the P18 system[1] was investigated using homogeneous, liquid tissue phantoms based on water, Intralipid and ink; see further Table 5.2. Phantom 1 was manufactured to match the average absorption and reduced scattering levels of *in vivo* prostate tissue as observed in patient with primary prostate cancer [110]. Phantoms 2 and 3 presented increasing absorption levels and Phantoms 4-8 were employed to investigate the performance of the setup for a larger range of absorption and reduced scattering levels. In the test setup, shown in Figure 5.15, the fibres were positioned at four discrete depths (5, 15, 20 and 25 mm) from the imaginary prostate apex. Although delineated in the sketch, the urethra and rectum were not included in the experimental phantom. Measurement sequences according to the clinical protocol were performed in the phantoms listed in Table 5.2 and the TR spectroscopy setup described in Ref. [110] was utilised to cross-check actual optical properties. In Figures 5.16, 5.17 and 5.18

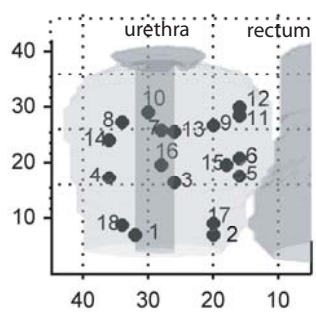

Figure 5.15. *The "test" geometry used for phantom measurements also indicating patient fibre numbers. Dimensions in millimetres.*

[1] unpublished data

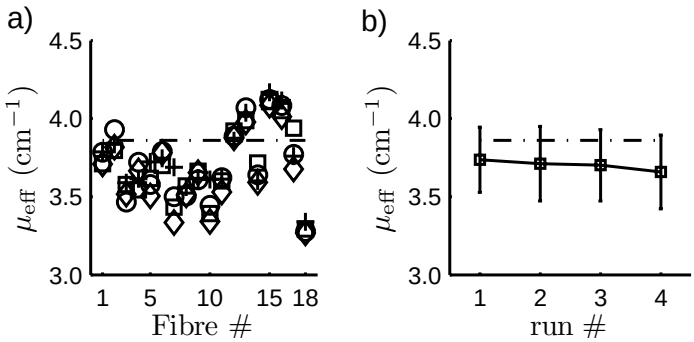

Figure 5.16. ***a)*** *$\mu_{\text{eff(i)}}$ evaluated by the P18 system. Markers represent separate measurement sequences in Phantom 1.* ***b)*** *μ_{eff} averaged for 18 fibres. Dashed lines represent TR data and error bars denote ±1SD.*

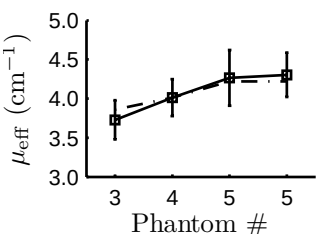

Figure 5.17. *μ_{eff} evaluated by the P18 (solid) and TR (dashed) setups for increasing absorption coefficient. Error bars denote ±1SD.*

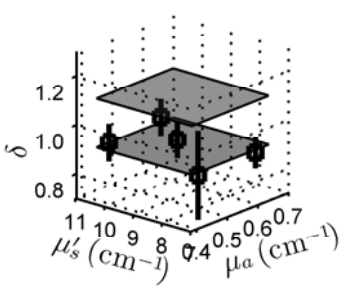

Figure 5.18. *The ratio, δ, between μ_{eff} as evaluated by the P18 and TR setups. Error bars denote ±1SD and grey planes indicate $\delta = 1 \pm 0.1$.*

the dashed lines represent the effective attenuation coefficient as evaluated by the TR setup.

As shown in Figure 5.16 and Figure 5.17, μ_{eff} as determined by the P18 system agrees relatively well with the TR data. Figure 5.17 also illustrates the ability of the setup to track an absorption increase. However, it seems μ_{eff} is often underestimated as compared to the results of the TR setup. At the present, our group is investigating different evaluating techniques for the TR data and preliminary data indicate that the TR values reported in Figures 5.16, 5.17 and 5.18 tend to slightly (i.e. within 5-10%) overestimate both μ_a and μ_s'. This seems to be due to that the instrumental response function of the time-of-flight system has been measured in a way not exactly representing the tissue phantom measurements[2]. The accuracy of the IPDT instrument might thus be slightly better than indicated here.

The assumption of diffuse light propagation inherent in our model can be justified by the relatively high albedo, ranging between 0.92 and 0.96 in Figure 5.17, as well as the large source-detector distances, ranging between eight and 22 millimetres in this "test" geometry. In Figure 5.18, the ratio between μ_{eff} as evaluated by the P18 system and the TR setup is shown for $\mu_a \in [0.4, 0.7]$ cm^{-1}and $\mu_s' \in [7.4, 10.7]$ cm^{-1}. As expected, the lowest albedo results in a slightly larger error. In summary, our results are estimated to yield an accuracy within ±10% for the investigated range of μ_{eff}, in agreement with previously reported results for which SR spectroscopy and the theory of diffuse light propagation have been employed; see further Section 4.6.2.

[2]E. Alerstam, MSc. Thesis, Lund University, to be published.

The IDOSE module

Paper **VIII** presents an extensive evaluation of the IDOSE module. The FEM was utilised for solving the diffusion equation within a realistic prostate geometry, thus providing input data for the IDOSE software module. As shown in Figure 5.19**a**, μ_{eff} was underestimated at all absorption levels investigated. This underestimation could be explained by the geometry model; here, the presence of an air-filled urethra and surrounding tissue, which was characterised by a lower overall attenuation, influenced light transmission between fibres. We thus concluded that the finite size of the prostate gland and the heterogeneous tissue structure influence the diffuse light distribution and hence the results obtained by the SR measurement technique. In Figure 5.19**b**, the dose-volume histograms (DVHs), i.e. plots of the tissue fractional volumes that receive a certain treatment dose, of the fluence are shown corresponding to true (dashed curve) and evaluated (solid curve) μ_{eff}. These DVHs indicate a less efficient targeting of the prostate resulting from underestimating the attenuation coefficient. On the other hand, the treatment fractions, defined as the tissue fraction that receives the 100% threshold dose, of the remaining organs are rather insensitive to the error associated with the evaluation of μ_{eff}.

The IDOSE module was also tested on a treatment scenario displaying temporally varying μ_{eff}; see Figure 5.20**a**. For this simulated treatment session, measurement sequences were performed after 0, 1, 2, 3, 4, 5, 7, 9 and 11 min of therapeutic irradiation. Following each measurement sequence, $\mu_{\text{eff}(i)}$ were evaluated and used as input for the Block-Cimmino algorithm, thus updating the irradiation times of individual fibres. Figure 5.20**b** illustrates the resulting DVHs of the delivered fluence for the cases of no treatment feedback, i.e. irradiation times as calculated based on the first measurement sequence (dashed lines), and with treatment feedback (solid lines). The feedback scheme obviously improves the treatment fraction; ∼96% as compared to ∼86% without treatment feedback.

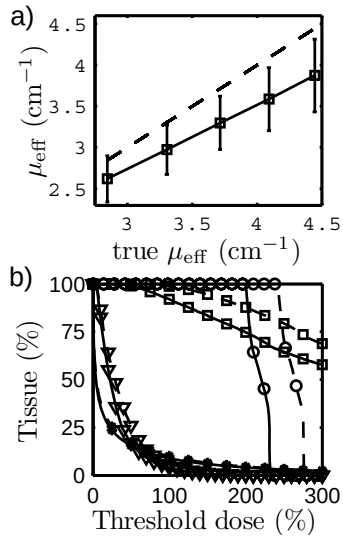

Figure 5.19. ***a)*** *Evaluated μ_{eff} (solid) averaged over all fibres as a function of the true μ_{eff} (dashed). Error bars denote ±1SD. μ_s'=8.7 cm^{-1} within the prostate for all data points.* ***b)*** *DVHs of the delivered light dose for evaluated (solid) and true (dashed) μ_{eff}. Here, the true μ_{eff}=3.7 cm^{-1}. □ prostate, ∘ urethra, ∇ rectum, ∗ normal tissue.*

Is feedback worthwhile?

The ultimate question is whether the proposed feedback scheme makes it practically possible to deliver a prescribed fluence to the target tissue irrespective of temporally and spatially varying optical properties.

It all boils down to how well our assumed model represents the *in vivo* situation. First there are errors associated with the light distribution model, of which the perhaps most incorrect assumption is that of sub-domains characterised by homogeneous optical properties. As already discussed above, this assumption causes an underestimation of $\mu_{\text{eff(i)}}$. For the geometry investigated in

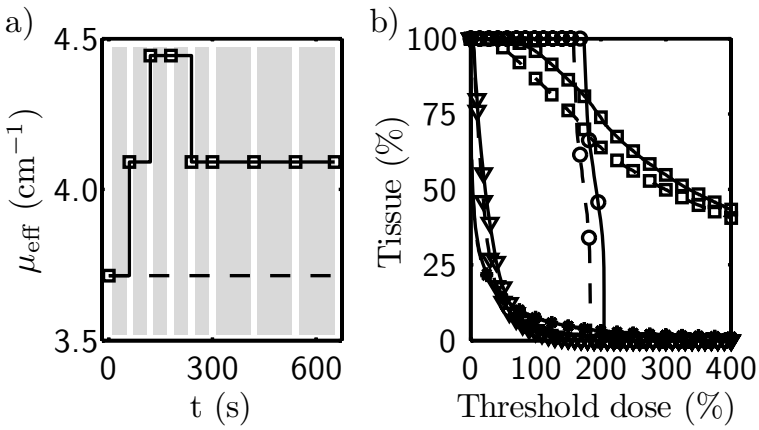

Figure 5.20. ***a)*** *μ_{eff} (solid) during the simulated treatment session compared to the default effective attenuation coefficient used for the pre-treatment plan (dashed). Shaded areas indicate treatment sequences and square markers denote measurement sequences.* ***b)*** *DVHs of the delivered light dose without (dashed) and with (solid) treatment feedback. Symbols as in Figure 5.19.*

Paper **VIII**, the μ_{eff}-underestimation decreases the treatment fraction of the target tissue by 7% at μ_{eff}=3.7 cm^{-1}. Furthermore, the present evaluation scheme relies on the assumption of a constant μ_s'. However, the error analysis presented in Paper **VIII** reveals that a varying scattering level only influences the resulting treatment fraction within a few percent. Another important error source is related to the practical problem of correctly positioning the patient fibres. With ultrasound guidance one might achieve an accuracy of ±1-2 mm. We thus studied the influence on the treatment fraction of adding randomised deviations of the fibre positions and observed a 6% reduction of the treatment fraction. Note, however, that these two types of error were analysed within a homogeneous medium in which the analytical expression for the fluence rate from an isotropic point source, Equation (4.10), could be used. These reductions of the treatment fraction are slightly less than the under-treatment caused by not enabling treatment feedback (∼10%); see Figure 5.20. Thus, for the investigated geometry the feedback scheme affects the light dose coverage to a similar or slightly higher extent than do a heterogeneous tissue and slightly deviating source fibre positions. Furthermore, as the deviations from the assumed model all tend to decrease the treatment fraction, in the case of a treatment-induced μ_a-increase the feedback is of even greater importance in delivering a sufficient light dose.

The evaluation scheme also disregards the flux contribution to the detected transmission signals. However, for the range of

absorption and scattering levels typically found in *in vivo* prostate tissue and for the source-detector distances employed, the fluence rate exceeds the flux as shown in Figure 5.21.

We have not yet investigated the influence of other heterogeneities, such as tissue calcification, inhomogeneous vasculature and possible blood accumulation at the front surface of the patient fibres, on the dose distribution predicted by the IDOSE module. These factors are likely to influence measurement data and resulting treatment fractions to a similar or even higher degree than the effects analysed above. For example, blood pooling at the fibre tip would heavily absorb the therapeutic irradiation, causing a many-fold decrease of the apparent fibre output power and/or detected transmission signal. Hence, a lower threshold for the signal-to-noise ratio (SNR) of the detected transmission signals has been implemented as a part of the IDOSE module. Measurement data with poor SNR, for example originating from such occluded fibres, might thus be excluded from the analysis. Only light transmission data, assessed during *in vivo* IPDT in prostate tissue, can provide an indication on whether our feedback scheme can handle this situation.

To summarise, deviations between the actual fluence distribution and a pre-treatment model thereof, based on some default absorption and scattering coefficients, likely result in significant differences in the treatment fraction of the prostate gland. The IDOSE module has been shown to improve light dose coverage as compared to the pre-treatment plan within a simplified geometry model. At the moment, we are initiating a clinical phase I trial on mTHPC-mediated PDT for primary prostate cancer. Thus, clinical data on *in vivo* light transmission, mTHPC fluorescence and NIR absorbance of the target tissue will become available. Ahead lies extensive but interesting work in interpreting these signals and extend the PDT dose model to include also the photosensitiser concentration and tissue oxygenation. With the help of knowledge gained from the far-reaching studies on PDT lying ahead, the full answer to the expected benefits of realtime feedback for improving PDT efficacy will be given.

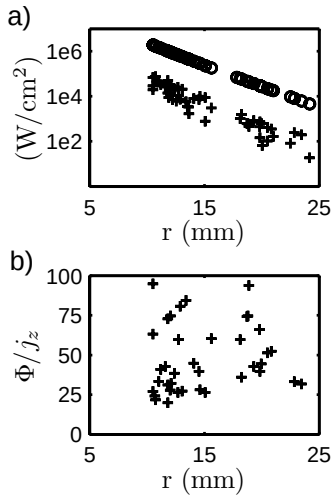

Figure 5.21. ***a)*** *The fluence rate (○) and flux (+) as a function of source-detector distance, r. Here, μ_a=0.5 cm^{-1} and μ_s'=9 cm^{-1}. r corresponds to the geometry employed in Paper* ***VIII****.* ***b)*** *The ratio between the fluence rate and the vertical (z) component flux as a function of source-detector distance.*

Comments on the Papers

I **Fluorescence and absorption assessment of a lipid mTHPC formulation following topical application in a non-melanotic skin tumor model**

A. Johansson, J. Svensson, N. Bendsoe, K. Svanberg, E. Alexandratou, M. Kyriazi, D. Yova, S. Gräfe, T. Trebst, S. Andersson-Engels

This paper is the first report on photosensitiser pharmacokinetics following topical application of a liposomal mTHPC formulation. Here, the mTHPC distribution was investigated four and six hours after topical administration in a murine skin tumour model. Good tumour-selective mTHPC uptake was observed with chemical extraction, fluorescence and absorption spectroscopy.

I took part in hardware development, experimental preparation and work as well as data analysis. I prepared the manuscript.

II **Fluorescence monitoring of a topically applied liposomal Temoporfin formulation and photodynamic therapy of non-pigmented skin malignancies**

N. Bendsoe, L. Persson, A. Johansson, J. Svensson, J. Axelsson, S. Andersson-Engels, S. Svanberg, K. Svanberg

In this work, we extended the study presented in Paper **I** to include human skin tumours. 35 relatively advanced skin lesions were treated at the Lund University Hospital, Sweden, utilising the liposomal mTHPC formulation and application times of four hours. Fluorescence spectroscopy, both in imaging and point-monitoring mode, was used to study photosensitiser distribution and photobleaching induced by the therapeutic irradiation. As reported in Paper **I**, good tumour-selective mTHPC uptake was observed.

I took part in the experimental work and performed minor parts of the data evaluation. I also contributed to parts of the manuscript.

III **Tumor selectivity at short times following systemic administration of a liposomal Temoporfin formulation in a murine tumor model**

J. Svensson, A. Johansson, S. Gräfe, B. Gitter, T. Trebst, N. Bendsoe, S. Andersson-Engels, K. Svanberg

As in Papers **I** and **II**, a liposomal mTHPC formulation was used. Here, the systemic photosensitiser administration route was used in a murine subcutaneous tumour model. The photosensitiser pharmacokinetics were studied in tumour, skin and muscle as well as in various internal organs. Good tumour-to-skin and tumour-to-muscle selectivity was observed already at two to eight hours after mTHPC administration. Our results indicated a rapid biodistribution and clearance from the blood stream.

I took part in hardware development, experimental preparation and work work as well as data analysis. I also prepared parts of the manuscript.

IV **Clinical system for interstitial photodynamic therapy with combined on-line dosimetry measurements**

M. Soto Thompson, A. Johansson, T. Johansson, S. Andersson-Engels, S. Svanberg, N. Bendsoe, K. Svanberg

This paper is the first report on our novel instrument for interstitial PDT combined with realtime monitoring of light transmission, photosensitiser (PpIX) fluorescence and tissue absorbance in the NIR wavelength region. Here, focus was on instrument performance but we also presented some initial clinical data from treatments of nodular skin lesions performed at the Lund University Hospital, Sweden.

I took part in instrumental development and clinical work. I performed major part of the data evaluation and prepared substantial parts of the manuscript.

V **In vivo measurement of parameters of dosimetric importance during interstitial photodynamic therapy of thick skin tumors**

A. Johansson, T. Johansson, M. Soto Thompson, N. Bendsoe, K. Svanberg, S. Svanberg, S. Andersson-Engels

In this paper, we present extended evaluation of the data gathered during the clinical work described in Paper **IV**. We tried to interpret the temporal variations of tissue light absorption and PpIX fluorescence in terms of existing PDT dose models and treatment-induced physiological changes. We speculated on the feasibility of implementing realtime treatment feedback based on the spectroscopic measurements.

I took part in instrumental development and clinical work. I performed the data evaluation and prepared the manuscript.

VI **Influence of treatment-induced changes in tissue absorption on treatment volume during interstitial photodynamic therapy of thick skin tumors**

A. Johansson, N. Bendsoe, K. Svanberg, S. Svanberg, S. Andersson-Engels

This manuscript is again a continuation of the results presented in Paper **IV**. Here, we utilised the clinical data on tissue light transmission at the therapeutic wavelength to model the tissue volume exposed to a certain light dose. This post-PDT analysis indicated significant differences between the intended and actual light dose distributions. Hence, we concluded there is a need for treatment monitoring in order to ascertain delivery of a prescribed light dose to the entire target tissue.

I took part in instrumental development and clinical work. I performed data evaluation and prepared the manuscript.

VII **Pre-treatment dosimetry for interstitial photodynamic therapy**

A. Johansson, J. Hjelm, A. Eriksson, S. Andersson-Engels

In this conference proceeding, we present the use of a generic algorithm for optimising light source positions in arbitrary geometries. The performance of the algorithm was tested on a prostate geometry model and the tissue weights were varied to reflect the sensitivity of the different risk organs.

I supervised the software development, carried out data analysis and prepared the manuscript.

VIII **Realtime light dosimetry software tools for interstitial photodynamic therapy of the human prostate**

A. Johansson, J. Axelsson, J. Swartling, S. Andersson-Engels

This manuscript presents the most recent software module for realtime treatment supervision and feedback. These algorithms have been implemented on a novel IPDT instrument to be used for mTHPC-mediated PDT on primary prostate cancer. Experience gained from the work described in Papers **IV**, **V**, **VI** and **VII** was used for developing realtime feedback based on a light dose threshold model. The algorithms were tested on a realistic prostate geometry and it was concluded that the realtime dosimetry module made it possible to deliver a certain light dose to the target tissue despite spatial and temporal variations of the target tissue optical properties at the therapeutic wavelength.

I took part in developing software and data analysis. Finally, I prepared most parts of the manuscript.

Acknowledgements

During the years as a PhD student I have been given the opportunity to interact with many interesting, highly skilled and generous people. I am grateful for this opportunity and would like to express my appreciation of all collaborators. In particular I would like to mention the following people;

First of all I want to express my deepest gratitude towards my supervisors; Prof. Sune Svanberg, Dr. Katarina Svanberg and Prof. Stefan Andersson-Engels. I particular, I want to thank Sune for his never ending enthusiasm, optimistic view-points and constant encouragement. Katarina, I appreciate all trips we have had together and your support of the "few women in optics". Finally, I'm especially indebted to Stefan for all the fascinating, scientific discussions we have had throughout the years as well as for your always being there as a friend. Activities such as jogging tours in foreign cities, kayaking and more or less serious soccer games have constituted appreciated pauses from many a conference.

I would also like to thank present and past colleagues at work; Jenny Skans for always being there both as a colleague and close friend. Tomas Svensson for spreading his wonderful sense of humour in our office. Johan Axelsson for all our interesting scientific discussions and some wonderful skiing. Christoffer Abrahamsson for his relaxed attitude and tough manners on the soccer field. Pontus Svenmarker for the short time we overlapped at the department. I would also like to thank Sara Pålsson, Johan Stensson and Johannes Swartling for many frustrating but in the end fruitful hours in the laboratory.

Furthermore, I have appreciated working together with Thomas Johansson and Marcelo Soto Thompson. You did an expert job in guiding me in the field of IPDT during my very first years as a researcher.

I would also like to thank various co-authors; Rasmus Grönlund, Niels Bendsoe, Linda Persson, Tilmann Trebst, Susanna Gräfe, Burkhard Gitter, Maria Kyriazi, Eleni Alexandratou and Dido Yova. Special thanks to Rasmus for good company during the frightfully cold nights in Rome and to Susanna for her expertise in animal handling and mTHPC biochemistry.

Throughout the years I have enjoyed the company of some guest researchers such as Florian Forster, Nazila Yavari and Bastiaan Kruijt. Although you spent a limited amount of time within the group you made an ever-lasting impression.

Minna Ramkull, Henrik Steen and Bertil Hermansson; you have provided invaluable help when running into either administrative or computer-related problems.

I have appreciated the relaxing activities enjoyed together with Erik Gustafsson, Thierry Rouchon, Tomas Remetter, Marko Swoboda, Guillaume Genoud and Miguel Miranda. Running, climbing and playing soccer have constituted a perfect complement to the dark laboratory and the computer screen.

Finally, my family deserves my deepest gratitude for putting up with me throughout the ups and downs of my scientific projects. This thesis would never have been finished were it not for your constant support and encouragement.

With my deepest gratitudes,

References

[1]. H. von Tappeiner and A. Jodlbauer. *Die sensibiliserende Wirkung fluorescierender Substanzen. Gesammelte Untersuchungen über die photodynamische Erscheinung.* FCW Vogel Leipzig (1907).

[2]. O. Raab. *Über die Wirkung fluoreszierenden Stoffe auf Infusoria.* Zeitschrift für Biologie **39**, 524–546 (1900).

[3]. H. von Tappeiner and A. Jesionek. *Therapeutische Versuche mit fluorescierenden Stoffen.* Münch. Med. Wochenschr. **47**, 2042–2044 (1903).

[4]. H. von Tappeiner and A. Jodlbauer. *Über Wirkung der photodynamischen (fluorieszierenden) Stoffe auf Protozoan und Enzyme.* Dtsch. Arch. Klin. Med. **80**, 427–487 (1904).

[5]. F. Meyer-Betz. *Untersuchungen über die biologische (photodynamische) Wirkung des Hämatoporphyrins und andere Derivate des Blut- und Gallenfarbstoffs.* Dtsch. Arch. Klin. Med. **112**, 476–450 (1913).

[6]. R. Ackroyd, C. Kelty, N. Brown and M. Reed. *The history of photodetection and photodynamic therapy.* Photochem. Photobiol. **74**, 656–669 (2001).

[7]. S.K. Schwartz, K. Abolon and H. Vermund. *Some relationships of porphyrins, X-rays and tumors.* Univ. Minn. Med. Bull. **27**, 7–8 (1955).

[8]. R.L. Lipson, E.J. Baldes and A.M. Olsen. *The use of a derivative of haematoporphyrin in tumour detection.* J. Nat. Cancer Inst. **26**, 1–11 (1961).

[9]. R.L. Lipson, E.J. Baldes and M.J. Gray. *Hematoporphyrin derivative for detection and management of cancer.* Cancer **20**, 2255–2257 (1967).

[10]. T.J. Dougherty, G.B. Grindey, R. Fiel, K.R. Weishaupt and D.G. Boyle. *Photoradiation therapy. II. Cure of animal tumors with hematoporphyrin and light.* J. Natl. Cancer Inst. **55**, 115–121 (1975).

[11]. J.F. Kelly, M.E. Snell and M.C. Berenbaum. *Photodynamic destruction of human bladder carcinoma.* Br. J. Cancer **31**, 237–244 (1975).

[12]. T.J. Dougherty, J.E. Kaufman, A. Goldfarb, K.R. Weishaupt, D. Boyle and A. Mittleman. *Photoradiation therapy for the treatment of malignant tumors.* Cancer Res. **38**, 2628–2635 (1978).

[13]. M.D. Daniell and J.S. Hill. *A history of photodynamic therapy.* Aust. N. Z. J. Surg. **61**, 340–348 (1991).

[14]. S. Andersson-Engels, J. Johansson, D. Killander, E. Kjellen, L.O. Svaasand, K. Svanberg and S. Svanberg. *Photodynamic therapy and simultaneous near-infrared light-induced hyperthermia in human malignant tumors: A methodological case study.* L.I.A. ICALEO **60**, 67–74 (1987).

[15]. K. Svanberg, T. Andersson, D. Killander, I. Wang, U. Stenram, S. Andersson-Engels, R. Berg, J. Johansson and S. Svanberg. *Photo-*

dynamic therapy of non-melanoma malignant tumours of the skin using topical δ-amino levulinic acid sensitization and laser irradiation. Br. J. Dermatol. **130**, 743–751 (1994).

[16]. M. Ochsner. *Photophysical and photobiological processes in the photodynamic therapy of tumours.* J. Photochem. Photobiol. B: Biol. **39**, 1–18 (1997).

[17]. K.R. Weishaupt, C.J. Gomer and T.J. Dougherty. *Identification of singlet oxygen as the cytotoxic agent in photo-inactivation of a murine tumor.* Cancer Res. **36**, 2326–2329 (1976).

[18]. J.D. Chapman, C.C. Stobbe, M.R. Arnfield, R. Santus, J. Lee and M.S. McPhee. *Oxygen dependency of tumor cell killing in vitro by light-activated Photofrin II.* Radiat. Res. **126**, 73–79 (1991).

[19]. B.W. Henderson and V.H. Fingar. *Relationship of tumor hypoxia and response to photodynamic treatment in an experimental mouse tumor.* Cancer Res. **47**, 3110–3114 (1987).

[20]. D.E.J.G. Dolmans, D. Fukumura and R.K. Jain. *Photodynamic therapy for cancer.* Nat. Rev. Cancer **3**, 380–387 (2003).

[21]. I.J. MacDonald and T.J. Dougherty. *Basic principles of photodynamic therapy.* J. Porphyrins and Phthalocyanines **5**, 105–129 (2001).

[22]. T.M.A.R. Dubbelman, C. Prinsze, L.C. Penning, J. van Steveninck, B.W. Hendersson and T.J. Dougherty. *Photodynamic therapy: Membrane and enzyme photobiology.* In *Photodynamic Therapy: Basic Principles and Clinical Applications* pp 37–47. Marcel Dekker, Inc. New York, USA (1992).

[23]. J. Moan and K. Berg. *The photodegradation of porphyrins in cells can be used to estimate the lifetime of singlet oxygen.* Photochem. Photobiol. **53**, 549–553 (1991).

[24]. J.W. Snyder, E. Skovsen, J.D.C. Lambert, L. Poulsen and P.R. Ogilby. *Optical detection of singlet oxygen from single cells.* Phys. Chem. Chem. Phys. **8**, 4280–4293 (2006).

[25]. K. Berg and J. Moan. *Lysosomes and microtubules as targets for photochemotherapy of cancer.* Photochem. Photobiol. **65**, 403–409 (1997).

[26]. J. Moan, K. Berg, H.B. Steen, T. Warloe, K. Madslien, T.J. Dougherty and B.W. Hendersson. *Fluorescence and photodynamic effects of phthalocyanines and porphyrins in cells.* In *Photodynamic Therapy: Basic Principles and Clinical Applications* pp 19–35. Marcel Dekker, Inc. New York, USA (1992).

[27]. H.I. Pass. *Photodynamic therapy in oncology: Mechanisms and clinical use [review].* J. Natl. Cancer Inst. **85**, 443–456 (1993).

[28]. T.J. Dougherty, C.J. Gomer, B.W. Henderson, G. Jori, D. Kessel, M. Korbelik, J. Moan and Q. Peng. *Photodynamic therapy.* J. Natl. Cancer Inst. **90**, 889–905 (1998).

[29]. M.L. Agarwal, M.E. Clay, E.J. Harvey, H.H. Evans, A.R. Antunez and N.L. Oleinick. *Photodynamic therapy induces rapid cell death by apoptosis in L5178Y mouse lymphoma cells.* Cancer Res. **51**, 5993–5996 (1991).

[30]. S. Marchal, A. Fadloun, E. Maugain, M.A. D'Hallewin, F. Guillemin and L. Bezdetnaya. *Necrotic and apoptotic features of cell death in response to Foscan® photosensitization of HT29 monolayer and multicell spheroids.* Biochem. Pharmacol. **69**, 1167–1176 (2005).

[31]. L. Lilge, M. Portnoy and B.C. Wilson. *Apoptosis induced in vivo by photodynamic therapy in normal brain and intracranial tumour tissue.* Br. J. Cancer **83**, 1110–1117 (2000).

[32]. N.L. Oleinick, R.L. Morris and T. Belichenko. *The role of apoptosis in response to photodynamic therapy: What, where, why, and how.*

Photochem. Photobiol. Sci. **1**, 1–21 (2002).

[33]. G. Kroemer, B. Dallaporta and M. Resche-Rigon. *The mitochondrial death/life regulator in apoptosis and necrosis.* Ann. Rev. Phys. **60**, 619–642 (1998).

[34]. L. Bourre, N. Rousset, S. Thibaut, S. Eleouet, Y. Lajat and T. Patrice. *PDT effects of m-THPC and ALA, phototoxicity and apoptosis.* Apoptosis **7**, 221–230 (2002).

[35]. D. Kessel and Y. Luo. *Mitochondrial photodamage and PDT-induced apoptosis.* J. Photochem. Photobiol. B: Biol. **42**, 89–95 (1998).

[36]. R.D. Almeida, B.J. Manadas, A.P. Carvalho and C.B. Duarte. *Intracellular signaling mechanisms in photodynamic therapy.* Biochim. Biophys. Acta **1704**, 59–86 (2004).

[37]. A.C.E. Moor. *Signaling pathways in cell death and survival after photodynamic therapy.* J. Photochem. Photobiol. B: Biol. **57**, 1–13 (2000).

[38]. D. Kessel, M.G.H. Vicente and J.J. Reiners. *Initiation of apoptosis and autophagy by photodynamic therapy.* Lasers Surg. Med. **38**, 482–488 (2006).

[39]. W. Hausmann. *Die sensiblisierende Wirkung des Hematoporphyrins.* Biochem. Zeitung **30**, 276–316 (1911).

[40]. B.W. Henderson, S.M. Waldow, T.S. Mang, W.R. Potter, P.B. Malone and T.J. Dougherty. *Tumor destruction and kinetics of tumor cell death in two experimental mouse tumors following photodynamic therapy.* Cancer Res. **45**, 572–576 (1985).

[41]. W.M. Star, H.P.A. Marijnissen, A.E. van den Berg-Blok, J.A.C. Versteeg, K.A.P. Franken and H.S. Reinhold. *Destruction of rat mammary tumor and normal tissue microcirculation by hematoporphyrin derivative photoradiation observed in vivo in sandwich observation chambers.* Cancer Res. **46**, 2532–2540 (1986).

[42]. B.W. Henderson and T.J. Dougherty. *How does photodynamic therapy work?* Photochem. Photobiol. **55**, 145–157 (1992).

[43]. F. Stewart, P. Baas and W. Star. *What does photodynamic therapy have to offer radiation oncologists (or their cancer patients)?* Radiothermal Oncology **48**, 233–248 (1998).

[44]. M. Korbelik and G. Krosl. *Cellular levels of photosensitisers in tumours: The role of proximity to the blood supply.* Br. J. Cancer **70**, 604–610 (1994).

[45]. S. Mitra, E. Maugain, L. Bolotine, F. Guillemin and T.H. Foster. *Temporally and spatially heterogeneous distribution of mTHPC in a murine tumor observed by two-color confocal fluorescence imaging and spectroscopy in a whole-mount model.* Photochem. Photobiol. **81**, 1123–1130 (2005).

[46]. Q. Peng, J. Moan, G. Farrants, H.E. Danielsen and C. Rimington. *Localization of potent photosensitizers in human tumor LOX by means of laser scanning microscopy.* Cancer Lett. **58**, 17–27 (1991).

[47]. Q. Peng, J.M. Nesland, J. Moan, J.F. Evensen, M. Kongshaug and C. Rimington. *Localization of fluorescent Photofrin II and aluminum phthalocyanine tetrasulfonate in transplanted human malignant tumor lox and normal tissues of nude mice using highly light-sensitive video intensification microscopy.* Int. J. Cancer **45**, 972–979 (1990).

[48]. D. Kessel, P. Thompson, K. Saatio and K.D. Nantwi. *Tumor localization and photosensitization by sulphonated derivatives of tetraphenylporphine.* Photochem. Photobiol. **45**, 787–790 (1987).

[49]. G. Jori. *Factors controlling the selectivity and efficiency of tumor damage in photodynamic therapy.* Lasers Med. Sci. **5**, 115–120 (1990).

[50]. V.H. Fingar. *Vascular effects of photodynamic therapy.* J. Clin. Laser Med. Surg. **14**, 323–328 (1996).

[51]. B. Chen, B.W. Pogue, J.M. Luna, R.L. Hardman, P.J. Hoopes and T. Hasan. *Tumor vascular permeabilization by vascular-targeting photosensitization: Effects, mechanism, and therapeutic implications.* Clin. Cancer Res. **12**, 917–923 (2006).

[52]. B.W. Henderson and V.H. Fingar. *Oxygen limitation of direct tumor cell kill during photodynamic treatment of a murine tumor model.* Photochem. Photobiol. **49**, 299–304 (1989).

[53]. T.M. Busch. *Photodynamic therapy creates fluence rate-dependent gradients in the intratumoral spatial distribution of oxygen.* Cancer Res. **62**, 7273–7279 (2002).

[54]. B.J. Tromberg, A. Orenstein, S. Kimel, S.J. Barker, J. Hyatt, J.S. Nelson and M.W. Berns. *In vivo tumor oxygen tension measurements for the evaluation of the efficiency of photodynamic therapy.* Photochem. Photobiol. **52**, 375–385 (1990).

[55]. A.P. Castano, P. Mroz and M.R. Hamblin. *Photodynamic therapy and anti-tumour immunity.* Nat. Rev. Cancer **6**, 535–545 (2006).

[56]. F.H. van Duijnhoven, R.I.J.M. Aalbers, J.P. Rovers, O.T. Terpstra and P.J.K. Kuppen. *The immunological consequences of photodynamic treatment of cancer, a literature review.* Immunobiology **207**, 105–113 (2003).

[57]. W.J. de Vree. *Evidence for an important role of neutrophils in the efficacy of photodynamic therapy in vivo.* Cancer Res. **56**, 2908–2911 (1996).

[58]. M. Korbelik. *Induction of tumor immunity by photodynamic therapy.* J. Clin. Laser Med. Surg. **14**, 329–334 (1996).

[59]. M. Korbelik and G.J. Dougherty. *Photodynamic therapy-mediated immune response against subcutaneous mouse tumors.* Cancer Res. **59**, 1941–1946 (1999).

[60]. M. Korbelik, G. Krosl, J. Krosl and G.J. Dougherty. *The role of host lymphoid populations in the response of mouse EMT6 tumor to photodynamic therapy.* Cancer Res. **56**, 5647–5652 (1996).

[61]. W.R. Chen, W.G. Zhu, J.R. Dynlacht, H. Liu and R.E. Nordquist. *Long-term tumor resistance induced by laser photo-immunotherapy.* Int. J. Cancer **81**, 808–812 (1999).

[62]. S.O. Gollnick, L. Vaughan and B.W. Henderson. *Generation of effective antitumor vaccines using photodynamic therapy.* Cancer Res. **62**, 1604–1608 (2002).

[63]. A. Rendon, R. Weersink and L. Lilge. *Towards conformal light delivery using tailored cylindrical diffusers: Attainable light dose distributions.* Phys. Med. Biol. **51**, 5967–5975 (2006).

[64]. R.L.P. van Veen, H. Nyst, S.R. Indrasari, M.A. Yudharto, D.J. Robinson, I.B. Tan, C. Meewis, R. Peters, S. Spaniol, F.A. Stewart, P.C. Levendag and H.J.C.M. Sterenborg. *In vivo fluence rate measurements during Foscan®-mediated photodynamic therapy of persistent and recurrent nasopharyngeal carcinomas using a dedicated light applicator.* J. Biomed. Opt. **11**, 041107 (2006).

[65]. M. Triesscheijn, P. Baas, J.H.M. Schellens and F.A. Stewart. *Photodynamic therapy in oncology.* Oncologist **11**, 1034–1044 (2006).

[66]. I. Wang, N. Bendsoe, C. af Klinteberg, A.M.K. Enejder, S. Andersson-Engels, S. Svanberg and K. Svanberg. *Photodynamic therapy vs. cryosurgery of basal cell carcinomas: Results of a phase III clinical trial.* Br. J. Dermatol. **144**, 832–840 (2001).

[67]. L.R. Braathen, R.M. Szeimies, N. Basset-Seguin, R. Bissonnette, P. Fo-

ley, D. Pariser, R. Roelandts, A.M. Wennberg and C.A. Morton. *Guidelines on the use of photodynamic therapy for nonmelanoma skin cancer: An international consensus.* J. Am. Acad. Dermatol. **56**, 125–143 (2007).

[68]. J. Moan, E. Kvam, E. Hovig, K. Berg and E. Riklis. *Effects of PDT on DNA and chromosomes.* In *Photobiology* pp 821–829. Plenum Press New York (1991).

[69]. J. Arnold *et al. Verteporfin therapy of subfoveal choroidal neovascularization in age-related macular degeneration: Two-year results of a randomized clinical trial including lesions with occult with no classic choroidal neovascularization-verteporfin in photodynamic therapy report 2.* Am. J. Ophthalmol. **131**, 541–560 (2001).

[70]. U. Chakravarthy, G. Soubrane, F. Bandello, V. Chong, C. Creuzot-Garcher, S.A. Dimitrakos, J.F. Korobelnik, M. Larsen, J. Mones, D. Pauleikhoff, C.J. Pournaras, G. Staurenghi, G. Virgili and S. Wolf. *Evolving European guidance on the medical management of neovascular age related macular degeneration.* Br. J. Ophthalmol. **90**, 1188–1196 (2006).

[71]. S.B. Brown, E.A. Brown and I. Walker. *The present and future role of photodynamic therapy in cancer treatment.* Lancet Oncol. **5**, 497–508 (2004).

[72]. J.J. Schuitmaker, P. Baas, H.L.L.M. van Leengoed, F.W. van der Meulen, W.M. Star and N. van Zandwijk. *Photodynamic therapy: A promising new modality for the treatment of cancer.* J. Photochem. Photobiol. B: Biol. **34**, 3–12 (1996).

[73]. M.A. Ortner. *Photodynamic therapy in cholangiocarcinomas.* Best. Pract. Res. Clin. Gastroenterol. **18**, 147–154 (2004).

[74]. M. Wiedmann, F. Berr, I. Schiefke, H. Witzigmann, K. Kohlhaw, J. Mossner and K. Caca. *Photodynamic therapy in patients with nonresectable hilar cholangiocarcinoma: 5-year follow-up of a prospective phase II study.* Gastrointest. Endosc. **60**, 68–75 (2004).

[75]. S.G. Bown, A.Z. Rogowska, D.E. Whitelaw, W.R. Lees, L.B. Lovat, P. Ripley, L. Jones, P. Wyld, A. Gillams and A.W. Hatfield. *Photodynamic therapy for cancer of the pancreas.* Gut **50**, 549–557 (2002).

[76]. H. Kostron, A. Obwegeser and R. Jakober. *Photodynamic therapy in neurosurgery: A review.* J. Photochem. Photobiol. B: Biol. **36**, 157–168 (1996).

[77]. S.S. Stylli and A.H. Kaye. *Photodynamic therapy of cerebral glioma - A review Part II - Clinical studies.* J. Clin. Neurosci. **13**, 709–717 (2006).

[78]. P.J. Muller and B.C. Wilson. *Photodynamic therapy of brain tumors - A work in progress.* Lasers Surg. Med. **38**, 384–389 (2006).

[79]. J. Mehrkens, W. Stummer, T. Beck, J. Tonn and F. Kreth. *Interstitial photodynamic therapy of recurrent malignant gliomas using 5-aminolevulinic acid (5-ALA).* Neuro-Oncology **7**, 310–310 (2005).

[80]. W. Stummer, U. Pichlmeier, T. Meinel, O.D. Wiestler, F. Zanella and H.J. Reulen. *Fluorescence-guided surgery with 5-aminolevulinic acid for resection of malignant glioma: A randomised controlled multicentre phase III trial.* Lancet Oncol. **7**, 392–401 (2006).

[81]. J.S. Friedberg, R. Mick, J. Stevenson, J. Metz, T. Zhu, J. Buyske, D.H. Sterman, H.I. Pass, E. Glatstein and S.M. Hahn. *A phase I study of Foscan-mediated photodynamic therapy and surgery in patients with mesothelioma.* Ann. Thorac. Surg. **75**, 952–959 (2003).

[82]. S.K. Hendren, S.M. Hahn, F.R. Spitz, T.W. Bauer, S.C. Rubin, T. Zhu, E. Glatstein and D.L. Fraker. *Phase II trial of debulking surgery and photodynamic therapy for disseminated intraperitoneal tumors.* Ann.

Surg. Oncol. **8**, 65–71 (2001).

[83]. Q. Peng, T. Warloe, K. Berg, J. Moan, M. Kongshaug, K.-E. Giercksky and J.M. Nesland. *5-aminolevulinic acid-based photodynamic therapy: Clinical research and future challenges*. Cancer **79**, 2282–2308 (1997).

[84]. Q. Peng, K. Berg, J. Moan, M. Kongshaug and J.M. Nesland. *5-aminolevulinic acid-based photodynamic therapy: Principles and experimental research*. Photochem. Photobiol. **65**, 235–251 (1997).

[85]. M.V. Holmes, R.S. Dawe, J. Ferguson and S.H. Ibbotson. *A randomized, double-blind, placebo-controlled study of the efficacy of tetracaine gel (Ametop®) for pain relief during topical photodynamic therapy*. Br. J. Dermatol. **150**, 337–340 (2004).

[86]. S. Mitra and T.H. Foster. *Carbogen breathing significantly enhances the penetration of red light in murine tumours in vivo*. Phys. Med. Biol. **49**, 1891–1904 (2004).

[87]. L.O. Svaasand, B.J. Tromberg, P. Wyss, M.-T. Wyss-Desserich, Y. Tadir and M.W. Berns. *Light and drug distribution with topically administered photosensitizers*. Lasers Med. Sci. **11**, 261–265 (1996).

[88]. J.C. Kennedy, R.H. Pottier and D.C. Pross. *Photodynamic therapy with endogenous protoporphyrin IX: Basic principles and present clinical experience*. J. Photochem. Photobiol. B: Biol. **6**, 143–148 (1990).

[89]. E. Balasubramaniam and P. Natarajan. *Photophysical properties of protoporphyrin IX and thionine covalently attached to macromolecules*. J. Photochem. Photobiol. A: Chem. **103**, 201–211 (1997).

[90]. N.C. Zeitouni, S. Shieh and A.R. Oseroff. *Laser and photodynamic therapy in the management of cutaneous malignancies*. Clin. Dermatol. **19**, 328–339 (2001).

[91]. H. Lui, L. Hobbs, W.D. Tope, P.K. Lee, C. Elmets, N. Provost, A. Chan, H. Neyndorff, X.Y. Su, H. Jain, I. Hamzavi, D. McLean and R. Bissonnette. *Photodynamic therapy of multiple nonmelanoma skin cancers with verteporfin and red light-emitting diodes - Two-year results evaluating tumor response and cosmetic outcomes*. Arch. Dermatol. **140**, 26–32 (2004).

[92]. M. Triesscheijn, M. Ruevekamp, N. Antonini, H. Neering, F.A. Stewart and P. Baas. *Optimizing meso-tetra-hydroxyphenyl-chlorin mediated photodynamic therapy for basal cell carcinoma*. Photochem. Photobiol. **82**, 1686–1690 (2006).

[93]. S.C. Chang, G. Buonaccorsi, A. MacRobert and S.G. Bown. *Interstitial and transurethral photodynamic therapy of the canine prostate using meso-tetra-(m-hydroxyphenyl) chlorin*. Int. J. Cancer **67**, 555–562 (1996).

[94]. D. Zaak, R. Sroka, M. Höppner, W. Khoder, O. Reich, S. Tritschler, R. Muschter, R. Knüchel and A. Hofstetter. *Photodynamic therapy by means of 5-ALA induced PPIX in human prostate cancer - Preliminary reults*. Med. Laser Appl. **18**, 91–95 (2003).

[95]. Z. Huang, Q. Chen, D. Luck, J. Beckers, B.C. Wilson, N. Trncic, S.M. Larue, D. Blanc and F.W. Hetzel. *Studies of a vascular-acting photosensitizer, Pd-bacteriopheophorbide (Tookad), in normal canine prostate and spontaneous canine prostate cancer*. Lasers Surg. Med. **36**, 390–397 (2005).

[96]. R. Kirby. *Treatment options for early prostate cancer*. Urology **52**, 948–962 (1998).

[97]. C.M. Moore, T.R. Nathan, W.R. Lees, C.A. Mosse, A. Freeman, M. Emberton and S.G. Bown. *Photodynamic therapy using meso tetra hydroxy phenyl chlorin (mTHPC) in early prostate cancer*. Lasers Surg. Med. **38**, 356–363 (2006).

[98]. T.R. Nathan, D.E. Whitelaw, S.C. Chang, W.R. Lees, P.M. Ripley, H. Payne, L. Jones, M.C. Parkinson, M. Emberton, A.R. Gillams, A.R. Mundy and S.G. Bown. *Photodynamic therapy for prostate cancer recurrence after radiotherapy: A phase I study.* J. Urol. **168**, 1427–1432 (2002).

[99]. C.M. Moore, I.M. Hoh, S.G. Bown and M. Emberton. *Does photodynamic therapy have the necessary attributes to become a future treatment for organ-confined prostate cancer?* BJU Int. **96**, 754–758 (2005).

[100]. R.A. Weersink, A. Bogaards, M. Gertner, S.R.H. Davidson, K. Zhang, G. Netchev, J. Trachtenberg and B.C. Wilson. *Techniques for delivery and monitoring of TOOKAD (WST09)-mediated photodynamic therapy of the prostate: Clinical experience and practicalities.* J. Photochem. Photobiol. B: Biol. **79**, 211–222 (2005).

[101]. J.H. Pinthus, A. Bogaards, R. Weersink, B.C. Wilson and J. Trachtenberg. *Photodynamic therapy for urological malignancies: Past to current approaches.* J. Urol. **175**, 1201–1207 (2006).

[102]. M.A. Haider, S.R. Davidson, A.V. Kale, R.A. Weersink, A.J. Evans, A. Toi, M.R. Gertner, A. Bogaards, B.C. Wilson, J.L. Chin, M. Elhilali and J. Trachtenberg. *Prostate gland: MR imaging appearance after vascular targeted photodynamic therapy with Palladium-Bacteriopheophorbide.* Radiology **244**, 196–204 (2007).

[103]. K.L. Du, R. Mick, T. Busch, T.C. Zhu, J.C. Finlay, G. Yu, A.G. Yodh, S.B. Malkowicz, D. Smith, R. Whittington, D. Stripp and S.M. Hahn. *Preliminary results of interstitial motexafin lutetium-mediated PDT for prostate cancer.* Lasers Surg. Med. **38**, 427–434 (2006).

[104]. T.C. Zhu, J.C. Finlay and S.M. Hahn. *Determination of the distribution of light, optical properties, drug concentration, and tissue oxygenation in-vivo in human prostate during motexafin lutetium-mediated photodynamic therapy.* J. Photochem. Photobiol. B: Biol. **79**, 231–241 (2005).

[105]. G. Jori. *Tumour photosensitizers: Approach to enhance the selectivity and efficiency of photodynamic therapy.* J. Photochem. Photobiol. B: Biol. **36**, 87–93 (1996).

[106]. J. Moan. *Properties for optimal PDT sensitizers.* J. Photochem. Photobiol. B: Biol. **5**, 521–524 (1990).

[107]. A.J. MacRobert, S.G. Bown, D. Phillips, G. Bock and S. Harnett. *What are the ideal photoproperties for a sensitizer?* In *Photosensitizing compounds: Their chemistry, biology and clinical use. Ciba Foundation Symposium* pp 4–12. John Wiley & Sons Ltd Chichester, UK (1989).

[108]. E.S. Nyman and P.H. Hynninen. *Research advances in the use of tetrapyrrolic photosensitizers for photodynamic therapy.* J. Photochem. Photobiol. B: Biol. **73**, 1–28 (2004).

[109]. J.F. Savary, P. Grosjean, P. Monnier, C. Fontolliet, G. Wagnières, D. Braichotte and H. van den Bergh. *Photodynamic therapy of early squamous cell carcinomas of the esophagus: A review of 31 cases.* Endoscopy **30**, 258–265 (1998).

[110]. T. Svensson, M. Einarsdóttír, K. Svanberg and S. Andersson-Engels. *In vivo optical characterization of human prostate tissue using near-infrared time-resolved spectroscopy.* J. Biomed. Opt. **12**, 014022–1–014022–10 (2006).

[111]. T. Svensson, J. Swartling, P. Taroni, A. Torricelli, P. Lindblom, C. Ingvar and S. Andersson-Engels. *Characterization of normal breast tissue heterogeneity using time-resolved near-infrared spectroscopy.* Phys. Med. Biol. **50**, 2559–2571 (2005).

[112]. M.W.R. Reed, F.N. Miller, T.J. Wieman, M.T. Tseng and C.G. Pietsch.

The effect of photodynamic therapy on the microcirculation. J. Surg. Res. **45**, 452–459 (1988).

[113]. F. Ricchelli, S. Gobbo, G. Jori, G. Moreno, F. Vinzens and C. Salet. *Photosensitization of mitochondria by liposome-bound porphyrins.* Photochem. Photobiol. **58**, 53–58 (1993).

[114]. R.W. Boyle and D. Dolphin. *Structure and biodistribution relationships of photodynamic sensitizers.* Photochem. Photobiol. **64**, 469–485 (1996).

[115]. B.W. Henderson, D.A. Bellnier, G. Bock and S. Harnett. *Tissue localization of photosensitizers and the mechanism of photodynamic tissue destruction.* In *Photosensitizing compounds: Their chemistry, biology and clinical use. Ciba Foundation Symposium* pp 112–125. John Wiley & Sons Ltd Chichester, UK (1989).

[116]. D.A. Bellnier, B.W. Henderson, B.W. Hendersson and T.J. Dougherty. *Determinants for photodynamic tissue destruction.* In *Photodynamic Therapy: Basic Principles and Clinical Applications* pp 117–127. Marcel Dekker, Inc. New York, USA (1992).

[117]. W. Alian, S. Andersson-Engels, K. Svanberg and S. Svanberg. *Laser-induced fluorescence studies of meso-tetra(hydroxyphenyl)chlorin in malignant and normal tissues in rat.* Br. J. Cancer **70**, 880–885 (1994).

[118]. H. Barr, S.G. Bown, B.W. Henderson and T.J. Dougherty. *Normal tissue damage following photodynamic therapy: Are there biological advantages?* In *Photodynamic therapy: Basic Principles and Clinical Applications* pp 201–216. Marcel Dekker New York (1992).

[119]. J. Moan and Q. Peng. *An outline of the hundred-year history of PDT.* Anticancer Res. **23**, 3591–3600 (2003).

[120]. J.P. Thomas and A.W. Girotti. *Glucose administration augments in vivo uptake and phototoxicity of the tumor-localizing fraction of hematoporphyrin derivative.* Photochem. Photobiol. **49**, 241–247 (1989).

[121]. R.K. Jain. *Delivery of molecular and cellular medicine to solid tumors.* Adv. Drug Deliv. Rev. **46**, 149–168 (2001).

[122]. M. Korbelik, G. Krosl, P.L. Olive and D.J. Chaplin. *Distribution of Photofrin between tumour cells and tumour associated macrophages.* Br. J. Cancer **64**, 508–512 (1991).

[123]. G. Jori and E. Reddi. *The role of lipoproteins in the delivery of tumour-targeting photosensitisers.* Int. J. Biochem. **25**, 1369–1375 (1993).

[124]. B.A. Allison, E. Waterfield, A.M. Richter and J.G. Levy. *The effects of plasma lipoproteins on in vitro tumor cell killing and in vivo tumor photosensitization with benzoporphyrin derivative.* Photochem. Photobiol. **54**, 709–715 (1991).

[125]. B.A. Allison, P.H. Pritchard, A.M. Richter and J.G. Levy. *The plasma distribution of benzoporphyrin derivative and the effects of plasma-lipoproteins on its biodistribution.* Photochem. Photobiol. **52**, 501–507 (1990).

[126]. A.S.L. Derycke and P.A.M. de Witte. *Liposomes for photodynamic therapy.* Adv. Drug Deliv. Rev. **56**, 17–30 (2004).

[127]. Y.N. Konan, R. Gurny and E. Allemann. *State of the art in the delivery of photosensitizers for photodynamic therapy.* J. Photochem. Photobiol. B: Biol. **66**, 89–106 (2002).

[128]. A.M. Richter, E. Waterfield, A.K. Jain, A.J. Canaan, B.A. Allison and J.G. Levy. *Liposomal delivery of a photosensitizer, benzoporphyrin derivative monoacid ring A (BPD), to tumor tissue in a mouse tumor model.* Photochem. Photobiol. **57**, 1000–1006 (1993).

[129]. Z.J. Wang, Y.Y. He, C.G. Huang, J.S. Huang, Y.C. Huang, J.Y. An,

Y. Gu and L.J. Jiang. *Pharmacokinetics, tissue distribution and photodynamic therapy efficacy of liposomal-delivered hypocrellin A, a potential photosensitizer for tumor therapy.* Photochem. Photobiol. **70**, 773–780 (1999).

[130]. K.K.H. Wang, S. Mitra and T.H. Foster. *A comprehensive mathematical model of microscopic dose deposition in photodynamic therapy.* Med. Phys. **34**, 282–293 (2007).

[131]. S. Mitra and T.H. Foster. *Photophysical parameters, photosensitizer retention and tissue optical properties completely account for the higher photodynamic efficacy of meso-tetra-hydroxyphenyl-chlorin vs Photofrin.* Photochem. Photobiol. **81**, 849–859 (2005).

[132]. D.J. Ball, D.I. Vernon and S.B. Brown. *The high photoactivity of m-THPC in photodynamic therapy. Unusually strong retention of m-THPC by RIF-1 cells in culture.* Photochem. Photobiol. **69**, 360–363 (1999).

[133]. I.P.J. van Geel, H. Oppelaar, Y.G. Oussoren, M.A. van der Valk and F.A. Stewart. *Photosensitizing efficacy of mTHPC-PDT compared to Photofrin-PDT in the RIF1 mouse tumour and normal skin.* Int. J. Cancer **60**, 388–394 (1995).

[134]. J.Y. Chen, N.K. Mak, C.M.N. Yow, M.C. Fung, L.C. Chiu, W.N. Leung and N.H. Cheung. *The binding characteristics and intracellular localization of temoporfin (mTHPC) in myeloid leukemia cells: Phototoxicity and mitochondrial damage.* Photochem. Photobiol. **72**, 541–547 (2000).

[135]. M.H. Teiten, L. Bezdetnaya, P. Morlière, R. Santus and F. Guillemin. *Endoplasmic reticulum and Golgi apparatus are the preferential sites of Foscan localisation in cultured tumor cells.* Br. J. Cancer **88**, 146–152 (2003).

[136]. T.H. Foster, B.D. Pearson, S. Mitra and C.D. Bigelow. *Fluorescence anisotropy imaging reveals localization of meso-tetrahydroxyphenyl chlorin in the nuclear envelope.* Photochem. Photobiol. **81**, 1544–1547 (2005).

[137]. P. Cramers, M. Ruevekamp, H. Oppelaar, O. Dalesio, P. Baas and F.A. Stewart. *Foscan® uptake and tissue distribution in relation to photodynamic efficacy.* Br. J. Cancer **88**, 283–290 (2003).

[138]. A.M. Ronn, J. Batti, C.J. Lee, D. Yoo, M.E. Siegel, M. Nouri, L.A. Lofgren and B.M. Steinberg. *Comparative biodistribution of meta-tetra(hydroxyphenyl) chlorin in multiple species: Clinical implications for photodynamic therapy.* Lasers Surg. Med. **20**, 437–442 (1997).

[139]. R. Whelpton, A.T. Michaeltitus, R.P. Jamdar, K. Abdillahi and M.F. Grahn. *Distribution and excretion of radiolabeled temoporfin in a murine tumor model.* Photochem. Photobiol. **63**, 885–891 (1996).

[140]. R. Whelpton, A.T. Michaeltitus, S.S. Basra and M. Grahn. *Distribution of Temoporfin, a new photosensitizer for the photodynamic therapy of cancer, in a murine tumor model.* Photochem. Photobiol. **61**, 397–401 (1995).

[141]. R. Veenhuizen, H. Oppelaar, M. Ruevekamp, J. Schellens, O. Dalesio and F. Stewart. *Does tumour uptake of Foscan determine PDT efficacy?* Int. J. Cancer **73**, 236–239 (1997).

[142]. M. Triesscheijn, M. Ruevekamp, M. Aalders, P. Baas and F.A. Stewart. *Outcome of mTHPC mediated photodynamic therapy is primarily determined by the vascular response.* Photochem. Photobiol. **81**, 1161–1167 (2005).

[143]. H.B. Ris, H.J. Altermatt, C.M. Stewart, T. Schaffner, Q. Wang, C.K. Lim, R. Bonnett and U. Althaus. *Photodynamic therapy with m-*

tetrahydroxyphenylchlorin in vivo: Optimization of the therapeutic index. Int. J. Cancer **55**, 245–249 (1993).

[144]. Q. Peng, J. Moan, L.W. Ma and J.M. Nesland. *Uptake, localization, and photodynamic effect of meso-tetra(hydroxyphenyl)porphine and its corresponding chlorin in normal and tumor tissues of mice bearing mammary carcinoma*. Cancer Res. **55**, 2620–2626 (1995).

[145]. E. Maugain, S. Sasnouski, V. Zorin, J.L. Merlin, F. Guillemin and L. Bezdetnaya. *Foscan®-based photodynamic treatment in vivo: Correlation between efficacy and Foscan accumulation in tumor, plasma and leukocytes*. Oncol. Rep. **12**, 639–645 (2004).

[146]. P. Baas, A.E. Saarnak, H. Oppelaar, H. Neering and F.A. Stewart. *Photodynamic therapy with meta-tetrahydroxyphenylchlorin for basal cell carcinoma: A phase I/II study*. Br. J. Dermatol. **145**, 75–78 (2001).

[147]. E. Reddi. *Role of delivery vehicles for photosensitizers in the photodynamic therapy of tumours;* New trends in photobiology. J. Photochem. Photobiol. B: Biol. **37**, 189–195 (1997).

[148]. X. Damoiseau, H.J. Schuitmaker, J.W.M. Lagerberg and M. Hoebeke. *Increase of the photosensitizing efficiency of the Bacteriochlorin a by liposome incorporation*. J. Photochem. Photobiol. B: Biol. **60**, 50–60 (2001).

[149]. L. Bourre, S. Thibaut, M. Fimiani, Y. Ferrand, G. Simonneaux and T. Patrice. *In vivo photosensitizing efficency of a diphenylchlorin sensitizer: Interest of a DMPC liposome formulation*. Pharmacol. Res. **47**, 253–261 (2003).

[150]. S. Sasnouski, V. Zorin, I. Khludeyev, M.A. D'Hallewin, F. Guillemin and L. Bezdetnaya. *Investigation of Foscan interactions with plasma proteins*. Biochim. Biophys. Acta **1725**, 394–402 (2005).

[151]. P. Westermann, T. Glanzmann, S. Andrejevic, D.R. Braichotte, M. Forrer, G.A. Wagnières, P. Monnier, H. van den Bergh, J.P. Mach and S. Folli. *Long circulating half-life and high tumor selectivity of the photosensitizer meta-tetrahydroxyphenylchlorin conjugated to polyethylene glycol in nude mice grafted with a human colon carcinoma*. Int. J. Cancer **76**, 842–850 (1998).

[152]. T. Glanzmann, C. Hadjur, M. Zellweger, P. Grosiean, M. Forrer, J.P. Ballini, P. Monnier, Bergh H. van den, C.K. Lim and G. Wagnières. *Pharmacokinetics of tetra(m-hydroxyphenyl)chlorin in human plasma and individualized light dosimetry in photodynamic therapy*. Photochem. Photobiol. **67**, 596–602 (1998).

[153]. S. Sasnouski, D. Kachatkou, V. Zorin, F. Guillemin and L. Bezdetnaya. *Redistribution of Foscan® from plasma proteins to model membranes*. Photochem. Photobiol. Sci. **5**, 770–777 (2006).

[154]. H.J. Jones, D.I. Vernon and S.B. Brown. *Photodynamic therapy effect of m-THPC (Foscan®) in vivo: Correlation with pharmacokinetics*. Br. J. Cancer **89**, 398–404 (2003).

[155]. H.J. Hopkinson, D.I. Vernon and S.B. Brown. *Identification and partial characterization of an unusual distribution of the photosensitizer meta-tetrahydroxyphenyl chlorin (temoporfin) in human plasma*. Photochem. Photobiol. **69**, 482–488 (1999).

[156]. L.W. Ma, J. Moan and K. Berg. *Evaluation of a new photosensitizer, meso-tetra-hydroxyphenyl-chlorin, for use in photodynamic therapy - A comparison of its photobiological properties with those of two other photosensitizers*. Int. J. Cancer **57**, 883–888 (1994).

[157]. I. Belitchenko, V. Melnikova, L. Bezdetnaya, H. Rezzoug, J.L. Merlin, A. Potapenko and F. Guillemin. *Characterization of photodegradation of meta-tetra(hydroxyphenyl)chlorin (mTHPC) in solution: Biological*

consequences in human tumor cells. Photochem. Photobiol. **67**, 584–590 (1998).

[158]. L. Rodriguez, A. Batlle, G. Di Venosa, S. Battah, P. Dobbin, A.J. MacRobert and A. Casas. *Mechanisms of 5-aminolevulic acid ester uptake in mammalian cells.* Br. J. Pharmacol. **147**, 825–833 (2006).

[159]. M. Soto Thompson. *Photodynamic therapy utilizing intestitial light delivery combined with spectroscopic methods.* Lund Reports on Atomic Physics LRAP-331 (LTH, Lund 2004). PhD thesis (2004).

[160]. M.M.H. El-Sharabasy, A.M. El-Waseef, M.M. Hafez and S.A. Salim. *Porphyrin metabolism in some malignant diseases.* Br. J. Cancer **65**, 409–412 (1992).

[161]. R. van Hillegersberg, J.W.O. van den Berg, W.J. Kort, O.T. Terpstra and J.H.P. Wilson. *Selective accumulation of endogenously produced porphyrins in a liver metastasis model in rats.* Gastroenterology **103**, 647–651 (1992).

[162]. M. Kondo, N. Hirota, T. Takaoka and M. Kajiwara. *Heme-biosynthetic enzyme activities and porphyrin accumulation in normal liver and hepatoma cell lines of rat.* Cell Biol. Toxicol. **9**, 95–105 (1993).

[163]. L. Leibovici, N. Schoenfeld, H.A. Yehoshua, R. Mamet, E. Rakowski, A. Shindel and A. Atsmon. *Activity of porphobilinogen deaminase in peripheral blood mononuclear cells of patients with metastatic cancer.* Cancer **62**, 2297–2300 (1988).

[164]. Q. Peng, J.F. Evensen, C. Rimington and J. Moan. *A comparison of different photosensitizing dyes with respect to uptake C3H-tumors and tissues of mice.* Cancer Lett. **36**, 1–10 (1987).

[165]. C. af Klinteberg, A.M.K. Enejder, I. Wang, S. Andersson-Engels, S. Svanberg and K. Svanberg. *Kinetic fluorescence studies of 5-aminolaevulinic acid-induced protoporphyrin IX accumulation in basal cell carcinomas.* J. Photochem. Photobiol. B: Biol. **49**, 120–128 (1999).

[166]. J. Moan, L.W. Ma, A. Juzeniene, V. Iani, P. Juzenas, F. Apricena and Q. Peng. *Pharmacology of protoporphyrin IX in nude mice after application of ALA and ALA esters.* Int. J. Cancer **103**, 132–135 (2003).

[167]. J. Regula, A.J. MacRobert, A. Gorchein, G.A. Buonaccorsi, S.M. Thorpe, G.M. Spencer, A.R. Hatfield and S.G. Bown. *Photosensitisation and photodynamic therapy of oesophageal, duodenal and colorectal tumours using 5 aminolaevulinic acid induced protoporphyrin IX - A pilot study.* Gut **36**, 67–75 (1995).

[168]. H. Heyerdahl, I. Wang, D.L. Liu, R. Berg, S. Andersson-Engels, Q. Peng, J. Moan, S. Svanberg and K. Svanberg. *Pharmacokinetic studies on 5-aminolevulinic acid-induced protoporphyrin IX accumulation in tumours and normal tissues.* Cancer Lett. **112**, 225–231 (1997).

[169]. S.C. Chang, G. Buonaccorsi, A.J. MacRobert and S.G. Bown. *5-aminolevulinic acid (ALA)-induced protoporphyrin IX fluorescence and photodynamic effects in the rat bladder: An in vivo study comparing oral and intravesical ALA administration.* Lasers Surg. Med. **20**, 254–264 (1997).

[170]. P. Hinnen, F.W.M. de Rooij, M.L.F. van Velthuysen, A. Edixhoven, R. van Hillegersberg, H.W. Tilanus, J.H.P. Wilson and P.D. Siersema. *Biochemical basis of 5-aminolaevulinic acid-induced protoporphyrin IX accumulation: A study in patients with (pre)malignant lesions of the oesophagus.* Br. J. Cancer **78**, 679–682 (1998).

[171]. N. Lange, P. Jichlinski, M. Zellweger, M. Forrer, A. Marti, L. Guillou, P. Kucera, G. Wagnières and H. van den Bergh. *Photodetection of early human bladder cancer based on the fluorescence of 5-aminolaevulinic acid hexylester-induced protoporphyrin IX: A pilot study.* Br. J. Cancer

80, 185–193 (1999).

[172]. C. af Klinteberg, M. Andreasson, O. Sandström, S. Andersson-Engels and S. Svanberg. *Compact medical fluorosensor for minimally invasive tissue characterisation.* Rev. Sci. Instrum. **76**, 034303 (2005).

[173]. A. Lavi, H. Weitman, R.T. Holmes, K.M. Smith and B. Ehrenberg. *The depth of porphyrin in a membrane and the membrane's physical properties affect the photosensitizing efficiency.* Biophys. J. **82**, 2101–2110 (2002).

[174]. S. Ahmadi, P.A. McCarron, R.F. Donnelly, A.D. Woolfson and K. Mckenna. *Evaluation of the penetration of 5-aminolevulinic acid through basal cell carcinoma: A pilot study.* Exp. Dermatol. **13**, 445–451 (2004).

[175]. P. Uehlinger, M. Zellweger, G. Wagnières, L. Juillerat-Jeanneret, H. van den Bergh and N. Lange. *5-Aminolevulinic acid and its derivatives: Physical chemical properties and protoporphyrin IX formation in cultured cells.* J. Photochem. Photobiol. B: Biol. **54**, 72–80 (2000).

[176]. J. Kloek and G.M.J. Beijersbergen van Henegouwen. *Prodrugs of 5-aminolevulinic acid for photodynamic therapy.* Photochem. Photobiol. **64**, 994–1000 (1996).

[177]. J.-M. Gaullier, K. Berg, Q. Peng, H. Anholt, P.K. Selbo, L.W. Ma and J. Moan. *Use of 5-aminolevulinic acid esters to improve photodynamic therapy on cells in culture.* Cancer Res. **57**, 1481–1486 (1997).

[178]. J. Kloek, W. Akkermans and G.M.J. Beijersbergen van Henegouwen. *Derivatives of 5-aminolevulinic acid for photodynamic therapy: Enzymatic conversion into protoporphyrin.* Photochem. Photobiol. **67**, 150–154 (1998).

[179]. C.E. Bigelow, S. Mitra, R. Knuechel and T.H. Foster. *ALA- and ALA-hexylester-induced protoporphyrin IX fluorescence and distribution in multicell tumour spheroids.* Br. J. Cancer **85**, 727–734 (2001).

[180]. J.T.H.M. van den Akker, V. Iani, W.M. Star, H.J.C.M. Sterenborg and J. Moan. *Topical application of 5-aminolevulinic acid hexyl ester and 5-aminolevulinic acid to normal nude mouse skin: Differences in protoporphyrin IX fluorescence kinetics and the role of the stratum corneum.* Photochem. Photobiol. **72**, 681–689 (2000).

[181]. A. Juzeniene, P. Juzenas, V. Iani and J. Moan. *Topical application of 5-aminolevulinic acid and its methylester, hexylester and octylester derivatives: Considerations for dosimetry in mouse skin model.* Photochem. Photobiol. **76**, 329–334 (2002).

[182]. Q. Peng, J. Moan, T. Warloe, V. Iani, H.B. Steen, A Bjorseth and J.M. Nesland. *Build-up of esterified aminolevulinic-acid-derivative-induced porphyrin fluorescence in normal mouse skin.* J. Photochem. Photobiol. B: Biol. **34**, 95–96 (1996).

[183]. J. Moan, L.W. Ma and V. Iani. *On the pharmacokinetics of topically applied 5-aminolevulinic acid and two of its esters.* Int. J. Cancer **92**, 139–143 (2001).

[184]. J.T.H.M. van den Akker, J.A. Holroyd, D.I. Vernon, H.J.C.M. Sterenborg and S.B. Brown. *Comparative in vitro percutaneous penetration of 5-aminolevulinic acid and two of its esters through excised hairless mouse skin.* Lasers Surg. Med. **33**, 173–181 (2003).

[185]. A. Casas, H. Fukuda, G. Di Venosa and A.M.D. Batlle. *The influence of the vehicle on the synthesis of porphyrins after topical application of 5-aminolaevulinic acid. Implications in cutaneous photodynamic sensitization.* Br. J. Dermatol. **143**, 564–572 (2000).

[186]. M.B. Pierre, A.C. Tedesco, J.M. Marchetti and M.V. Bentley. *Stratum corneum lipids liposomes for the topical delivery of 5-aminolevulinic*

acid in photodynamic therapy of skin cancer: Preparation and in vitro permeation study. BMC Dermatol. **1**, 5 (2001).

[187]. G. Gupta, C.A. Morton, C. Whitehurst, J.V. Moore and R.M. Mackie. *Photodynamic therapy with meso-tetra(hydroxyphenyl) chlorin in the topical treatment of Bowen's disease and basal cell carcinoma.* Br. J. Dermatol. **141**, 385–386 (1999).

[188]. Q. Peng, A.M. Soler, T. Warloe, J.M. Nesland and K.E. Giercksky. *Selective distribution of porphyrins in skin thick basal cell carcinoma after topical application of methyl 5-aminolevulinate.* J. Photochem. Photobiol. B: Biol. **62**, 140–145 (2001).

[189]. R.S. Bradley and M.S. Thorniley. *A review of attenuation correction techniques for tissue fluorescence.* J. R. Soc. Interface **3**, 1–13 (2006).

[190]. B.W. Pogue and G. Burke. *Fiber-optic bundle design for quantitative fluorescence measurements.* Appl. Opt. **37**, 7429–7436 (1998).

[191]. H. Stepp, T. Beck, W. Beyer, C. Pfaller, R. Sroka and R. Baumgartner. *Measurement of fluorophore concentration in scattering media by a single optical fiber.* Proc. SPIE vol. 6139 (2006).

[192]. S. Andersson-Engels, J. Johansson, U. Stenram, K. Svanberg and S. Svanberg. *Malignant tumor and atherosclerotic plaque diagnosis using laser-induced fluorescence.* IEEE J. Quant. Electron. **26**, 2207–2217 (1990).

[193]. H.J.C.M. Sterenborg, A.E. Saarnak, R. Frank and M. Motamedi. *Evaluation of spectral correction techniques for fluorescence measurements on pigmented lesions in vivo.* J. Photochem. Photobiol. B: Biol. **35**, 159–165 (1996).

[194]. J. Wu, M.S. Feld and R.P. Rava. *Analytical model for extracting intrinsic fluorescence in turbid media.* Appl. Opt. **32**, 3585–3595 (1993).

[195]. M.G. Müller, I. Georgakoudi, Q. Zhang, J. Wu and M.S. Feld. *Intrinsic fluorescence spectroscopy in turbid media: Disentangling effects of scattering and absorption.* Appl. Opt. **40**, 4633–4646 (2001).

[196]. E.L. Hull and T.H. Foster. *Steady-state reflectance spectroscopy in the P-3 approximation.* JOSA A **18**, 584–599 (2001).

[197]. J.C. Finlay and T.H. Foster. *Recovery of hemoglobin oxygen saturation and intrinsic fluorescence with a forward-adjoint model.* Appl. Opt. **44**, 1917–1933 (2005).

[198]. U. Gustafsson, E. McLaughlin, E. Jacobson, J. Håkansson, P. Troy, M.J. DeWeert, S. Pålsson, M. Soto Thompson, S. Svanberg, A. Vaitkuviene, K. Svanberg, R.M. Levenson, G.H. Bearman and A. Mahadevan-Jensen. *Fluorescence and reflectance monitoring of human cervical tissue in vivo - A case study.* pp 100–110. Proc. SPIE vol. 4959 (2003).

[199]. C. af Klinteberg, A.M.K. Nilsson, I. Wang, S. Andersson-Engels, S. Svanberg and K. Svanberg. *Laser-induced fluorescence diagnostics of basal cell carcinomas of the skin following topical ALA application.* Biomed. Opt. Newsletter **5**, 1–6 (1996).

[200]. C. Fritsch and T. Ruzicka. *Fluorescence diagnosis and photodynamic therapy in dermatology from experimental state to clinic standard methods.* J. Environ. Pathol. Toxicol. Oncol. **25**, 425–439 (2006).

[201]. P. Hillemanns, H. Weingandt, R. Baumgartner, J. Diebold, W. Xiang and H. Stepp. *Photodetection of cervical intraepithelial neoplasia using 5-aminolevulinic acid-induced porphyrin fluorescence.* Cancer **88**, 2275–2282 (2000).

[202]. D. Zaak, A. Karl, R. Knuchel, H. Stepp, A. Hartmann, O. Reich, A. Bachmann, M. Siebels, G. Popken and C. Stief. *Diagnosis of urothelial carcinoma of the bladder using fluorescence endoscopy.* BJU Int. **96**, 217–222 (2005).

[203]. R. Richards-Kortum and E. Sevick-Muraca. *Quantitative optical spectroscopy for tissue diagnosis.* Ann. Rev. Phys. Chem. **47**, 555–606 (1996).

[204]. N. Ramanujam and R.A. Meyers. *Fluorescence spectroscopy in vivo.* In *Encyclopedia of analytical chemistry* pp 20–56. John Wiley & Sons Ltd Chichester (2000).

[205]. R. Drezek, R. Richards-Kortum, M.A. Brewer, M.S. Feld, C. Pitris, A. Ferenczy, M.L. Faupel and M. Follen. *Optical imaging of the cervix.* Cancer (Suppl.) **98**, 2015–2027 (2003).

[206]. S. Andersson-Engels, J. Johansson, K. Svanberg and S. Svanberg. *Fluorescence imaging and point measurements of tissue: Applications to the demarcation of malignant tumors and atherosclerotic lesions from normal tissue.* Photochem. Photobiol. **53**, 807–814 (1991).

[207]. S. Andersson-Engels, K. Svanberg and S. Svanberg. *Fluorescence imaging in medical diagnostics.* In *Biomedical Optics,* J. Fujimoto (Ed.) (2007, to appear).

[208]. S. Andersson-Engels, G. Canti, R. Cubeddu, C. Eker, C. af Klinteberg, A. Pifferi, K. Svanberg, S. Svanberg, P. Taroni, G. Valentini and I. Wang. *Preliminary evaluation of two fluorescence imaging methods for detection of basal cell carcinomas of the skin.* Lasers Surg. Med. **26**, 76–82 (2000).

[209]. G.A. Wagnières, W.M. Star and B.C. Wilson. *In vivo fluorescence spectroscopy and imaging for oncological applications.* Photochem. Photobiol. **68**, 603–632 (1998).

[210]. M. Kress, T. Meier, R. Steiner, F. Dolp, R. Erdmann, U. Ortmann and A. Rück. *Time-resolved microspectrofluorometry and fluorescence lifetime imaging of photosensitizers using picosecond pulsed diode lasers in laser scanning microscopes.* J. Biomed. Opt. **8**, 26–32 (2003).

[211]. A. Colasanti, A. Kisslinger, G. Fabbrocini, R. Liuzzi, M. Quarto, P. Riccio, G. Roberti and F. Villani. *MS-2 fibrosarcoma characterization by laser induced autofluorescence.* Lasers Surg. Med. **26**, 441–448 (2000).

[212]. W.H. Press, S.A. Teukolsky, W.T. Vetterling and B.P. Flannery. *Numerical recipes in C: The art of scientific computing.* Cambridge University Press New York (1992).

[213]. W.J. Cottrell, A.R. Oseroff and T.H. Foster. *Portable instrument that integrates irradiation with fluorescence and reflectance spectroscopies during clinical photodynamic therapy of cutaneous disease.* Rev. Sci. Instrum. **77**, 064302 (2006).

[214]. R. Bonnett and G. Martinez. *Photobleaching of sensitisers used in photodynamic therapy.* Tetrahedron **57**, 9513–9547 (2001).

[215]. B.C. Wilson, M.S. Patterson and L. Lilge. *Implicit and explicit dosimetry in photodynamic therapy: A new paradigm.* Lasers Med. Sci. **12**, 182–199 (1997).

[216]. J.C. Finlay, D.L. Conover, E.L. Hull and T.H. Foster. *Porphyrin bleaching and PDT-induced spectral changes are irradiance dependent in ALA-senstitized normal rat skin in vivo.* Photochem. Photobiol. **73**, 54–63 (2001).

[217]. D.J. Robinson, H.S. de Bruijn, N. van der Veen, M.R. Stringer, S.B. Brown and W.M. Star. *Protoporphyrin IX fluorescence photobleaching during ALA-mediated photodynamic therapy of UVB-induced tumors in hairless mouse skin.* Photochem. Photobiol. **69**, 61–70 (1999).

[218]. I.A. Boere, D.J. Robinson, H.S. de Bruijn, J. van den Boogert, H.W. Tilanus, H.J.C.M. Sterenborg and R.W.F. de Bruin. *Monitoring in situ dosimetry and protoporphyrin IX fluorescence photobleaching in the normal rat esophagus during 5-aminolevulinic acid photodynamic*

therapy. Photochem. Photobiol. **78**, 271–2 (2003).

[219]. J.S. Dysart, M.S. Patterson, T.J. Farrell and G. Singh. *Relationship between mTHPC fluorescence photobleaching and cell viability during in vitro photodynamic treatment of DP16 cells.* Photochem. Photobiol. **75**, 289–295 (2002).

[220]. D. Balsara. *Fast and accurate discrete ordinates methods for multidimensional radiative transfer. I. Basic methods.* J. Quantitative Spectroscopy & Radiative Transfer **69**, 671–707 (2001).

[221]. P. Kubelka and F. Munk. *Ein Beitrag zur Optik der Farbanstriche.* Z. Tech. Phys. **12**, 593–601 (1931).

[222]. S.A. Prahl, A.J. Welch and M.J.C. van Gemert. *The adding-doubling method.* In *Optical-thermal response of laser-irradiated tissue* pp 101–129. Plenum Press New York (1995).

[223]. J. Mobley and T. Vo-Dinh. *Optical properties of tissue.* In *Biomedical Photonics Handbook* pp 2(1)–2(74). CRC Press Boca Raton, USA (2005).

[224]. W.M. Star, A.J. Welch and M.J.C. van Gemert. *Diffusion theory of light transport.* In *Optical-thermal response of laser-irradiated tissue* pp 131–206. Plenum Press New York, USA (1995).

[225]. T. Durduran, A.G. Yodh, B. Chance and D.A. Boas. *Does the photon-diffusion coefficient depend on absorption?* JOSA A **14**, 3358–3365 (1997).

[226]. S.R. Arridge. *Optical tomography in medical imaging.* Inverse Probl. **15**, R41–R93 (1999).

[227]. R. Aronson and N Corngold. *Photon diffusion coefficient in an absorbing medium.* JOSA A **16**, 1066–1071 (1999).

[228]. J. Ripoll, D. Yessayan, G. Zacharakis and V. Ntziachristos. *Experimental determination of photon propagation in highly absorbing and scattering media.* JOSA A **22**, 546–551 (2005).

[229]. A.H. Hielscher, R.E. Alcouffe and R.L. Barbour. *Comparison of finite-difference transport and diffusion calculations for photon migration in homogeneous and heterogeneous tissues.* Phys. Med. Biol. **43**, 1285–1302 (1998).

[230]. D. Contini, F. Martelli and G. Zaccanti. *Photon migration through a turbid slab described by a model based on diffusion approximation. 1. Theory.* Appl. Opt. **36**, 4587–4599 (1997).

[231]. A. Kienle and T. Glanzmann. *In vivo determination of the optical properties of muscle with time-resolved reflectance using a layered model.* Phys. Med. Biol. **44**, 2689–2702 (1999).

[232]. F. Martelli, A. Sassaroli, Y. Yamada and G. Zaccanti. *Analytical approximate solutions of the time-domain diffusion equation in layered slabs.* JOSA A **19**, 71–80 (2002).

[233]. D.A. Boas, M.A. O'Leary, B. Chance and A.G. Yodh. *Scattering of diffuse photon density waves by spherical inhomogeneities within turbid media: Analytic solution and applications.* Proc. Natl. Acad. Sci. U.S.A. **91**, 4887–4891 (1994).

[234]. A. Kienle. *Light diffusion through a turbid parallelepiped.* JOSA A **22**, 1883–1888 (2005).

[235]. S.R. Arridge, M. Schweiger, M. Hiraoka and D.T. Delpy. *A finite element approach for modeling photon transport in tissue.* Med. Phys. **20**, 299–309 (1993).

[236]. N.S. Ottosen and H. Petersson. *Introduction to the Finite Element Method.* vol. 1. Prentice Hall International New York (1992).

[237]. H. Dehghani, B.W. Pogue, S.D. Jiang, B. Brooksby and K.D. Paulsen.

Three-dimensional optical tomography: Resolution in small-object imaging. Appl. Opt. **42**, 3117–3128 (2003).

[238]. S. Srinivasan, B.W. Pogue, S.D. Jiang, H. Dehghani and K.D. Paulsen. *Spectrally constrained chromophore and scattering near-infrared tomography provides quantitative and robust reconstruction.* Appl. Opt. **44**, 1858–1869 (2005).

[239]. A. Ishimaru. *Wave propagation and scattering in random media.* Academic Press New York, USA (1978).

[240]. M.S. Patterson, B. Chance and B.C. Wilson. *Time resolved reflectance and transmittance for the non-invasive measurement of tissue optical properties.* Appl. Opt. **28**, 2331–2336 (1989).

[241]. S.J. Madsen, B.C. Wilson, M.S. Patterson, Y.D. Park, S.L. Jacques and Y. Hefetz. *Experimental tests of a simple diffusion model for the estimation of scattering and absorption coefficients of turbid media from time-resolved diffuse reflectance measure.* Appl. Opt. **31**, 3509–3517 (1992).

[242]. M. Keijzer, W.M. Star and P.R.M. Storchi. *Optical diffusion in layered media.* Appl. Opt. **27**, 1820–1824 (1988).

[243]. R.C. Haskell, L.O. Svaasand, T.-T. Tsay, T.-C. Feng, M.S. McAdams and B.J. Tromberg. *Boundary conditions for the diffusion equation in radiative transfer.* JOSA A **11**, 2727–2741 (1994).

[244]. T.J. Farrell, M.S. Patterson and B. Wilson. *A diffusion theory model of spatially resolved, steady-state diffuse reflectance for noninvasive determination of tissue optical properties in vivo.* Med. Phys. **19**, 879–888 (1992).

[245]. R.A.J. Groenhuis, H.A. Ferwerda and J.J. ten Bosch. *Scattering and absorption of turbid materials determined from reflection measurements. 1: Theory.* Appl. Opt. **22**, 2456–2462 (1983).

[246]. M.S. Patterson, S.J. Madsen, J.D. Moulton and B.C. Wilson. *Diffusion equation representation of photon migration in tissue.* IEEE MTT-S Int. **2**, 905–908 (1991).

[247]. A. Sassaroli and S. Fantini. *Comment on the modified Beer-Lambert law for scattering media.* Phys. Med. Biol. **49**, N255–N257 (2004).

[248]. S.J. Matcher and C.E. Cooper. *Absolute quantification of deoxyhaemoglobin concentration in tissue near infrared spectroscopy.* Phys. Med. Biol. **39**, 1295–1312 (1994).

[249]. S.A. Prahl, M. Keijzer, S.L. Jacques and A.J. Welch. *A Monte Carlo Model of light propagation in tissue.* pp 102–111. Proc. SPIE vol. IS 5 (1989).

[250]. L. Wang, S.L. Jacques and L. Zheng. *MCML - Monte Carlo modeling of light transport in multi-layered tissues.* Comput. Methods Programs Biomed. **47**, 131–146 (1995).

[251]. J. Heiskala, I. Nissila, T. Neuvonen, S. Jarvenpaa and E. Somersalo. *Modeling anisotropic light propagation in a realistic model of the human head.* Appl. Opt. **44**, 2049–2057 (2005).

[252]. J. Swartling, A. Pifferi, A.M.K. Enejder and S. Andersson-Engels. *Accelerated Monte Carlo model to simulate fluorescence spectra from layered tissues.* JOSA A **20**, 714–727 (2003).

[253]. K Vishwanath, B.W. Pogue and M.A. Mycek. *Quantitative fluorescence lifetime spectroscopy in turbid media: Comparison of theoretical, experimental and computational methods.* Phys. Med. Biol. **74**, 3387–3405 (2002).

[254]. B.C. Wilson, A.J. Welch and M.J.C. van Gemert. *Measurements of tissue optical properties: Methods and theories.* In *Optical-thermal response of laser-irradiated tissue* pp 233–274. Plenum Press New York

(1995).

[255]. W.-F. Cheong, S.A. Prahl and A.J. Welch. *A review of the optical properties of biological tissues.* IEEE J. Quant. Electron. **26**, 2166–2185 (1990).

[256]. S.A. Prahl. Optical Absorption of Hemoglobin (2004). URL http://omlc.ogi.edu/spectra/hemoglobin/index.html.

[257]. R.C. Smith and K.S. Baker. *Optical properties of the clearest natural waters (200-800 nm).* Appl. Opt. **20**, 177–184 (1981).

[258]. R.L.P. van Veen, H.J.C.M. Sterenborg, A. Pifferi, A. Torricelli, E. Chikoidze and R. Cubeddu. *Determination of visible near-IR absorption coefficients of mammalian fat using time- and spatially resolved diffuse reflectance and transmission spectroscopy.* J. Biomed. Opt. **10** (2005).

[259]. S.A. Prahl, R.L.P. van Veen, H.J.C.M. Sterenborg, A. Pifferi and R. Cubeddu. Determination of VIS- NIR absorption coefficients of mammalian fat, with time- and spatially resolved diffuse reflectance and transmission spectroscopy (2007). URL http://omlc.ogi.edu/spectra/fat/fat.txt.

[260]. S.L. Jacques. Optical absorption of melanin (1998). URL http://omlc.ogi.edu/spectra/melanin/index.html.

[261]. E. Antonini and M. Brunori. *Hemoglobin and myoglobin in their reactions with ligands.* In *Frontiers of biology.* North-Holland Publishing Company Amsterdam (1971).

[262]. R. Wariar, J.N. Gaffke, R.G. Haller and L.A. Bertocci. *A modular NIRS system for clinical measurement of impaired skeletal muscle oxygenation.* J. Appl. Phys. **88**, 315–325 (2000).

[263]. M. Cope. *The application of near infrared spectroscopy to non invasive monitoring of cerebral oxygenation in the newborn infant.* PhD thesis London, UK (1991).

[264]. E.L. Hull, M.G. Nichols and T.H. Foster. *Quantitative broadband near-infrared spectroscopy of tissue-simulating phantoms containing erythrocytes.* Phys. Med. Biol. **43**, 3381–3404 (1998).

[265]. F.P. Bolin, L.E. Preuss, R.C. Taylor and R.J. Ference. *Refractive index of some mammalian tissue using a fiber optic cladding method.* Appl. Opt. **28**, 2297–2303 (1989).

[266]. R.M.P. Doornbos, R. Lang, M.C. Aalders, F.W. Cross and H.J.C.M. Sterenborg. *The determination of in vivo human tissue optical properties and absolute chromophore concentrations using spatially resolved steady-state diffuse reflectance spectroscopy.* Phys. Med. Biol. **44**, 967–981 (1999).

[267]. J.R. Mourant, T. Fuselier, J. Boyer, T.M. Johnson and I.J. Bigio. *Predictions and measurements of scattering and absorption over broad wavelength ranges in tissue phantoms.* Appl. Opt. **36**, 949–957 (1997).

[268]. R. Graaff, J.G. Aarnoudse, J.R. Zijp, P.M.A. Sloot, F.F.M. de Mul, J. Greve and M.H. Koelink. *Reduced light-scattering properties for mixtures of spherical particles: A simple approximation derived from Mie calculations.* Appl. Opt. **31**, 1370–1376 (1992).

[269]. A.M.K. Nilsson, C. Sturesson, D.L. Liu and S. Andersson-Engels. *Changes in spectral shape of tissue optical properties in conjunction with laser-induced thermotherapy.* Appl. Opt. **37**, 1256–1267 (1998).

[270]. H.J. van Staveren, C.J.M. Moes, J. van Marle, S.A. Prahl and M.J.C. van Gemert. *Light scattering in Intralipid-10 % in the wavelength range of 400-1100 nm.* Appl. Opt. **30**, 4507–4514 (1991).

[271]. S.A. Prahl, I.A. Vitkin, U. Bruggemann, B.C. Wilson and R.R. Anderson. *Determination of optical properties of turbid media using pulsed*

photothermal radiometry. Phys. Med. Biol. **37**, 1203–1217 (1992).

[272]. I.J. Bigio and J.R. Mourant. *Ultraviolet and visible spectroscopies for tissue diagnostics: Fluorescence spectroscopy and elastic-scattering spectroscopy.* Phys. Med. Biol. **42**, 803–814 (1997).

[273]. D. Levitz, L. Thrane, M.H. Frosz, P.E. Andersen, C.B. Andersen, P.R. Hansen, J. Valanciunaite, J. Swartling and S. Andersson-Engels. *Determination of optical scattering properties of highly-scattering media in optical coherence tomography images.* Opt. Exp. **12**, 249–259 (2004).

[274]. A.P. Gibson, J.C. Hebden and S.R. Arridge. *Recent advances in diffuse optical imaging.* Phys. Med. Biol. **50**, R1–43 (2005).

[275]. J.S. Dam, T. Dalgaard, P.E. Fabricius and S. Andersson-Engels. *Multiple polynomial regression method for determination of biomedical optical properties from integrating sphere measurements.* Appl. Opt. **39**, 1202–1209 (2000).

[276]. J. Swartling, A. Pifferi, E. Giambattistelli, E. Chikoidze, A. Torricelli, P. Taroni, M. Andersson, A. Nilsson and S. Andersson-Engels. *Rigorous characterization of time-resolved diffuse spectroscopy systems for measurements of absorption and scattering properties using solid phantoms.* Proc. SPIE vol. 5138 (2003).

[277]. S.L. Jacques, L. Wang, A.H. Hielscher, A.J. Welch and M.J.C. van Gemert. *Time-resolved photon propagation in tissues.* In *Optical-thermal response of laser-irradiated tissue* pp 305–332. Plenum Press New York (1995).

[278]. B. Chance, M. Cope, E. Gratton, N. Ramanujam and B. Tromberg. *Phase measurements of light absorption and scatter in human tissue.* Rev. Sci. Instrum. **69**, 3457–3481 (1998).

[279]. B.J. Tromberg, O. Coquoz, J.B. Fishkin, T. Pham, E.R. Anderson, J. Butler, M. Cahn, J.D. Gross, V. Venugopalan and D. Pham. *Non-invasive measurements of breast tissue optical properties using frequency-domain photon migration.* Philos. Trans. R. Soc. Lond., B, Biol. Sci. **352**, 661–668 (1997).

[280]. M.S. Patterson, A.J. Welch and M.J.C. van Gemert. *Principles and applications of frequency-domain measurements of light propagation.* In *Optical-thermal response of laser-irradiated tissue* pp 333–364. Plenum Press New York (1995).

[281]. A.H. Hielscher, S.L. Jacques, L.H. Wang and F.K. Tittel. *The influence of boundary-conditions on the accuracy of diffusion-theory in time-resolved reflectance spectroscopy of biological tissues.* Phys. Med. Biol. **40**, 1957–1975 (1995).

[282]. A. Kienle and M.S. Patterson. *Improved solutions of the steady-state and the time-resolved diffusion equations for reflectance from a semi-infinite turbid medium.* JOSA A **14**, 246–254 (1997).

[283]. S.L. Jacques, A. Gutsche, J. Schwartz, L. Wang, F. Tittel, G.J. Müller, B. Chance, R.R. Alfano, S.R. Arridge, J. Beuthan, E. Gratton, M. Kaschke, B.R. Masters, S. Svanberg and P. van der Zee. *Video reflectometry to specify optical properties of tissue in vivo.* In *Medical Optical Tomography: Functional Imaging and Monitoring SPIE Institute Series 5* pp 211–226. SPIE Optical Engineering Press Bellingham, Washington, USA (1993).

[284]. M.G. Nichols, E.L. Hull and T.H. Foster. *Design and testing of a white-light, steady-state diffuse reflectance spectrometer for determination of optical properties of highly scattering systems.* Appl. Opt. **36**, 93–104 (1997).

[285]. A. Kienle, L. Lilge, M.S. Patterson, R. Hibst, R. Steiner and B.C. Wilson. *Spatially resolved absolute diffuse reflectance measurements*

for noninvasive determination of the optical scattering and absorption coefficients of biological tissue. Appl. Opt. **35**, 2304–2314 (1996).

[286]. F. Martelli, D. Contini, A. Taddeucci and G. Zaccanti. *Photon migration through a turbid slab described by a model based on diffusion approximation. 2. Comparison with Monte Carlo results.* Appl. Opt. **36**, 4600–4612 (1997).

[287]. Q. Chen, B.C. Wilson, S.D. Shetty, M.S. Patterson, J.C. Cerny and F.W. Hetzel. *Changes in in vivo optical properties and light distributions in normal canine prostate during photodynamic therapy.* Radiat. Res. **147**, 86–91 (1997).

[288]. T.C. Zhu, S.M. Hahn, A.S. Kapatkin, A. Dimofte, C.E. Rodriguez, T.G. Vulcan, E. Glatstein and R.A. Hsi. *In vivo optical properties of normal canine prostate at 732 nm using motexafin lutetium-mediated photodynamic therapy.* Photochem. Photobiol. **77**, 81–88 (2003).

[289]. T.C. Zhu, E. Glatstein, S.M. Hahn, A. Dimofte, J.C. Finlay, D. Stripp, T. Busch, J. Miles, R. Whittington, S.B. Malkowicz and Z. Tochner. *Optical properties of human prostate at 732 nm measured in vivo during motexafin lutetium-mediated photodynamic therapy.* Photochem. Photobiol. (2004).

[290]. A. Dimofte, J.C. Finlay and T.C. Zhu. *A method for determination of the absorption and scattering properties interstitially in turbid media.* Phys. Med. Biol. **50**, 2291–2311 (2005).

[291]. P.R. Bargo, S.A. Prahl and S.L. Jacques. *Collection efficiency of a single optical fiber in turbid media.* Appl. Opt. **42**, 3187–3197 (2003).

[292]. P.R. Bargo, S.A. Prahl and S.L. Jacques. *Optical properties effects upon the collection efficiency of optical fibers in different probe configurations.* IEEE JSTQR **9**, 314–321 (2003).

[293]. A. Kienle, M.S. Patterson, N. Dögnitz, R. Bays, G. Wagnières and H. van den Bergh. *Noninvasive determination of the optical properties of two-layered turbid media.* Appl. Opt. **37**, 779–791 (1998).

[294]. B.W. Pogue and M.S. Patterson. *Frequency-domain optical absorption spectroscopy of finite tissue volumes using diffusion theory.* Phys. Med. Biol. **39**, 1157–1180 (1994).

[295]. T.J. Farrell, M.S. Patterson, M. Essenpreis, M. Hein and D. Bocker. *Influence of tissue inhomogeneities on estimates of tissue optical properties obtained from steady-state reflectometry.* pp 335–342. Proc. SPIE vol. 2979 (1997).

[296]. R.A. Weersink, J.E. Hayward, K.R. Diamond and M.S. Patterson. *Accuracy of noninvasive in vivo measurements of photosensitizer uptake based on a diffusion model of reflectance spectroscopy.* Photochem. Photobiol. **66**, 326–335 (1997).

[297]. D. Stasic, T.J. Farrell and M.S. Patterson. *The use of spatially-resolved fluorescence and reflectance to determine interface depth in layered fluorophore distributions.* Phys. Med. Biol. **48**, 3459–3474 (2003).

[298]. D.E. Hyde, T.J. Farrell, M.S. Patterson and B.C. Wilson. *A diffusion theory model of spatially resolved fluorescence from depth-dependent fluorophore concentrations.* Phys. Med. Biol. **46**, 369–383 (2001).

[299]. J. Swartling, J. Svensson, D. Bengtsson, K. Terike and S. Andersson-Engels. *Fluorescence spectra provide information on the depth of fluorescent lesions in tissue.* Appl. Opt. **44**, 1934–1941 (2005).

[300]. J. Svensson and S. Andersson-Engels. *Modeling of spectral changes for depth localization of fluorescent inclusion.* Opt. Express **13**, 4263–4274 (2005).

[301]. R.A.J. Groenhuis, J.J. ten Bosch and H.A. Ferwerda. *Scattering and absorption of turbid materials determined from reflection measurements.*

2: Measuring method and calibration. Appl. Opt. **22**, 2463–2467 (1983).

[302]. F. Bevilacqua, D. Piguet, P. Marquet, J.D. Gross, B.J. Tromberg and C. Depeursinge. *In vivo local determination of tissue optical properties: Applications to human brain.* Appl. Opt. **38**, 4939–4950 (1999).

[303]. J.S. Dam, C.B. Pedersen, T. Dalgaard, P.E. Fabricius, P. Aruna and S. Andersson-Engels. *Fiber optic probe for non-invasive real-time determination of tissue optical properties at multiple wavelengths.* Appl. Opt. **40**, 1155–1164 (2001).

[304]. A. Amelink and H.J. Sterenborg. *Measurement of the local optical properties of turbid media by differential path-length spectroscopy.* Appl. Opt. **43**, 3048–3054 (2004).

[305]. R.L.P. van Veen, A. Amelink, M. Menke-Pluymers, C. van der Pol and H.J.C.M. Sterenborg. *Optical biopsy of breast tissue using differential path-length spectroscopy.* Phys. Med. Biol. **50**, 2573–2581 (2005).

[306]. A. Amelink, H.J. Sterenborg, M.P. Bard and S.A. Burgers. *In vivo measurement of the local optical properties of tissue by use of differential path-length spectroscopy.* Opt. Lett. **29**, 1087–1089 (2004).

[307]. A. Amelink, A. van den Heuvel van der Ploeg, W.J. de Wolf, D.J. Robinson and H.J.C.M. Sterenborg. *Monitoring PDT by means of superficial reflectance spectroscopy.* J. Photochem. Photobiol. B: Biol. **79**, 243–251 (2005).

[308]. L. Wang and S.L. Jacques. *Use of a laser beam with an oblique angle of incidence to measure the reduced scattering coefficient of a turbid medium.* Appl. Opt. **34**, 2362–2366 (1995).

[309]. T.H. Pham, C. Eker, A. Durkin, B.J. Tromberg and S. Andersson-Engels. *Quantifying the optical properties and chromophore concentrations of turbid media by chemometric analysis of hyperspectral, diffuse reflectance data collected using a Fourier interferrometric imaging system.* Appl. Spectrosc. **55**, 1035–1045 (2001).

[310]. T.H. Pham, F. Bevilacqua, T. Spott, J.S. Dam, B.J. Tromberg and S. Andersson-Engels. *Quantifying the absorption and reduced scattering coefficients of tissue-like turbid media over a broad spectral range using a non-contact Fourier interferometric, hyperspectral imaging system.* Appl. Opt. **39**, 6487–6497 (2000).

[311]. D.J. Cuccia, F. Bevilacqua, A.J. Durkin and B.J. Tromberg. *Modulated imaging: Quantitative analysis and tomography of turbid media in the spatial-frequency domain.* Opt. Lett. **30**, 1354–1356 (2005).

[312]. M. Hiraoka, M. Firbank, M. Essenpreis, M. Cope, S.R. Arridge, P. van der Zee and D.T. Delpy. *A Monte Carlo investigation of optical pathlength in inhomogeneous tissue and its application to near-infrared spectroscopy.* Phys. Med. Biol. **38**, 1859–1876 (1993).

[313]. D.T. Delpy, M. Cope, P. van der Zee, S. Arridge, S. Wray and J. Wyatt. *Estimation of optical pathlength through tissue from direct time of flight measurement.* Phys. Med. Biol. **33**, 1433–1442 (1988).

[314]. S.R. Arridge, M. Cope and D.T. Delpy. *The theoretical basis for the determination of optical pathlengths in tissue: Temporal and frequency analysis.* Phys. Med. Biol. **37**, 1531–1560 (1992).

[315]. M. Cope and D.T. Delpy. *System for long-term measurement of cerebral blood and tissue oxygenation on newborn infants by near infra-red transillumination.* Medical and Biological Engineering and Computing **26**, 289–294 (1988).

[316]. K. Uludag, J. Steinbrink, M. Kohl-Bareis, R. Wenzel, A. Villringer and H. Obrig. *Cytochrome-c-oxidase redox changes during visual stimulation measured by near-infrared spectroscopy cannot be explained by a mere cross talk artefact.* Neuroimage **22**, 109–119 (2004).

[317]. J.R. Mourant, I.J. Bigio, D.A. Jack, T.M. Johnson and H.D. Miller. *Measuring absorption coefficients in small volumes of highly scattering media: Source-detector separations for which path lengths do not depend on scattering properties.* Appl. Opt. **36**, 5655–5661 (1997).

[318]. J.R. Mourant, T.M. Johnson, G. Los and I.J. Bigio. *Non-invasive measurement of chemotherapy drug concentrations in tissue: Preliminary demonstrations of in vivo measurements.* Phys. Med. Biol. **44**, 1397–1417 (1999).

[319]. G. Kumar and J.M. Schmitt. *Optimal probe geometry for near-infrared spectroscopy of biological tissue.* Appl. Opt. **36**, 2286–2293 (1997).

[320]. M.T. Jarvi, M.J. Niedre, M.S. Patterson and B.C. Wilson. *Singlet oxygen luminescence dosimetry (SOLD) for photodynamic therapy: Current status, challenges and future prospects.* Photochem. Photobiol. **82**, 1198–1210 (2006).

[321]. J.G. Parker. *Optical monitoring of singlet oxygen generation during photodynamic treatment of tumors.* IEEE Circuits and Devices Magazine **3**, 10–21 (1987).

[322]. M.S. Patterson, S.J. Madsen and B.C. Wilson. *Experimental tests of the feasibility of singlet oxygen luminescence monitoring in vivo during photodynamic therapy.* J. Photochem. Photobiol. B: Biol. **5**, 69–84 (1990).

[323]. M Niedre, M.S. Patterson and B.C. Wilson. *Direct near-infrared luminiscence detection of singlet oxygen generated by photodynamic therapy in cells in vitro and tissues in vivo.* Photochem. Photobiol. **75**, 382–391 (2002).

[324]. M.J. Niedre, A.J. Secord, M.S. Patterson and B.C. Wilson. *In vitro tests of the validity of singlet oxygen luminescence measurements as a dose metric in photodynamic therapy.* Cancer Res. **63**, 7986–7994 (2003).

[325]. M.J. Niedre, C.S. Yu, M.S. Patterson and B.C. Wilson. *Singlet oxygen luminescence as an in vivo photodynamic therapy dose metric: Validation in normal mouse skin with topical amino-levulinic acid.* Br. J. Cancer **92**, 298–304 (2005).

[326]. M.J. Niedre, M.S. Patterson, A. Giles and B.C. Wilson. *Imaging of photodynamically generated singlet oxygen luminescence in vivo.* Photochem. Photobiol. **81**, 941–943 (2005).

[327]. D.W. Lubbers, C. Ince, J. Kesecioglu, L. Telci and K. Akpir. *Oxygen electrodes and optodes and their application in vivo.* In *Oxygen transport to tissue XVII* pp 13–34. Plenum Press New York (1996).

[328]. B.W. Pogue, J.A. O'Hara, I.A. Goodwin, C.J. Wilmot, G.P. Fournier, A.R. Akay and H. Swartz. *Tumor p_{O2} changes during photodynamic therapy depend upon photosensitizer type and time after injection.* Comp. Biochem. Physiol., Part A Mol. Integr. Physiol. **132**, 177–184 (2002).

[329]. R.B. Moore, J.D. Chapman, J.R. Mercer, R.H. Mannan, L.I. Wiebe, A.J. McEwan and M.S. McPhee. *Measurement of PDP-induced hypoxia in Dunning prostate tumors by Iodine-123-iodoazomycin arabinoside.* J. Nucl. Med. **34**, 405–411 (1993).

[330]. C.J. Tralau, A.J. MacRobert, P.D. Coleridge-Smith, H. Barr and S.G. Bown. *Photodynamic therapy with phthalocyanine sensitisation: Quantitative studies in a transplantable rat fibrosarcoma.* Br. J. Cancer **55**, 389–395 (1987).

[331]. D.R. Braichotte, J.F. Savary, P. Monnier and H.E. van den Bergh. *Optimizing light dosimetry in photodynamic therapy of early stage carcinomas of the esophagus using fluorescence spectroscopy.* Lasers Surg.

Med. **19**, 340–346 (1996).

[332]. T.J. Farrell, B.C. Wilson, M.S. Patterson and M.C. Olivo. *Comparison of the in vivo photodynamic threshold dose of Photofrin, mono- and tetrasulfonated aluminum phthalocyanine using a rat liver model.* Photochem. Photobiol. **68**, 394–399 (1998).

[333]. W.R. Potter, T.S. Mang and T.J. Dougherty. *The theory of photodynamic therapy dosimetry: Consequences of photodestruction of sensitizer.* Photochem. Photobiol. **46**, 97–101 (1987).

[334]. L.I. Grossweiner. *PDT light dosimetry revisited.* J. Photochem. Photobiol. B: Biol. **38**, 258–268 (1997).

[335]. J.P.A. Marijnissen, J.A.C. Versteeg, W.M. Star and W.L.J. van Putten. *Tumor and normal response to interstitial photodynamic therapy of the rat R-1 rhabdomyosarcoma.* Int. J. Radiat. Oncol. Biol. Phys. **22**, 963–972 (1992).

[336]. L. Lilge, K. Molpus, T. Hasan and B.C. Wilson. *Light dosimetry for intraperitoneal photodynamic therapy in a murine xenograft model of human epithelial ovarian carcinoma.* Photochem. Photobiol. **68**, 281–288 (1998).

[337]. W.M. Star. *Light dosimetry in vivo.* Phys. Med. Biol. **42**, 763–787 (1997).

[338]. B.W. McIlroy, A. Curnow, G. Buonaccorsi, M.A. Scott, S.G. Bown and A.J. MacRobert. *Spatial measurement of oxygen levels during photodynamic therapy using time-resolved optical spectroscopy.* J. Photochem. Photobiol. B: Biol. **43**, 47–55 (1998).

[339]. A. Curnow, J.C. Haller and S.G. Bown. *Oxygen monitoring during 5-aminolaevulinic acid induced photodynamic therapy in normal rat colon: Comparison of continuous and fractionated light regimes.* J. Photochem. Photobiol. B: Biol. **58**, 149–155 (2000).

[340]. S. Coutier, L.N. Bezdetnaya, T.H. Foster, R.M. Parache and F. Guillemin. *Effect of irradiation fluence rate on the efficacy of photodynamic therapy and tumor oxygenation in meta-tetra (hydroxyphenyl) chlorin (mTHPC)-sensitized HT29 Xenografts in nude mice.* Radiat. Res. **158**, 339–345 (2002).

[341]. S. Coutier, S. Mitra, L.N. Bezdetnaya, R.M. Parache, I. Georgakoudi, T.H. Foster and F. Guillemin. *Effects of fluence rate on cell survival and photobleaching in meta-tetra-(hydroxyphenyl)chlorin-photosensitized colo 26 multicell tumor spheroids.* Photochem. Photobiol. **73**, 297–303 (2001).

[342]. T.M. Sitnik and B.W. Henderson. *The effect of fluence rate on tumor and normal tissue responses to photodynamic therapy.* Photochem. Photobiol. **67**, 462–466 (1998).

[343]. B.W. Henderson, T.M. Busch and J.W. Snyder. *Fluence rate as a modulator of PDT mechanisms.* Lasers Surg. Med. **38**, 489–493 (2006).

[344]. S. Iinuma, K.T. Schomacker, G. Wagnières, M. Rajadhyaksha, M. Bamberg, T. Momma and T. Hasan. *In vivo fluence rate and fractionation effects on tumor response and photobleaching: Photodynamic therapy with two photosensitizers in an orthotopic rat tumor model.* Cancer Res. **59**, 6164–6170 (1999).

[345]. D.J. Robinson, H.S. de Bruijn, N. van der Veen, M.R. Stringer, S.B. Brown and W.M. Star. *Fluorescence photobleaching of ALA-induced protoporphyrin IX during photodynamic therapy of normal hairless mouse skin: The effect of light dose and irradiance and the resulting biological effect.* Photochem. Photobiol. **67**, 140–149 (1998).

[346]. H. Tsutsui, A.J. MacRobert, A. Curnow, A. Rogowska, G. Buonaccorsi, H. Kato and S.G. Bown. *Optimisation of illumination for photodynamic*

therapy with mTHPC on normal colon and a transplantable tumour in rats. Lasers Med. Sci. **17**, 101–109 (2002).

[347]. S.A. Blant, A. Woodtli, G. Wagnières, C. Fontolliet, H. van den Bergh and P. Monnier. *In vivo fluence rate effect in photodynamic therapy of early cancers with tetra(m-hydroxyphenyl)chlorin.* Photochem. Photobiol. **64**, 963–968 (1996).

[348]. I.P. van Geel, H. Oppelaar, J.P. Marijnissen and F.A. Stewart. *Influence of fractionation and fluence rate in photodynamic therapy with Photofrin or mTHPC.* Radiat. Res. **145**, 602–609 (1996).

[349]. S.K. Bisland, L. Lilge, A. Lin, R. Rusnov and B.C. Wilson. *Metronomic photodynamic therapy as a new paradigm for photodynamic therapy: Rationale and preclinical evaluation of technical feasibility for treating malignant brain tumors.* Photochem. Photobiol. **80**, 22–30 (2004).

[350]. B.W. Pogue and T. Hasan. *A theoretical study of light fractionation and dose-rate effects in photodynamic therapy.* Radiat. Res. **147**, 551–559 (1997).

[351]. T.H. Foster, R.S. Murant, R.G. Bryant, R.S. Knox, S.L. Gibson and R. Hilf. *Oxygen consumption and diffusion effects in photodynamic therapy.* Radiat. Res. **126**, 296–303 (1991).

[352]. H. Messmann, P. Mlkvy, G. Buonaccorsi, C.L. Davies, A. MacRobert and S.G. Bown. *Enhancement of photodynamic therapy with 5-aminolaevulinic acid-induced porphyrin photosensitisation in normal rat colon by threshold and light fractionation studies.* Br. J. Cancer **72**, 589–594 (1995).

[353]. I.A. Boere, D.J. Robinson, H.S. de Bruijn, J. Kluin, H.W. Tilanus, H.J.C.M. Sterenborg and R.W.F. de Bruin. *Protoporphyrin IX fluorescence photobleaching and the response of rat Barrett's esophagus following 5-aminolevulinic acid photodynamic therapy.* Photochem. Photobiol. **82**, 1638–1644 (2006).

[354]. L.E. Rhodes, M.M. Tsoukas, R.R. Anderson and N. Kollias. *Iontophoretic delivery of ALA provides a quantitative model for ALA pharmacokinetics and PpIX phototoxicity in human skin.* J. Invest. Dermatol. **108**, 87–91 (1997).

[355]. L. Kunz and A.J. MacRobert. *Intracellular photobleaching of 5,10,15,20-tetrakis(m-hydroxyphenyl) chlorin (Foscan®) exhibits a complex dependence on oxygen level and fluence rate.* Photochem. Photobiol. **75**, 28–35 (2002).

[356]. J.S. Dysart, G. Singh and M.S. Patterson. *Calculation of singlet oxygen dose from photosensitizer fluorescence and photobleaching during mTHPC photodynamic therapy of MLL cells.* Photochem. Photobiol. **81**, 196–205 (2005).

[357]. T.J. Farrell, R.P. Hawkes, M.S. Patterson and B.C. Wilson. *Modeling of photosensitizer fluorescence emission and photobleaching for photodynamic therapy dosimetry.* Appl. Opt. **37**, 7168–7183 (1998).

[358]. J. Moan, G. Streckyte, S. Bagdonas, O. Bech and K. Berg. *Photobleaching of protoporphyrin IX in cells incubated with 5-aminolevulinic acid.* In. J. Cancer **70**, 90–97 (1997).

[359]. I. Georgakoudi and T.H. Foster. *Singlet oxygen- versus nonsinglet oxygen-mediated mechanisms of sensitizer photobleaching and their effects on photodynamic dosimetry.* Photochem. Photobiol. **67**, 612–625 (1998).

[360]. M. Forrer, T. Glanzmann, D.R. Braichotte, G.A. Wagnières and H.E. van den Bergh. *In vivo measurement of fluorescence bleaching of meso-tetra hydroxyphenyl chlorin (mTHPC) in the esophagus and the oral cavity.* pp 33–39. Proc. SPIE vol. 2627 (1995).

[361]. I. Georgakoudi, M. Nichols and T.H. Foster. *The mechanism of Photofrin photobleaching and its consequences for photodynamic dosimetry.* Photochem. Photobiol. **65**, 135–144 (1997).

[362]. J.C. Finlay, S. Mitra, M.S. Patterson and T.H. Foster. *Photobleaching kinetics of Photofrin in vivo and in multicell tumour spheroids indicate two simultaneous bleaching mechanisms.* Phys. Med. Biol. **49**, 4837–4860 (2004).

[363]. G.Q. Yu, T. Durduran, C. Zhou, H.W. Wang, M.E. Putt, H.M. Saunders, C.M. Sehgal, E. Glatstein, A.G. Yodh and T.M. Busch. *Noninvasive monitoring of murine tumor blood flow during and after photodynamic therapy provides early assessment of therapeutic efficacy.* Clin. Cancer Res. **11**, 3543–3552 (2005).

[364]. B. Chen, B.W. Pogue, I.A. Goodwin, J.A. O'Hara, C.M. Wilmot, J.E. Hutchins, P.J. Hoopes and T. Hasan. *Blood flow dynamics after photodynamic therapy with verteporfin in the RIF-1 tumor.* Radiat. Res. **160**, 452–459 (2003).

[365]. A.M.K. Enejder, C. af Klinteberg, I. Wang, S. Andersson-Engels, N. Bendsoe, S. Svanberg and K. Svanberg. *Blood perfusion studies on basal cell carcinomas in conjunction with photodynamic therapy and cryotherapy employing laser Doppler perfusion imaging.* Acta Derm. Venereol. **80**, 19–23 (2000).

[366]. I. Wang, S. Andersson-Engels, G.E. Nilsson, K. Wårdell and K. Svanberg. *Superficial blood flow following photodynamic therapy of malignant skin tumours measured by laser Doppler perfusion imaging.* Br. J. Dermatol. **136**, 184–189 (1997).

[367]. H. Li, B.A. Standish, A. Mariampillai, N.R. Munce, Y.X. Mao, S. Chiu, N.E. Alarcon, B.C. Wilson, A. Vitkin and V.X.D. Yang. *Feasibility of interstitial Doppler optical coherence tomography for in vivo detection of microvascular changes during photodynamic therapy.* Lasers Surg. Med. **38**, 754–761 (2006).

[368]. B.W. Pogue, R.D. Braun, J.L. Lanzen, C. Erickson and M.W. Dewhirst. *Analysis of the heterogeneity of p_{O2} dynamics during photodynamic therapy with verteporfin.* Photochem. Photobiol. **74**, 700–706 (2001).

[369]. J.H. Woodhams, L. Kunz, S.G. Bown and A.J. MacRobert. *Correlation of real-time haemoglobin oxygen saturation monitoring during photodynamic therapy with microvascular effects and tissue necrosis in normal rat liver.* Br. J. Cancer **91**, 788–794 (2004).

[370]. A. Molckovsky and B.C. Wilson. *Monitoring of cell and tissue responses to photodynamic therapy by electrical impedance spectroscopy.* Phys. Med. Biol. **46**, 983–1002 (2001).

[371]. V. Plaks, N. Koudinova, U. Nevo, J.H. Pinthus, H. Kanety, Z. Eshhar, J. Ramon, A. Scherz, M. Neeman and Y. Salomon. *Photodynamic therapy of established prostatic adenocarcinoma with TOOKAD: A biphasic apparent diffusion coefficient change as potential early MRI response marker.* Neoplasia **6**, 224–233 (2004).

[372]. T.C. Zhu, A. Dimofte, J.C. Finlay, D. Stripp, T. Busch, J. Miles, R. Whittington, S.B. Malkowicz, Z. Tochner, E. Glatstein and S.M. Hahn. *Optical properties of human prostate at 732 nm measured in vivo during motexafin lutetium-mediated photodynamic therapy.* Photochem. Photobiol. **81**, 96–105 (2005).

[373]. J.C. Finlay, T.C. Zhu, A. Dimofte, D. Stripp, S.B. Malkowcz, T.M. Busch and S.M. Hahn. *Interstitial fluorescence spectroscopy in the human prostate during motexafin lutetium-mediated photodynamic therapy.* Photochem. Photobiol. **82**, 1270–1278 (2006).

[374]. J.P.A. Marijnissen, W.M. Star, H.J.A. in't Zandt, M.A. D'Hallewin and L. Baert. *In situ light dosimetry during whole bladder wall photo-*

dynamic therapy: Clinical results and experimental verification. Phys. Med. Biol. **38**, 567–582 (1993).

[375]. R.L.P. van Veen, D.J. Robinson, P.D. Siersema and H.J.C.M. Sterenborg. *The importance of in situ dosimetry during photodynamic therapy of Barrett's esophagus.* Gastrointest. Endosc. **64**, 786–788 (2006).

[376]. X.D. Zhou, B.W. Pogue, B. Chen, E. Demidenko, R. Joshi, J. Hoopes and T. Hasan. *Pretreatment photosensitizer dosimetry reduces variation in tumor response.* Int. J. Radiat. Oncol. Biol. Phys. **64**, 1211–1220 (2006).

[377]. C. Sheng, P.J. Hoopes, T. Hasan and B.W. Pogue. *Photobleaching-based dosimetry predicts deposited dose in ALA-PpIX PDT of rodent esophagus.* Photochem. Photobiol. **83**, 738–748 (2007).

[378]. Y. Censor, M.D. Altschuler and W.D. Powlis. *On the use of Cimmino simultaneous projections method for computing a solution of the inverse problem in radiation-therapy treatment planning.* Inv. Probl. **4**, 607–623 (1988).

[379]. Y. Xiao, J. Galvin, M. Hossain and R. Valicenti. *An optimized forward-planning technique for intensity modulated radiation therapy.* Med. Phys. **27**, 2093–2099 (2000).

[380]. M.D. Altschuler, T.C. Zhu, J. Li and S.M. Hahn. *Optimized interstitial PDT prostate treatment planning with the Cimmino feasibility algorithm.* Med. Phys. **32**, 3524–3536 (2005).

[381]. A. Johansson, J. Axelsson, J. Swartling, T. Johansson, S. Pålsson, J. Stensson, M. Einarsdóttír, K. Svanberg, N. Bendsoe, K.M. Kälkner, S. Nilsson, S. Svanberg and S. Andersson-Engels. *Interstitial photodynamic therapy for primary prostate cancer incorporating realtime treatment dosimetry.* Proc. SPIE vol. 6427 (2007).

Papers

Paper I

Fluorescence and absorption assessment of a lipid mTHPC formulation following topical application in a non-melanotic skin tumor model

A. Johansson, J. Svensson, N. Bendsoe, K. Svanberg,
E. Alexandratou, M. Kyriazi, D. Yova, S. Gräfe, T. Trebst,
S. Andersson-Engels.

Journal of Biomedical Optics **12(3)**, 034026 (2007).

Journal of Biomedical Optics 12(3), 034026 (May/June 2007)

Fluorescence and absorption assessment of a lipid mTHPC formulation following topical application in a non-melanotic skin tumor model

Ann Johansson
Jenny Svensson
Lund University
Department of Physics
P.O. Box 118
SE-221 00 Lund, Sweden

Niels Bendsoe
Lund University Hospital
Department of Dermatology and Venereology
SE-221 85 Lund, Sweden

Katarina Svanberg
Lund University Hospital
Department of Oncology
SE-221 85 Lund, Sweden

Eleni Alexandratou
Maria Kyriazi
Dido Yova
National Technical University of Athens
Department of Electrical Engineering and Computing
Biomedical Optics and Applied Biophysics Laboratory
G-15780 Athens, Greece

Susanna Gräfe
Biolitec AG
Research and Development
D-07745 Jena, Germany

Tilmann Trebst
CeramOptec GmbH
D-53121 Bonn, Germany

Stefan Andersson-Engels
Lund University
Department of Physics
P.O. Box 118
SE-221 00 Lund, Sweden

Abstract. Although the benefits of topical sensitizer administration have been confirmed for photodynamic therapy (PDT), ALA-induced protoporphyrin IX is the only sensitizer clinically used with this administration route. Unfortunately, ALA-PDT results in poor treatment response for thicker lesions. Here, selectivity and depth distribution of the highly potent sensitizer *meso*-tetra(hydroxyphenyl)chlorin (mTHPC), supplied in a novel liposome formulation was investigated following topical administration for 4 and 6 h in a murine skin tumor model. Extraction data indicated an average [± standard deviation (SD)] mTHPC concentration within lesions of 6.0(±3.1) ng/mg tissue with no significant difference ($p<0.05$) between 4- and 6-h application times and undetectable levels of generalized photosensitivity. Absorption spectroscopy and chemical extraction both indicated a significant selectivity between lesion and normal surrounding skin at 4 and 6 h, whereas the more sensitive fluorescence imaging setup revealed significant selectivity only for the 4-h application time. Absorption data showed a significant correlation with extraction, whereas the results from the fluorescence imaging setup did not correlate with the other methods. Our results indicate that this sensitizer formulation and administration path could be interesting for topical mTHPC-PDT, decreasing the effects of extended skin photosensitivity associated with systemic mTHPC administration. [DOI: 10.1117/1.2743080]

Keywords: pharmacokinetics; fluorescence imaging; absorption spectroscopy; photodynamic therapy; mTHPC.

Paper 06158RR received Jun. 12, 2006; revised manuscript received Feb. 19, 2007; accepted for publication Feb. 20, 2007; published online May 22, 2007. This paper is a revision of a paper presented at the SPIE conference on Optical Diagnostics and Sensing VI, Jan. 2006, San Jose, Calif. The paper presented there appears (unrefereed) in SPIE Proceedings Vol. 6094.

1 Introduction

Photodynamic therapy (PDT) as a cancer treatment modality has shown promising results both in terms of efficacy and selectivity.[1] The PDT effect is caused by a combination of treatment induced apoptosis and direct necrosis,[2] vascular damage,[3] and possibly an elicited immune response,[4] where the extent of tissue damage depends on the total light dose, the tissue oxygenation, and the sensitizer concentration.[5] The most common administration route is intravenous injection, leading to an extended photosensitivity following treatment for some sensitizers.[6]

In the case of easily accessible and thin lesions, e.g., superficial skin malignancies, topical sensitizer application is highly desirable from a clinical point of view. ALA-induced protoporphyrin IX is a photosensitizer that has been used with this administration route for the treatment of various skin

Address all correspondence to Ann Johansson, Department of Physics, Lund University, PO Box 118-Lund, 221 00 Sweden; Tel: +46462223120; Fax: +46462224250; E-mail: ann.johansson@fysik.lth.se

1083-3668/2007/12(3)/034026/9/$25.00 © 2007 SPIE

tumors.[7] To overcome the poor skin permeability caused by the hydrophilic character of the ALA molecule, several groups have investigated the selectivity and penetration depths of some of its esters. Utilizing the less hydrophilic methyl esterified ALA-Me, good tumor selectivity has been observed both in animal skin tumor models and in human basal cell carcinomas[8,9] (BCCs). However, the limited light penetration of the activating light,[10] the localization of the protoporphyrin IX molecule within biological tissue,[11] and the relatively low extinction coefficient of this sensitizer[12] are additional factors that might limit the treatment efficacy.[7,13]

In contrast to protoporphyrin IX, *meso*-tetra(hydroxyphenyl)chlorin (mTHPC) has been reported as one of the most efficient sensitizers, as relatively small drug and light doses are required to achieve treatment response.[14] However, the hydrophobic mTHPC molecules form aggregates in aqueous surroundings, leading to limited transportation of the sensitizer within biological media, tumor selectivity, and PDT efficacy.[15–17] Gupta et al.[18] reported on PDT following topical mTHPC administration for treatment of Bowen's disease and BCCs. In this study, the overall pathological tumor clearance was limited to 32% at the 2-month follow-up. The authors suggest the method of topical sensitizer application and mTHPC formulation were the primary limiting factors. In an effort to improve efficiency of topically administered drugs, the use of liposomes as drug delivery vehicles has been reported to increase skin penetration for some active substances.[19] For example, ALA has been encapsulated into liposomes, leading to an improved retention within the epidermis and dermis in an *in vitro* skin model.[20] By incorporating the hydrophobic PDT agent bacteriochlorin into liposomes, an increased oxygen consumption and decreased cell survival during PDT in cell cultures was observed as compared to the raw formulation.[21] Furthermore, the use of liposomes as carrier of benzoporphyrin derivative monoacid ring A resulted in better PDT efficiency in a mouse tumor model.[22] These effects have been explained by monomerization of the sensitizer,[21] a different microlocalization within the cells and an increased association with low density lipoproteins when incorporating the sensitizers into liposomes.[21,22]

In this paper, the sensitizer distribution following topical application of a novel gel formulation containing liposome-encapsulated mTHPC, referred to as mTHPC-gel, is investigated in an animal skin tumor model. The drug-accumulation interval in this study is restricted to 4 and 6 h, as clinically relevant for topically applied PDT photosensitizers.[23] In addition, the application of this new mTHPC formulation for several hours is possible as the compound is supplied in a heat-setting gel. Chemical extraction and noninvasive optical methods are utilized for investigating the selectivity between lesion and normal skin. In addition, the mTHPC concentration within the internal organs is monitored to assess the level of generalized photosensitivity.

A further incentive of the present study is the comparison of fluorescence and absorption spectroscopy to chemical extraction as methods for quantifying sensitizer concentration. The combination of a strongly fluorescing and absorbing PDT agent and superficially located lesions makes fluorescence imaging and absorption spectroscopy attractive tools for noninvasive studies of sensitizer concentration. These methods have the additional advantage that they can provide information in real time. On the other hand, as the fluorescence signal depends on tissue optical properties, it is difficult to utilize the absolute fluorescence level to quantify the sensitizer concentration, especially within heterogeneous media. For the absorption spectroscopy data, the effect of varying tissue absorption can be handled by studying the total absorption imprint of tissue and exogenous chromophore over a sufficiently broad spectral interval.

In this work, imaging of the tissue and sensitizer fluorescence levels is performed utilizing a near-UV light source and detection at a few selected wavelengths. The absorption spectroscopy setup utilizes a fiber optical source-detector pair, where the source-detector separation has been chosen to make the method insensitive to variations in scattering parameters for the range of scattering values typically found in biological tissue.[24] The predicted sensitizer concentration is tested for correlation between the two optical methods and the chemical extraction and we comment on the accuracy of the optical methods for this tumor model and measurement geometry.

2 Materials and Methods

2.1 *mTHPC-gel Preparation*

The compound is comprised of a liposomal formulation of mTHPC in a thermogel matrix (biolitec AG, Jena, Germany) with a sensitizer concentration of 0.5 mg mTHPC/ml gel. The liposome formulation (Foslip) is based on dipalmitoylphosphatidylcholine (DPPC), monosaccharide, water, and polyoxyethylene polyoxypropylene block copolymers and encapsulates the mTHPC (Ref. 25). The mTHPC-gel is liquid at the storage temperature of 4 °C but forms a highly viscous gel when heated by the skin to temperatures above 26 °C. The thermothickening thus aids in increasing the retention time of the applied gel and transfer of the sensitizer into the tissue. No penetration enhancers are added to the mTHPC-gel.

2.2 *Animal Procedures*

Malignant skin tumors were induced in seven male albino hairless mice (SKH-HR1), 8 to 10 weeks old and weighing 30 to 35 g. For skin carcinoma induction, a two-stage model of carcinogenesis was utilized with DMBA [7,12-dimethylbenz(a)anthracene] as initiator and ultraviolet radiation as skin cancer promoter. Details on the procedure for induction of skin carcinogenesis have been published by Kyriazi et al.[26] Tumors first appear as benign papillomas, progressing toward more malignant states, and finally developing into basal (10%) and squamous (80%) cell carcinomas as determined after histopathological examination of representative specimens. In the remaining 10%, no malignant transformation appears. This progress is consistent with previously described studies in hairless mice.[27] Here, tumor diameters ranged between 0.2 and 1 cm, where mice with tumor diameter greater than 1 cm were euthanatized for ethical reasons. The study was carried out according to the guidelines established by the European Parliament and Council Directive 2003/65/EC and the Greek Animal Ethics Committee.

Twenty microliters of mTHPC-gel was applied topically on each of the areas investigated, i.e., tumor, normal skin, and skin in the immediate vicinity of the tumor. The sensitizer concentration was studied at 4 or 6 h after mTHPC-gel administration utilizing noninvasive optical techniques. Three

animals with a total of 10 lesions and another three animals with 5 lesions were investigated at the 4- and 6-h time points, respectively. All tissue regions were carefully cleaned prior to fluorescence and absorption measurements to remove any gel remaining on the skin surface. In addition, the optical measurements were performed on all animals prior to administration of the mTHPC-gel. For all animals, application of the sensitizer and optical measurements were performed under general anesthesia [intraperiteneal (i.p.) injection of 20 μl of γ-hydroxybutiric lactone solution in 0.9% sodium chloride (50:50, v:v)]. Following the optical measurements at 4 or 6 h, animals were killed by cervical dislocation and the tissue regions previously treated with the mTHPC-gel were excised for extraction measurements. In addition, the mTHPC concentration in blood, liver, spleen, muscle, and normal skin where no sensitizer had been applied was also investigated by means of extraction.

In vivo optical measurements were also performed for two lesions in another animal at 1.5, 3, and 5 h after sensitizer application in an attempt to follow the temporal mTHPC concentration profile within a single animal. However, prior to the spectroscopic investigations at 1.5, 3, and 5 h, the tissue regions had to be carefully cleaned to avoid measuring fluorescence from mTHPC within the gel remaining only on top of the skin surface. After the optical measurements at 1.5 and 3 h, another 20 μl of the mTHPC-gel was administered to enable further sensitizer accumulation. This procedure was thus slightly different from that employed for the remaining animals as it resulted in the application of three 20-μl aliquots of the sensitizer gel. After sacrificing the animal at the 5-h drug-light interval, the mTHPC fluorescence and absorption levels were also investigated throughout a vertical cut of the two excised tumors to study the depth distribution.

2.3 *Fluorescence Imaging*

A 405-nm continuous-wave diode laser (Power Technology Inc., Little Rock, Arkansas) emitting 2.1 mW was used to induce fluorescence within a 27-mm-diam area. The tissue autofluorescence at 500 (±10 nm) and mTHPC fluorescence at 654 nm (±20 nm) were filtered out using bandpass filters (Oriel, Stratford, Connecticut) and imaged using a cooled, intensified CCD (iStar, Andor Technology, Belfast, Northern Ireland). Two cut-off filters, GG475 and GG455 (Schott, Mainz, Germany), were used to attenuate the reflected excitation light. All data was compensated for differences in spectral response using a National Institute of Standards and Technology (NIST)-traceable light source.

For each animal, the fluorescence intensities at 654 and 500 nm were averaged within each investigated tissue region. The mTHPC distribution was quantified by a dimensionless contrast function resulting from forming a spectral ratio between the two detection bands:

$$F = \frac{I(654\ \text{nm}) - I_{\text{bkg}}}{I(500\ \text{nm}) - I_{\text{bkg}}}, \tag{1}$$

where $I(654\ \text{nm})$ and $I(500\ \text{nm})$ denote the fluorescence intensity at the two wavelengths, and I_{bkg} is a constant background level originating from the dark current of the detector.

For this setup, the mTHPC detection limit was below 0.005 μM in liquid phantoms containing ink (Pelikan Fount India Ink, Hannover, Germany) at volume concentrations of 0.35 to 1.05%, giving background absorption of 0.2 to 0.6 cm^{-1}, and Intralipid (Fresenius Kabi, Uppsala, Sweden) at volume concentrations of 2.8 to 3.7%, resulting in a reduced scattering coefficient between 7 and 9 cm^{-1}.

2.4 *Absorption Spectroscopy*

The optical absorption setup together with the accuracy and validity of the method have been described in greater detail elsewhere.[24,28] Briefly, the output from a pulsed xenon short-arc lamp was delivered by a 400-μm-diam optical fiber and, after interacting with the tissue, the transmitted light was collected by a 200-μm-diam fiber. The center-to-center distance between delivery and collection fibers measured 2.0 mm. An S2000 miniature spectrometer (Ocean Optics Inc., Dunedin, Florida) was used to disperse and detect the collected light. Wavelength-dependent fluctuations in source output and detector response were accounted for by taking a reference measurement from a spectrally flat diffuse reflector based on Spectralon material (Lab Sphere Inc., Cranfield, UK) in connection to each measurement sequence.

For source-detector separations in the range 1.5 to 2.6 mm, the path length of the collected photons has been shown to be relatively insensitive to variations in tissue scattering.[24] Therefore, Beer-Lambert's law can be used to assess changes in tissue absorption. The negative logarithm of the transmission signal measured after the addition of an absorber, $I_2(\lambda) = I(\Delta\mu_a + \mu_a^0)$, to that before, $I_1(\lambda) = I(\mu_a^0)$, is given by[28]

$$\begin{aligned} R(\lambda) &= -\ln\left(\frac{I_2}{I_1}\right) \\ &= -\ln\left[\frac{I(\Delta\mu_a + \mu_a^0)}{I(\mu_a^0)}\right] = \Delta\mu_a L_{\text{eff}}(\Delta\mu_a + \mu_a^0) + B. \end{aligned} \tag{2}$$

In Eqs. (2) to (6), the wavelength dependence of the absorption coefficients and the transmission signals is omitted for the purpose of clarity. Although the path length is insensitive to scattering variations, the amount of collected light might change between measurements and hence the appearance of the factor B. Here, $L_{\text{eff}}(\Delta\mu_a + \mu_a^0)$ denotes the effective path length, which depends on the total absorption coefficient. To determine this dependence, a nonsequential ray tracing software package (ASAP 8.0.3, Breault Research Organization, Tucson, Arizona) was used to track the pathlengths of collected rays for a geometry matching the experimental setup. For these simulations, the source and detection fibers, having diameters as already stated and a numerical aperture of 0.22, were separated by 2 mm. The scattering and anisotropy coefficients were kept constant at 10 cm^{-1} and 0.9, respectively. We simulated 167 million rays in the absence of absorption and the optical path lengths L_i for all detected rays were stored. The effect of tissue absorption on the optical path lengths was added to the simulation results and the effective path length for different absorption coefficients was evaluated by

$$L_{\text{eff}}(\mu_a) = -\frac{1}{\mu_a}\ln\left[\frac{\sum_{i=1}^{N}\exp(-\mu_a L_i/n)}{N}\right]. \quad (3)$$

Here n denotes the refractive index, and N equals the number of detected rays, in this case 1.4 and 1000, respectively. The absorption coefficient μ_a was allowed to vary between 0.001 and 5 cm^{-1} in steps of 0.001 cm^{-1}. In contrast to the work by Mourant et al.,[28] where a slightly smaller fiber separation was used, no single functional dependency could adequately fit the effective path length to the total absorption coefficient over the entire absorption range. Therefore, a nearest-neighbor spline interpolation was used to describe the dependence of the effective path length on the total absorption coefficient.

In earlier work, Eq. (2) was in fact evaluated from measurements before and after addition of an exogenous absorber.[28] Here, both I_1 and I_2 are evaluated from a single measurement. By assuming that tissue absorption at 900 nm is dominated by water at a constant concentration of 60%, I_1 can be expressed as

$$\begin{aligned} I_1 = I(\mu_a^{60\%\ \text{water}}) = I(900\ \text{nm}) \\ \times\exp[-L_{\text{eff}}(\mu_a^{60\%\ \text{water}})\mu_a^{60\%\ \text{water}}]\cdots \\ \times\exp\{-L_{\text{eff}}[\mu_a^{60\%\ \text{water}}(900\ \text{nm})] \\ \times\mu_a^{60\%\ \text{water}}(900\ \text{nm})\}^{-1}, \end{aligned} \quad (4a)$$

where $I(900\ \text{nm})$ is the detected signal at 900 nm. Furthermore, I_2 is given by the detected signal and is described, as before,

$$I_2 = I(\Delta\mu_a + \mu_a^0) = I(\Delta\mu_a + \mu_a^{60\%\ \text{water}}). \quad (4b)$$

Since both transmission signals originate from a single measurement, the factor B is eliminated and Eq. (2) is modified to

$$\begin{aligned} R(\lambda) &= -\ln\left[\frac{I(\Delta\mu_a + \mu_a^{60\%\ \text{water}})}{I(\mu_a^{60\%\ \text{water}})}\right] \\ &= \Delta\mu_a L_{\text{eff}}(\Delta\mu_a + \mu_a^{60\%\ \text{water}}). \end{aligned} \quad (5)$$

The function "lsqnonlin" in MATLAB (MathWorks, Natick, Massachusetts) was used to solve for $\Delta\mu_a$ from Eq. (5). The spectral fitting interval was 500 to 800 nm. A singular value decomposition (SVD) algorithm was used to fit the extinction coefficients of relevant tissue chromophores to the calculated change in absorption coefficient. The SVD algorithm provides the best fit of a linear combination of a certain number of basis spectra to a data set and has been used previously in order to analyze fluorescence[29] and broad-banded reflectance spectra.[30] The extinction coefficients included in the evaluation of the absorbance data were those of mTHPC, deoxy- (Hb) and oxyhemoglobin[31](HbO). In addition, the mTHPC fluorescence spectrum was included in the model since experimental work gave evidence that the shorter wavelengths within the light source did induce detectable sensitizer fluorescence also in the presence of strong tissue absorption. This fluorescence component partly overlaps the absorption peak at 652 nm, leading to an underestimated mTHPC concentration if fitting the sensitizer extinction coefficient to this peak only. Thus, $\Delta\mu_a$ could be expressed as

$$\begin{aligned} \Delta\mu_a = \Delta c_{\text{mTHPC}}\varepsilon_{\text{mTHPC}} + \Delta c_{\text{Hb}}\varepsilon_{\text{Hb}} + \Delta c_{\text{HbO}}\varepsilon_{\text{HbO}} + AM(\lambda) \\ + \sum_{i=0}^{2}\omega_i C_i\lambda^i, \end{aligned} \quad (6)$$

where the Δc's denote concentration changes; the ε's are the corresponding extinction coefficients; and $M(\lambda)$ and A are the sensitizer fluorescence spectrum and fluorescence amplitude, respectively. The last summation on the right-hand side of Eq. (6) was included to account for tissue autofluorescence overlapping the absorption signals. The number of components within this summation was determined empirically by minimizing the residuals returned by the algorithm. The magnitude of $M(\lambda)$ and the weights ω_i were chosen to match the magnitudes of the chromophore extinction coefficients. For each absorption spectrum, the SVD algorithm returned the chromophore concentrations, i.e., the Δc's, the mTHPC fluorescence amplitude A, and the individual C_i's. The Δc_{mTHPC} was used to predict the mTHPC concentration from each measurement. The sensitizer level was determined by the average Δc_{mTHPC} from two to five absorption spectra acquired for each animal, tissue type, and investigation time point, i.e., at 0 and 4 or 6 h. For the absorption spectroscopy data, the error of the fit was quantified as

$$r = \left[\frac{1}{m-1}\sum_{\lambda}(y_{\text{measured},\lambda} - y_{\text{fit},\lambda})^2\right]^{1/2}, \quad (7)$$

where the summation includes the spectral fitting interval 500 to 800 nm, and m denotes the number of data points within this interval. In the case of negative sensitizer concentration prediction, the mTHPC concentration was set to zero and the error of the fit was reevaluated by only including deoxy- and oxyhemoglobin in the SVD algorithm.

Figure 1(a) illustrates the different basis spectra used for the SVD algorithm within the spectral fitting range. Figure 1(b) shows *in vivo* data from a lesion 4 h after sensitizer administration together with the fit and the corresponding residuals. For this measurement, the predicted concentrations were 1.3, 11.6, and 8.9 μM for mTHPC, deoxy-, and oxyhemoglobin. The mTHPC fluorescence amplitude was $+1.7 \times 10^{-6}$ a.u. (arbitrary units). Note that the analysis of the absorption spectra assumes homogeneous medium. For this situation, the accuracy of the setup and method of data analysis was confirmed in TiO-based liquid phantoms with scattering similar to those levels encountered in normal tissue ($\mu_s' \sim 5$ to 15 cm^{-1}) and sensitizer concentration between 2 and 20 μM. The lower mTHPC detection limit was approximately 0.5 μM within the same set of liquid phantoms as described in Sec. 2.3.

2.5 *Extraction*

Tissue samples, weighing 100 to 200 mg, were homogenized in 3 ml of dimethyl sulfoxide (DMSO) at 24,000 rpm (T18 Basic Ultra Turrax, IKA, Staufen, Germany). The homogenate was centrifuged at 800 g (3000 rpm) for 20 min (EconoSpin, Sorvall Instruments DuPont, Wilmington, Delaware). The su-

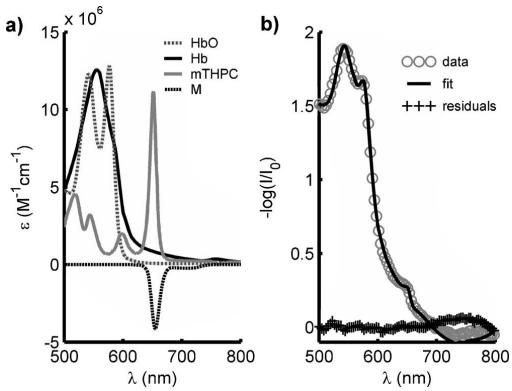

Fig. 1 (a) mTHPC fluorescence and extinction coefficients of mTHPC in ethanol, deoxy- (Hb) and oxyhemoglobin (HbO). The components constituting the background signal are not shown for purpose of clarity. Absorption and fluorescence data for mTHPC was kindly provided by biolitec AG. (b) Absorption data from animal 2. Also shown are the fit and the corresponding residuals. The error of the fit was 0.029.

pernatant was collected and following excitation at 420 nm, the fluorescence signal was recorded between 460 and 700 nm using a luminescence spectrometer (LS 45, Perkin Elmer, Buckinghamshire, UK). The detected fluorescence intensity at 652 nm was used to provide an absolute measure of sensitizer concentration after appropriate calibration. Blood samples were centrifuged at 360 g (2000 rpm) for 10 min to separate out the plasma. Fifty microliters of plasma were mixed with 2950 μl DMSO for further analysis according to the same procedure as for the other organs. The lower detection limit for the extraction setup was 0.04 ng mTHPC/mg tissue, which corresponds to approximately 0.06 μM assuming a tissue density of 1.06 g/ml.

2.6 *Statistical Analysis*

To study agreement between two methods, the correlation of the data from each technique was calculated using:

$$R(x,y) = \frac{\mathrm{cov}(x,y)}{[\mathrm{cov}(x,x)\mathrm{cov}(y,y)]^{1/2}}. \qquad (8)$$

Here, $\mathrm{cov}(x,y) = E[(x-m_x)(y-m_y)]$, where E denotes the mathematical expectation, x and y represent the mTHPC quantity as determined by each method, and m_x and m_y are the corresponding averaged mTHPC quantities. For comparison of two means, a two-sided Student's t test was used, where $P \leq 0.05$ was considered significant.

3 Results

The extraction results indicated preferential accumulation of mTHPC in lesions as compared to normal skin both at 4 and 6 h after sensitizer application. The average mTHPC concentration in lesions was 6.0 ng/mg tissue with a SD of 3.1 ng/mg. No significant difference could be identified between the two drug-light intervals. Sensitizer levels in liver, spleen, blood, muscle, and normal skin where no mTHPC-gel had been applied were below the detection limit, indicating mTHPC concentrations below 0.04 ng/mg tissue.

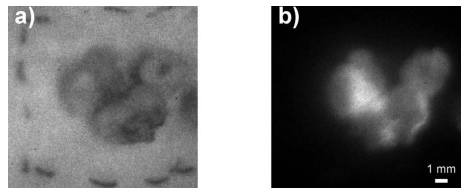

Fig. 2 (a) Room-light image showing lesions and surrounding skin for animal 3 and (b) fluorescence signal at 654 nm showing selective accumulation of mTHPC.

Figure 2 shows room-light and 654-nm fluorescence images of three lesions 4 h after application of the mTHPC-containing gel. The temporal profile of the mTHPC buildup assessed by the fluorescence imaging technique is shown in Fig. 3(a), where the averaged contrast function value is plotted as a function of mTHPC-gel application time for lesion (t), normal skin (n), and skin surrounding the visible lesion (tn). The data indicated significant sensitizer selectivity within lesions for the 4- but not the 6-h drug-light interval. Only normal skin (n) indicated a significant difference between 4- and 6-h application times.

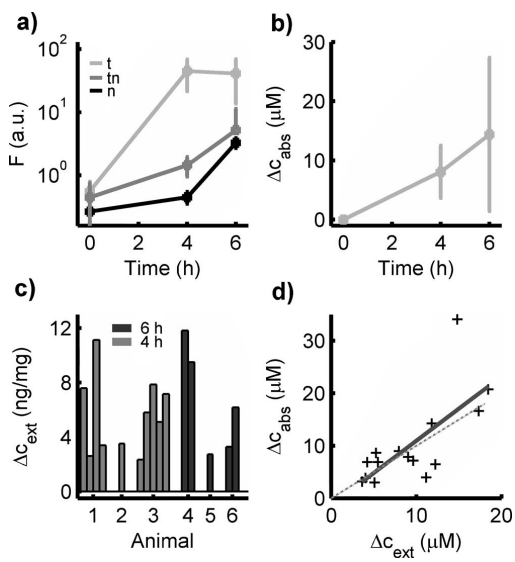

Fig. 3 (a) Contrast function value for normal tissue (n), tissue in close proximity to lesion (tn), and lesion (t). Each marker represents the averaged F value and error bars denote ±1 SD. (b) Temporal profile of the average mTHPC concentration within lesions as estimated by the absorption spectroscopy probe. (c) mTHPC concentration as determined by extraction for each lesion in six animals. (d) Scatter plot illustrating the covariance between absorption and extraction data for all lesions.

As for the extraction data but in contrast to the fluorescence results, the absorption spectroscopy data revealed a selective sensitizer accumulation within lesions for both drug-light intervals. The temporal profile of the calculated mTHPC concentration within lesions is shown in Fig. 3(b). For this tissue type, no significant differences in sensitizer buildup could be identified for the two different mTHPC accumulation times. Resulting mTHPC levels for normal skin and intact skin in close proximity to the lesion were below the detection limit of the setup and are therefore not shown. The model for the SVD algorithm, including mTHPC, deoxy- and oxyhemoglobin extinction coefficients, and mTHPC fluorescence, resulted in good agreement with measurement data. The average fitting errors, evaluated according to Eq. (7), were 0.064 and 0.050 for lesion and intact skin in close proximity to the lesion, respectively. The fitting errors displayed no statistically significant differences with tissue type and drug-light interval.

Figure 3(c) shows the extraction data for each individual lesion, illustrating large intertumor variations in sensitizer concentration. In general, lesions displayed a heterogeneous tissue structure sometimes also presenting necrotic areas. The high variability in mTHPC concentration was most likely influenced by the differences in tissue composition. Figure 3(d) is a scatter plot illustrating the agreement between absorption and extraction data where each marker represents data from a specific lesion. The solid line shows the best fit in a linear least-squares sense, whereas the dashed line represents the ideal fit. The slope of the correlation curve was 1.2. The overestimation of the mTHPC concentration by the absorption data is mostly due to the outlier at $>30\ \mu$M as measured by the absorption technique. For tumor tissue, the absorption and extraction data showed a significant correlation ($P<0.05$) with a correlation coefficient of 0.72. On the other hand, the fluorescence contrast ratio displayed no significant correlation to the other methods.

Figure 4(a) is a photograph of one excised lesion, approximately 4 mm in depth, sliced parallel to its depth axis. The fluorescence contrast function image of the same lesion is presented in Fig. 4(b), illustrating the heterogeneous structure of the mTHPC content. Figure 4(c) shows the fluorescence contrast value (F value) along the depth profile marked by the thin dashed line in Fig. 4(b). As a comparison, the average (±1 SD) F value for all lesions *in vivo* is also included in the graph. The mTHPC concentration assessed by the absorption technique is plotted in Fig. 4(d) for three measurement positions, also showing the decrease in sensitizer concentration with depth. Possibly due to the administration of a total of three 20-μl aliquots of the mTHPC-gel, *in vivo* absorption measurements on this lesion via the surface of the intact tumor indicated sensitizer levels slightly higher than for the remaining animals as tested by a one-sided Student's t test ($P\leqslant 0.05$). The second lesion used for investigating the sensitizer depth penetration did not display significantly higher mTHPC concentration as compared to the other lesions. However, some caution should be exercised when interpreting the sensitizer depth distribution from Fig. 4.

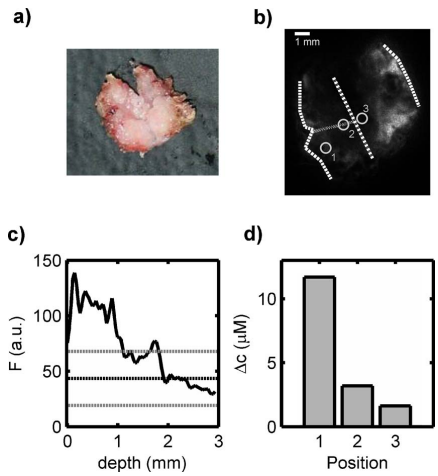

Fig. 4 (a) Digital photograph showing cross section of a vertical cut through a tumor. (b) Fluorescence contrast function image for the same tumor. The tumor surface and deepest tissue region are indicated by the bright dashed lines. (c) Fluorescence contrast function value along the thin dashed line in (b). The dashed lines indicate the average F value ±1 SD for all lesions. (d) mTHPC concentration as measured by the absorption spectroscopy probe. Measurement positions are marked in (b).

4 Discussion

Topical application of ALA was successfully used in combination with superficial PDT of skin malignancies.[7] By employing methyl esterified ALA-Me, an improved tumor selectivity[8] as well as homogeneous protoporphyrin distribution down to 2 mm in human BCCs (Ref. 9) was achieved. However, protoporphyrin IX remains a PDT agent resulting in relatively limited treatment efficacies.[7,13]

This paper reports on the first use of a topically applied liposomal mTHPC-formulation in a nonmelanoma skin carcinoma model. This mTHPC-gel was investigated as a possible alternative to ALA-PDT and systemic administration of mTHPC, suffering from poor treatment outcome for thicker lesions and prolonged photosensitivity, respectively. In this study, significant sensitizer selectivity in lesions as compared to skin with intact stratum corneum was observed from extraction and optical absorption data for both 4- and 6-h drug-light intervals. In fact, the mTHPC concentration within tissue characterized by an undamaged upper skin layer was below the detection limits of these setups. The extraction results from internal organs and normal skin where no mTHPC-gel had been applied showed no trace of the sensitizer, indicating undetectable levels of generalized photosensitivity. Data from the fluorescence imaging setup also indicated no significant variation in sensitizer concentration within lesions for the two application times. However, increased mTHPC fluorescence was observed between the 4- and 6-h application times for gel-treated normal skin with an intact stratum corneum, possibly due to the higher sensitivity of this setup. For the fluorescence spectroscopy data set, the selectivity between lesion and normal skin was thus only significant for the shorter drug-light interval, indicating an optimal drug-light interval of 4 h for the present skin tumor model.

The observed sensitizer distribution is likely due to differences in the ability of mTHPC and liposomes to penetrate the tissue layers. The absence of stratum corneum over the lesion seems to facilitate the sensitizer penetration, whereas intact skin prevents the lower tissue layers from accumulating any substantial amount of mTHPC. Supporting the present observations, Schmid and Karting state that intact liposomes penetrate only very superficial parts of the normal epidermis, whereas damaged skin constitutes a less efficient barrier.[32] The diffusion of liposome-encapsulated ALA through healthy mouse skin has been shown to require tens of hours,[20] and this slow process could be explained by the way liposomes are believed to interact with intact skin, first adhering to and then disrupting the upper tissue membranes. The liposomes hence act as penetration enhancers.[19] These previously published results are in agreement with the increasing, although still low, mTHPC levels found in normal mouse skin for the 6-h administration time.

For tumor tissue, the large variations in mTHPC concentration and the lack of significant differences between 4- and 6-h drug-light intervals could be due to a sensitizer buildup within lesions mostly determined by the tissue composition and the status of the uppermost layers. For example, it was noted that necrotic regions displayed overall lower sensitizer levels. It is also reasonable to suspect the depth penetration of the sensitizer to depend on the status of the upper skin layers. Within the lesions for which the sensitizer depth penetration was investigated, the mTHPC concentration was in the micromolar range to depths of 3 to 4 mm. Similar results were reported by Peng et al.,[9] where good selectivity and homogeneous sensitizer distribution down to 2 mm in human BCCs were observed following topical application of ALA-Me. Since the liposomal mTHPC formulation was not compared to its pure analog, it is difficult to determine the effect the use of liposomes had on the sensitizer distribution and depth penetration within this study.

The mTHPC levels observed within lesions in this study are in the range shown to induce significant PDT effects once irradiated at an appropriate wavelength.[33] However, another factor important to the PDT outcome is the localization of the sensitizer molecule within the tissue and the cell. In the case of systemic mTHPC administration, short drug-light intervals result[33] in vascularly targeted PDT, whereas longer time periods enable the sensitizer to localize within the cells, targeting, for example, mitochondria.[34] In the case of topical mTHPC administration, the mTHPC levels found in blood were low for all time points investigated. We thus anticipate the PDT effect to more strongly correlate with maximum sensitizer concentration within the lesion and display less pronounced vascular effects.

In parallel with the extraction study, fluorescence imaging and absorption spectroscopy were evaluated as noninvasive methods for assessing sensitizer content *in vivo*. The fluorescence imaging setup has the advantage of being a more sensitive tool than the absorption spectroscopy probe. Furthermore, the ability to image larger areas quickly provides valuable information on the spatial sensitizer distribution. However, for the range of optical properties found in biological tissue, the effective penetration depth of the near-UV light used for exciting the mTHPC fluorescence is of the order of a couple of hundred micrometers, making the fluorescence imaging method applicable only when studying very superficial tissue regions. In addition, the fluorescence signal is highly dependent on tissue optical properties, making it difficult to use the absolute fluorescence level as a reliable concentration estimate. Within this study, the surface of the lesions displayed a heterogeneous structure, sometimes including superficial areas of dark necrotic regions. The shallow investigation volume in combination with sensitivity to the optically heterogeneous tissue could thus explain the lack of significant correlation between extraction and fluorescence data.

In contrast to the fluorescence signal, the absorption spectroscopy data correlated rather well with the extraction results. One reason for the better agreement could be the higher overlap of probing volume of the two methods. A previous publication has reported on approximate probing depth of 1 to 2 mm for the absorption probe,[28] matching the depth of skin tumors likely to be treated by PDT using topical irradiation. In addition, since the analysis of the absorption spectrum takes into account the average tissue chromophore content, these results are not as easily corrupted by variations in tissue optical properties as is the fluorescence data. However, the relatively high detection limit for the absorption spectroscopy probe is a major drawback. It is therefore highly desirable to combine the sensitivity of the fluorescence level with the ability of the absorption signal to account for varying tissue absorption. Finlay and Foster demonstrated a probe combining white-light absorption with fluorescence spectroscopy to recover the intrinsic tissue autofluorescence, i.e., the fluorescence spectra corrected for tissue absorption and scattering.[35] By utilizing the absorption spectrum to assess the tissue optical properties, the corrected fluorescence signal would constitute a more reliable fluorophore concentration estimate. A further drawback of the absorption spectroscopy probe is the inherent sensitivity to measurement site within the spatially heterogeneous structure of the lesions. The latter effect most likely explains part of the scattered appearance of the absorption data in relation to the ideal fit in Fig. 3(d). Furthermore, the outlier at $>30\ \mu$M as measured by the absorption spectroscopy setup could possibly be due to a small amount of mTHPC-gel remaining on the skin surface due to its inherent roughness. This effect highlights the importance of careful cleansing of the tissue surface prior to optical measurements in order to detect the true sensitizer distribution, i.e., the amount of mTHPC that has penetrated into the tissue.

In connection with this discussion, note the importance of including the mTHPC fluorescence as one of the components of the SVD algorithm. The shorter wavelengths present in the output from the xenon arc lamp induce sensitizer fluorescence overlapping the absorption peak at 652 nm. In contrast to the effective path length, the fluorescence level is dependent on the sample scattering for this source-detector separation. Although this was not taken into account in the analysis process as it was outlined in Sec. 2.4, including the fluorescence component significantly improved the accuracy of the setup. By simply excluding the sensitizer fluorescence component from the analysis resulted in underestimation of the sensitizer concentration by a factor of 1.5 for the investigated lesions. Furthermore, if also limiting the spectral fitting range to 630 to 750 nm to avoid the strong hemoglobin absorption bands, the mTHPC concentration was underestimated by a factor 2. We conclude that sensitizer fluorescence should be

taken into account when utilizing the tissue absorption imprint for absolute concentration estimates. A significant underestimation has also been reported by Weersink et al. when utilizing a reflectance spectroscopy probe with multiple source-detector fibers for determining $AlPcS_4$ concentration in *in vivo* rabbit skin.[36] The underestimation of the sensitizer concentration by a factor of 3 was attributed the layered skin structure and nonuniform $AlPcS_4$ distribution. Within our work, the investigated tissue was highly heterogeneous also presenting a depth-dependent sensitizer concentration. Therefore, these effects constitute another source of error as they were not considered in our current evaluation of the optical absorption signal, which assumes homogeneous medium.

In conclusion, we reported on the use of a topically administered mTHPC formulation in a murine skin tumor model. In this sensitizer formulation, the hydrophobic mTHPC molecule was incorporated into conventional liposomes, rendering the sensitizer preparation water soluble. By administering the compound via a heat-setting gel, the retention time of the applied gel could be increased. Fluorescence and absorption spectroscopy as well as extraction data indicated significant mTHPC accumulation within lesions but no difference in tumor sensitizer concentration between the 4- and 6-h application times. The more sensitive fluorescence setup indicated optimal tumor selectivity for the 4-h drug-light interval. Furthermore, the topical administration route led to low levels of systemic photosensitization. Based on these results, this sensitizer formulation and administration path would be interesting to pursue for topical mTHPC PDT. Currently, a phase I clinical trial has been initiated to study the feasibility of using the mTHPC-gel for treatment of skin tumors.

Acknowledgments

This work was funded by the European Commission (EC) integrated project BRIGHT IST-511-722-2003 and the National Institutes of Health (NIH) Prime Cooperative Agreement No. 1 U54 CA 104677. The authors gratefully acknowledge Irving Bigio at Boston University for providing instrumentation and technical support for the optical absorption spectroscopy setup.

References

1. T. J. Dougherty, C. J. Gomer, B. W. Henderson, G. Jori, D. Kessel, M. Korbelik, J. Moan, and Q. Peng, "Photodynamic therapy," *J. Natl. Cancer Inst.* **90**(12), 889–905 (1998).
2. R. D. Almeida, B. J. Manadas, A. P. Carvalho, and C. B. Duarte, "Intracellular signaling mechanisms in photodynamic therapy," *Biochim. Biophys. Acta* **1704**(2), 59–86 (2004).
3. M. Triesscheijn, M. Ruevekamp, M. Aalders, P. Baas, and F. A. Stewart, "Outcome of mTHPC mediated photodynamic therapy is primarily determined by the vascular response," *Photochem. Photobiol.* **81**(5), 1161–1167 (2005).
4. F. H. van Duijnhoven, R. I. J. M. Aalbers, J. P. Rovers, O. T. Terpstra, and P. J. K. Kuppen, "Immunological aspects of photodynamic therapy of liver tumors in a rat model for colorectal cancer," *Photochem. Photobiol.* **78**(3), 235–240 (2003).
5. J. S. Dysart, G. Singh, and M. S. Patterson, "Calculation of singlet oxygen dose from photosensitizer fluorescence and photobleaching during mTHPC photodynamic therapy of MLL cells," *Photochem. Photobiol.* **81**(1), 196–205 (2005).
6. C. Hopper, A. Kubler, H. Lewis, I. BingTan, and G. Putnam, "mTHPC-mediated photodynamic therapy for early oral squamous cell carcinoma," *Int. J. Cancer* **111**(1), 138–146 (2004).
7. Q. Peng, T. Warloe, K. Berg, J. Moan, M. Kongshaug, K.-E. Giercksky, and J. M. Nesland, "5-aminolevulinic acid-based photodynamic therapy: Clinical research and future challenges," *Cancer* **79**, 2282–2308 (1997).
8. P. Juzenas, S. Sharfaei, J. Moan, and R. Bissonnette, "Protoporphyrin IX fluorescence kinetics in UV-induced tumours and normal skin of hairless mice after topical application of 5-aminolevulinic acid methyl ester," *J. Photochem. Photobiol., B* **67**(1), 11–17 (2002).
9. Q. Peng, A. M. Soler, T. Warloe, J. M. Nesland, and K. E. Giercksky, "Selective distribution of porphyrins in skin thick basal cell carcinoma after topical application of methyl 5-aminolevulinate," *J. Photochem. Photobiol., B* **62**(3), 140–145 (2001).
10. S. Mitra and T. H. Foster, "Carbogen breathing significantly enhances the penetration of red light in murine tumours *in vivo*," *Phys. Med. Biol.* **49**(10), 1891–1904 (2004).
11. Q. G. Ren, S. M. Wu, Q. Peng, and Y. J. Chen, "Comparison of 5-aminolevulinic acid and its hexylester mediated photodynamic action on human hepatoma cells," *Acta Biochim. Biophys. Sinica* **34**(5), 650–654 (2002).
12. E. Balasubramaniam and P. Natarajan, "Photophysical properties of protoporphyrin IX and thionine covalently attached to macromolecules," *J. Photochem. Photobiol., A* **103**(3), 201–211 (1997).
13. P. Schleier, A. Berndt, S. Kolossa, and M. Wood, "Comparison between mALA- and ALA-PDT in the treatment of basal cell carcinomas," *Oral Oncol. Suppl.* **1**(1), 67–68 (2005).
14. S. Mitra and T. H. Foster, "Photophysical parameters, photosensitizer retention and tissue optical properties completely account for the higher photodynamic efficacy of meso-tetra-hydroxyphenyl-chlorin vs Photofrin," *Photochem. Photobiol.* **81**(4), 849–859 (2005).
15. S. Sasnouski, V. Zorin, I. Khludeyev, M. A. D'Hallewin, F. Guillemin, and L. Bezdetnaya, "Investigation of Foscan interactions with plasma proteins," *Biochim. Biophys. Acta* **1725**(3), 394–402 (2005).
16. P. Westerman, T. Glanzmann, S. Andrejevic, D. R. Braichotte, M. Forrer, G. A. Wagnieres, P. Monnier, H. van den Bergh, J. P. Mach, and S. Folli, "Long circulating half-life and high tumor selectivity of the photosensitizer meta-tetrahydroxyphenylchlorin conjugated to polyethylene glycol in nude mice grafted with a human colon carcinoma," *Int. J. Cancer* **76**(6), 842–850 (1998).
17. J. P. Keene, D. Kessel, E. J. Land, R. W. Redmond, and T. G. Truscott, "Direct detection of singlet oxygen sensitized by haematoporphyrin and related compounds," *Photochem. Photobiol.* **43**(2), 117–120 (1986).
18. G. Gupta, C. A. Morton, C. Whitehurst, J. V. Moore, and R. M. Mackie, "Photodynamic therapy with meso-tetra(hydroxyphenyl) chlorin in the topical treatment of Bowen's disease and basal cell carcinoma," *Br. J. Dermatol.* **141**(2), 385–386 (1999).
19. M. J. Choi and H. I. Maibach, "Liposomes and niosomes as topical drug delivery systems," *Skin Pharmacol. Appl. Skin Physiol.* **18**(5), 209–219 (2005).
20. M. B. Pierre, A. C. Tedesco, J. M. Marchetti, and M. V. Bentley, "Stratum corneum lipids liposomes for the topical delivery of 5-aminolevulinic acid in photodynamic therapy of skin cancer: preparation and *in vitro* permeation study," *BMC Dermatol.* **1**(1), 5 (2001).
21. X. Damoiseau, H. J. Schuitmaker, J. W. M. Lagerberg, and M. Hoebeke, "Increase of the photosensitizing efficiency of the Bacteriochlorin a by liposome-incorporation," *J. Photochem. Photobiol., B* **60**(1), 50–60 (2001).
22. A. M. Richter, "Liposomal delivery of a photosensitizer, benzoporphyrin derivative monoacid ring A (BPD), to tumor tissue in a mouse tumor model," *Photochem. Photobiol.* **57**, 1000–1006 (1993).
23. C. af Klinteberg, A. M. K. Enejder, I. Wang, S. Andersson-Engels, S. Svanberg, and K. Svanberg, "Kinetic fluorescence studies of 5-aminolaevulinic acid-induced protoporphyrin IX accumulation in basal cell carcinomas," *J. Photochem. Photobiol., B* **49**(2–3), 120–128 (1999).
24. J. R. Mourant, I. J. Bigio, D. A. Jack, T. M. Johnson, and H. D. Miller, "Measuring absorption coefficients in small volumes of highly scattering media: source-detector separations for which path lengths do not depend on scattering properties," *Appl. Opt.* **36**(22), 5655–5661 (1997).
25. B. Pegaz, E. Debefve, J. P. Ballini, G. Wagnieres, S. Spaniol, V. Albrecht, D. V. Scheglmann, N. E. Nifantiev, H. van den Bergh, and Y. N. Konan-Kouakou, "Photothrombic activity of m-THPC-loaded liposomal formulations: pre-clinical assessment on chick chorioallantoic membrane model," *Eur. J. Pharm. Sci.* **28**, 134–140 (2006).
26. M. Kyriazi, D. Yova, M. Rallis, and A. Lima, "Cancer chemopreven-

tive effects of Pinus Maritima bark extract on ultraviolet radiation and ultraviolet radiation-7,12,dimethylbenz(a)anthracene induced skin carcinogenesis of hairless mice," *Cancer Lett.* **237**(2), 234–241 (2006).
27. C. H. Gallagher, P. J. Canfield, G. E. Greenoak, and V. E. Reeve, "Characterization and histogenesis of tumors in the hairless mouse produced by low-dosage incremental ultraviolet radiation," *J. Invest. Dermatol.* **83**(3), 169–174 (1984).
28. J. R. Mourant, T. M. Johnson, G. Los, and I. J. Bigio, "Non-invasive measurement of chemotherapy drug concentrations in tissue: preliminary demonstrations of in vivo measurements," *Phys. Med. Biol.* **44**(5), 1397–1417 (1999).
29. W. J. Cottrell, A. R. Oseroff, and T. H. Foster, "Portable instrument that integrates irradiation with fluorescence and reflectance spectroscopies during clinical photodynamic therapy of cutaneous disease," *Rev. Sci. Instrum.* **77**(6), 064302 (2006).
30. E. L. Hull, M. G. Nichols, and T. H. Foster, "Quantitative broadband near-infrared spectroscopy of tissue-simulating phantoms containing erythrocytes," *Phys. Med. Biol.* **43**(11), 3381–3404 (1998).
31. S. A. Prahl, "Tabulated molar extinction coefficient for hemoglobin in water," http://omlc.ogi.edu/spectra/hemoglobin/summary.html (1999).
32. M. H. Schmid and H. C. Korting, "Therapeutic progress with topical liposome drugs for skin disease," *Adv. Drug Delivery Rev.* **18**(3), 335–342 (1996).
33. P. Cramers, M. Ruevekamp, H. Oppelaar, O. Dalesio, P. Baas, and F. A. Stewart, "Foscan® uptake and tissue distribution in relation to photodynamic efficacy," *Br. J. Cancer* **88**(2), 283–290 (2003).
34. C. M. N. Yow, J. Y. Chen, N. K. Mak, N. H. Cheung, and A. W. N. Leung, "Cellular uptake, subcellular localization and photodamaging effect of Temoporfin (mTHPC) in nasopharyngeal carcinoma cells: comparison with hematoporphyrin derivative," *Cancer Lett.* **157**(2), 123–131 (2000).
35. J. C. Finlay and T. H. Foster, "Recovery of hemoglobin oxygen saturation and intrinsic fluorescence with a forward-adjoint model," *Appl. Opt.* **44**(10), 1917–1933 (2005).
36. R. A. Weersink, J. E. Hayward, K. R. Diamond, and M. S. Patterson, "Accuracy of noninvasive *in vivo* measurements of photosensitizer uptake based on a diffusion model of reflectance spectroscopy," *Photochem. Photobiol.* **66**(3), 326–335 (1997).

Paper II

Fluorescence monitoring of a topically applied liposomal Temoporfin formulation and photodynamic therapy of non-pigmented skin malignancies

N. Bendsoe, L. Persson, A. Johansson, J. Svensson, J. Axelsson, S. Andersson-Engels, S. Svanberg, K. Svanberg.

Journal of Environmental Pathology, Toxicology and Oncology **26(2)**, 117-226 (2007).

Journal of Environmental Pathology, Toxicology, and Oncology, 26(2)117–126 (2007)

Fluorescence Monitoring of a Topically Applied Liposomal Temoporfin Formulation and Photodynamic Therapy of Nonpigmented Skin Malignancies

*Niels Bendsoe,[1] Linda Persson,[2] Ann Johansson,[2] Johan Axelsson,[2] Jenny Svensson,[2] Susanna Gräfe,[3] Tilmann Trebst,[3] Stefan Andersson-Engels,[2] Sune Svanberg,[2] & Katarina Svanberg[4,]**

[1]Department of Dermatology, Lund University Hospital, Lund, Sweden; [2]Department of Physics, Lund University, Lund, Sweden; [3]Research & Development, Biolitec AG, Jena, Germany; [4]Department of Oncology, Lund University Hospital, SE-221 85 Lund, Sweden

****Corresponding author***. E-mail: Katarina.Svanberg@onk.lu.se

Meso-tetra(hydroxyphenyl)chlorin (mTHPC) (INN: Temoporfin) is a potent photodynamically active substance in clinical use today. Usually, the substance is given systemically and a known drawback with this administration route is a prolonged skin light sensitization. For the first time to our knowledge, a liposomal Temoporfin gel formulation for topical application was studied in connection with photodynamic therapy (PDT) of nonpigmented skin malignancies in humans. Intervals of 4 hr between drug administration and light irradiation were used. Sensitizer distribution within tumor and surrounding normal skin was investigated by means of point monitoring and imaging fluorescence spectroscopy before, during, and after PDT, showing high tumor selectivity. Furthermore, the bleaching of Temoporfin was studied during the PDT procedure by monitoring the fluorescence following excitation by using a therapeutic light. A 30–35% light-induced photometabolization was shown. No pain occurred during or after treatment. It was also observed that the treated area did not show any swollen tissue or reddening, as is often seen in PDT using topical δ-aminolevulinic acid. On controlling the patients one week after treatment, healing progress was observed in several patients and no complications were registered.

KEY WORDS: mTHPC, PDT, basal cell carcinoma, fluorescence, bleaching, spectroscopic monitoring, Temoporfin topically

Introduction

This paper presents, to our knowledge, the first use of a new photosensitizer, a liposomal Temoporfin gel formulation, for topical application in humans. Photodynamic therapy (PDT) is a modality for local treatment of cancer and relies on a photosensitizing agent being activated by light at an appropriate wavelength, usually within the red wavelength region to optimize light penetration within tissue.[1] Many of the sensitizers are selectively located in malignant cells due to a variety of biological reasons[2] and therefore selectivity in the therapy is achieved. Provided the simultaneous presence of sensitizer and oxygen, a cytotoxic reaction can be photochemically induced, causing selective cell destruction. The PDT outcome is governed by a combination of the effect of direct cell kill and induction of apoptosis,[3] vascular damage,[4] and an elicited immune response.[5]

The majority of photosensitizers are administered systemically, which causes an unwanted side effect of skin sensitization. In PDT of certain types of skin abnormalities, topical application of a sensitizer is preferable in order not to cause general skin sensitization. Topical administration of δ-aminolevulinic acid (ALA) in combination with illumination from a laser or a light-emitting diode with light doses in the range of 35 and 200 J/cm^2 has been successfully used for treatment of nonmelanoma skin malignancies over the past decades.[6,7] ALA is often supplied in a cream at a concentration of 20%, and application times range between three and six hours.[8] During this time period, the ALA molecules diffuse into the tissue, followed by the synthesis of protoporphyrin IX (PPIX), which is the photodynamically active metabolite.[2] Because of an increased permeability of the ALA molecules through the damaged epidermis of many cutaneous tumors and differences in the enzymatic activity, the accumulation of PPIX often displays a significant selectivity between normal and malignant tissue for shorter application times up to about three to six hours.[2] The sensitizer distribution can easily be monitored via the characteristic PPIX fluorescence within the red wavelength region, thus making optical methods highly desirable as noninvasive tools for sensitizer monitoring.

For superficial basal cell carcinomas (sBCC), PDT following topical application of ALA has led to cure rates (CRs) of 79–100%.[6] Although, for nodular lesions, the reported CRs are often about 50–70%,[7] a fact that has been partly explained by the limited penetration (1–3mm) of the hydrophilic ALA molecules. A further drawback of ALA-mediated PDT is skin sensation, such as itching and sometimes pain reported in many trials.[9,10] ALA-PDT also induces immediate posttherapy tissue reactions with swollen, reddening, and oozing skin.

Due to the lipophilic character of ALA esters, these derivatives are expected to show better biological availability and tissue penetration than ALA. Peng et al. reported on a highly selective and homogeneous sensitizer distribution following topical administration of methyl δ-aminolaevulinate, Metvix®.[11] A high tumor selectivity was observed by means of PPIX fluorescence both in animal skin tumor models and in human basal cell carcinomas (BCCs).[12,13] On the other hand, as the PPIX molecule is activated at slightly shorter wavelengths than many other PDT agents, the light absorption of hemoglobin limits the light penetration and treatment depth to approximately a few millimeters.[14] Furthermore, the PPIX molecule itself presents some shortcomings in terms of the localization of the substance within the tissue,[15] and the relatively low extinction coefficient of this sensitizer.[16] These factors might limit the treatment outcome irrespective of which kind of ALA is used.[6,17]

Meso-tetra(hydroxyphenyl)chlorin (mTHPC) (INN: Temoporfin) has been reported as one of the most efficient sensitizers, since relatively small drug and light doses are required in order to achieve treatment response.[18] Another advantage with Temoporfin is the wavelength of the absorption maximum at 652 nm as compared to 635 nm for ALA, resulting in an enhanced light penetration. Systemically administered Temoporfin in ethanolic formulation, Foscan®, has been successfully used for PDT of head and neck malignancies,[19] prostate,[20] and for BCCs.[21] A major drawback utilizing systemic administration of Temoporfin is the prolonged photosensitivity, subjecting patients to subdued light conditions for several weeks following

sensitizer administration. In addition, due to the hydrophobic character of the mTHPC molecules, it is practically insoluble in aqueous media. Following systemic administration of the ethanolic formulation, the sensitizer therefore forms aggregates, leading to limited transportation of the sensitizer within biological media as well as poor tumor selectivity and PDT efficacy.[22–24] The above factors can also lead to an intense inflammation at the injection site.[21]

To overcome the problem of the extended photosensitization associated with systemic administration of Temoporfin, Gupta et al. have reported on PDT combined with topical mTHPC administration for treatment of Bowen's disease and BCCs.[25] In this study, the CR was 32% at the two month follow-up. The authors suggested that the formulation of Temoporfin they used was a limiting factor for the treatment outcome.

Previously, our group has reported on sensitizer distribution studies following topical administration of a novel liposomal formulation of Temoporfin in a murine skin tumor model.[26] For Temoporfin gel application times of four and six hours, the chemical extraction from different organs revealed a selective accumulation of the substance within tumor tissue. The average sensitizer concentration within lesions was 6.0 ng/mg, whereas no detectable levels of generalized photosensitivity were shown. Within the study, the strongly fluorescing and absorbing characteristics of Temoporfin were also used for monitoring the drug distribution by fluorescence imaging and absorption spectroscopy. These noninvasive methods confirmed the selective sensitizer distribution and indicated sensitizer penetration depths of 3–4 mm within the investigated tumors.

Following these initial promising results on the animal skin tumor model, the same liposomal Temoporfin formulation is introduced for nonpigmented skin malignancies in patients. In this study, we include spectroscopic measurements in order to monitor the uptake of the liposomal Temoporfin formulation in connection with PDT using laser light at 652 nm. By incorporating Temoporfin in a liposomal formulation, the substance is made more suitable and transport within biological media is facilitated. The liposome encapsulated Temoporfin is supplied in a water-based heat-setting gel, rendering application times of several hours possible. Fluorescence spectroscopy data are presented as a tool to study sensitizer distribution and treatment-induced photobleaching. Clinical parameters, such as skin sensations during the treatment and other local skin reactions during the first week after treatment, are monitored.

Material and Methods

Sensitizer

The sensitizer compound is comprised of a liposomal formulation of mTHPC (Temoporfin) in a thermogel matrix with a sensitizer concentration of 0.5 mg mTHPC/ml gel (Biolitec AG, Jena, Germany). The liposome formulation is based on dipalmitoylphosphatidylcholine (DPPC), monosaccharide, water, and polyoxyehthylene polyoxypropylene block copolymers encapsulating mTHPC.[27] The mTHPC gel is in a liquid phase at the storage temperature of 4°C, but forms a highly viscous gel when heated by the skin to temperatures above 26°C. The thermothickening thus aids in increasing the retention time of the applied gel and transfer of the sensitizer into the tissue. No penetration enhancers are added to the Temoporfin gel.

Patients

The Temoporfin gel was used for topical PDT of 35 lesions in 10 consecutive patients in the ambulatory outpatient ward. The histopathology showed basal cell carcinoma for 29 and squamous cell carcinoma for the remaining 6 lesions. The gel was applied on the visible lesion and an additional margin of about 10 mm on the surrounding skin. Tegaderm® was used to cover the area (Fig. 1A). Four hours later, the gel was removed and the site was carefully cleaned with alcohol. PDT was performed by irradiating lesions with diode laser light at 652 nm (Ceralas, Bonn, Germany) at a light dose of 20 J/cm^2. Two tumors in one patient were treated with a different light doses; one with 40 J/cm^2 and one with 60 J/cm^2. The optical fiber used for light delivery was equipped with a mi-

crolens, giving a uniform irradiance adjusted to 100 mW/cm^2.

Optical Measurements

Point-monitoring fluorescence spectroscopy measurements were performed pre- and post-PDT to study both the Temoporfin-related signal and tissue autofluorescence. Several sites within and in close proximity to the lesions were studied. The point-monitoring fluorosensor utilizes a nitrogen laser pumping a dye laser emitting pulsed excitation light at 405 nm. The light is guided to the tissue through an optical fiber with a core diameter of 600 μm. The induced fluorescence light is transmitted through the same fiber back to a detection unit. This unit incorporates an RG435 cutoff filter, a spectrometer, and a cooled intensified CCD recording fluorescence spectra in the range from 450 to 800 nm.[28]

In addition, a fluorescence imaging system was used to monitor the whole treatment site, including the surrounding normal skin margin prior to, during, and after PDT. Fluorescence images were collected by a CCD camera (C4742-80-12AG, Hamamatsu) equipped with a liquid crystal tunable filter (LCTF VIS 20-35, Varispec) and a zoom objective lens (50 mm focal length and f/1.8, Nikon). For the measurements performed pre- and post-PDT, the excitation light source consisted of 12 light emitting diodes with optical output centered at 405 nm, and the fluorescence was imaged at 652 nm.

Measurements performed in order to study the sensitizer photobleaching during PDT utilized the treatment light at 652 nm to induce Temoporfin fluorescence, which was detected at 720 nm. In each treatment session, a total of 60 fluorescence images were collected at 3 s intervals in order to follow the photobleaching of the sensitizer. For evaluation of the Temoporfin bleaching kinetics, a subset of 12 images, separated by approximately 16 s, were extracted from the data set. In each image, four regions with an area of about 0.2 mm^2 were selected, and the mean of the intensity within these regions was calculated. This procedure was performed for the same four regions in the consecutive images. By normalizing the mean intensity for each image to the mean intensity at the start of the irradiation, a normalized temporal profile of the fluorescence intensity was calculated.

Results and Discussion

The use and handling of the novel liposomal Temoporfin gel was very convenient since the gel was fluid only at the low storage temperature in the refrigerator. As soon as the gel was applied on the skin of the patients, it became more viscous and was not as easily smeared off the surface. Despite this, a covering film was placed over the area in order to keep the gel in place during the four hours before PDT illumination (Fig. 1A). In contrast to the use of the PPIX-precursor ALA, this liposomal Temoporfin formulation is not dependent on an enzymatic transformation. The application time is only for the purpose of letting the substance diffuse into the tumor tissue. The use of a four hour drug-light interval was motivated by the results from a

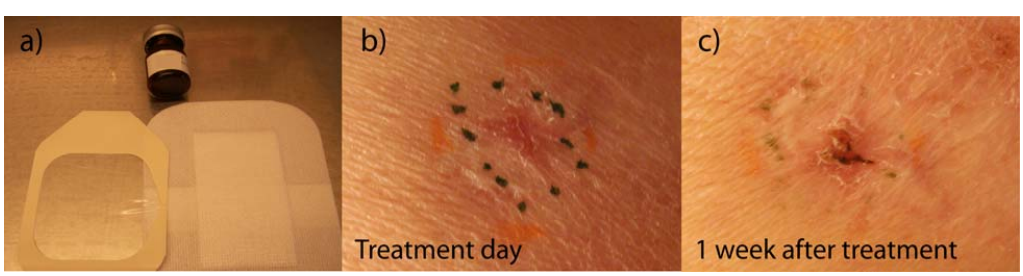

FIGURE 1. (a) A picture of a Temoporfin vial together with Tegaderm® dressing and a light protecting cover. **(b)** and **(c)** Digital images from a tumor prior to the PDT procedure and one week after, respectively. Remaining scar structures are due to previous non-PDT treatments.

previous study in a murine skin tumor model.[26] Unlike ALA, mTHPC is a strongly fluorescing substance. Any Temoporfin gel remaining on the skin surface will thus cause a false non-tissue-uptake-related fluorescence signal. Within this study, a careful cleansing of the skin was of importance in order to avoid influence by superficially located Temoporfin gel.

Further comparison to ALA and its esters shows an advantage for Temoporfin-PDT in that it did not cause any discomfort to the patients. Previous work has reported that a majority of the patients experience painful sensations in the skin during ALA-PDT.[9] Our own clinical experience includes rare cases of patients feeling inclined to interrupt the ALA-PDT and not accepting another PDT treatment using the same type of sensitizer. Different methods, such as spraying water or using a fan on the area treated, have been reported to relieve the ALA-PDT-related pain. However, other studies show less discomfort where only 25% of the patients experienced some kind of skin sensation and very few patients felt any pain.[10] In the present Temoporfin study, none of the treated patients spontaneously complained about any pain. Also, on interviewing all 10 patients concerning their sensations during the treatment, no one reported on any pain, itching, or stinging, and all patients could finish the treatments without any complaints. As mentioned above, the PDT light dose was generally 20 J/cm² delivered at 100 mW/cm². This rendered the treatment time acceptably short (approximately 200 s), an attractive feature, especially for elderly patients. This light dose resulted in only a partial bleaching of the Temoporfin as monitored by the fluorescence levels. Due to this fact, we increased the light dosage up to 40–60 J/ cm² for a few treatment procedures, as mentioned above. This increased light dose also did not result in any inconvenience for the patient. All the patients, treated with the novel Temoporfin formulation and PDT, were reviewed in order to record immediate post-PDT reactions (Figs. 1B and 1C). In the case of ALA-PDT, it is normal to see swollen tissue and some reddening, oozing, and formation of small pustules in the area where ALA is applied. No such reactions were seen in the patients, who had undergone Temoporfin-PDT. It was also noted that tumor sites oozing or bleeding before the Temoporfin-PDT seemed to dry out during the first week following the treatment. Therefore, no posttreatment dressings or other medical procedures were necessary.

Fluorescence spectroscopy, both in point-monitoring and imaging mode, was used to study Temoporfin distribution within the PDT target area. Point-monitoring fluorescence spectra recorded in a scan over a tumor, tumor border, and surrounding normal skin margin out to 10 mm before and after PDT are shown in Fig. 2, together with a digital photo of the tumor. In the region outside the tumor, the spectra shown are the average of data recorded at 2, 5, and 10 mm outside the visible boundary of the tumor. For the center of the tumor, the spectra displayed are the average of three recorded spectra, whereas fluorescence spectra for the tumor border represent single acquisitions. The Temoporfin fluorescence emission is clearly seen in the red part of the wavelength region, peaking at about 653 nm, and also a second broader peak at approximately 720 nm. Beside the drug-related fluorescence, the autofluorescence from the tissue itself, characterized by broad emission in the blue/green part of the wavelength region, is also seen. As known from earlier studies, the autofluorescence shows very low intensity within the tumor area as well as in the tumor border zones.[8] It can be noted that in one of the areas outside the visible border of the tumor, the autofluorescence is very low and the Temoporfin signal high (the rightmost spectrum), which may well represent an outstretching part of the tumor. Even if it is not histopathologically proven, it is a clear indication to also include this part in the PDT-irradiated field to enhance the radicality of the treatment. After PDT, the substance-related emission is shown with a decreased intensity, which is a sign of photobleaching of the drug during the PDT procedure.

By using both the Temoporfin-related signal and the tissue autofluorescence, a diagnosis-related contrast function, C_{diag}, can be calculated (Fig. 3A) as

$$C_{diag} = \frac{\mathrm{mTHPC}_{\lambda[640\text{-}690]} - \mathrm{Auto}_{\lambda[640\text{-}690]}}{\mathrm{Auto}_{\lambda[470\text{-}520]}}$$

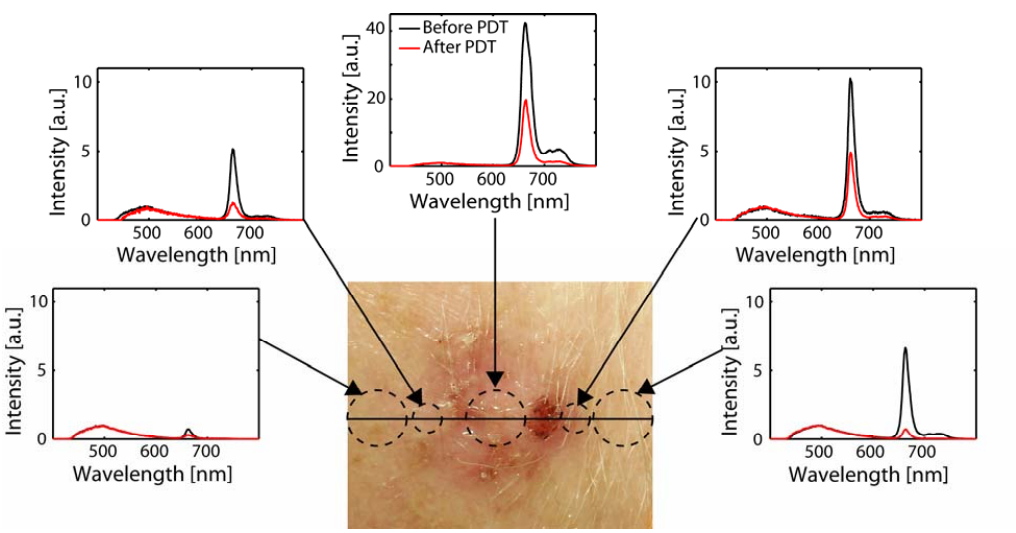

FIGURE 2. Fluorescence spectra induced by 405 nm excitation recorded from outside the lesion, border of the lesion, and center of the lesion before and after the PDT procedure.

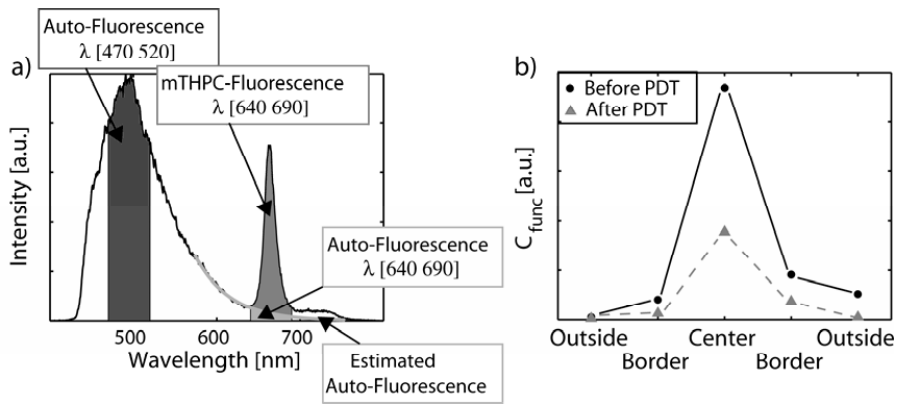

FIGURE 3. (a) Indications of the different areas used in the contrast function, C_{diag}. **(b)** The contrast function, C_{diag}, applied on spectra in Fig. 2 before and after PDT procedure. The data points are connected by lines for the guidance of the eye.

The function results in higher values in tumor, since the Temoporfin intensity is high and the autofluorescence is low compared to normal tissue (Fig. 2). This contrast function is slightly different from a contrast based only on the Temoporfin fluorescence amplitude without taking into account the tissue autofluorescence at this wavelength. Although the latter is perhaps more related to the sensitizer concentration and the PDT effect, C_{diag}, was employed in the present work. The values of this contrast function obtained before and after PDT for the tissue region in Fig. 2 are plotted in Fig. 3B. As can be seen, the contrast between tumor and manifest normal skin (the outermost left point) is very high. It can also be noted that the effect of bleaching due to PDT is substantial (about a factor of 2).

Typical fluorescence images of a tumor and surrounding skin following excitation at 405 nm with detection at 652 nm are shown in Fig. 4A. The images are monitored before and after the PDT procedure. The presented images are background subtracted, where the background was acquired without excitation light. For comparison, both images are normalized using the maximum intensity in the first image. It can be observed that the sensitizer distribution is heterogeneous within the tumor, an effect that was observed in most of the tumors studied. Similar results were observed in the murine skin tumor model following administration of this liposome-encapsulated Temoprofin gel.[26] In that study, the increased penetration within lesions was ascribed to the absence of the *stratum corneum*, whereas an intact epidermis prevented normal skin from accumulating any detectable levels of the photosensitizer. Thus, the heterogeneous fluorescence signals observed within this study may reflect the status of the uppermost skin layers. A further explanation of the heterogeneous Temoporfin distribution might be the tumor growth pattern, since it is well known that BCCs grow in spots or patches with normal tissue intermixed within the tumor site, as illustrated in the photograph in Fig. 2.

Fluorescence spectra acquired with the point-monitoring setup are also presented before and after PDT (Fig. 4B). The spectra are normalized to the maximum of the autofluorescence from sur-

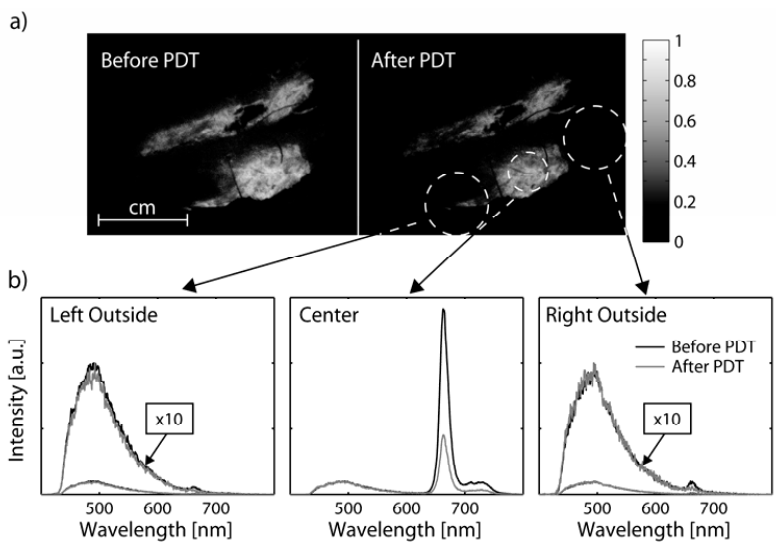

FIGURE 4. (a) Images of a tumor showing the fluorescence intensity at 652 nm for excitation at 405 nm before and after the PDT procedure, respectively. **(b)** The fluorescence spectra obtained in point monitoring for excitation at 405 nm from three different locations marked by circles; outside to the left and to the right of the visible tumor location, and inside the tumor area.

rounding skin between 470 and 520 nm. Since the Temoporfin signal shows a very low intensity in surrounding normal skin, the spectra are shown also with a tenfold magnification. A tumor demarcation based on the diagnosis-related contrast function, C_{diag}, of approximately 10:1 can be seen when comparing the tumor center spectrum with the two spectra from normal tissue outside the tumor. This is comparable to the contrast obtained for the majority of the tumors included in the study. Post-PDT, a decrease of the Temoporfin fluorescence in the center of the tumor as well as in the surrounding tissue can clearly be seen.

The laser light at 652 nm used for treatment also excites mTHPC fluorescence at 720 nm. Figure 5A shows the mean relative fluorescence intensity over time for ten representative tumors following excitation by the therapeutic laser light. The photodegradation of Temoporfin as monitored at 720 nm can clearly be seen. A photobleaching of about 30–35% is recorded after 200 s of therapeutic irradiation (20 J/cm^2), which concurs well with previously reported results for the photobleaching in mTHPC-sensitized spheroids.[29] Fluorescence images of a tumor are shown at three different time intervals during the PDT procedure (Fig. 5B); before, in the middle, and at the end of the session. These fluorescence images, detected at 720 nm following excitation by the therapeutic light at 652 nm, also illustrate the treatment-induced photobleaching. An apparent lower overall photobleaching can be observed following fluorescence excitation at 652 nm as compared to 405 nm excitation; see, for example, Figs. 4B and 5A. This effect might be explained by the different effective penetration depths of the two excitation wavelengths, i.e., violet light probes the superficial tissue regions where the therapeutic irradiation has efficiently bleached away most of the photosensitizer, whereas the red excitation wavelength also probes deeper into the tissue volume

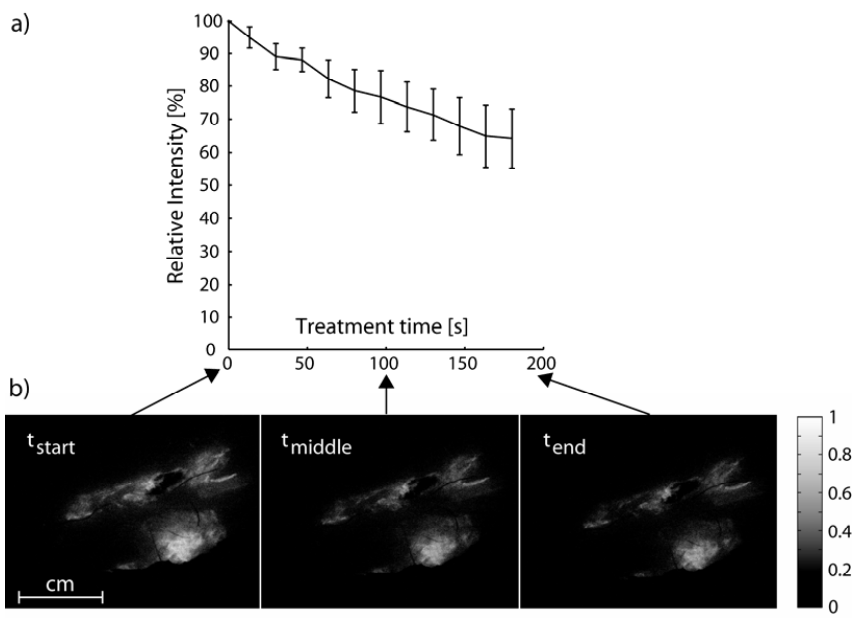

FIGURE 5. (a) Decrease of the normalized fluorescence intensity at 720 nm detected over time for ten tumors following excitation by the therapeutic radiation at 652 nm. Error bars represent ±1 SD. **(b)** Fluorescence images at 720 nm showing one of the tumors included in the data analysis after 0, 100, and 200 s of therapeutic irradiation, corresponding to 0, 10, and 20 J/cm^2.

where less bleaching has occurred due to the lower irradiance during treatment. These observations might suggest that sensitizer photobleaching as a parameter related to PDT outcome should be monitored utilizing the same excitation wavelength as for PDT induction whenever possible. Then a more representative tissue volume is probed.

Conclusions

In conclusion, we have reported a significant selectivity between tumor and surrounding skin at four hours following administration of liposome-encapsulated Temoporfin embedded into a thermosetting gel, constituting a novel Temoporfin formulation for topical use. The uptake of the substance was monitored by point-monitoring as well as imaging fluorescence spectroscopy. Fluorescence was induced either at 405 nm or by the treatment light at 652 nm. The bleaching of the sensitizer was estimated from the fluorescence levels by comparing the fluorescence images before, during, and after PDT. Furthermore, our initial results show that this new formulation is easily applicable due to its temperature-dependent viscosity, rendering the gel to firm after application onto the lesions. The light illumination is not connected with any treatment-related pain or other adverse reactions. As compared to ALA-PDT, no swollen tissue or oozing were noticed at the weekly follow-up. In cases where the tumor area was associated with a wound with or without bleeding, it was noted that these lesions seemed to dry up after a few days. After these promising initial results, further studies are needed in order to understand the penetration of the Temoporfin in skin following topical administration. Furthermore, studies for following long-term tumor response are being planned.

Acknowledgments

The economical support from the Swedish Research Council and the Knut and Alice Wallenberg Foundation is highly appreciated, as well as the valuable support from Stefan Spaniol at Biolitec, Bonn. The work was performed within the frameworks of the EU-BRIGHT Project No. IST-511-722-2003 and the EU project "Molecular imaging" LSHG-CT-2003-503259.

References

1. Dougherty TJ, Gomer CJ, Henderson BW, Jori G, Kessel D, Korbelik M, et al. Photodynamic therapy. J Natl Cancer Inst. 1998;90(12):889–905.
2. Peng Q, Berg K, Moan J, Kongshaug M, Nesland JM. 5-aminolevulinic acid-based photodynamic therapy: Principles and experimental research. Photochem Photobiol. 1997;65(2):235–51.
3. Almeida RD, Manadas BJ, Carvalho AP, Duarte CB. Intracellular signaling mechanisms in photodynamic therapy. Biochim Biophys Acta. 2004;1704(2):59–86.
4. Triesscheijn M, Ruevekamp M, Aalders M, Baas P, Stewart FA. Outcome of mTHPC mediated photodynamic therapy is primarily determined by the vascular response. Photochem Photobiol. 2005;81(5):1161–7.
5. van Duijnhoven FH, Aalbers RIJM, Rovers JP, Terpstra OT, Kuppen PJK. Immunological aspects of photodynamic therapy of liver tumors in a rat model for colorectal cancer. Photochem Photobiol. 2003;78(3):235–40.
6. Peng Q, Warloe T, Berg K, Moan J, Kongshaug M, Giercksky K-E, et al. 5-aminolevulinic acid-based photodynamic therapy: Clinical research and future challenges. Cancer. 1997;79:2282–308.
7. Svanberg K, Andersson T, Killander D, Wang I, Stenram U, Andersson-Engels S, et al. Photodynamic therapy of non-melanoma malignant tumours of the skin using topical δ-amino levulinic acid sensitization and laser irradiation. Br J Dermatol. 1994;130:743–51.
8. af Klinteberg C, Enejder AMK, Wang I, Andersson-Engels S, Svanberg S, Svanberg K. Kinetic fluorescence studies of 5-aminolaevulinic acid-induced protoporphyrin IX accumulation in basal cell carcinomas. J Photochem Photobiol B. 1999;49(2-3):120–8.
9. Holmes MV, Dawe RS, Ferguson J, Ibbotson SH. A randomized, double-blind, placebo-controlled study of the efficacy of tetracaine gel (Ametop®) for pain relief during topical photodynamic therapy. Br J Dermatol. 2004;150(2):337–40.
10. Wang I, Bendsoe N, af Klinteberg C, Enejder AMK, Andersson-Engels S, Svanberg S, et al.

Photodynamic therapy versus cryosurgery of basal cell carcinomas; results of a phase III randomized clinical trial. Br J Dermatol. 2001;144(4):832–40.

11. Peng Q, Soler AM, Warloe T, Nesland JM, Giercksky KE. Selective distribution of porphyrins in skin thick basal cell carcinoma after topical application of methyl 5-aminolevulinate. J Photochem Photobiol B. 2001;62(3):140–5.
12. Moan J, Ma LW, Iani V. On the pharmacokinetics of topically applied 5-aminolevulinic acid and two of its esters. Int J Cancer. 2001;92(1):139–43.
13. Juzenas P, Sharfaei S, Moan J, Bissonnette R. Protoporphyrin IX fluorescence kinetics in UV-induced tumours and normal skin of hairless mice after topical application of 5-aminolevulinic acid methyl ester. J Photochem Photobiol B. 2002; 67(1):11–7.
14. Mitra S, Foster TH. Carbogen breathing signifycantly enhances the penetration of red light in murine tumours in vivo. Phys Med Biol. 2004;-49(10):1891–904.
15. Ren QG, Wu SM, Peng Q, Chen YJ. Comparison of 5-aminolevulinic acid and its hexylester mediated photodynamic action on human hepatoma cells. Acta Biochim Biophys Sinica. 2002; 34(5):-650–4.
16. Balasubramaniam E, Natarajan P. Photophysical properties of protoporphyrin IX and thionine covalently attached to macromolecules. J Photochem Photobiol A. 1997;103(3):201–11.
17. Schleier P, Berndt A, Kolossa S, Wood M. Comparison between mALA- and ALA-PDT in the treatment of basal cell carcinomas. 50 Apr; 10th International Congress on Oral Cancer: Oral Onc Suppl. 2005;1(1):67–8.
18. Mitra S, Foster TH. Photophysical parameters, photosensitizer retention and tissue optical properties completely account for the higher photodynamic efficacy of meso-tetra-hydroxyphenyl-chlorin vs Photofrin. Photochem Photobiol. 2005;-81(4):849–59.
19. Lou PJ, Jager HR, Jones L, Theodossy T, Bown SG, Hopper C. Interstitial photodynamic therapy as salvage treatment for recurrent head and neck cancer. Br J Cancer. 2004;91(3):441–6.
20. Moore CM, Nathan TR, Lees WR, Mosse CA, Freeman A, Emberton M, et al. Photodynamic therapy using meso tetra hydroxy phenyl chlorin (mTHPC) in early prostate cancer. Lasers Surg Med. 2006;38(5):356–63.
21. Triesscheijn M, Ruevekamp M, Antonini N, Neering H, Stewart FA, Baas P. Optimizing meso-tetrahydroxyphenyl-chlorin mediated photodynamic therapy for basal cell carcinoma. Photochem Photobiol. 2006;82(6):1686–90.
22. Sasnouski S, Zorin V, Khludeyev I, D'Hallewin MA, Guillemin F, Bezdetnaya L. Investigation of Foscan interactions with plasma proteins. Biochim Biophys Acta. 2005;1725(3):394–402.
23. Westerman P, Glanzmann T, Andrejevic S, Braichotte DR, Forrer M, Wagnieres GA, et al. Long circulating half-life and high tumor selectivity of the photosensitizer meta-tetrahydroxyphenylchlorin conjugated to polyethylene glycol in nude mice grafted with a human colon carcinoma. Int J Cancer. 1998;76(6):842–50.
24. Keene JP, Kessel D, Land EJ, Redmond RW, Truscott TG. Direct detection of singlet oxygen sensitized by haematoporphyrin and related compounds. Photochem Photobiol. 1986;43(2):117–20.
25. Gupta G, Morton CA, Whitehurst C, Moore JV, Mackie RM. Photodynamic therapy with meso-tetra(hydroxyphenyl) chlorin in the topical treatment of Bowen's disease and basal cell carcinoma. Br J Dermatol. 1999;141(2):385–6.
26. Johansson A, Svensson J, Andersson-Engels S, Svanberg K, Bendsoe N, Alexandratou E, et al. Fluorescence and absorption assessment of a lipid mTHPC formulation following topical application in a skin tumor model. J Biomed Opt. 2007;12(3): 034026.
27. Pegaz B, Debefve E, Ballini JP, Wagnieres G, Spaniol S, Albrecht V, et al. Photothrombic activity of m-THPC-loaded liposomal formulations: Pre-clinical assessment on chick chorioallantoic membrane model. Eur J Pharm Sci. 2006;28: 134–40.
28. af Klinteberg C, Andreasson M, Sandström O, Andersson-Engels S, Svanberg S. Compact medical fluorosensor for minimally invasive tissue characterisation. Rev Sci Instrum. 2005;76(3): 034303–6.
29. Coutier S, Mitra S, Bezdetnaya LN, Parache RM, Georgakoudi I, Foster TH, et al. Effects of fluence rate on cell survival and photobleaching in meta-tetra-(hydroxyphenyl)chlorin-photosensitized colo 26 multicell tumor spheroids. Photochem Photobiol. 2001;73(3):297–303.

Paper III

Tumor selectivity at short times following systemic administration of a liposomal Temoporfin formulation in a murine tumor model

J. Svensson, A. Johansson, S. Gräfe, B. Gitter, T. Trebst, N. Bendsoe, S. Andersson-Engels, K. Svanberg.

Photochemistry and Photobiology, in press (2007).

Tumor Selectivity at Short Times Following Systemic Administration of a Liposomal Temoporfin Formulation in a Murine Tumor Model

Jenny Svensson[*1], Ann Johansson[1], Susanna Gräfe[2], Burkhard Gitter[2], Tilmann Trebst[3], Niels Bendsoe[4], Stefan Andersson-Engels[1] and Katarina Svanberg[5]

[1] Department of Physics, Lund University, Lund, Sweden
[2] Research & Development, Biolitec AG, Jena, Germany
[3] CeramOptec GmbH, Bonn, Germany
[4] Department of Dermatology, Lund University Hospital, Lund, Sweden
[5] Department of Oncology, Lund University Hospital, Lund, Sweden

[*]Corresponding author: Jenny Svensson, Department of Physics, Lund University, Professorsgatan 1, SE-223 62 Lund, Sweden, Phone: +46 46 222 31 19, Fax: +46 46 222 42 50, E-mail: jenny.svensson@fysik.lth.se

Abbreviations: AMD, age-related macular degeneration; CCD, charge-coupled device; DMSO, Dimethyl sulfoxide; DPPC, dipalmitoylphosphatidylcholine; HPLC, high performance liquid chromatography; LCTF, liquid crystal tunable filter; mTHPC, m*eso*-tetra(hydroxyphenyl)chlorin; PDT, photodynamic therapy; PEG, poly(ethylene glycol); ROI, region of interest; SVD, singular value decomposition.

ABSTRACT

M*eso*-tetra(hydroxyphenyl)chlorin (mTHPC) (INN: Temoporfin) is one of the most potent photodynamically active substances in clinical use. Treatment protocols for Temoporfin-mediated photodynamic therapy often rely on drug-light intervals of several days in order for the photosensitizer to accumulate within the target tissue, though tumor selectivity is limited. Here, the mTHPC localization was studied at 2-8 hours following systemic administration of a liposomal Temoporfin formulation (0.15 mg/kg b.w.) in HT29 human colon adenocarcinoma in NMRI nu/nu mice. Photosensitizer distribution within tumor and internal organs was investigated by means of HPLC following chemical extraction, as well as *in situ* fluorescence imaging and point-monitoring fluorescence spectroscopy. For tumor tissue, the Temoporfin concentrations at 4 (0.16±0.024 ng/mg) and 8 (0.18±0.064 ng/mg) hours were significantly higher than at 2 (0.08±0.026 ng/mg) hours. The average tumor-to-muscle and the tumor-to-skin selectivity were 6.6 and 2, respectively, and did not vary significantly with time after photosensitizer injection. In plasma, the Temoporfin concentration was low (0.07±0.07 ng/mg) and showed no significant variation with time. Our results indicate a rapid biodistribution and clearance from the blood stream. Within the same type of organ, data from both fluorescence methods generally exhibited a significant correlation with the extraction results.

INTRODUCTION

Photodynamic therapy (PDT) is an investigational clinical method for local treatment of certain types of malignancies in various organs. The modality exhibits interesting advantages such as the possibility of repeated treatment and restriction of the treatment-induced tissue damage to irradiated sites. In PDT, a photosensitizer is excited by absorption of light at an appropriate wavelength followed by energy transfer to oxygen molecules or other tissue constituents. The toxic radicals thus formed, of which singlet oxygen is believed to be the most important, cause tissue destruction by means of direct cell kill, vascular damage and activation of the anti-tumor immune system components (1).

M*eso*-tetra(hydroxyphenyl)chlorin (mTHPC) (INN: Temoporfin) is one of the most potent photosensitizers for PDT in present use (2) and it has been successfully applied in the treatment of various indications, for example head and neck (3), prostate (4) and pancreatic (5) cancer. Strong response to Temoporfin-mediated PDT has been observed for short drug-light intervals, when the treatment outcome is mostly influenced by vascular response as the photosensitizer is located within blood vessels, vascular endothelial cells and tissue close to blood vessels (6-8). On the other hand, longer drug-light intervals, i.e. exceeding two days, allow the photosensitizer to diffuse further away from blood vessels and into tumor cells (8) possibly leading to a selective uptake in tumors (9,10). Clinical Temoporfin-PDT therefore often relies on drug-light intervals in the order of several days during which patients are restricted to limited light exposures (3-5). This prolonged skin photosensitivity is one of the disadvantages when using Temoporfin. Due to the high affinity of the drug to bind to lipid structures, which is of importance for its relatively high PDT efficiency, the drug diffuses rapidly from the blood stream into surrounding tissues, an effect that has been observed to cause problems at the injection site (5,7). Furthermore, the hydrophobic character of the molecule leads to poor water solubility and formation of aggregates within aqueous media (11), altering the spectroscopic and photosensitizing characteristics of the compound (12).

In order to prevent formation of aggregates, prolong photosensitizer circulating lifetimes and to improve water solubility, tumor selectivity and PDT response, several research groups have tried different delivery vehicles such as liposomes, nano-particles and conjugation to antibodies (13,14). The potential importance of avoiding aggregation was observed within a cell culture medium, where encapsulation of the hydrophobic photosensitizer bacteriochlorin a in liposomes, thereby promoting monomerization, was shown to increase oxygen consumption during PDT and decrease cell survival as compared to its partly aggregated original formulation (15). Possible evidence of mTHPC aggregation *in vivo* has been observed by Hopkinson *et al*. (16). Richter *et al.* have studied the use of liposomes as carrier of the hydrophobic benzoporphyrin derivative monoacid ring A (BPD-MA), reporting on higher absolute photosensitizer concentration within tumor and more pronounced PDT effect as compared to the original formulation (17). These findings were attributed to a different micro-localization within the cells and an increased association with low density lipoproteins (LDLs) when incorporated into liposomes. Pegaz *et al.* have recently compared two different liposomal Temoporfin formulations (Foslip, containing conventional liposomes based on dipalmitoylphosphatidylcholine (DPPC), and Fospeg, based on poly(ethylene glycol) (PEG)-modified liposomes) in terms of plasma circulation half-life times and PDT-induced photothrombic activity (18). The Temoporfin levels within the vasculature were studied up to 1200 s after photosensitizer injection, which is relevant for the treatment of age-related macular degeneration (AMD) by means of PDT. For the two formulations investigated,

similar fluorescence pharmacokinetic profiles were observed, whereas the Temoporfin within the PEGylated liposome carrier proved more efficient for vascularly targeted PDT. In addition, the observation of plasma half lives exceeding that of Visudyne®, a photosensitizer commonly used in the treatment of AMD, was ascribed to the more stable composition of the liposomes incorporating the mTHPC molecules. Fospeg has also been compared to an ethanol formulation of Temoporfin in PDT of feline skin tumors (19). In that study, the use of Fospeg demonstrated PDT response in all subjects, higher bioavailability, faster distribution and a slightly improved tumor selective uptake as compared to an ethanol formulation of Temoporfin.

An important issue in improving the understanding of various transportation vehicles for PDT photosensitizers is to be able to non-invasively measure the photosensitizer concentration. Optical methods are promising tools for tissue diagnostics and measurement of photosensitizer tissue levels in clinical environments. Fluorescence spectroscopy can provide signals related to the photosensitizer concentration and has the advantage of being a non-invasive technique that reveals results in real time (20). Fluorescence can either be studied in a point-monitoring mode (21), often using an optical fiber or a thin fiber probe for light delivery and collection, or in an imaging mode (22), where larger areas can be examined in a non-contact configuration. An imaging approach provides additional information on heterogeneities that are difficult to obtain with a point-monitoring detection technique. As Temoporfin is characterized by a relatively strong fluorescence yield, where excitation within the near-ultraviolet wavelength region results in distinctive fluorescence around 652 nm, fluorescence spectroscopy is a valuable tool in estimating photosensitizer concentration *in situ* within various tissue types.
In this work we present *ex vivo* pharmacokinetic studies following systemic administration of Temoporfin incorporated into conventional liposomes based on DPPC. The use of these liposomes provides a good biocompatibility. High performance liquid chromatography (HPLC), in this work considered as the 'gold standard', and fluorescence spectroscopy, both in point-monitoring and imaging mode, are used to assess Temoporfin levels in a subcutaneously implanted HT29 human colon adenocarcinoma model as well as in internal organs in a murine model. By employing these three methods, issues such as possible selectivity at short times following drug administration (2-8 hours) and heterogeneity of the photosensitizer accumulation are addressed. This study adds to the previous work by Pegaz *et al.* (18) the use of longer time intervals after administration and to that by Buchholz *et al.* (19) the monitoring of Temoporfin concentration within internal organs. Furthermore, the possibilities of using non-invasive fluorescence spectroscopy to quantify Temoporfin concentration in exposed tissues are explored. The resulting photosensitizer concentrations are tested for correlation between the three methods employed and we speculate on how to improve the accuracy in absolute fluorescence level as a photosensitizer concentration estimate.

MATERIALS AND METHODS
Photosensitizer. Temoporfin is a dark purple, non-hygroscopic, non-solvated crystalline powder, which is soluble in alcohol/acetone/ethyl acetate and practically insoluble in all aqueous media. The single component is of 98 % purity with a molecular weight of 680.24 and a fluorescence emission peak at 652 nm. In the novel formulation used, Foslip (Biolitec Pharma Ltd, Dublin, Ireland), the hydrophobic mTHPC is bound to the membrane compartment of a phospholipid bilayer. The liposome formulation is based on DPPC, monosaccharide, water and polyoxyethylene polyoxypropylene block copolymers (18). The liposomes were reconstituted and dissolved in 3 ml

of sterile water to give a photosensitizer concentration of 1.5 mg/ml. Further dilution in 5 % aqueous glucose solution provided a photosensitizer concentration of 0.075 mg/ml Foslip. All compounds were stored at 4°C in the dark.

Animal model. The study was performed on adult female athymic NMRI nu/nu mice (Harlan Winkelmann GmbH, Borchen, Germany). All animal experiments were carried out in compliance with the German Animal Protection Act. Six to eight-week old mice, weighing 22-24 g, were inoculated subcutaneously in the left and right hind thigh with a suspension of HT29 human colorectal carcinoma cells (0.1 ml of $8x10^7$ cells/ml in 5 % glucose). Experiments were performed 11 days later, when the tumors had reached a surface diameter of 5-8 mm, and a thickness of 2-4 mm. Mice were injected with 50 µL of Foslip, corresponding to 0.15 mg Temoporfin/kg b.w., into the lateral tail vein. A dose of 50 mg/kg b.w. sodium pentobarbital injected i.p. was used for anaesthesia. Animals were sacrificed at four different time-intervals after injection of Foslip (2, 4, 6 or 8 hours) and samples of plasma, spleen, liver, lung, heart, kidney, skin, muscle and the two tumors were excised for HPLC analysis. Furthermore, spleen, liver, skin, muscle and tumors were also investigated by imaging and point-monitoring fluorescence spectroscopy immediately after animal sacrifice. Both muscle and skin tissues studied were excised from regions just at the tumor periphery. All excised tissue samples were stored in darkness at -80°C until the HPLC analysis. Three animals without Foslip injection were used as controls. The number of samples investigated for each organ, time following photosensitizer administration and method of photosensitizer quantification are listed in Table 1.

Table 1. The number of samples for the time points 2, 4, 6 and 8 hours, respectively.

Organ/Fluid	HPLC	Fluorescence point	Fluorescence imaging
Plasma	[6 3 3 3]	-	-
Spleen	[5† 3 3 3]	[5 3 3 3]	[6 3 3 3]
Liver	[6 3 3 3]	[5 3 3 3]	[6 3 3 3]
Lung	[6 3 3 3]	-	-
Heart	[6 3 3 3]	-	-
Kidney	[6 3 3 3]	-	-
Skin	[6 3 3 3]	[5 3 3 3]	[6 3 3 3]
Tumor	[11 6 6 3]	[11 6 5† 6]	[6 3 3 3]
Muscle	[6 3 3 2†]	[5 3 3 3]	[6 3 3 3]

†: 1 sample identified as outlier

HPLC analysis. All tissue samples were minced by cutting with a scalpel, weighed and freeze dried (freeze drying system Alpha 1-4 LSC, Martin Christ Gefriertrocknungsanlagen GmbH, Osterode, Germany). The resulting powdered tissue was weighed and 10-20 mg was transferred to a 2.0 ml reaction tube after which 1.5 ml of methanol:DMSO (3:5, v:v) was added. The samples were immediately mixed for 3 to 5 s periods using a vortex mixer operating at 2,400 rpm and then incubated at 60°C under continuous shaking for at least 12 hours. All samples were spun at 16,000 g in a centrifuge for five minutes. One ml of the supernatant was transferred to a HPLC vial for subsequent HPLC analysis. The HPLC device had the following specifications; Pump: "System

Gold, 126 Solvent Module" (Beckman Coulter Inc., Fullerton, CA, USA), Autosampler: "Triathlon", Diode Array Detector: "System Gold, Module 168" (Beckman Coulter Inc., Fullerton, CA, USA) and a Fluorescence detector: "RF-10A XL" with interface SS420x (Shimadzu Europa GmbH, Duisburg, Germany). The fluorescence was excited at 410 nm and detected at 653 nm. The separation was carried out on a "LiChroCART 250-4" column (Merck KGaA, Darmstadt, Germany) with Purospher STAR RP-18 endcapped; 5 µm Guard column: "LiChroCART 4-4" with Purospher STAR RP-18e; 5 µm (Merck KGaA, Darmstadt, Germany) Temperature: 30°C. The mobile phase consisted of acetonitrile: H_2O + 0.1 % trifluoroacetic acid (TFA) = 57.5 %: 42.5 % with a flow rate of 1 ml/min. The tissue concentration of Temoporfin, given in ng/mg wet weight, was calculated from a calibration curve constructed by plotting the peak height values of Temoporfin standard solutions versus their concentrations.

Fluorescence imaging system. Fluorescence e*x vivo* measurements using both imaging and point detection were performed on the two tumors, skin, muscle, liver and spleen. For the imaging setup, the light source for fluorescence induction consisted of 12 light emitting CW diodes with peak emission at 405 nm. The beam radius of the spot focused onto the organs was 2.5 cm and the irradiance was approximately 30 µW/cm^2. Fluorescence emitted by the tissue was recorded by a detection unit consisting of a CCD-camera (C4742-80-12AG, Hamamatsu Photonics, Hamamatsu, Japan), a liquid crystal tunable filter having a full-width-half-maximum (FWHM) of 20 nm (LCTF VIS 20-35, Varispec, CRI, Inc., Woburn, CA, USA) and a zoom objective lens (50 mm focal length and f/1.8, Nikon, Tokyo, Japan). The object distance was 23 cm and the field of view of the detection system was 3.2 x 4.2 cm. Room light images at 550 nm and fluorescence images at 500 and 653 nm, corresponding to wavelengths within the tissue autofluorescence and Temoporfin fluorescence bands, respectively, were collected. The exposure time was set to 3 s for each wavelength. All fluorescence images were recorded with dimmed room light to avoid any influence from background light. Background images in the absence of excitation light were also acquired using the same wavelengths and exposure times.

For each fluorescence image, the background was subtracted pixel by pixel and the data were normalized with respect to the exposure time. Each fluorescence image was divided by a fluorescence image at 653 nm from a fluorescence standard (USFS 336020, LabSphere, North Sutton, NH, USA) to account for the non-uniform distribution of the excitation light. In connection to the measurements, the output from a calibrated white-light source was recorded at 500 and 653 nm and all fluorescence images were corrected for the difference in relative detection efficiency between these two fluorescence wavelengths. For each animal and organ, mean and standard deviations of the fluorescence intensity at 500 and 653 nm were calculated within a region of interest (ROI) corresponding to the entire organ as outlined from the room-light images. The Temoporfin concentration within each organ was estimated by calculating a fluorescence contrast ratio, R (23);

$$R = \frac{I_a(653) - k \cdot I_c(653)}{I_a(500)} \qquad (1)$$

where $I_a(653)$ and $I_a(500)$ represent the mean value of the intensities within the ROI at 653 and 500 nm, respectively, for each Temoporfin-injected animal. $I_c(653)$ and $I_c(500)$ refer to tissue autofluorescence at 653 and 500 nm in the absence of mTHPC, assessed as the average fluorescence signals from the control animals. $k = I_a(500) / I_c(500)$, constituting a scaling factor between data from each Temoporfin-injected animal and the mean of the three control animals.

Point-monitoring fluorescence. The Temoporfin concentration was also measured by point-monitoring fluorescence spectroscopy using an instrument described in detail in Ref (24). Briefly, approximately 1 mW at 375 nm was delivered through a 400 µm quartz fiber with a clear cut distal end in contact with the tissue. The induced fluorescence was collected using the same optical fiber and reflected laser light was removed by a dichroic beamsplitter (LWP-45-RS396-TU450-700PW1012UV, CVI Technical Optics LTD, Onchan, UK) and a long pass filter (RG395, Schott AG, Mainz, Germany). The fluorescence signal, $F(\lambda)$, was detected by a spectrometer (USB4000, Ocean Optics, Dunedin, FL, USA) and normalized at 500 nm.
A singular value decomposition (SVD) algorithm was used to fit a set of normalized basis spectra to the data (25), where these basis spectra consisted of the Temoporfin fluorescence signal (26), a fluorescence signal peaking in the blue-green spectral region representing the combined tissue and fiber autofluorescence and assessed as an average of the detected fluorescence signal in each organ of the control animals, and a constant offset representing background in the detection unit. The algorithm was implemented in the software program MATLAB (The MathWorks Inc., Natick, MA, USA). In addition, a 15-term Fourier series was included in the fit to account for the influence of varying blood content on the autofluorescence spectra (25);

$$F(\lambda) = A_{mTHPC} f_{mTHPC}(\lambda) + A_{auto} f_{auto}(\lambda) + A_{offset} + \ldots \left[\omega \sum_{i=1}^{15} \left(B_i \cos\left(\frac{\pi i (\lambda - \lambda_{start})}{\lambda_{end} - \lambda_{start}} \right) + C_i \sin\left(\frac{\pi i (\lambda - \lambda_{start})}{\lambda_{end} - \lambda_{start}} \right) \right) \right], \quad (2)$$

where the A's, B's and C's are the spectral amplitudes resulting from the fit and the $f(\lambda)$'s denote the normalized basis spectra. The spectral fitting range was 500-700 nm but the terms within the square brackets were included only between 500 (λ_{start}) and 640 nm (λ_{end}). The number of components included in the Fourier series was determined by minimizing the error of the fit;

$$E = \left(\sum_i \frac{\left(y_{measured,i} - y_{fit,i} \right)^2}{(n-1)} \right)^{1/2}, \quad (3)$$

where the summation is taken within the fitting range and n denotes the number of data points in this spectral interval. The factor ω, representing the weighting of the Fourier components in relation to the other factors, was not critical for the performance of the algorithm and was arbitrarily set to 1. The SVD algorithm was used to evaluate each of the fluorescence spectra acquired at 1-3 sites in each organ and the Temoporfin concentration was quantified by averaging the resulting A_{mTHPC}.

Statistical analysis: For each organ, the Temoporfin concentration estimate of every sample was compared with the mean value from the 15 animals. If the difference was greater than three standard deviations, the data point was considered to be an outlier and removed from the following analysis. Identified outliers are indicated in Table 1. With an ANOVA-test the null hypothesis, stating that the four time points do not result in different Temoporfin concentrations, was tested for each individual organ. The agreement between the three methods used for assessing the Temoporfin concentration was quantified by studying the correlation of the HPLC data, the fluorescence contrast ratio and the Temoporfin fluorescence spectral amplitude. The hypothesis of no correlation for each organ was tested. For all tests, $P<0.01$ was considered significant.

RESULTS

HPLC results

The Temoporfin concentration as a function of time after injection is shown in Fig. 1. For all organs except the tumors, the error bars indicate the standard deviations arising due to inter-animal variations, whereas for tumor tissue, the error bars also partly reflect intra-animal differences as each animal had two inoculated tumors. For tumor tissue, the Temoporfin levels at 4 (0.16±.024 ng/mg) and 8 (0.18±.064 ng/mg) hours were significantly higher than at 2 (0.08±.026 ng/mg) hours. Within the entire time interval, the average Temoporfin concentration was 0.12 ng/mg, ranging between 0.04-0.25 ng/mg. No difference in photosensitizer concentration was found between left and right tumors. Also, no trace of Temoporfin was found in any of the control animals. According to the ANOVA-test, only within tumor tissue did the photosensitizer concentration display any significant variation with time after injection. In Table 2, the average selectivity of Temoporfin in tumor compared to other organs investigated is listed for the time points investigated. The tumor-to-muscle ratio averaged for each time point is between 5.5 and 8.1 in the time interval of 2-8 hours, with the highest selectivity achieved at 2 hours. The tumor-to-muscle ratio did not change significantly with time and displayed a total average of 6.6. The large variation of tumor-to-muscle selectivity at 8 hours is partly due to the small number of samples. At 2 hours the tumor-to-muscle ratio ranges between 2.8 and 26.5, mostly reflecting a large biological variation at this short time point. A tumor-to-skin selectivity in the order of 2 was observed, which did not vary significantly with time. The Temoporfin selectivity in tumor tissue as compared to the internal organs is low, and exhibits a slight increase for the later time points.

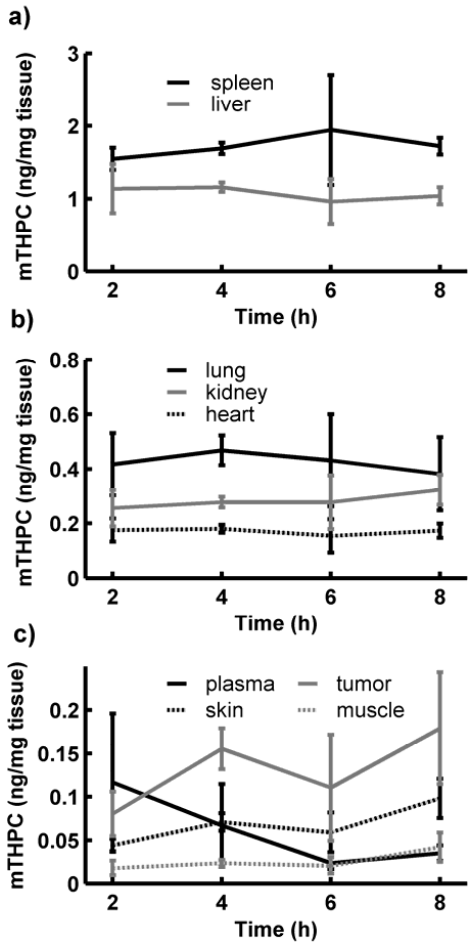

Figure 1.a) - c) Temoporfin concentration as a function of time following injection within organs investigated by HPLC. Error bars represent ±1 standard deviation (SD).

Table 2. Selectivity of Temoporfin analyzed from HPLC data. The average value and standard deviation are given for each time point and organ investigated. A P-value less than 0.01 rejects the hypothesis of time-independent selectivity.

	Tumor/ Spleen	Tumor/ Liver	Tumor/ Lung	Tumor/ Heart	Tumor/ Kidney	Tumor/ Skin	Tumor/ Muscle
2 hour	0.049± 0.016	0.072± 0.017	0.19± 0.054	0.47± 0.10	0.31± 0.058	1.8± 0.47	8.1± 8.1
4 hour	0.092± 0.012	0.13± 0.016	0.33± 0.043	0.86± 0.099	0.56± 0.068	2.2± 0.45	6.6± 0.99
6 hour	0.056± 0.018	0.11± 0.037	0.24± 0.047	0.69± 0.13	0.38± 0.088	1.8± 0.43	5.5± 1.3
8 hour	0.11± 0.048	0.17± 0.036	0.52± 0.21	1.0± 0.34	0.55± 0.090	1.8± 0.28	6.2± 5.4
P-value	<0.01	<0.01	<0.01	<0.01	<0.01	0.24	0.83

Fluorescence measurements

A typical fluorescence spectrum from skin overlying the tumor 8 hours after Foslip injection is shown in Fig. 2a. The tissue autofluorescence, the Temoporfin fluorescence and the total fit including the Fourier components are also shown. For the purposes of clarity, the autofluorescence component is displayed at 50 % of its true value. The fluorescence peak at 635 nm, present only in skin samples, is believed to originate from endogenous porphyrins in the mouse skin. Fig. 2b shows the corresponding fluorescence signal and the fitted fluorescence components from tumor tissue. Figs. 2c and d illustrate the corresponding residuals, ε, calculated as the difference between measured and modeled data, and the error of the fit, calculated according to Eq. (3).

The fluorescence contrast ratio, R, as a function of time after injection is shown in Fig. 3a. For the control animals, the contrast ratio was not significantly different from zero. The heterogeneity in evaluated Temoporfin concentration within an organ was characterized by the relative standard deviation arising when averaging the fluorescence contrast function within each ROI. Data from liver and spleen resulted in relative standard deviations approximately 4 times higher compared to the other organs. The Temoporfin fluorescence amplitude, A_{mTHPC}, resulting from the point-monitoring measurements, as a function of time after injection is shown in Fig. 3b. No peak at 653 nm was present in the spectra from any of the control animals. The average fitting errors, $\hat{E}$, for each organ are also shown. For all tissue types, the fitting errors were small compared to the fluorescence signal amplitude, indicating a good fit. The influence of the Fourier terms on the total fit was typically less than 10 % of the autofluorescence component and their appearance mostly reflected the heterogeneous blood distribution within the tissue. Furthermore, the magnitudes of

Fourier components 11-15 were less than 5 % of the maximum Fourier component, reflecting the smaller importance of the higher order terms in Eq. (2).
The results from the fluorescence methods demonstrate similar time dependence in tumor tissue as the HPLC data, with a significantly lower value of Temoporfin at 2 hours compared to 4 and 8 hours after injection. The order of the magnitudes of the estimated Temoporfin levels in investigated organs is overall similar for the three analysis methods. The average tumor-to-muscle ratios were 3.3±0.92, 3.9±0.93, 3.1±1.1 and 4.0±1.5 for the four time intervals investigated with the fluorescence imaging method and corresponding average tumor-to-skin ratios were 5.4±1.8, 7.5±6.4, 2.9±1.6 and 2.8±0.36. For the point-monitoring method average tumor-to-muscle ratios were 6.1±2.9, 9.5±8.9, 6.4±3.6 and 8.4±5.4 and average tumor-to-skin ratios were 6.3±2.9, 10±5.1, 4.9±3.2 and 6.7±2.1. For both fluorescence methods, the Temoporfin tumor selectivity displayed no time-dependence. The different values of the selectivity are obtained with the fluorescence methods as compared to HPLC. This can be explained by the sensitivity of the optical methods to differences in tissue optical properties. The influence of optical properties in the fluorescence measurements are discussed in a later section.

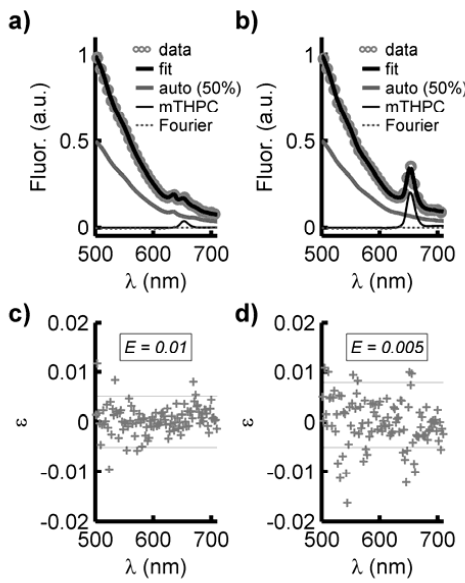

Figure 2. *Ex vivo* a) skin and b) tumor fluorescence spectra, the fit components representing autofluorescence and Temoporfin fluorescence, and the total fit, which also includes the Fourier terms. The autofluorescence component is displayed at 50 % of the true value and only every 30 data points are shown for purposes of clarity. c) and d) illustrate the residuals, ε, corresponding to a and b, respectively. The dashed lines indicate ±2 SD of the residuals and E denotes the fitting error according to Eq. (3). For the residuals, only every ten data points are plotted for purpose of clarity.

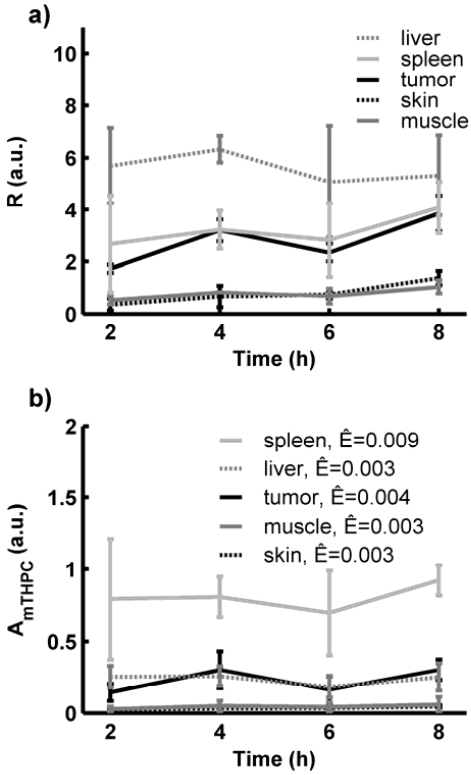

Figure 3.a) The fluorescence contrast ratio, R, as a function of time after injection. b) Point-monitoring Temoporfin fluorescence amplitude, A_{mTHPC}, as a function of time following injection. Also shown are the average fitting errors. Error bars represent ±1 standard deviation.

Correlation of HPLC and fluorescence data

The possibility of using the fluorescence image contrast ratio or the point-monitoring Temoporfin fluorescence amplitude as absolute photosensitizer measures was investigated by studying the correlation between the Temoporfin quantities predicted by each method and the HPLC data, in this study considered 'gold standard'. Table 3 lists the correlation between data from the three methods for the individual organs as well as the P-value for testing the hypothesis of no significant correlation. The obtained correlation values and the magnitudes of the P-values indicate a significant agreement between the three methods for all organs with a few exceptions; poor correlation was noted between optical methods and HPLC for spleen as well as between point-monitoring fluorescence and HPLC for skin. Also, for all organs except spleen and skin, the 95% confidence intervals of the predicted correlation coefficients greatly overlap, indicating no significant difference of the degree of correlation of data from different organs.

Table 3. Correlation between data sets from the three methods used for assessing Temoporfin concentration within five organs. The P-values for testing the hypothesis of no correlation are also given.

	Spleen	Liver	Skin	Tumor	Muscle
HPLC vs fluo. point	0.43 (P=0.15)	0.74 (P<0.01)	0.56 (P=0.04)	0.76 (P<0.01)	0.88 (P<0.01)
HPLC vs fluo. imag	0.53 (P=0.05)	0.85 (P<0.01)	0.70 (P<0.01)	0.87 (P<0.01)	0.78 (P<0.01)
Fluo. imag vs fluo. point	0.67 (P<0.01)	0.78 (P<0.01)	0.75 (P<0.01)	0.63 (P<0.01)	0.70 (P<0.01)

The co-variation between HPLC and fluorescence data for each of the organs investigated by HPLC and both fluorescence spectroscopy methods is illustrated in Figs. 4a-d. The correlation between HPLC and fluorescence data illustrated in Table 3 is also clearly visualized in Figs. 4a-d, while the disjoint data sets underline the necessity of multiple correlation curves to adequately describe the connection between the fluorescence contrast ratio or the fluorescence amplitude and the HPLC data for all organs combined. The varying slope of the correlation curves, shown by the solid lines in Figs. 4a-d, could be partly explained by differences in tissue optical properties. For example, the high blood content in liver and spleen causes a higher overall light absorption and thus a comparatively smaller fluorescence signal. Other factors that influence the slope of the correlation curve, especially for the high Temoporfin concentrations encountered within liver and spleen, include saturation and re-absorption of the Temoporfin fluorescence and the possibly formation of less fluorescent mTHPC aggregates (11). The optically more transparent character of the remaining organs leads to a much steeper slope of the correlation curve in Figs. 4a-d. The co-variation between the two fluorescence methods is shown in Fig. 4e and f. In contrast to Figs. 4a and c, the slopes of the correlation curves in Fig. 4e vary less for the different organs. As the tissue volumes probed by the optical methods show a better overlap than that of HPLC and the fluorescence data are influenced by the tissue optical properties whereas the HPLC result is not, the slope should ideally be identical for all organs. Though, the differences in excitation wavelength and detection geometry lead to slightly different tissue volumes probed by the two fluorescence methods, a fact that might limit the agreement between the optical data sets.

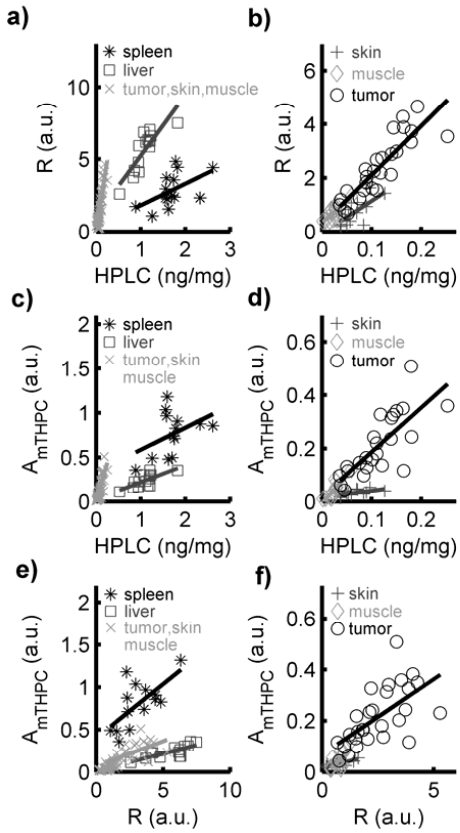

Figure 4. Scatter plots showing the correlation between a) and b) Temoporfin concentrations acquired from HPLC and the fluorescence imaging contrast ratio, R, calculated from Eq. (1). c) and d) illustrate the co-variation between Temoporfin concentrations acquired from HPLC and the Temoporfin fluorescence amplitude, A_{mTHPC}, obtained from point-monitoring fluorescence data. Correspondingly, e) and f) show the covariance of the fluorescence contrast ratio, R, and the Temoporfin fluorescence amplitude, A_{mTHPC}. In all subplots, the markers represent data points from individual animals and the solid lines illustrate correlation curves.

DISCUSSION

By incorporating hydrophobic photosensitizers into liposomes, improved selectivity and more pronounced PDT effect have been observed for PDT agents such as benzoporphyrin derivative monoacid ring A (BPD-MA) (17) and bacteriochlorin a (15) as compared to the original formulation. The compound Temoporfin, also a hydrophobic photosensitizer, is one of the most potent sensitizers (2) in present use. This photosensitizer possesses interesting photophysical

properties, e.g. a strong absorption band in the red wavelength region and a high fluorescence yield, making it desirable to use optical methods in order to study photosensitizer pharmacokinetics and distribution. The ethanol formulation of Temoporfin is associated with prolonged general photosensitivity, limited tumor selective uptake, and aggregation within aqueous media.

Here, we investigated photosensitizer distribution for short times following systemic administration of a liposomal Temoporfin formulation utilizing chemical extraction as well as fluorescence spectroscopy. In the animal tumor model used, athymic NMRI nu/nu mice with implanted HT29 human colon adenocarcinoma, both HPLC and optical methods demonstrated selectivity in Temoporfin accumulation between tumor and muscle and tumor and skin for time intervals of 2 to 8 hours after drug administration.

The tumor-to-muscle and tumor-to-skin selectivity displayed no significant time-dependence. The average tumor-to-muscle ratio observed in the present study indicates an early Temoporfin selectivity that is slightly higher than found following administration of mTHPC dissolved in ethanol, polyethylene glycol (PEG) and water. For example, Westermann *et al.* reported on a selectivity around 3-4 at 2-8 hours after administration of mTHPC dissolved in an ethanol-PEG-water solution in nude mice with a human colon carcinoma model (LS174T) (27). For that study, the selectivity increased slightly for drug-light intervals exceeding 8 hours. Further comparison of our results to those of Westermann *et al.* shows that the average tumor-to-skin selectivity displays slight improvement over the original formulation. Pharmacokinetic studies of liposome-encapsulated BPD-MA (M1 tumors in DBA/2 mice) (17) and SIM01 (28) have also reported on an improved tumor-to-muscle selectivity as compared to administration of the original formulation of the photosensitizer. In agreement with our results, neither of these PDT-agents showed improved tumor-to-skin selectivity when incorporated into liposomes. In contrast to the results published by Westermann *et al.*, no selectivity has been observed between human mesothelioma xenograft and muscle in nude BALB/c mice (29) or only little selectivity within a mammary carcinoma model in C_3D_2/F_1 mice (9) for similar short times after administration of Temoporfin in an ethanol-PEG-water solution. Our results thus indicate an early Temoporfin selectivity that is higher than observed for its original ethanol formulation.

Selective accumulation of liposome-encapsulated photosensitizers has previously been explained by the fact that the liposomes serve as donors of photosensitizer molecules to lipoproteins (13,14). Since proliferating cells show an increased number of low-density lipoprotein (LDL) receptors, the association of the photosensitizer to these proteins has been shown to promote selective accumulation and increased treatment efficiency (14,30,31). Conventional liposomes, such as DPPC used in the present study, are quickly opsonized by plasma proteins. Following this, the liposomes are taken up by phagocytosis and transported to organs with a rich mononuclear phagocyte system, such as liver and spleen (13). This process also affects the bioavailability of the mTHPC molecules, supporting our observation of high Temoporfin concentration within liver, spleen and lung. The association to the mononuclear phagocyte system could perhaps also contribute to the selectivity of Temoporfin in the tumor, as a higher degree of inflammatory cells, such as macrophages, phagocytes and leucocytes, are present in close proximity of the tumor periphery.

The photosensitizer concentration within tumor was significantly higher at 4 and 8 hours than at 2 hours. For the entire time interval, the average Temoporfin level in tumor tissue was 0.12 ng/mg. This can be compared to an observed photosensitizer concentration below approximately 0.04 ng/mg in tumor tissue between 5 min and 6 hours after administration of the original ethanol formulation of Temoporfin at the double photosensitizer dose (29). Our data for tumor tissue are also slightly higher than reported by Westermann *et al.* for similar time points after administration of mTHPC in ethanol, polyethylene glycol and water (27). The Temoporfin levels detected in plasma were relatively low for all time points investigated, resulting in an average concentration of 0.07 ng/mg. Cramers *et al.* reported on Temoporfin levels in plasma ranging between 0.3 and 2 ng/mg for similar time periods following systemic administration of mTHPC in an ethanol-PEG-water solution (29). Within muscle, skin, liver, lung, kidney and heart the Temoporfin levels were in the range previously published (9,27,29). Despite the use of conventional liposomes, which are known to accumulate within organs rich in mononuclear phagocytic cells, the photosensitizer concentration within liver, spleen and lung in the present study was not higher than previously published.

In agreement with our results, a higher bioavailability has previously been noted for other hydrophobic PDT substances incorporated into liposomes (15,17,32). Maximum photosensitizer concentrations within tumor tissue, using photosensitizers incorporated with liposomes, have been shown to peak either at earlier (17), similar (28) or at later (32) time points after administration as compared to the original formulation of the photosensitizer. These differences might be due to the specific liposome and/or photosensitizer used as well as the tumor and animal model. The pharmacokinetic profile of liposome-encapsulated Temoporfin observed in the present study for short times after injection might mostly reflect the fate of the liposomes. Opsonization and association with lipoproteins or phagocytosis of conventional liposomes, such as used in the present study, are rapid processes that lead to a fast transfer of the sensitizer from the vascular compartment. These effects can explain the low photosensitizer levels in plasma and the almost flat pharmacokinetic profiles within the internal organs. Further improvements of tumor selectivity and bioavailability might be possible by prolonging the circulation time of the liposomes, for example by utilizing a pegylated liposomal formulation, also referred to as a stealth liposome (19). Another reason for the delayed concentration maximum within tumor tissue when using ethanol formulations of Temoporfin as compared to liposome-encapsulated Temoporfin could be the formation of photosensitizer aggregates in blood when administering an ethanol photosensitizer formulation. These aggregates need to be disassociated before the photosensitizer molecules can bind to plasma proteins (11,16).

The present study is limited in that photosensitizer distribution and the generalized photosensitivity were only studied up to 8 hours. Within a different animal group, the photosensitizer levels displayed a decrease within the internal organs at 24 hours (unpublished data). These data, which were not merged with the present study due to slightly different experimental procedures, also indicated that the Temoporfin concentration within skin, muscle and tumor did in fact not increase for this later time point. More extensive studies are needed in order to understand the pharmacokinetics of Temoporfin at later time points following systemic administration of this novel liposomal formulation.

In this study, HPLC was considered the 'gold standard' to which the optical methods were compared and the data correlated. As seen in Figs. 4a-d, the extraction and fluorescence data showed a relatively good agreement within individual organs but one could also see that no single correlation curve could adequately fit the HPLC and fluorescence data for all organs. One factor that dramatically influences the overall correlation between the HPLC and fluorescence results is varying optical properties of the tissue under investigation. Optically opaque tissues, such as liver and spleen, result in comparatively lower fluorescence signals than in for example muscle, characterized by a higher albedo. Clearly, this indicates the importance of taking into account the influence of scattering and absorption on the detected fluorescence signal. Several authors have utilized white-light reflectance signal probing the same tissue volume as the fluorescence, to assess the tissue absorption and scattering levels. Based on this information, empirical and theoretical models have been used to solve for the intrinsic tissue fluorescence (33,34). White-light reflectance measurements could thus yield information on how to “unmask” the fluorescence amplitude and possibly improve agreement between extraction and Temoporfin fluorescence level.

Another reason is that the extraction data represent the average Temoporfin concentration within the entire organ, whereas the fluorescence methods probe only the most superficial tissue regions. Furthermore, the differences in excitation wavelength and measurement geometry cause slightly different probing depths for the two optical methods. Any variation in Temoporfin concentration with depth from the exposed tissue surface in combination with varying, tissue-specific optical properties would negatively influence the agreement between the three methods both within and between individual organs. Finally, within aqueous media, the hydrophobic mTHPC molecules are known to form non-fluorescent oligomers. Despite being in monomeric form when incorporated into liposomes, it is possible that the photosensitizer molecules aggregate upon distribution within cells, especially in the case of high concentrations (35). The HPLC results are independent of such aggregation, whereas the fluorescence measurements are not, possibly resulting in the lower slope observed for liver and spleen in Figs. 4a and c.

The liver and spleen are surrounded by a capsule rich in collagen and elastin. For liver, its capsule was cut open and measurements were performed directly on the liver parenchyma, whereas the capsule of the spleen was kept intact during the optical measurements. The combination of differences in photosensitizer concentration between capsule and parenchymal tissue and the shallow probing depth of the fluorescence signals could explain the lack of significant agreement between HPLC and fluorescence data for the spleen. The poor correlation between point-monitoring and extraction data for skin may be explained by the difference in probing depth in combination with the layered skin structure. The measurement geometry (36) and the strong scattering within the epidermis, that mostly consists of dead cells with a low uptake of Temoporfin and high collagen content, limit the probing depth of the 375-nm light used for the point-monitoring fluorescence spectroscopy.

The two fluorescence methods showed similar agreement with the extraction data despite being based on different methods of analysis. Each method has its individual advantages. The fluorescence imaging method performs better within heterogeneous organs as it allows e.g. for spatial averaging of specific areas. The point-monitoring setup yields more detailed spectroscopic information making it possible to separately monitor individual tissue fluorophores, such as tissue autofluorescence and skin porphyrin content. The ultimate system would provide full spectroscopic data in each spatial point of an image plane possibly allowing a precise delineation of tissue types. Future use of more detection bands of the LCTF would develop into such a

system.

In conclusion, we have reported on significant photosensitizer selectivity between tumor and muscle tissue at 2 to 8 hours following systemic administration of Temoporfin incorporated into conventional liposomes. The average tumor-to-muscle selectivity was slightly higher than observed for mTHPC dissolved in ethanol, polyethylene glycol and water (27) and other hydrophobic PDT agents incorporated into liposomes (17) upon investigation at similar times after injection. The tumor-to-muscle selectivity was not significantly dependent on time, whereas the ratio of photosensitizer concentration in tumor to internal organs increased for the later time points. These observations in combination with the overall low photosensitizer concentration within plasma, indicates a rapid photosensitizer distribution process. The biocompatibility of the liposomes, the rapid pharmacokinetics and the early selectivity observed for the liposome-encapsulated Temoporfin are interesting features in trying to limit the drug-light interval used clinically and need further investigation. Furthermore, we have observed that within individual homogeneous organs the Temoporfin fluorescence level, both in imaging and point-monitoring mode, can be used as a reasonable substance concentration estimate. Though, when studying numerous and optically different tissues one needs to take into account the influence of background optical properties on the resulting fluorescence signal.

Acknowledgments-- This work was partly funded by the EC integrated projects BRIGHT.EU FP6-IST-2003-511722 and Molecular Imaging LSHG-CT-2003-503259.

REFERENCES

1. Pass, H. I. (1993) Photodynamic therapy in oncology: mechanisms and clinical use [review]. *J. Natl. Cancer Inst.* **85,** 443-456.

2. Mitra, S. and T. H. Foster (2005) Photophysical parameters, photosensitizer retention and tissue optical properties completely account for the higher photodynamic efficacy of meso-tetra-hydroxyphenyl-chlorin vs Photofrin. *Photochem. Photobiol.* **81,** 849-859.

3. D'Cruz, A. K., M. H. Robinson, and M. A. Biel (2004) mTHPC-mediated photodynamic therapy in patients with advanced, incurable head and neck cancer: a multicenter study of 128 patients. *Head Neck* **26,** 232-240.

4. Moore, C. M., T. R. Nathan, W. R. Lees, A. Freeman, C. A. Mosse, M. Emberton, and S. G. Bown (2004) Photodynamic therapy for primary prostate cancer - A pilot study using MTHPC. *Br. J. Cancer* **91,** S35.

5. Bown, S. G., A. Z. Rogowska, D. E. Whitelaw, W. R. Lees, L. B. Lovat, P. Ripley, L. Jones, P. Wyld, A. Gillams, and A. W. Hatfield (2002) Photodynamic therapy for cancer of the pancreas. *Gut* **50,** 549-557.

6. Triesscheijn, M., M. Ruevekamp, M. Aalders, P. Baas, and F. A. Stewart (2005) Outcome of mTHPC mediated photodynamic therapy is primarily determined by the vascular response. *Photochem. Photobiol.* **81,** 1161-1167.

7. Triesscheijn, M., M. Ruevekamp, N. Antonini, H. Neering, F. A. Stewart, and P. Baas (2006) Optimizing Meso-tetra-hydroxyphenyl-chlorin Mediated Photodynamic Therapy for Basal Cell Carcinoma. *Photochem. Photobiol.* **82,** 1686-1690.

8. Mitra, S., E. Maugain, L. Bolotine, F. Guillemin, and T. H. Foster (2005) Temporally and spatially heterogeneous distribution of mTHPC in a murine tumor observed by two-color confocal fluorescence imaging and spectroscopy in a whole-mount model. *Photochem. Photobiol.* **81,** 1123-1130.

9. Peng, Q., J. Moan, L. W. Ma, and J. M. Nesland (1995) Uptake, localization, and photodynamic effect of meso-tetra(hydroxyphenyl)porphine and its corresponding chlorin in normal and tumor tissues of mice bearing mammary carcinoma. *Cancer Res.* **55,** 2620-2626.

10. Alian, W., S. Andersson-Engels, K. Svanberg, and S. Svanberg (1994) Laser-induced fluorescence studies of *meso*-tetra(hydroxyphenyl)chlorin in malignant and normal tissues in rat. *Br. J. Cancer* **70,** 880-885.

11. Sasnouski, S., V. Zorin, I. Khludeyev, M. A. D'Hallewin, F. Guillemin, and L. Bezdetnaya (2005) Investigation of Foscan interactions with plasma proteins. *Biochim. Biophys. Acta* **1725,** 394-402.

12. Bonnett, R., B. D. Djelal, and A. Nguyen (2001) Physical and chemical studies related to the development of m-THPC (FOSCAN®) for the photodynamic therapy (PDT) of tumours. *J. Porphyrins Phthalocyanines* **5,** 652-661.

13. Derycke, A. S. L. and P. A. M. de Witte (2004) Liposomes for photodynamic therapy. *Adv. Drug. Deliv. Rev.* **56,** 17-30.

14. Konan, Y. N., R. Gurny, and E. Allemann (2002) State of the art in the delivery of photosensitizers for photodynamic therapy. *J. Photochem. Photobiol. B.* **66,** 89-106.

15. Damoiseau, X., H. J. Schuitmaker, J. W. M. Lagerberg, and M. Hoebeke (2001) Increase of the photosensitizing efficiency of the Bacteriochlorin a by liposome-incorporation. *J. Photochem. Photobiol. B* **60,** 50-60.

16. Hopkinson, H. J., D. I. Vernon, and S. B. Brown (1999) Identification and partial characterization of an unusual distribution of the photosensitizer meta-tetrahydroxyphenyl chlorin (temoporfin) in human plasma. *Photochem. Photobiol.* **69,** 482-488.

17. Richter, A. M. (1993) Liposomal delivery of a photosensitizer, benzoporphyrin derivative monoacid ring A (BPD), to tumor tissue in a mouse tumor model. *Photochem. Photobiol.* **57,** 1000-1006.

18. Pegaz, B., E. Debefve, J. P. Ballini, G. Wagnieres, S. Spaniol, V. Albrecht, D. V. Scheglmann, N. E. Nifantiev, H. van den Bergh, and Y. N. Konan-Kouakou (2006) Photothrombic activity of m-THPC-loaded liposomal formulations: Pre-clinical assessment on chick chorioallantoic membrane model. *Eur. J. Pharm. Sci.* **28,** 134-140.

19. Buchholz, J., B. Kaser-Hotz, T. Khan, C. R. Bleyl, K. Melzer, R. A. Schwendener, M. Roos, and H. Walt (2005) Optimizing photodynamic therapy: In vivo pharmacokinetics of liposomal meta-(tetrahydroxyphenyl)chlorin in feline squamous cell carcinoma. *Clin. Cancer Res.* **11,** 7538-7544.

20. Ramanujam, N. (2000) Fluorescence spectroscopy of neoplastic and non-neoplastic tissues. *Neoplasia* **2,** 89-117.

21. af Klinteberg, C., M. Andreasson, O. Sandström, S. Andersson-Engels, and S. Svanberg (2005) Compact medical fluorosensor for minimally invasive tissue characterisation. *Rev. Sci. Instrum.* **76,** 034303-034306.

22. Andersson-Engels, S., J. Johansson, and S. Svanberg (1994) Medical diagnostic system based on simultaneous multispectral fluorescence imaging. *Appl. Opt.* **33,** 8022-8029.

23. Andersson-Engels, S., J. Ankerst, S. Montán, K. Svanberg, and S. Svanberg (1988) Aspects of tumour demarcation in rats by means of laser-induced fluorescence and hematoporphyrin derivatives. *Lasers Med. Sci.* **3,** 239-248.

24. Gustafsson, U., S. Pålsson, and S. Svanberg (2000) Compact fibre-optic fluorosensor using a continuous wave violet diode laser and an integrated spectrometer. *Rev. Sci. Instrum.* **71,** 3004-3006.

25. Finlay, J. C., S. Mitra, and T. H. Foster (2002) In vivo mTHPC photobleaching in normal rat skin exhibits unique irradiance-dependent features. *Photochem. Photobiol.* **75,** 282-288.

26. Angotti, M. (2001) Etude par spectrometrie de masse des photoreactions laser de sensibilisants colores utilises en therapie photodynamique (PDT). Thesis. University Paul Verlaine, Metz, France.

27. Westerman, P., T. Glanzmann, S. Andrejevic, D. R. Braichotte, M. Forrer, G. A. Wagnieres, P. Monnier, B. H. van den, J. P. Mach, and S. Folli (1998) Long circulating half-life and high tumor selectivity of the photosensitizer meta-tetrahydroxyphenylchlorin conjugated to polyethylene glycol in nude mice grafted with a human colon carcinoma. *Int. J. Cancer* **76,** 842-850.

28. Bourre, L., S. Thibaut, M. Fimiani, Y. Ferrand, G. Simonneaux, and T. Patrice (2003) In vivo photosensitizing efficency of a diphenylchlorin sensitizer: interest of a DMPC liposome formulation. *Pharmacol. Res.* **47,** 253-261.

29. Cramers, P., M. Ruevekamp, H. Oppelaar, O. Dalesio, P. Baas, and F. A. Stewart (2003) Foscan® uptake and tissue distribution in relation to photodynamic efficacy. *Br. J. Cancer* **88,** 283-290.

30. Allison, B. A., E. Waterfield, A. M. Richter, and J. G. Levy (1991) The effects of plasma lipoproteins on *in vitro* tumor cell killing and *in vivo* tumor photosensitization with benzoporphyrin derivative. *Photochem. Photobiol.* **54,** 709-715.

31. Jori, G. and E. Reddi (1993) The role of lipoproteins in the delivery of tumour-targeting photosensitisers. *Int. J. Biochem.* **25,** 1369-1375.

32. Wang, Z. J., Y. Y. He, C. G. Huang, J. S. Huang, Y. C. Huang, J. Y. An, Y. Gu, and L. J. Jiang (1999) Pharmacokinetics, tissue distribution and photodynamic therapy efficacy of liposomal-delivered hypocrellin A, a potential photosensitizer for tumor therapy. *Photochem. Photobiol.* **70,** 773-780.

33. Finlay, J. C. and T. H. Foster (2005) Recovery of hemoglobin oxygen saturation and intrinsic fluorescence with a forward-adjoint model. *Appl. Opt.* **44,** 1917-1933.

34. Muller, M. G., I. Georgakoudi, Q. Zhang, J. Wu, and M. S. Feld (2001) Intrinsic fluorescence spectroscopy in turbid media: disentangling effects of scattering and absorption. *Appl. Opt.* **40,** 4633-4646.

35. Sasnouski, S. (2006) Aggregation state and phototoxicity of Foscan in MCF-7 cells. Thesis. University Henri Poincaré, Nancy, France.

36. Pfefer, T. J., L. S. Matchette, and R. Drezek (2004) Influence of illumination-collection geometry on fluorescence spectroscopy in multilayer tissue. *Med. Biol. Eng. Comput.* **42,** 669-673.

Paper IV

Clinical system for interstitial photodynamic therapy with combined on-line dosimetry measurements

M. Soto Thompson, A. Johansson, T. Johansson,
S. Andersson-Engels, S. Svanberg, N. Bendsoe, K. Svanberg.

Applied Optics **44(19)**, 4023-4031 (2005).

Clinical system for interstitial photodynamic therapy with combined on-line dosimetry measurements

Marcelo Soto Thompson, Ann Johansson, Thomas Johansson, Stefan Andersson-Engels, Sune Svanberg, Niels Bendsoe, and Katarina Svanberg

A system for interstitial photodynamic therapy with δ-aminolaevulinic acid and multiple optical fibers has been developed. The system enables photodynamic treatment of large embedded tumor volumes and utilizes real-time measurements to allow on-line dosimetry. Important parameters such as light fluence rate, sensitizer fluorescence intensity, and changes in local blood oxygen saturation are measured with the same fibers that deliver the therapeutic light. Data from the first clinical treatments on nodular basal cell carcinomas indicate a major treatment-induced light absorption increase, rapid sensitizer photobleaching, and a relatively constant global tissue oxygen saturation level during the treatment.

OCIS codes: 170.5180, 120.389, 170.6510, 170.1460.

1. Introduction

As malignant diseases continue to plague humanity, much effort is put into trying to develop new and better treatment modalities. One such method is photodynamic therapy (PDT).[1–3] PDT relies on the application of a photosensitizer (or its precursor) followed by the activation of the photosensitizer with light. The activated sensitizer will react with the oxygen present in the tissue forming highly toxic radicals and will induce tissue necrosis or apoptosis. Since most photosensitizers will accumulate to a higher extent in malignant tissue than in healthy tissue, the treatment targets the malignancies while sparing the surrounding healthy tissue. The introduction of δ-aminolaevulinic acid (ALA) as a sensitizer precursor, inducing protoporphyrin IX (PpIX) as a sensitizing agent, has led to a substantial increase in the clinical acceptance of the method, especially for some types of skin lesion where ALA PDT now can be considered the treatment of choice.[4–9]

Use of PDT is usually considered to be limited to thin (<3 mm) superficial lesions or lesions accessible through body cavities. Thus, in an effort to extend the possible indications for PDT, we present a system for interstitial PDT (IPDT), where thick or embedded tumors are treated using optical fibers inserted into the tumor. IPDT has been pursued for many indications, for example, prostate,[10] liver,[11] and pancreatic cancer[12]; and in this clinical or preclinical work it has been stated that the main drawbacks of the method as applied today are the limited light penetration and the lack of a more precise light dosimetry. A special aspect of the work performed in our group is to use the optical fibers not only to deliver the therapeutic light but also to perform optical measurements to assess parameters of therapeutic interest and to monitor the treatment progression. Examples of such parameters are tissue oxygenation, light fluence rate, and sensitizer fluorescence. The basic concept has been previously described in more detail elsewhere[13] and is schematically shown in Fig. 1. The development of this concept has been pursued in incremental steps[14,15] with promising experimental[16] and clinical results.[17]

In the previous system[14] it was possible to measure the therapeutic light flux in the lesion but the system

When this research was performed, M. Soto Thompson (marcelo@fysik.lth.se), A. Johansson, T. Johansson, S. Andersson-Engels, and S. Svanberg were with the Department of Physics, Lund Institute of Technology, P.O. Box 118, SE-221 00 Lund, Sweden. T. Johansson is now with SpectraCare AB, Ideon Research Park, Ole Römers väg 16, SE-223 70 Lund, Sweden. N. Bendsoe is with the Department of Dermatology and Venereology, Lund University Hospital, SE-221 85 Lund, Sweden, and the Lund University Medical Center Laser Centre, P.O. Box 118, SE-221 00 Lund, Sweden. K. Svanberg is with the Department of Oncology, Lund University Hospital, SE-221 85 Lund, Sweden, and the Lund University Medical Laser Centre, P.O. Box 118, SE-221 00 Lund, Sweden.

Received 20 July 2004; revised manuscript received 14 February 2005; accepted 20 February 2005.
0003-6935/05/194023-09$15.00/0

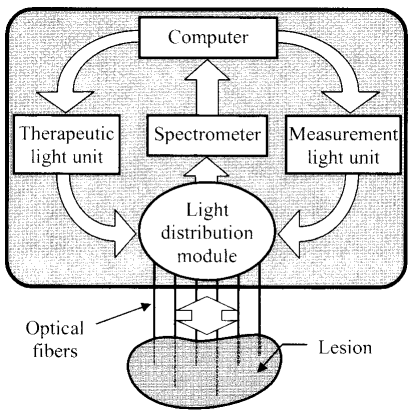

Fig. 1. Schematic diagram of an interactive system for IPDT.

construction did not allow the measurements of other parameters. The sensitizer fluorescence was in that case assessed by using a separate fluorosensor[18,19] with a separate measurement fiber. The novel approach[20] reported in the present paper enables us to perform light flux as well as sensitizer fluorescence and oxygenation monitoring through the same fibers that deliver the therapeutic light.

In Section 2 the construction of the new interactive system is described, followed by a presentation of the implementation of the dosimetry calculations and the measurements of therapeutic interest. Finally, results from the first clinical application of the new system are presented, and future development toward a fully interactive system for IPDT is discussed.

2. System Description

A. Hardware Overview

The equipment is controlled by a laptop computer with a custom-made program based on LabVIEW (National Instruments, Austin, Texas). As shown in Fig. 1, the central part of the system consists of a light distribution module that determines whether the system is running in therapeutic mode or measurement mode. The system (except the computer) is enclosed in a clinically compatible case measuring 30 cm × 43 cm × 21 cm (length × width × height) and weighing 12 kg (see Fig. 2).

The light distribution module consists of two metal disks positioned at close proximity on a common axis (see Fig. 3). One of the disks can be rotated on the axis and has six fiber ports hexagonally placed at a fixed distance from the axis. These fiber ports have connectors where the patient fibers are attached. The fixed disk has a similar set of fiber ports, with the therapeutic light sources attached, facing the ports on the turnable disk. During the therapeutic mode, the light from the fiber-coupled light sources can be directly transmitted through the light distribution module into the patient fibers in a highly efficient

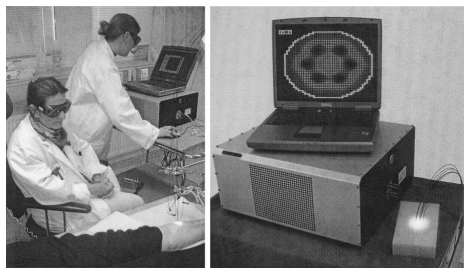

Fig. 2. System as seen in a clinical treatment situation and system overview during calibration.

way. The maximum therapeutic output power distributed on the six patient fibers is approximately 1.2 W. These fibers have a core diameter of 400 μm, a numerical aperture of 0.22, and an outer diameter of 0.88 mm. Before each treatment session, the patient fibers are calibrated to emit equal output powers while in therapeutic mode.

For the measurement mode the turnable disk is rotated 30 deg. The fiber ports on the turnable disk now face another similar set of fiber ports on the fixed disk. Now the light distribution module serially couples one of up to three measurement light sources (in our case two) into one of the patient fibers, as shown in Fig. 4. These light sources are selected with a coupling unit that can be of a similar construction as the main light distribution module. The two light sources used are a diode laser at 635 nm and a light-emitting diode covering the wavelength interval from 750 to 800 nm. The third light source (not implemented) might, for example, be a violet diode laser emitting light at 405 nm to monitor the PpIX fluorescence before the therapeutic irradiation starts, which would enable the possibility to interactively insert the fibers where the PpIX concentration is the highest. The mechanism behind the light distribution modules is stable enough to allow for accurate repositioning, which means that the output power in each of the six patient fibers while in diagnostic mode is

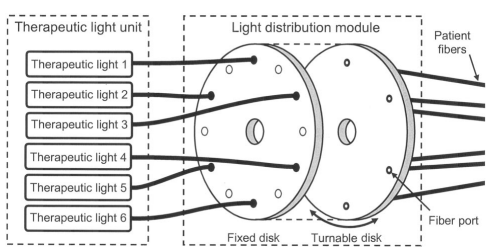

Fig. 3. Interactive IPDT system shown in the treatment mode. The disks in the light distribution module are placed in close proximity (here drawn apart) to each other on a common axis (not shown). The therapeutic light is coupled through the disks into the patient fibers. The components used in the measurement mode were omitted for clarity.

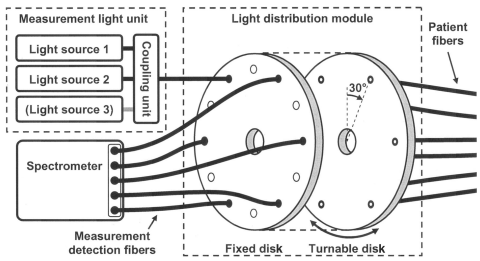

Fig. 4. Interactive IPDT system shown in the measurement mode, assessed by rotating the turnable light distributor disk 30 deg with respect to the disk position for treatment. Nonactive measurement light sources are shown in gray. The active light source is coupled into one patient fiber while the other five patient fibers collect the tissue response back into the spectrometer. By rotating the turnable disk in steps of 60 deg, all patient fibers can be made to act as transmitters for the individual light sources. The therapeutic components were omitted for clarity.

similar (±10%). The measurement light interacts with the tissue and is collected by the other five patient fibers. This light is guided back through the light distribution module that now redirects the light, by way of the measurement detection fibers, onto the entrance slit of an imaging spectrometer. The detection fibers are aligned linearly along the entrance slit of the spectrometer, and the collected light can therefore be resolved as five individual signals for each light source. After collecting a signal with sufficient signal-to-noise ratio from each light source, the light distribution module shifts the transmitting measurement fiber to each and every one of the patient fibers. The resulting number of data sets for every measurement session is 60 (2 light sources × 5 detection fibers × 6 excitation fibers). One full measurement session lasts for approximately 45 s.

B. Dosimetry Calculations

The fluence rate $\phi(\mathbf{r})$ in the treatment volume is determined by solving the steady-state diffusion equation[21]:

$$\nabla^2\phi(\mathbf{r}) - \mu_{\text{eff}}{}^2\phi(\mathbf{r}) = \sum_i S(\mathbf{r}_i), \tag{1}$$

where $\mu_{\text{eff}} = [3\mu_a(\mu_a + \mu_s')]^{1/2}$; here μ_a and μ_s' are the effective attenuation, absorption, and reduced scattering coefficients (see Table 1).[22] The source term $\Sigma S(\mathbf{r}_i)$ is modeled as isotropic point sources, denoted by the index i. In the case of superficial lesions, the extrapolated boundary condition is used to solve Eq. (1).[23] A commercial program (FEMLAB, Comsol, Sweden) is used to model the fluence rate distribution with the finite-element method. The tumor geometries are approximated with either ellipsoids or flat cylinders with an elliptical cross section. To give a fluence rate distribution within the tumor that is as homogeneous as possible, while sparing normal surrounding tissue, the fibers are placed in either one or two planes depending on the tumor thickness and at a distance from the tumor center of approximately 7/10 of the tumor radius. This distance has been determined by maximizing the fluence rate, as given by the analytical solution of the diffusion equation in an infinite homogeneous medium, at the boundary of an ellipsoid. On the basis of the fluence rate distribution, the absorbed dose throughout the tumor volume is calculated. With a threshold (15 J/cm^{-3}) for the absorbed light dose considered sufficient to induce cell necrosis, an estimate of the necessary treatment time is calculated.[14] This prediction is dependent on fiber positions, tissue optical properties, and choice of threshold for the absorbed light dose.

Table 1. Optical Parameters of Normal Tissue and Tumor Used

Tissue Type	μ_a (cm^{-1})	μ_s' (cm^{-1})
Normal	0.16	12.0
Tumor	0.31	12.4

C. Treatment Monitoring Measurements

As described above, the treatment is repeatedly interrupted to perform measurements to monitor the treatment. First, the fluence rate at 635 nm of the light emitted by each fiber is measured at the tip of all the other fibers. This measurement monitors the transmittance of the tissue during the treatment. Drastic changes in light transmission as a consequence of, e.g., blood coagulation or bleeding at the fiber tips can then be detected and an insufficient treatment may thus be prevented. The measurements make it also possible to compensate for treatment-induced variations in light transmission. Second, the sensitizer fluorescence at 705 nm induced by the measurement light source at 635 nm and its characteristic photobleaching are monitored during the treatment.[24] The final parameter measured is the oxygen saturation level S_{O_2} defined as

$$S_{O_2} = \frac{[HbO_2]}{[Hb] + [HbO_2]}, \tag{2}$$

with $[HbO_2]$ and [Hb] denoting the oxyhemoglobin and deoxyhemoglobin concentrations, respectively. Assuming that hemoglobin is the main absorbing tissue constituent, the absorption coefficients at 760 and 800 nm can be written as[25]

$$\mu_a^{760} \propto \varepsilon_{Hb}^{760}[Hb] + \varepsilon_{HbO_2}^{760}[HbO_2],$$

$$\mu_a^{800} \propto \varepsilon_{Hb}^{800}[Hb] + \varepsilon_{HbO_2}^{800}[HbO_2], \tag{3}$$

where ε_i^X is the extinction coefficient of species i at wavelength X. By utilizing Eqs. (2) and (3), the oxygen saturation can eventually be expressed as

$$S_{O_2} = \frac{1}{\varepsilon_{Hb}^{760} - \varepsilon_{HbO_2}^{760}} \left(\varepsilon_{Hb}^{760} - \varepsilon^{800} \frac{\mu_a^{760}}{\mu_a^{800}} \right), \quad (4)$$

utilizing that the extinction coefficients of Hb and HbO_2 are equal at the isobestic point at 800 nm.[25] Using the second diagnostic light source, the overall absorption can be monitored in the spectral interval between 750 and 800 nm. The fluence rate from the source fiber is approximated by the analytical solution to Eq. (1) for a point source in an infinite medium:

$$\phi(r) = \frac{P\mu_{eff}^{\ 2}}{4\pi\mu_a r} \exp(-\mu_{eff} r), \quad (5)$$

where P is the power irradiated by the source fiber. By measuring the fluence rate with several detection fibers at different distances from the source fiber and fitting a curve to the measured values, μ_{eff} can be extracted both for 760 and 800 nm. Finally, by forming the ratio

$$\left(\frac{\mu_{eff}^{760}}{\mu_{eff}^{800}} \right)^2 = \frac{\mu_a^{760}(\mu_a^{760} + \mu_s'^{760})}{\mu_a^{800}(\mu_a^{800} + \mu_s'^{800})} \approx \frac{\mu_s'^{760}}{\mu_s'^{800}} \frac{\mu_a^{760}}{\mu_a^{800}}, \quad (6)$$

and inserting this into Eq. (4) we can calculate the oxygen saturation level. The last step in Eq. (6) is valid under the assumption that the reduced scattering coefficient is much larger than the absorption coefficient. The ratio of the reduced scattering coefficients can be calculated by assuming the following wavelength dependence of the tissue scattering[26]:

$$\mu_s' \propto \lambda^{-1.11}. \quad (7)$$

On the basis of the result of the latter measurement, a fractionized irradiation might be necessary to allow for an increased oxygen inflow to the treated region. The oxygenation data evaluation method is similar to the method used for a commercial product by Hamamatsu, C7473-36, in the sense that they both explore the absorption imprint of hemoglobin on the transmitted signal.

3. Patients

A total of ten treatments in eight patients were performed. The patients treated had histopathologically verified nodular basal cell carcinomas and were referred to the oncology clinic at the Lund University Hospital, Lund, Sweden. The clinical motivation of the study was to reduce the tumor volume prior to surgery or other conventional treatment. The study was performed with approval of the local ethics committee. At the time of treatment the tumor geometry was determined visually and by palpation by an experienced oncologist. The lesion was photosensitized by mixing ALA (MEDAC GmbH, Hamburg, Germany) into an oil-in-water emulsion (Essex Cream, Schering Corp., Kenilworth, New Jersey) to a concentration by weight of 20%, which was applied to the lesion 4–6 h before the therapeutic irradiation. The lesion was prepared according to clinical praxis by disinfecting the treatment area and subsequently administering Xylocain (AstraZeneca, Södertälje, Sweden) subcutaneously as anaesthetics. The sterilized fibers were inserted and subsequently fixed in a holder that in turn was attached to the patient stretcher.

4. Results

To show the capability of the instrument to measure parameters of therapeutic importance, typical data from an 80-year-old patient with a basil cell carcinoma are presented as a case study. The geometry of the lesion was found to be approximately cylindrical with a diameter of 14 mm and a depth of 3 mm. An output power of 75 mW for each of the six patient fibers resulted in an initial estimated treatment time of 400 s.

A. Light Fluence

In Fig. 5 the fluence rates at 635 nm as measured during the treatment are shown. To clearly resolve changes in the light transmission despite the different magnitudes of the detected signals from the various fibers, all signals were normalized to their respective initial value. In Fig. 5(a) treatment fiber 1 acts as the light transmitter and fibers 2–6 serve as detectors. In Figs. 5(b)–5(f) the light transmitter is fibers 2–6, respectively.

It can be seen that the light transmission between the fibers decreases during the treatment, and a similar trend was established during all but two treatment sessions. In some cases this transmission decrease is much more pronounced, as can be seen in fiber 3 in Fig. 5(f). This fiber was characterized by a significantly lowered transmission as compared with the other fibers during the entire treatment, although the magnitudes of the detected and transmitted signals were not significantly lower than the other transmission signals. This decrease could possibly be explained by either some local inhomogeneity, for example, a blood vessel, or that the distance between this fiber to the others was much larger than the distance between the other fibers. Hemorrhage at the fiber tip was not believed to cause this particular transmission decrease since blood pooling would have significantly decreased the magnitude of the transmission signal.

The six treatment lasers were turned off after 400 s at the predicted treatment time; however, the fluence rate, sensitizer fluorescence, and oxygenation measurements were carried out for another 320 s. According to, e.g., Fig. 5(b), some regions show a slight reversal of the treatment-induced absorption increase after the therapeutic irradiation has ended.

Assuming that the transmission changes are due to changes in tissue optical properties, the degree of transmission decrease depends on the interfiber distances. This is also reflected in Figs. 5(a)–5(f) where signals between fibers with the largest separations

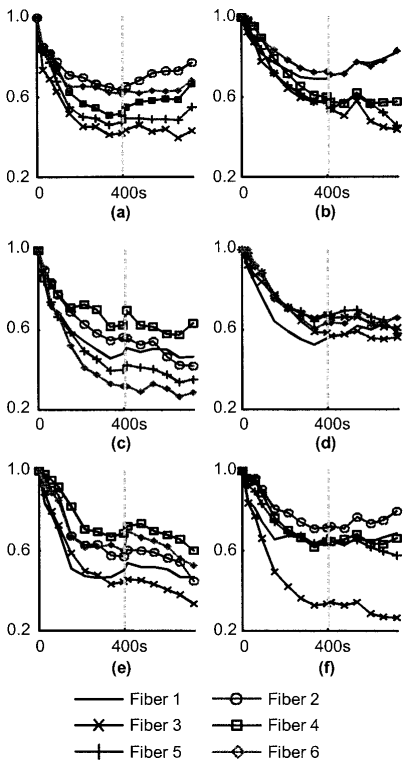

Fig. 5. Fluence rate at 635 nm as measured during the treatment. The time interval between measurement sequences was 30 s for the first 90 s of treatment; thereafter measurements were performed every minute up to an effective treatment time of 720 s. The end of the therapeutic irradiation is indicated by the dashed line.

show a more marked transmission decrease. If only including neighboring fibers, positioned in such a way that the interfiber distances are equal, the average transmission decrease was found to be 39% for this particular patient. A significant transmission decrease was found in seven of nine treatment sessions, where the significance was tested using a one-sided Student's t-test ($P < 0.02$). The average transmission decrease was 24% when taking into account data from nine treatment sessions, although an average decrease of 60% was found during one treatment session. Data from one of the treatment sessions were excluded from the analysis since the optical fibers lost their positions when the patient started coughing.

B. Sensitizer Fluorescence

The sensitizer fluorescence, induced with 635 nm light, measured at 705 nm as a function of the treatment time is shown in Fig. 6. The detected signals measured in each and every fiber were individually normalized to their respective initial value. Figure 6 shows the average of these normalized signals between neighboring fibers with the error bars denoting standard deviations (SDs). The reason for including only the fluorescence signal as measured in between nearby fibers is to obtain a photobleaching curve that is not influenced by the varying fiber separations. Note that the absorption increase as seen in Subsection 4.A was not compensated for when we plotted this average fluorescence signal.

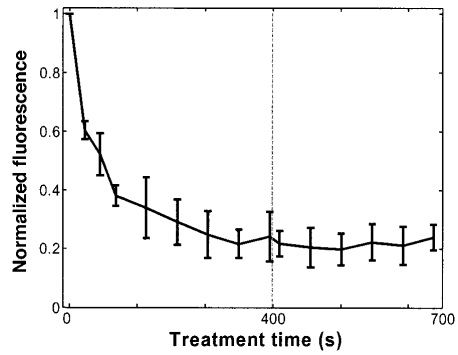

Fig. 6. Average of the normalized sensitizer fluorescence signal (±SD) at 705 nm during treatment. The therapeutic irradiation was turned off after 400 s, indicated by the dashed line.

The fluorescence level decreased to 22% of the initial signal for this particular treatment session, as compared with an average decrease to 15% of the initial level for the nine completed treatments.

C. Tissue Oxygenation

The final parameter monitored during the treatment is the local tissue oxygenation, and the average oxygen saturation level (±SD) during the treatment session is shown in Fig. 7. The vertical dashed line at 400 s indicates the time point when the therapeutic

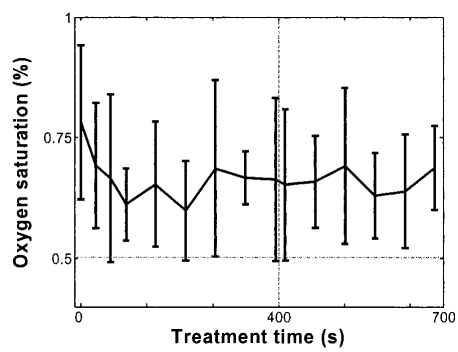

Fig. 7. Tissue oxygenation (±SD) as a function of the treatment time as measured during one treatment. The therapeutic irradiation was turned off after 400 s, indicated by the vertical dashed line. The horizontal dashed line indicates the 50% tissue oxygen saturation level.

irradiation was turned off, whereas the horizontal dashed line marks the 50% oxygen saturation level.

Data from all treatment sessions show that the average initial oxygen saturation level was 77% and no significant changes could be observed, apart from an indication of a small initial fast reduction, during the treatments. The significance level was tested using a Student's t-test at significance level $P = 0.01$. Lesions located in the face displayed slightly higher oxygenation levels than those located on the lower extremities, although these differences were not significant.

5. Discussion

PDT relies on the presence of three components: light, sensitizer, and oxygen; and in this study much effort has been put into monitoring these parameters in parallel to the treatment session to supervise and hopefully in the future be able to control the treatment progression. Here we describe the implementation of a system for IPDT using up to six treatment fibers for light delivery. The same fibers can be used for real-time monitoring of the fluence rate, the sensitizer fluorescence, and the tissue oxygenation allowing for on-line treatment supervision. In addition, by the monitoring of these parameters, possible correlations can be studied, which might add useful knowledge in the field of cancer treatment by means of PDT. One example of such a correlation is the higher rate of initial PpIX photobleaching in well-oxygenated tissue regions, a process that supports the idea of an oxygen dependence of the sensitizer bleaching.[27] Since a stable oxygen supply promotes an effective PDT treatment, other groups have proposed monitoring of the sensitizer fluorescence as a possible real-time treatment feedback.[24] Soumya and Foster have shown a 3- to 15-fold increase in light penetration at 630 nm when comparing a hypoxic to a well-oxygenated tissue phantom containing human erythrocytes, an effect that is explained by the stronger absorption of deoxyhemoglobin as compared to oxyhemoglobin at 630 nm.[28] This result implies that there is a strong connection between oxygen saturation level and tissue transmission. Conversely, a high fluence rate leads to oxygen depletion,[29] which in turn affects the photobleaching rate.

Addressing the fluence rate measurement, a significant absorption increase was found in seven of nine treatment sessions. Other groups have also reported on treatment-induced light transmission decrease in tissue during PDT. Chen *et al.* have observed 40%–80% reduction in fluence rate in normal canine prostate and give alterations of the local blood flow and perfusion as possible explanations.[30] Using an integrating sphere measurement setup, Nilsson *et al.* found a 60%–100% increase in the absorption coefficient after PDT of normal rat muscle sensitized with ALA-induced PpIX.[31] These authors argue that the increase in tissue absorption is due to damage to the tissue microcirculation. Other explanations include local hyperthermia, bleeding at the fiber tips,[32] and tissue deoxygenation as a consequence of the oxygen consumption by the photodynamical reaction.[28] Further evaluation of our data indicates that the light transmission changes are in fact due to tissue deoxygenation and changes in blood volume, and these results will be part of a future publication.[33]

The PDT-induced absorption increase causes the delivered light dose at the end of the treatment to fall below the calculated threshold dose and therefore prevents the peripheral tumor regions from being fully treated. On the basis of the dosimetric measurement, an interactive treatment could easily be implemented by prolonging the treatment time or increasing the fiber output power to compensate for the decreased light penetration. It should also be mentioned that, although the observed transmission decrease is present in all but two patients treated so far, the degree of transmission decrease varies on an interpatient basis. It is therefore necessary to monitor these changes during each individual treatment session and adjust the treatment parameters according to the measurement results.

Monitoring the sensitizer photobleaching is of course essential, since according to Robinson *et al.*[27] and Boere *et al.*[34] a strong correlation exists between the initial sensitizer photobleaching rate and the treatment outcome. This signal could be of importance for early-stage treatment feedback, but exactly how the treatment should be modified as a result of this information has to be studied in more detail. One should note that our indirect method of monitoring the tissue oxygen saturation assumes that there is a connection between the concentration of free oxygen molecules and the oxygenation level of the tissue.[35]

Results from all treatment sessions show no significant variations in tissue oxygen saturation, although a small initial decrease in oxygenation could be observed in all patients. The evaluation method of the near-infrared spectra is based on determining the effective absorption coefficient by means of spatially resolved spectroscopy and therefore relies on signals measured between all possible fiber combinations. This means that the light transmission is measured across the entire tumor geometry, which involves large source–detector separations and the signals can therefore be used only for determination of the global tissue oxygen saturation. Oxygen depletion is a local process and initially occurs close to the fiber tip, where the fluence rate is highest. Curnow *et al.*[36] and Woodhams *et al.*[37] have shown that, close to the source fiber, the photodynamic reaction induces a dramatic decrease of the oxygen saturation as measured either by means of tissue oxygen pressure (p_{O_2}) or visible light spectroscopy. When increasing the source–detector separation, this effect was less obvious and no changes were observable for source–detector separations of 3 mm or larger for continuous irradiation at 100 mW. Comparing continuous with fractionated irradiation, a significant decrease in oxygen saturation level was found only where the detection point fell within the area of necrosis. The authors speculate whether the light delivery conditions can be optimized based on real-time oxygen

monitoring, leading to improved treatment outcome. The herein proposed global method of data evaluation might explain the lack of significant changes in measured tissue oxygen saturation since data evaluation is based on source–detector separations of 5–8 mm. Possibly, the treatment time or fiber output power was not sufficient to induce necrosis in the entire interfiber volume. Furthermore, the large source–detector separation makes the method sensitive to tissue inhomogeneities. Data evaluation based on single fiber pairs gives a more local measure of the tissue oxygen saturation and will be part of a future publication.[33] The oxygen saturation level reported here, which might be described as an average over the entire tumor volume, is in agreement with oxygenation baseline levels reported on by others.[26] The lower limit for the tissue oxygenation for an effective treatment is an issue that has been debated in both PDT and radiotherapy.[7,38] Using the instrument reported here, this will be a question that we will address in future work.

The calculation of the tissue oxygenation level as well as the derivation of changes in tissue optical properties that are consistent with the light transmission changes depend on the exact positioning of the fibers. Knowledge of the exact fiber positions would avoid this source of error and make the data evaluation more stable. Ultrasound monitoring has a high enough spatial resolution to detect the optical fiber tips, and this mode of guiding and determining the fiber positions is already in use in IPDT of the prostate.[39,40] Ultrasound guidance during fiber insertion is therefore an attractive possibility for future treatment sessions.

The evaluation of the oxygen saturation signal assumes that deoxyhemoglobin and oxyhemoglobin are the only tissue constituents whose absorption might change during the treatment session. The observed absorption increase might be influenced by concentration changes of other tissue chromophores, such as water resulting from treatment-induced oedema.

The oxygen saturation signal can be used to monitor the possible need of a fractionated irradiation. Because of the introduction of the measurement sequences that interrupt the therapeutic irradiation, some irradiation fractionation with dark intervals of 45 s is already implemented. Fractionated irradiation enables some reperfusion of the treatment volume and has been shown to increase treatment response.[41] Therefore these signals are important for improvement of the treatment outcome. Future work includes implementing such therapeutic feedback based on real-time data analysis of the monitoring measurements to make the treatment truly interactive. Transmission changes, which might affect the tissue volume being treated, can easily be followed and compensated for by changing treatment time or fiber output power. When six patient fibers are used, the fluence rate measurements as exemplified in Fig. 5 result in 30 light transmission signals since five fibers are used to detect the transmitted light from one source fiber, and this procedure is repeated for all six patient fibers. This set of light transmission signals can also be used for low-resolution tomography of the flux in the tissue being treated.[42] Likewise the 30 fluorescence and 30 white-light penetration data sets will be used to construct a tomographic presentation of sensitizer and oxygen levels, respectively.

Using the light transmission signals between patient fibers, it is possible to calculate the tissue effective attenuation coefficient for each individual patient. In the future, this information could be used as input to the light distribution modeling performed prior to the therapeutic light delivery, resulting in a more accurate treatment time prediction.

For the possible use of other sensitizers, it is easy to replace the six therapeutic laser diodes with units of a suitable wavelength. Furthermore, by use of the option of a third diagnostic light source, flexibility for inducing fluorescence in a large variety of sensitizers is maintained.

6. Conclusion

We have reported on the construction of a system for IPDT of solid tumors, and the initial clinical results have been presented. Future work will involve implementing a full model for interactive treatment based on the real-time monitoring of fluence rate, sensitizer fluorescence, and blood oxygenation. Also, improving the fiber positioning system with ultrasound guidance, several other indications, for example, lesions in the gastrointestinal tract, lie within the foreseeable future of this system.

Sara Pålsson is greatly acknowledged for contributing to the scientific discussions. This research was supported by the Swedish Foundation for Strategic Research and in an earlier phase by VINNOVA. We are grateful to Epsilon Technology AB, and in particular to Anders Jeppsson for providing technical solutions and hardware integration. The Karolinska Development AB, Stockholm, and Lund University Developmental AB support the project economically through SpectraCure AB, which is set up to bring the research project into a powerful health care reality. The dedication of Thomas Andersson in this task is especially appreciated.

References

1. S. L. Marcus, "Photodynamic therapy of human cancer: clinical status, potential and needs," in *Future Directions and Applications in Photodynamic Therapy*, C. J. Gomer, ed., Vol. IS06 of the SPIE Institute Series (SPIE, 1990), pp. 5–56.
2. L. I. Grossweiner, *The Science of Phototherapy* (CRC Press, 1994).
3. T. J. Dougherty, C. J. Gomer, B. W. Henderson, G. Jori, D. Kessel, M. Korbelik, J. Moan, and Q. Peng, "Photodynamic therapy," J. Natl. Cancer Inst. **90,** 889–905 (1998).
4. J. C. Kennedy, R. H. Pottier, and D. C. Pross, "Photodynamic therapy with endogenous protoporphyrin IX: basic principles and present clinical experience," J. Photochem. Photobiol. B. **6,** 143–148 (1990).
5. J. C. Kennedy and R. H. Pottier, "Endogenous protoporphyrin IX, a clinically useful photosensitizer for photodynamic therapy," J. Photochem. Photobiol. B. **14,** 275–292 (1992).
6. K. Svanberg, T. Andersson, D. Killander, I. Wang, U. Stenram,

S. Andersson-Engels, R. Berg, J. Johansson, and S. Svanberg, "Photodynamic therapy of non-melanoma malignant tumours of the skin using topical δ-amino levulinic acid sensitization and laser irradiation," Br. J. Dermatol. **130,** 743–751 (1994).
7. Q. Peng, T. Warloe, K. Berg, J. Moan, M. Kongshaug, K.-E. Giercksky, and J. M. Nesland, "5-aminolevulinic acid-based photodynamic therapy: clinical research and future challenges," Cancer **79,** 2282–2308 (1997).
8. I. Wang, N. Bendsoe, C. af Klinteberg, A. M. K. Enejder, S. Andersson-Engels, S. Svanberg, and K. Svanberg, "Photodynamic therapy versus cryosurgery of basal cell carcinomas; results of a phase III randomized clinical trial," Br. J. Dermatol. **144,** 832–840 (2001).
9. K. A. Salva, "Photodynamic therapy: unapproved uses, dosages, or indications," Clin. Dermatol. **20,** 571–581 (2002).
10. S. C. Chang, G. Buonaccorsi, A. MacRobert, and S. G. Bown, "Interstitial and transurethral photodynamic therapy of the canine prostate using *meso-tetra*-(*m*-hydroxyphenyl) chlorin," Int. J. Cancer **67,** 555–562 (1996).
11. T. J. Vogl, K. Eichler, M. G. Mack, S. Zangos, C. Herzog, A. Thalhammer, and K. Engelmann, "Interstitial photodynamic laser therapy in interventional oncology," Eur. Radiol. **14,** 1063–1073 (2004).
12. S. G. Bown, A. Z. Rogowska, D. E. Whitelaw, W. R. Lees, L. B. Lovat, P. Ripley, L. Jones, P. Wyld, A. Gillams, and A. W. Hatfield, "Photodynamic therapy for cancer of the pancreas," Gut **50,** 549–557 (2002).
13. S. Svanberg, S. Andersson-Engels, R. Berg, J. Johansson, and K. Svanberg, "System for laser treatments of tumours," Swedish patent SE 950 1278 (6 October 1996).
14. T. Johansson, M. Soto Thompson, M. Stenberg, C. af Klinteberg, S. Andersson-Engels, S. Svanberg, and K. Svanberg, "Feasibility study of a novel system for combined light dosimetry and interstitial photodynamic treatment of massive tumors," Appl. Opt. **41,** 1462–1468 (2002).
15. S. Andersson-Engels, N. Bendsoe, A. Johansson, T. Johansson, S. Pålsson, M. Soto Thompson, K. Svanberg, and S. Svanberg, "Integrated system for interstitial photodynamic therapy," in *Therapeutic Laser Applications and Laser-Tissue Interactions*, R. Steiner, ed., Proc. SPIE **5142,** 42–48 (2003).
16. M. Stenberg, M. Soto Thompson, T. Johansson, S. Pålsson, C. af Klinteberg, S. Andersson-Engels, U. Stenram, S. Svanberg, and K. Svanberg, "Interstitial photodynamic therapy—diagnostic measurements and treatment in malignant experimental rat tumours," in *Optical Biopsy and Tissue Optics*, I. J. Bigio, G. J. Mueller, G. J. Puppels, R. W. Steiner, and K. Svanberg, eds., Proc. SPIE **4161,** 151–157 (2000).
17. M. Soto Thompson, T. Johansson, S. Pålsson, S. Andersson-Engels, S. Svanberg, N. Bendsoe, U. Stenram, K. Svanberg, J. Spigulis, A. Derjabo, and J. Kapostins are preparing a manuscript to be called "Photodynamic therapy of basal cell carcinoma with multi-fibre contact light delivery."
18. C. af Klinteberg, M. Andreasson, O. Sandström, S. Andersson-Engels, and S. Svanberg, "Compact medical fluorosensor for minimally invasive tissue characterization," Rev. Sci. Instrum. **76,** 034303-1 (2005).
19. U. Gustafsson, S. Pålsson, and S. Svanberg, "Compact fibre-optic fluorosensor using a continuous wave violet diode laser and an integrated spectrometer," Rev. Sci. Instrum. **71,** 3004–3006 (2000).
20. S. Svanberg, S. Andersson-Engels, and K. Svanberg, "Divider for distributing radiation," Swedish patent SE 503 408 (14 November 2001).
21. K. M. Case and P. F. Zweifel, *Linear Transport Theory* (Addison-Wesley, 1967).
22. J. B. Fishkin, O. Coquoz, E. R. Anderson, M. Brenner, and B. J. Tromberg, "Frequency-domain photon migration measurements of normal and malignant tissue optical properties in a human subject," Appl. Opt. **36,** 10–20 (1997).
23. A. J. Welch and M. J. C. van Gemert, *Optical-Thermal Response of Laser-Irradiated Tissue* (Plenum, 1995).
24. K. König, H. Schneckenburger, A. Rück, and R. Steiner, "*In vivo* photoproduct formation during PDT with ALA-induced endogenous porphyrins," J. Photochem. Photobiol. B. **18,** 287–290 (1993).
25. S. A. Prahl, "Tabulated molar extinction coefficient for hemoglobin in water," Oregon Medical Laser Center (1998), omlc.ogi.edu/spectra/hemoglobin/summary.html.
26. R. M. P. Doornbos, R. Lang, M. C. Aalders, F. W. Cross, and H. J. C. M. Sterenborg, "The determination of *in vivo* human tissue optical properties and absolute chromophore concentrations using spatially resolved steady-state diffuse reflectance spectroscopy," Phys. Med. Biol. **44,** 967–981 (1999).
27. D. J. Robinson, H. S. de Bruijn, N. van der Veen, M. R. Stringer, S. B. Brown, and W. M. Star, "Protoporphyrin IX fluorescence photobleaching during ALA-mediated photodynamic therapy of UVB-induced tumors in hairless mouse skin," Photochem. Photobiol. **69,** 61–70 (1999).
28. M. Soumya and T. H. Foster, "Carbogen breathing significantly enhances the penetration of red light in murine tumours *in vivo*," Phys. Med. Biol. **49,** 1891–1904 (2004).
29. D. J. Robinson, H. S. de Bruijn, N. van der Veen, M. R. Stringer, S. B. Brown, and W. M. Star, "Fluorescence photobleaching of ALA-induced protoporphyrin IX during photodynamic therapy of normal hairless mouse skin: the effect of light dose and irradiance and the resulting biological effect," Photochem. Photobiol. **67,** 140–149 (1998).
30. Q. Chen, B. C. Wilson, S. D. Shetty, M. S. Patterson, J. C. Cerny, and F. W. Hetzel, "Changes in *in vivo* optical properties and light distributions in normal canine prostate during photodynamic therapy," Radiat. Res. **147,** 86–91 (1997).
31. A. M. K. Nilsson, R. Berg, and S. Andersson-Engels, "Measurements of the optical properties of tissue in conjunction with photodynamic therapy," Appl. Opt. **34,** 4609–4619 (1995).
32. J. P. A. Marijnissen and W. M. Star, "Quantitative light dosimetry in vitro and *in vivo*," Lasers Med. Sci. **2,** 235–242 (1987).
33. A. Johansson, T. Johansson, M. Soto Thompson, N. Bendsoe, K. Svanberg, S. Svanberg, and S. Andersson-Engels are preparing a manuscript to be called "*In vivo* measurement of parameters of dosimetric importance during photodynamic therapy of thick skin tumors."
34. I. A. Boere, D. J. Robinson, H. S. de Bruijn, J. van den Boogert, H. W. Tilanus, H. J. C. M. Sterenborg, and R. W. F. de Bruin, "Monitoring in situ dosimetry and protoporphyrin IX fluorescence photobleaching in the normal rat esophagus during 5-aminolevulinic acid photodynamic therapy," Photochem. Photobiol. **78,** 271–272 (2003).
35. F. B. Jensen, "Red blood cell pH, the Bohr effect, and other oxygenation-linked phenomena in blood O_2 and CO_2 transport," Acta Phys. Scand. **182,** 215–227 (2004).
36. A. Curnow, J. C. Haller, and S. G. Bown, "Oxygen monitoring during 5-aminolaevulinic acid induced photodynamic therapy in normal rat colon. Comparison of continuous and fractionated light regimes," J. Photochem. Photobiol. B. **58,** 149–155 (2000).
37. J. H. Woodhams, L. Kunz, S. G. Bown, and A. J. MacRobert, "Correlation of real-time haemoglobin oxygen saturation monitoring during photodynamic therapy with microvascular effects and tissue necrosis in normal rat liver," Br. J. Cancer **91,** 788–794 (2004).
38. Q. Chen, Z. Huang, H. Chen, and H. Shapiro, "Improvement of tumour response by manipulation of tumour oxygenation during PDT," Photochem. Photobiol. **76,** 197–203 (2002).
39. D. R. Holmes, B. J. Davis, C. J. Bruce, and R. A. Robb, "3D

visualization, analysis, and treatment of the prostate using trans-urethral ultrasound," Comput. Med. Imaging Graph. **27,** 339–349 (2003).
40. L. K. Lee, C. Whitehurst, M. L. Pantelides, and J. V. Moore, "An interstitial light assembly for photodynamic therapy in prostatic carcinoma," Br. J. Urol. Int. **84,** 821–826 (1999).
41. A. Curnow, B. W. McIlroy, M. J. Postle-Hacon, A. J. MacRobert, and S. G. Bown, "Light dose fractionation to enhance photodynamic therapy using 5-aminolevulinic acid in the normal rat colon," Photochem. Photobiol. **69,** 71–76 (1999).
42. S. R. Arridge, "Optical tomography in medical imaging," Inverse Probl. **15,** R41–R93 (1999).

Paper V

In vivo measurement of parameters of dosimetric importance during interstitial photodynamic therapy of thick skin tumors

A. Johansson, T. Johansson, M. Soto Thompson, N. Bendsoe, K. Svanberg, S. Svanberg, S. Andersson-Engels.

Journal of Biomedical Optics **11(3)**, 034029 (2006).

Journal of Biomedical Optics 11(3), 034029 (May/June 2006)

In vivo measurement of parameters of dosimetric importance during interstitial photodynamic therapy of thick skin tumors

Ann Johansson
Lund Institute of Technology
Department of Physics
P.O. Box 118
SE-221 00 Lund, Sweden
E-mail: Ann.Johansson@fysik.lth.se

Thomas Johansson
SpectraCure AB
Ideon Research Park
Ole Römers väg 16
SE-223 70, Lund, Sweden

Marcelo Soto Thompson*
Lund Institute of Technology
Department of Physics
P.O. Box 118
SE-221 00 Lund, Sweden

Niels Bendsoe
Lund University Hospital
Department of Dermatology and Venereology
P.O. Box 118
SE-221 00 Lund, Sweden

Katarina Svanberg
Lund University Hospital
Department of Oncology
P.O. Box 118
SE-221 00 Lund, Sweden

Sune Svanberg
Stefan Andersson-Engels
Lund Institute of Technology
Department of Physics
P.O. Box 118
SE-221 00 Lund, Sweden

Abstract. A system for interstitial photodynamic therapy is used in the treatment of thick skin tumors. The system allows simultaneous measurements of light fluence rate, sensitizer fluorescence, and tissue oxygen saturation by using the same fibers as for therapeutic light delivery. Results from ten tumor treatments using δ-aminolevulinic acid (ALA)-induced protoporphyrin IX show a significant, treatment-induced increase in tissue absorption at the therapeutic wavelength, and rapid sensitizer photobleaching. The changes in oxy- and deoxyhemoglobin content are monitored by means of near-infrared spectroscopy, revealing a varying tissue oxygenation and significant changes in blood volume during treatment. These changes are consistent with the temporal profiles of the light fluence rate at the therapeutic wavelength actually measured. We therefore propose the observed absorption increase to be due to treatment-induced deoxygenation in combination with changes in blood concentration within the treated volume. A higher rate of initial photobleaching is found to correlate with a less pronounced increase in tissue absorption. Based on the measured signals, we propose how real-time treatment supervision and feedback can be implemented. Simultaneous study of the fluence rate, sensitizer fluorescence, and local tissue oxygen saturation level may contribute to the understanding of the threshold dose for photodynamic therapy. [DOI: 10.1117/1.2204027]

Keywords: photodynamic therapy; δ-aminolevulinic acid; absorption spectroscopy; protoporphyrin IX fluorescence; photobleaching.

Paper 05128RR received May 26, 2005; revised manuscript received Jan. 17, 2006; accepted for publication Jan. 18, 2006; published online May 25, 2006.

1 Introduction

In the search for new modalities for cancer treatment, photodynamic therapy (PDT) has shown promising results in terms of selectivity and efficacy.[1] PDT relies on the presence of a photosensitizing agent which, once activated by light of the appropriate wavelength, generates cytotoxic species, mostly singlet oxygen and other reactive oxygen species. Tissue destruction is caused by a combination of immediate cell death and apoptosis induced by these radicals and indirect damage to the vascular system.[2,3] One commonly used photosensitizing compound is protoporphyrin IX (PPIX), generated by δ-aminolevulinic acid (ALA).[4] ALA-mediated PDT has been successfully used in the treatment of superficial lesions in the bladder, bronchus, aerodigestive tract, and skin, e.g., for the treatment of actinic keratosis.[5]

In an effort to extend PDT beyond that of treating superficial lesions or thin lesions easily accessible through body cavities, several research groups have investigated interstitial light delivery via optical fibers.[6–9] In addition to facilitating the treatment of thick and deeply lying tumors, interstitial light delivery via multiple fibers also allows for the treatment

*Present address: STI Medical Systems, 733 Bishop Street, Honolulu, HI 96813.

Address all correspondence to Ann Johansson, Atomic Physics, P.O. Box 118, Lund, 221 00 Sweden. Tel: +46462223120; Fax: +46462224250; E-mail: Ann.Johansson@fysik.lth.se

1083-3668/2006/11(3)/034029/10/$22.00 © 2006 SPIE

of irregularly shaped lesions while sparing normal surrounding tissue. To optimize the biological effect, accurate dosimetry needs to be implemented. A comprehensive dosimetry model could be based on detailed knowledge of the three parameters of importance in PDT: the fluence rate distribution, the sensitizer concentration, and the tissue oxygenation within the volume of interest.[10]

Studies aimed at correlating the treatment response to the total light dose alone in ALA-mediated PDT have shown varying success,[11–13] whereas better correlation has been found between PDT-induced damage and therapeutic light irradiance.[12,14] Higher irradiances have been shown to lead to smaller treatment volumes, an effect that has been explained by oxygen depletion.[15,16] In addition, a good correlation has been found between the initial rate of sensitizer photobleaching and treatment outcome.[11,12,14] The kinetics of PPIX photobleaching has shown a fluence rate dependency, in that a higher irradiance leads to a less pronounced loss of fluorescence and lower initial photobleaching rate.[14,17] Since PPIX photobleaching is suggested to be an oxygen-dependent process, during which PPIX is transformed to various photoproducts[12,17] that are also photobleached, these results support the hypothesis of oxygen depletion as a result of too high irradiances. It has been suggested that monitoring the bleaching via fluorescence spectroscopy could be a useful dosimetric tool in photodynamic therapy.[18] In addition, studies by Mitra and Foster have shown up to 15 times higher 630-nm light transmission at 1 cm depth when comparing a hypoxic to a well-oxygenated tissue phantom containing human erythrocytes.[19] These results further emphasize the disadvantage of inducing tissue hypoxia during PDT, since not only is the photodynamic reaction prevented, but deoxygenation also limits the light penetration within the tumor volume. Based on the work quoted, there seems to be a close interdependence between treatment outcome, sensitizer photobleaching, therapeutic light fluence rate, and tissue oxygenation. Adopting the ideas of an implicit dosimetry model for PDT, according to Wilson, Patterson, and Lilge,[10] there is a great need to intercorrelate these parameters and compare them to treatment outcome in clinical studies. In an implicit dosimetry model, one single parameter, e.g., the sensitizer photobleaching kinetics, is used to quantify PDT dose. Such a model has been formulated in contrast to explicit dosimetry, where the PDT dose is based on all three variables—light, sensitizer, and oxygen—necessary for the photodynamic reaction to take place.

We have recently reported on the construction of, and initial clinical treatment using an instrument for, interstitial photodynamic therapy (IPDT), which allows for diagnostic measurements to monitor treatment progression.[20] The present work reports on the results from the first ten clinical treatments, where changes in light transmission, sensitizer photobleaching, and tissue oxygen saturation level are monitored throughout the treatment. The study was aimed at monitoring the interplay between treatment-induced changes in absorption of the therapeutic irradiation, the sensitizer photobleaching, and the tissue oxygenation. The ultimate goal of simultaneous monitoring of parameters of dosimetric importance is the development of a dosimetry model for photodynamic therapy, taking into account spatial and time-resolved studies of the total light dose delivered, the sensitizer concentration, and the oxygen availability.

2 Materials and Methods

2.1 *Patients and Treatment Procedure*

An instrument for interstitial photodynamic therapy has been developed in which a maximum of six bare-end optical fibers are used to deliver the therapeutic light to the tumor mass. The same fibers can also be used to measure relevant dosimetry parameters during the treatment session. The clinical motivation for the treatment in this study was to reduce the tumor volume by means of interstitial photodynamic treatment prior to surgery. The study included eight patients with thick malignant skin lesions, within the approval by the Local Ethics Committee at Lund University Hospital. Six lesions were diagnosed as nodular basal cell carcinomas, whereas the remaining lesions were diagnosed as squamous cell carcinoma and keratoacanthoma/squamous cell carcinoma. Two of the patients diagnosed with basal cell carcinomas underwent two treatment sessions, resulting in a total of ten treatments. Table 1 lists detailed data concerning each patient and treatment. No controls, i.e., fiber insertion and light delivery without drug, were included because of restrictions posed by the ethical approval.

The tumor geometry was determined visually and by palpation by an experienced oncologist at the time of treatment. After removing possible crust and the *stratum corneum* overlying the lesion to facilitate the drug penetration, the lesion was photosensitized by ALA-methyl-esterified (ME) (methyl-esterified aminolevulinic acid, Medac GmbH, Hamburg, Germany) mixed into an oil-in-water emulsion (Essex Cream, Schering Corporation, Kenilworth, New Jersey) to a concentration by weight of 20%, which was applied topically with a 10-mm margin to the lesion 4 to 6 h before the therapeutic irradiation. Three patients were also given ALA intratumorally 30 min *prior* to the treatment by injecting 1 to 2 ml of a solution made from 1.5-g ALA powder dissolved in 10-ml 0.9% saline buffer at several sites within the more deeply lying tumor part.

After disinfecting the treatment area, Xylocain (AstraZeneca, Södertälje, Sweden) was administered subcutaneously as an anesthetic. The distal end of six sterilized optical fibers, hereafter referred to as the patient fibers, were inserted into the tumor mass at predetermined positions. Before commencing the therapeutic irradiation, one of these fibers was carefully translated stepwise throughout the tumor depth to confirm the presence of PPIX at up to four different depths by means of laser-induced fluorescence excited at 405 nm. The plastic coating of the fibers made them rigid enough not to deflect during insertion, and no metal needles guiding the fibers during insertion were needed. The fiber holder, consisting of one flexible metal-wire arm for each patient fiber, held the fibers in place during the treatment session. The fiber positions were chosen to obtain as homogeneous a light distribution inside the lesion as possible, while sparing the surrounding tissue. An algorithm for determining the near-optimal fiber positions has been published elsewhere.[21] Since all lesions could be approximated by rather flat cylinders, the resulting fiber positions were confined to one plane at half the tumor depth.

Table 1 Treatment and patient information. BCC is basal cell carcinoma, SCC is squamous cell carcinoma, and i.l is intralesional drug delivery. In treatment 2, four light delivering fibers were used during the treatment, two emitting 25 mW and the remaining two emitting 100 mW. Also in treatment 2, for the light dose of 70, the full dose was not delivered as a result of fibers losing their respective positions. In treatment 10, for the light dose of 320, the treatment time was based on a threshold dose of 100 J/cm^2.

Treatment number	Patient (male/female)	Diagnosis	Location	Size (mm) *length*×*width*×*depth*	ALA administration mode	Treatment power (mW)	Light dose (J)
1	1 (f)	Nodular BCC	Arm	20×20×9	Topical	75	395
2	4 (f)	Nodular BCC	Neck	12×14×5	Topical	25/100	70
3	5 (f)	Nodular BCC	Leg	12×14×3	Topical	75	180
4	5 (f)	Nodular BCC	Leg	20×20×5	Topical+i.l.	75	203
5	6 (m)	Nodular BCC	Ear	14×12×7	Topical	100	180
6	8 (f)	Nodular BCC	Shoulder	20×20×4	Topical+i.l.	75	270
7	7 (f)	Nodular BCC	Leg	30×25×3	Topical	75	495
8	7 (f)	Nodular BCC	Leg	20×20×1	Topical+i.l.	75	135
9	2 (m)	SCC	Ear	22×20×7	Topical	100	384
10	3 (m)	Keratoakantom/SCC	Nose	12×14×4	Topical	25	320

In the treatment mode, the individual fiber output power was kept constant throughout the treatment session at power levels ranging from 25 to 100 mW. The therapeutic irradiation was interrupted with varying time intervals (30 to 120 s) to perform the 45-s measurement sequences. Measurement sequences were performed more frequently at the beginning of the treatment session to follow the rapid sensitizer photobleaching, and also prior to and at the end of each treatment session. The total irradiation time was determined by the requirement to deliver a light dose exceeding 50 J/cm^2 to every part of the lesion,[20] leading to longer irradiation times for the larger lesions. Total light energy delivered and fiber output power are given in Table 1.

2.2 *Instrumentation*

The instrumentation used for the laser-induced fluorescence studies of the PPIX concentration throughout the tumor depth prior to therapeutic light delivery has been described in detail elsewhere.[22] A nitrogen laser pumped dye laser emits pulsed excitation light at 405 nm. After passing through a RG435 cut-off filter, fluorescent light between 450 and 800 nm is dispersed by a spectrometer and detected by an intensified and cooled charge-coupled device (CCD).

The setup of the interstitial photodynamic therapy (IPDT) instrument is shown in Fig. 1 and a more detailed description is given elsewhere.[20] The therapeutic light unit consists of six diode lasers emitting at 635 nm with an individual maximum output power of 250 mW. While in treatment mode, light from the therapeutic unit is guided into the distribution module and directed into the six 400-μm-diam optical fibers.

While in measurement mode, light from the diagnostic unit is coupled into one of the patient fibers via the light distribution module. The diagnostic light sources consist of a diode laser with the same wavelength as the treatment lasers and an LED covering the spectral range 760 to 810 nm. The term "diagnostic" is here used to describe the progression of the treatment and does not refer to diagnosis of the patient's status. One measurement sequence involves successively coupling the output from the two diagnostic light sources into each of the six patient fibers in turn. Transmitted light in the spectral range 620 to 810 nm is collected by the remaining five fibers, dispersed by an imaging spectrometer, and detected by a CCD camera. A cut-off filter (Schott RG665) is

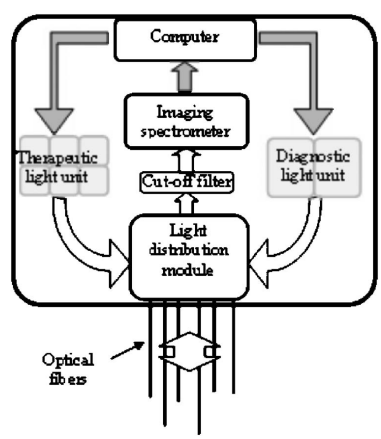

Fig. 1 The overall instrument setup. Shaded arrows indicate data flow, whereas unshaded arrows represent light paths.

used to attenuate the intense laser light, so that both the light transmission at 635 nm and the sensitizer fluorescence at 705 nm, which is excited by the light at 635 nm, can be monitored simultaneously with similar intensity. The output power of each of the patient fibers is measured before the treatment session commences to compensate for internal losses in the fiber couplings.

2.3 *Data Evaluation*

Following excitation at 405 nm, the fluorescence signal within the spectral interval 630 to 640 nm was used to quantify the PPIX concentration.

When evaluating data collected by the IPDT instrument, noise was suppressed by smoothing each acquired spectrum over 20 bands, which corresponds to approximately 5 nm in the CCD readout, and subtracting a constant background offset. Summing the detected signal within the spectral interval 625 to 645 nm resulted in a signal describing the light transmission at the treatment wavelength, also referred to as the light transmission. Similarly, the PPIX fluorescence signal was obtained by summing the detected light from 695 to 705 nm. Both for the light transmission and the sensitizer fluorescence measurements, the signals were normalized to their respective initial value. To get sufficient signal-to-noise, the data analysis was based on signals between neighboring fibers only. The patient fibers were always positioned with approximately equal separations within each patient. Distances between neighboring fibers were influenced by the tumor dimension and ranged from 4 mm for the smallest lesions up to 8 mm for the seventh treatment session.

The third parameter of dosimetric importance measured during PDT is related to the oxygen concentration. We used an indirect method of monitoring the tissue oxygen content by analyzing the tissue absorption spectrum and assuming that it is dominated by oxy- and deoxyhemoglobin. The relative concentration of these compounds is calculated to provide the tissue oxygen saturation level,

$$S(t) = \frac{[HbO(t)]}{[HbO(t)] + [Hb(t)]}. \tag{1}$$

$[Hb(t)]$ and $[HbO(t)]$ are the deoxy- and oxyhemoglobin concentrations, respectively. Since the absorbance by hemoglobin and myoglobin are indistinguishable,[23] $[Hb(t)]$ and $[HbO(t)]$ also include the absorption by myoglobin, if present.

The changes in optical density in the spectral interval 760 to 810 nm were measured using the LED as a light source:

$$\Delta A(t,\lambda) = -\ln \frac{I(t,\lambda)}{I(t=0,\lambda)}, \tag{2}$$

where $I(t=0,\lambda)$ is the initial light transmission between patient fibers and $I(t,\lambda)$ is the light transmission as detected during the subsequent measurement sequences. Assuming a semi-infinite medium where the extrapolated boundary condition applies and approximating the patient fibers with isotropic light sources, the light transmission can be expressed as:

$$I(t) \propto \frac{P\mu_{\text{eff}}^2(t)}{4\pi\mu_a(t)} \left\{ \frac{\exp[-\mu_{\text{eff}}(t) r_1]}{r_1} - \frac{\exp[-\mu_{\text{eff}}(t) r_2]}{r_2} \right\}, \tag{3}$$

where

$$\mu_{\text{eff}} = [3\mu_a(\mu_a + \mu_s')]^{1/2}$$

is the effective absorption coefficient, and μ_a and μ_s' denote the absorption and reduced scattering coefficients, respectively. The wavelength dependence has been omitted for simplicity. Furthermore,

$$r_1 = [(z - z_0)^2 + \rho^2]^{1/2} \text{ and } r_2 = [(z + z_0 + 2z_b)^2 + \rho^2]^{1/2},$$

where ρ is the radial interfiber distance, z_0 equals the fiber insertion depth plus the factor $1/\mu_s'$, and $z_b \approx 2/\mu_s'$. Combining Eqs. (2) and (3) yields the following expression for the change in optical density:

$$\begin{aligned}\Delta A(t,\lambda) &= -\ln \frac{I(t,\lambda)}{I(t=0,\lambda)} \\ &= r_1[3\mu_a(t=0)\mu_s']^{1/2} \left(\left[\frac{\Delta\mu_a}{\mu_a(t=0)} + 1 \right]^{1/2} - 1 \right) \\ &\quad - \ln \left\{ 1 - \frac{r_1}{r_2} \exp[-(r_2 - r_1) \right. \\ &\quad \left. \times \{3[\Delta\mu_a + \mu_a(t=0)]\mu_s'\}^{1/2}] \right\} \\ &\quad + \ln \left(1 - \frac{r_1}{r_2} \exp\{-(r_2 - r_1)[3\mu_s(t=0)\mu_s']^{1/2}\} \right),\end{aligned} \tag{4}$$

where

$$\Delta\mu_a = \varepsilon_{Hb}(\lambda)\Delta[Hb(t)] + \varepsilon_{HbO}(\lambda)\Delta[HbO(t)].$$

$\varepsilon_{HbO}(\lambda)$ and $\varepsilon_{Hb}(\lambda)$ are the wavelength-dependent extinction coefficients of oxy- and deoxyhemoglobin, respectively.[24] The changes in oxy- and deoxyhemoglobin concentration were assessed by nonlinear least-squares fitting of Eq. (4) to the measured change in optical density within the spectral interval 760 to 810 nm. After assuming initial oxy- and deoxyhemoglobin concentrations, the tissue oxygen saturation was calculated from Eq. (1). Here, $[Hb(t=0)]$ and $[HbO(t=0)]$ were set to 20 and 47 μM, respectively,[25] giving an initial tissue oxygen saturation level of 70%, in agreement with previously reported baseline levels.[26]

To derive Eq. (4), several assumptions have been made. First, a reduced scattering coefficient that remains constant over time and that is much larger in magnitude than the absorption coefficient was assumed. Second, Eq. (4) is assumed to be valid only in homogeneous tissues. By this way of analysis, attenuation of the transmitted light by a small amount of blood in front of either the detection or source fiber is attributed to a smaller increase in total hemoglobin content averaged throughout the probed tissue volume. In this work,

the initial absorption $[\mu_a(t=0)]$ and reduced scattering coefficients $[\mu_s'(t)=\mu_s'(t=0)]$ at 635 nm were set to 0.3 and 12 cm^{-1}, respectively.[27]

Based on the known extinction spectra of oxy- and deoxyhemoglobin, the changes in light transmission at the treatment wavelength could be approximated by extrapolating the measured optical density changes from the wavelength region 760 to 810 nm down to 635 nm. The motivation for doing this was to check whether the observed treatment-induced absorption changes could be explained by the measured changes in tissue oxygenation and blood volume. The wavelength dependence of the reduced scattering coefficient, which influences the calculation when extrapolating the measured optical density changes from the wavelength region 760 to 810 nm down to 635 nm, is given the following appearance:[28]

$$\mu_s'(t=0,\lambda) \propto \lambda^{-1.11}. \quad (5)$$

3 Results

Following excitation at 405 nm, the PPIX fluorescence signal prior to the treatment was found to decrease throughout the tumor depth. The sensitizer displayed a large interpatient variability, which seemed to depend more on tissue porosity than on ALA delivery path.

An example of a typical spectrum recorded when the diode laser emitting at 635 nm was used as the diagnostic light source is shown in Fig. 2(a). 635-nm light transmission curves as a function of delivered light dose are presented in Fig. 2(b). For this patient, the decrease in light transmission was rather homogeneous within the entire tumor volume.

A significant treatment-induced attenuation increase was established in seven of nine completed treatment sessions by performing a one-sided Student's *t*-test. $P<0.01$ was considered significant. Data from treatment 2 was excluded, since the optical fibers moved when the patient started coughing after 240 s of therapeutic irradiation. Figure 2(c) shows the light transmission level remaining at the end of each treatment session. The data displayed were obtained by averaging the normalized light transmission between neighboring fibers within time interval T_I, as indicated in Fig. 2(b). Out of a total of 60 fiber insertions, the detected signals from four fibers were characterized by a rapid (changes occurred between the first and second measurement sequences) and more pronounced transmission decrease (down to less than 20% of the initial level), possibly indicative of significant blood pooling at the fiber tip. Data from these fibers, characterized by poor signal-to-noise ratio, were excluded from the data analysis.

A typical sensitizer photobleaching curve is shown in Fig. 2(d), where the average of the normalized fluorescence signal, as detected between neighboring patient fibers in one patient, has been plotted as a function of the delivered light dose. Data from the treatments indicate rapid initial photobleaching, followed by a slowly decaying fluorescence level. It should be noted that the sensitizer fluorescence signal was not compensated for the absorption increase, as seen from the fluence rate measurements. Figure 2(e) shows the remaining fluorescence level for treatments 3 to 10. Treatment 1 was excluded from the analysis because the PPIX fluorescence was below the detection limit of the system with its initial CCD settings.

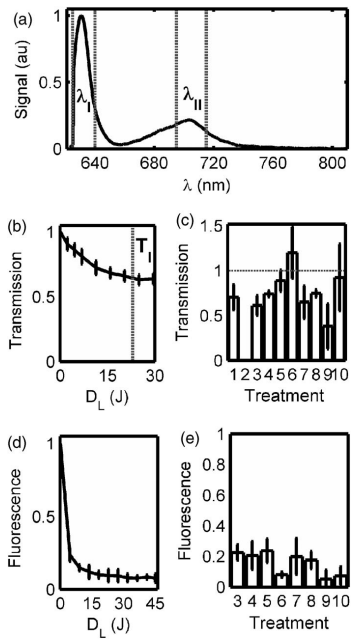

Fig. 2 (a) Raw spectrum from a diagnostic measurement using the 635-nm diode laser as a light source. Spectral intervals λ_I and λ_{II} indicate regions used for studying the light transmission at 635 nm and the PPIX fluorescence signals, respectively. (b) Average of the normalized light transmission between neighboring patient fibers as a function of the delivered light dose (D_L) from one patient. Signals within area T_I are averaged to constitute a measure of final light transmission. (c) The light transmission remaining at the end of each treatment. (d) Average of the normalized PPIX fluorescence as measured between neighboring patient fibers as a function of the delivered light dose (D_L) from one patient. (e) The PPIX fluorescence level remaining at the end of each treatment. In (b) through (e), the error bars denote ±1 standard deviation.

Figure 3(a) shows the changes in optical density at various times during treatment 3. The data were obtained by evaluating the recorded NIR transmission spectra according to Eq. (2). An increased absorbance can be seen around 760 nm as the treatment progressed. In this wavelength region, deoxyhemoglobin has a higher extinction coefficient than oxyhemoglobin, as shown in Fig. 3(b).[24] The changes in concentration of oxy- and deoxyhemoglobin were evaluated using Eq. (4). Figure 3(c) illustrates the concentration changes corresponding to the data shown in Fig. 3(a). The curves are not each other's opposite, indicating treatment-induced changes in total blood volume.

Figure 4(a) shows a schematic illustration of the tumor cross section for one of the treatments and the patient fiber configuration used during this treatment. Similar configurations were used for all treatments. In Fig. 4(b), the tissue oxygenation level according to Eq. (1) is shown when measured using the six fiber pairs, as indicated in the legend. As can be seen, during treatment 3 the volume probed when mea-

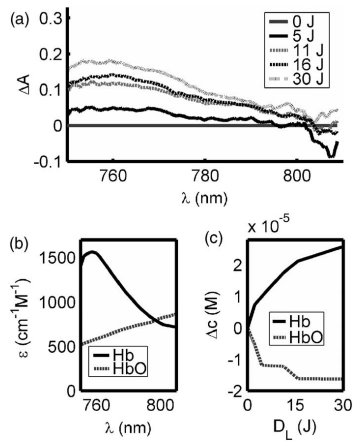

Fig. 3 (a) Changes in tissue optical density from the third treatment for five different treatment times. (b) Extinction coefficients of oxy- and deoxyhemoglobin as a function of wavelength. (c) Concentration changes of oxy- and deoxyhemoglobin as a function of the delivered light dose (D_L).

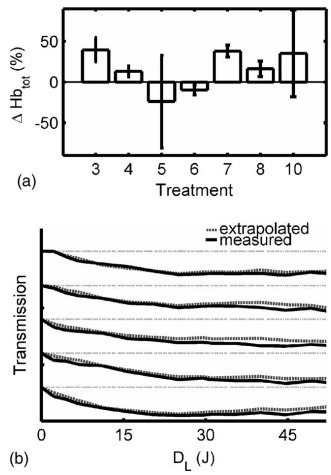

Fig. 5 (a) Change in total hemoglobin content for seven treatments. (b) Example of measured and extrapolated light transmission at 635 nm. The curves, which are offset for clarity, show the normalized light transmission between one source fiber and five detection fibers during the third treatment.

suring between fibers 1 and 2 displayed a higher degree of deoxygenation than the other parts of the tumor. Figure 4(c) shows the tumor oxygenation level after averaging the signals between all patient fibers. It should be noted that this graph includes transmission signals with source-detector separations of up to 8 mm. Figure 4(d) shows the minimum average tissue oxygen saturation level for seven treatment sessions.

The standard deviations for sessions 3, 4, 6, 7, and 8 result from averaging the transmission signals between many fiber combinations, thereby probing a highly heterogeneous tissue. The extremely large standard deviations for treatments 5 and 10 indicate either that the model used for describing the transmitted NIR signal was incorrect or that fiber positions changed during the treatment. Data for these two patients give no relevant information but have been included in the graph for completeness. Although not significant, smaller source-detector separations seemed to exhibit a higher degree of tissue deoxygenation than when analyzing transmission signals having traveled across larger tumor volumes. In addition to treatment sessions 1 and 2, data from session 9 have been excluded, because the CCD settings were incorrect during this particular treatment.

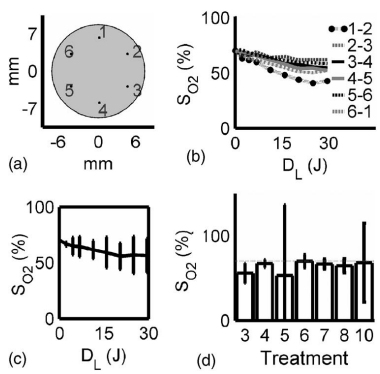

Fig. 4 (a) Example of tumor cross section and fiber positions. (b) Tissue oxygen saturation during treatment 3 as a function of the delivered light dose (D_L). The legend indicates source-detector fibers. (c) Average tissue oxygenation as a function of the delivered light dose (D_L). (d) Minimum tissue oxygen saturation level for seven treatments. Error bars denote standard deviations resulting when averaging signals between neighboring patient fibers. The dashed line represents the 70% oxygen saturation level.

Besides changes in tissue oxygen saturation level, the treatment also induced changes in the total hemoglobin content, as shown in Fig. 5(a). The plot shows the relative changes in total hemoglobin content for seven treatments when assuming initial deoxy- and oxyhemoglobin concentrations according to Sec. 2.3. Again, the large standard deviations for sessions 5 and 10 indicate a poor fit to the model. Here we tested the hypothesis that changes in tissue oxygen saturation and blood volume resulted in the observed increase in tissue absorption at the treatment wavelength. The change in light transmission at the therapeutic wavelength was approximated by extrapolating the measured optical density change from the wavelength region 760 to 810 nm down to 635 nm based on the known extinction coefficients of oxy- and deoxyhemoglobin. Figure 5(b) illustrates the agreement for a set of one source fiber and five detection fibers during one of the treatments. A relative error estimate was defined according to the following formula:

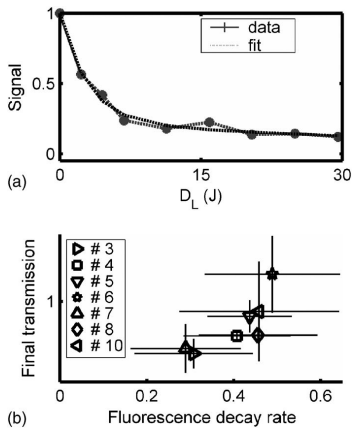

Fig. 6 (a) Example of a PPIX photobleaching curve and the double exponential fit. The exponent of the rapidly decaying term *b* was used to quantify the photobleaching rate. (b) Scatter plot illustrating the correlation between the initial photobleaching rate and the light transmission remaining at the end of the treatment. Error bars denote standard deviations and the treatment number is indicated in the legend.

$$E = \sum_{t,\text{fiber}} \frac{(x_{\text{measured}} - x_{\text{predicted}})^2}{x_{\text{measured}}} \frac{1}{n-1}, \tag{6}$$

where n is the number of measurements. Taking into account signals between neighboring fibers, the fit for the treatment session shown in Fig. 5(b) resulted in $E=0.006$. Of the other treatments, four showed error estimates of similar magnitude when fitting the predicted light transmission profile to the measured one, whereas the fit from treatment sessions 5 and 10 resulted in ten-fold larger errors. As explained before, data from treatments 1, 2, and 9 were excluded.

Figures 4(d), 5(a), and 5(b) indicate treatment-induced variations in tissue oxygenation and total hemoglobin content, which seem to explain the observed absorption increase at the treatment wavelength. To further explore the connection between the light transmission, the tissue oxygenation, and the total blood content, the correlation between the final light transmission, obtained by averaging the normalized transmission signal over time interval I, as indicated in Fig. 2(b), and the total change in tissue blood volume was studied for seven treatments. Comparing the averages of these two variables for each treatment session resulted in a correlation coefficient of −0.75. The correlation between the average final light transmission and the minimum tissue oxygen saturation was only 0.23.

Finally, the correlation between the overall absorption increase and the initial photobleaching rate was studied. The PPIX photobleaching rate was quantified by fitting a double exponential to the normalized fluorescence decay curve by means of a nonlinear least squares Levenberg-Marquardt method. The fit to the raw data, indicated in Fig. 6(a), was given the following principal appearance;

$$F = a\exp(-b\cdot D_J) + c\exp(-d\cdot D_J), \tag{7}$$

where F and D_J denote the PPIX fluorescence signal and the delivered light dose, respectively. The constants a through d were allowed to vary during the fit. Of the two constants b and d, the one with the largest magnitude was used to describe the initial photobleaching rate. The average value of this initial decay rate for each of eight treatment sessions is plotted along the abscissa in Fig. 6(b), whereas the ordinate gives the average of the normalized, final light transmission. Each marker in Fig. 6(b) indicates an average of the light transmission/fluorescence decay rate from each treatment, and therefore represents an average over the entire tumor volume. The standard deviations are a result of probing a rather large and heterogeneous tissue volume. The correlation coefficient between the final light transmission and the initial PPIX fluorescence decay rate was found to be 0.81. A similar analysis showed a correlation coefficient of −0.73 between the final light transmission and the final PPIX fluorescence level. In summary, Fig. 6(b) indicates a less pronounced absorption increase during treatment sessions that show more rapid photobleaching.

One-way analysis of variance (ANOVA) showed no significant differences between the two groups of patients receiving topical and topical plus intratumoral ALA administration, nor between different fiber output powers for the variables presented in Figs. 2(c), 2(e), 4(d), 5(a), and 6(b). $P<0.01$ was considered significant.

4 Discussion

Interstitial photodynamic therapy has been applied in the treatment of several conditions, for example, malignancies in the prostate,[29] liver,[30] and pancreas.[9] Various photosensitizers have been used in those studies, and relatively large treatment volumes have been obtained. This has been possible due to the low thresholds and long activation wavelengths for the sensitizers used.[31–33] The main limitations of IPDT as applied today are the limited light penetration and the lack of a more precise dosimetry. In this study, we used ALA because of our extensive experience of using this substance in the treatment of skin malignancies. The results presented are not focused on the treatment outcome of the tumors, but rather on treatment-induced changes in tissue absorption, PPIX photobleaching and tissue oxygenation level, and possible correlations between them.

The fluorescence measurements showed the typical characteristics of PPIX photobleaching, where the final sensitizer fluorescence constituted less than 25% of the initial fluorescence level. Both the overall amount of photobleaching and the initial photobleaching rate have been shown to correlate with tissue oxygenation and amount of PDT damage, possibly indicating the feasibility of using the sensitizer photobleaching as an implicit dosimetric parameter.[10,11,17] The sensitizer fluorescence signal could therefore possibly be used as a first indication of the treatment outcome, and not merely to provide information about the presence of the drug. More work is required to correlate the fluorescence kinetics to the treatment outcome, including results of long-term follow-up.

In this work, an indirect method of assessing the tissue oxygen content was used, which assumes there is a connec-

tion between the oxygen saturation of hemoglobin and the concentration of oxygen molecules $^3O_2$. On the time scale associated with a typical treatment and also during a measurement cycle, we believe that the balance between deoxy- and oxygenated tissue reflects the oxygen concentration level. The tissue oxygen saturation levels reported do not indicate any incidence of serious tissue hypoxia during the treatment sessions. One possible explanation might be that PDT following local administration of ALA is not associated with a pronounced vasoconstriction as PDT with many other sensitizers, for example, Foscan and HpD. When using topically administered ALA, increased blood perfusion has been observed during treatment of superficial skin malignancies.[34] Another possible explanation for us not seeing lower oxygenation levels is the relatively large tissue volume probed by the NIR light, determined by the relatively long distance between source and detector fibers. In contrast, one could expect oxygen consumption and depletion to be local processes occurring close to the light source, where the fluence rate is highest.[15,35] It is thus likely that these measurements probe tissue characterized by inhomogeneous oxygen saturation.

The influence of a good oxygen supply on tumor treatment outcome is well established. Following systemic administration of ALA, irradiation fractionation with dark intervals on the order of a couple of minutes has been shown to induce three times more necrosis than continuous therapeutic irradiation, an effect that has been explained by tissue reoxygenation during the dark periods.[15] Real-time monitoring of the tissue oxygen saturation levels is clearly desirable when trying to improve treatment outcome. Although not significant, for some treatments we observed a slightly higher oxygenation level for the earliest measurements during a measurement sequence. Since one such sequence interrupts the therapeutic irradiation for 45 sec, this might be in agreement with work done by Foster et al. who reported on tissue reoxygenation using dark intervals on the order of 5 to 45 sec.[36]

Other authors have also reported a decrease in the light penetration in tissue during PDT, and possible explanations include damage to the tissue microcirculation,[37] alteration of the local blood flow and perfusion,[3,38] and local hyperthermia or bleeding at the fiber tips.[39] Because of the high absorption coefficient of blood, bleeding at the fiber tips has a considerable impact on the light distribution in the tissue, and blood pooling at the light sources should be prevented to avoid insufficient treatment. By measuring the magnitude of the light transmission between patient fibers, fibers characterized by significant blood pooling can be identified and an insufficient treatment can be avoided by repositioning these fibers.

When using bare-end fibers for light delivery, one should not neglect the risk of inducing hyperthermia due to the high irradiance (<0.2 MW/m^2) close to the fiber tip. Recent work by our group using temperature-dependent fluorescence from alexandrite-doped treatment fibers has shown a local temperature increase of 4 to 5 °C *in vivo* at the fiber tip.[40] However, the small temperature increase observed using crystal-doped fiber tips can probably not explain the observed increase in tissue absorption.[41,42]

Another possible explanation for the observed decrease in light transmission during the treatment sessions is based on treatment-induced changes in oxy- and deoxyhemoglobin concentrations. Tissue deoxygenation as a consequence of oxygen consumption associated with the photodynamic reaction would cause an increase in tissue absorption at 635 nm, since deoxyhemoglobin is a much stronger absorber at this wavelength than oxyhemoglobin.[19,24] Furthermore, local blood accumulation at the fiber tips would increase the average tissue light attenuation. Here we have tested the hypothesis that changes in tissue oxygen saturation and blood volume induce changes in the average tissue absorption coefficient. Evaluation of the measured tissue optical density in the wavelength interval 760 to 800 nm indicates treatment-induced tissue deoxygenation in combination with a considerable change in blood volume. The changes in light transmission predicted by the calculated changes in hemoglobin content were compared to the light transmission actually measured at 635 nm, showing excellent agreement for some patients. Judging by the magnitudes of the correlation coefficients, the absorption increase seems to be more influenced by the observed changes in total hemoglobin content than by the varying tissue oxygen saturation. This poor correlation might originate from the assumption of homogeneous tissue associated with our analysis of the NIR signal. We are presently working on a way to incorporate tissue inhomogeneities in the geometry following the concept outlined in Ref. 43. In the case of light transmission, treatment 6 represents an outlier where we actually observed an increase in tissue light transmission. This lesion had previously been treated by cryotherapy, leading to hypopigmentation and loss of vascularity. A low average blood concentration, possibly in combination with tissue oedema induced by the treatment, could perhaps explain the transmission increase.

The observed increase in absorption influences the light distribution throughout the tumor volume, with the result that peripheral regions, which are important for tumor growth, may not receive a sufficient light dose. By carefully monitoring the light penetration during the treatment, information can be obtained on prolonging the treatment time or adjusting the individual fiber output power to deliver the planned light dose to these critical volumes. The aim of these dosimetric measurements performed in parallel with the therapy is treatment supervision and real-time feedback to improve treatment results. During the clinical work, we observed large interpatient variations in the detected signals, a fact that further supports the concept of individualized treatment control.

Even though we have had promising results when using bare-ended fibers for IPDT,[44] the extremely high fluence rate close to the light sources introduces two major issues that need to be addressed: first, the light absorption by tissue might introduce thermal effects such as charring, and second, the high fluence rate might introduce local oxygen depletion and thereby lack of treatment response close to the light sources. With these concerns in mind, we limited the fiber output power to 100 mW. Histopathology performed on excised tissue from some of the patients included in this work displayed no evidence of thermal effects or inefficient treatment close to the fiber tips. In support of our findings, Woodhams et al. have reported no thermal effects in controls with light only at 100 mW.[45]

Although not shown here, the results from histopathology studies on the excised tissue showed tumor necrosis down to a

depth of 9 mm following only topical ALA application. The presence of PPIX at depths of up to 5 mm following the combination of topical and intratumoral drug administration was confirmed by the point-monitoring laser-induced fluorescence studies. Experimentally determined and theoretically modeled ALA penetration depths between 2 and 5 mm have been reported by other groups.[46,47] In this study, possible explanations to the presence of PPIX at the relatively large depths might be increased drug diffusivity and skin permeability achieved by the use of ALA-ME, and the removal of crust and the superficial skin layer.[48]

The negative correlation between the light transmission and the sensitizer fluorescence level remaining at the end of the treatment indicates more efficient photobleaching during treatments characterized by a smaller increase in tissue absorption. This result might not seem very surprising, since a higher irradiance photobleaches the sensitizer more efficiently, given a sufficient oxygen concentration. The relatively high degree of correlation between the initial sensitizer photobleaching rate and the light transmission remaining at the end of the treatment session might thus also imply some oxygen dependence behind the increase in tissue light absorption. It should be noted that here we observed a correlation between the fluorescence signal during the first few minutes of the treatment session and the tissue absorption at the end of the treatment. These two parameters are separated in time by up to 15 minutes. The explanation might lie in the fact that a tumor with an overall stable blood supply can maintain this throughout the entire treatment, thereby avoiding oxygen depletion. The situation may, however, be completely different for sensitizers with more pronounced vascular effects than ALA-induced PPIX. However, care should be exercised when drawing any conclusions based merely on the correlation coefficients, due to the small number of patients included in the study. The need for a larger study also applies when trying to identify differences between the two ALA administration paths.

The analysis of the tissue oxygen saturation signal is subject to several assumptions and sources of error. Exact knowledge of the fiber positions, gained for example by means of ultrasound techniques, will minimize one of the sources of uncertainties in the data analysis. Furthermore, the assumption of a constant reduced scattering constant throughout the treatment and the values of the initial absorption and reduced scattering coefficients constitute another source of error. Although not shown here, the temporal profile of the tissue oxygen saturation level seems to be reasonably insensitive to variations in these coefficients within certain limits. An interesting task for the future would be to monitor the tissue's optical properties during the treatment session. Using a time-resolved system, it would be possible to separately measure the reduced scattering and absorption coefficients,[49] which could aid in interpreting the observed variations in light penetration reported here. Our indirect method of assessing the tissue oxygen saturation should be correlated to *in vivo* measurements of oxygen concentration, for example, by means of oxygen-sensitive microelectrodes or oxygen-dependent phosphorescence quenching probes.[35] The inclusion of controls, where fibers are inserted and light is delivered in the absence of photosensitizer, is a necessity when further interpreting the results from the diagnostic measurements.

In conclusion, we have reported on simultaneous measurements of fluence rate, sensitizer fluorescence, and tissue oxygen saturation during interstitial photodynamic therapy of thick malignant skin tumors. A significant increase in tissue light absorption was observed during seven completed treatments, possibly explained by treatment-induced tissue deoxygenation and blood volume increase. A high absorption increase was found to correlate to a lower initial sensitizer photobleaching rate. We emphasize the importance of the proposed real-time diagnostic measurements as a tool for treatment supervision and feedback.

Acknowledgments

This project was financially supported by the Swedish Foundation for Strategic Research, the Swedish Research Council (Scientific Council for Medicine), and also by Karolinska Development AB, Stockholm and Lund University Development AB through SpectraCure AB. The authors wish to thank Epsilon Technology AB for providing technical solutions and hardware integration.

References

1. T. J. Dougherty, C. J. Gomer, B. W. Henderson, G. Jori, D. Kessel, M. Korbelik, J. Moan, and Q. Peng, "Photodynamic therapy," *J. Natl. Cancer Inst.* **90**(12), 889–905 (1998).
2. B. B. Noodt, K. Berg, T. Stokke, Q. Peng, and J. M. Nesland, "Apoptosis and necrosis induced with light and 5-aminolaevulinic acid-derived protoporphyrin IX," *Br. J. Cancer* **74**(1), 22–29 (1996).
3. D. J. H. Roberts, F. Cairnduff, I. Driver, B. Dixon, and S. B. Brown, "Tumor vascular shutdown following photodynamic therapy based on polyhematoporphyrinor 5-aminolevulinic acid," *Int. J. Oncol.* **5**(4), 763–768 (1994).
4. J. C. Kennedy and R. H. Pottier, "Endogenous protoporphyrin IX, a clinically useful photosensitizer for photodynamic therapy," *J. Photochem. Photobiol., B* **14**, 275–292 (1992).
5. Q. Peng, T. Warloe, K. Berg, J. Moan, M. Kongshaug, K. E. Giercksky, and J. M. Nesland, "5-aminolevulinic acid-based photodynamic therapy: Clinical research and future challenges," *Cancer* **79**, 2282–2308 (1997).
6. T. Johansson, M. Soto Thompson, M. Stenberg, C. af Klinteberg, S. Andersson-Engels, S. Svanberg, and K. Svanberg, "Feasibility study of a novel system for combined light dosimetry and interstitial photodynamic treatment of massive tumors," *Appl. Opt.* **41**(7), 1462–1468 (2002).
7. S. F. Purkiss, M. F. Grahn, A. M. Abulafi, R. Dean, J. T. Allardice, and N. S. Williams, "Multiple fiber interstitial photodynamic therapy of patients with colorectal liver metastases," *Lasers Med. Sci.* **9**(1), 27–35 (1994).
8. P. J. Lou, H. R. Jager, L. Jones, T. Theodossy, S. G. Bown, and C. Hopper, "Interstitial photodynamic therapy as salvage treatment for recurrent head and neck cancer," *Br. J. Cancer* **91**(3), 441–446 (2004).
9. S. G. Bown, A. Z. Rogowska, D. E. Whitelaw, W. R. Lees, L. B. Lovat, P. Ripley, L. Jones, P. Wyld, A. Gillams, and A. W. Hatfield, "Photodynamic therapy for cancer of the pancreas," *Gut* **50**(4), 549–557 (2002).
10. B. C. Wilson, M. S. Patterson, and L. Lilge, "Implicit and explicit dosimetry in photodynamic therapy: a new paradigm," *Lasers Med. Sci.* **12**(3), 182–199 (1997).
11. I. A. Boere, D. J. Robinson, H. S. de Bruijn, J. van den Boogert, H. W. Tilanus, H. J. C. M. Sterenborg, and R. W. F. de Bruin, "Monitoring in situ dosimetry and protoporphyrin IX fluorescence photobleaching in the normal rat esophagus during 5-aminolevulinic acid photodynamic therapy," *Photochem. Photobiol.* **78**(3), 271–2 (2003).
12. D. J. Robinson, H. S. de Bruijn, N. van der Veen, M. R. Stringer, S. B. Brown, and W. M. Star, "Fluorescence photobleaching of ALA-induced protoporphyrin IX during photodynamic therapy of normal hairless mouse skin: The effect of light dose and irradiance and the resulting biological effect," *Photochem. Photobiol.* **67**(1), 140–149 (1998).

13. Z. W. Xiao, Y. Y. Tamimi, K. Brown, J. Tulip, and R. Moore, "Interstitial photodynamic therapy in subcutaneously implanted urologic tumors in rats after intravenous administration of 5-aminolevulinic acid," *Urologic Oncology* **7**(3), 125–132 (2002).
14. D. J. Robinson, H. S. de Bruijn, N. van der Veen, M. R. Stringer, S. B. Brown, and W. M. Star, "Protoporphyrin IX fluorescence photobleaching during ALA-mediated photodynamic therapy of UVB-induced tumors in hairless mouse skin," *Photochem. Photobiol.* **69**(1), 61–70 (1999).
15. A. Curnow, J. C. Haller, and S. G. Bown, "Oxygen monitoring during 5-aminolaevulinic acid induced photodynamic therapy in normal rat colon. Comparison of continuous and fractionated light regimes.," *J. Photochem. Photobiol., B* **58**(2–3), 149–155 (2000).
16. Q. Chen, Z. Huang, H. Chen, and H. Shapiro, "Improvement of tumour response by manipulation of tumour oxygenation during PDT," *Photochem. Photobiol.* **76**, 197–203 (2002).
17. J. C. Finlay, D. L. Conover, E. L. Hull, and T. H. Foster, "Porphyrin bleaching and PDT-induced spectral changes are irradiance dependent in ALA-senstitized normal rat skin in vivo," *Photochem. Photobiol.* **73**(1), 54–63 (2001).
18. K. König, H. Schneckenburger, A. Rück, and R. Steiner, "*In vivo* photoproduct formation during PDT with ALA-induced endogenous porphyrins," *J. Photochem. Photobiol., B* **18**, 287–290 (1993).
19. S. Mitra and T. H. Foster, "Carbogen breathing significantly enhances the penetration of red light in murine tumours *in vivo*," *Phys. Med. Biol.* **49**(10), 1891–1904 (2004).
20. M. Soto Thompson, A. Johansson, T. Johansson, S. Andersson-Engels, N. Bendsoe, K. Svanberg, and S. Svanberg, "Clinical system for interstitial photodynamic therapy with combined on-line dosimetry measurements," *Appl. Opt.* **44**(19), 4023–4031 (2005).
21. A. Johansson, J. Hjelm, E. Eriksson, and S. Andersson-Engels, "Pretreatment dosimetry for interstitial photodynamic therapy," *Proc. SPIE* **5863**, 121–131 (2005).
22. C. af Klinteberg, M. Andreasson, O. Sandström, S. Andersson-Engels, and S. Svanberg, "Compact medical fluorosensor for minimally invasive tissue characterisation," *Rev. Sci. Instrum.* **76**(3), 034303–034306 (2005).
23. R. Wariar, J. N. Gaffke, R. G. Haller, and L. A. Bertocci, "A modular NIRS system for clinical measurement of impaired skeletal muscle oxygenation," *J. Appl. Physiol.* **88**(1), 315–325 (2000).
24. S. A. Prahl, "Optical Absorption of Hemoglobin," see http://omlc.ogi.edu/spectra/hemoglobin/index.html (2004).
25. L. Rovati, A. Bandera, M. Donini, G. Salvatori, and L. Pollonini, "Design and performance of a wide-bandwidth and sensitive instrument for near-infrared spectroscopic measurements on human tissue," *Rev. Sci. Instrum.* **75**(12), 5315–5325 (2004).
26. D. A. Benaron, I. H. Parachikov, S. Friedland, R. Soetikno, J. Brock-Utne, P. J. van der Starre, C. Nezhat, M. K. Terris, P. G. Maxim, J. J. Carson, M. K. Razavi, H. B. Gladstone, E. F. Fincher, C. P. Hsu, F. L. Clark, W. F. Cheong, J. L. Duckworth, and D. K. Stevenson, "Continuous, noninvasive, and localized microvascular tissue oximetry using visible light spectroscopy," *Anesthesiology* **100**(6), 1469–1475 (2004).
27. J. B. Fishkin, O. Coquoz, E. R. Anderson, M. Brenner, and B. J. Tromberg, "Frequency-domain photon migration measurements of normal and malignant tissue optical properties in a human subject," *Appl. Opt.* **36**(1), 10–20 (1997).
28. R. M. P. Doornbos, R. Lang, M. C. Aalders, F. W. Cross, and H. J. C. M. Sterenborg, "The determination of *in vivo* human tissue optical properties and absolute chromophore concentrations using spatially resolved steady-state diffuse reflectance spectroscopy," *Phys. Med. Biol.* **44**, 967–981 (1999).
29. S. C. Chang, G. Buonaccorsi, A. MacRobert, and S. G. Bown, "Interstitial and transurethral photodynamic therapy of the canine prostate using meso-tetra-(m-hydroxyphenyl) chlorin," *Int. J. Cancer* **67**(4), 555–562 (1996).
30. T. J. Vogl, K. Eichler, M. G. Mack, S. Zangos, C. Herzog, A. Thalhammer, and K. Engelmann, "Interstitial photodynamic laser therapy in interventional oncology," *Eur. Radiol.* **14**(6), 1063–1073 (2004).
31. S. C. Chang, G. A. Buonaccorsi, A. J. MacRobert, and S. Bown, "Interstitial photodynamic therapy in the canine prostate with disulfonated aluminum phthalocyanine and 5-aminolevulinic acid-induced protoporphyrin IX," *Prostate* **32**(2), 89–98 (1997).
32. J. P. Rovers, M. L. de Jode, and M. F. Grahn, "Significantly increased lesion size by using the near-infrared photosensitizer 5,10,15,20-tetrakis (m-hydroxyphenyl) bacteriochlorin in interstitial photodynamic therapy of normal rat liver tissue," *Lasers Surg. Med.* **27**(3), 235–240 (2000).
33. L. K. Lee, C. Whitehurst, Q. Chen, M. L. Pantelides, F. W. Hetzel, and J. V. Moore, "Interstitial photodynamic therapy in the canine prostate," *Br. J. Urol.* **80**(6), 898–902 (1997).
34. I. Wang, S. Andersson-Engels, G. E. Nilsson, K. Wårdell, and K. Svanberg, "Superficial blood flow following photodynamic therapy of malignant skin tumours measured by laser Doppler perfusion imaging," *Br. J. Dermatol.* **136**, 184–189 (1997).
35. B. W. McIlroy, A. Curnow, G. Buonaccorsi, M. A. Scott, S. G. Bown, and A. J. MacRobert, "Spatial measurement of oxygen levels during photodynamic therapy using time-resolved optical spectroscopy," *J. Photochem. Photobiol., B* **43**(1), 47–55 (1998).
36. T. H. Foster, R. S. Murant, R. G. Bryant, R. S. Knox, S. L. Gibson, and R. Hilf, "Oxygen consumption and diffusion effects in photodynamic therapy," *Radiat. Res.* **126**, 296–303 (1991).
37. A. M. K. Nilsson, R. Berg, and S. Andersson-Engels, "Measurements of the optical properties of tissue in conjunction with photodynamic therapy," *Appl. Opt.* **34**(21), 4609–4619 (1995).
38. Q. Chen, B. C. Wilson, S. D. Shetty, M. S. Patterson, J. C. Cerny, and F. W. Hetzel, "Changes in in vivo optical properties and light distributions in normal canine prostate during photodynamic therapy," *Radiat. Res.* **147**(1), 86–91 (1997).
39. J. P. A. Marijnissen and W. M. Star, "Quantitative light dosimetry in vitro and in vivo," *Lasers Med. Sci.* **2**, 235–242 (1987).
40. J. Svensson, A. Johansson, K. Svanberg, and S. Andersson-Engels, "Tissue temperature monitoring during interstitial photodynamic therapy," *Proc. SPIE* **5698**, 126–136 (2005).
41. A. M. K. Nilsson, G. W. Lucassen, W. Verkruysse, S. Andersson-Engels, and M. J. C. van Gemert, "Optical properties of human whole blood—changes due to slow heating," *Proc. SPIE* **2923**, 24–34 (1996).
42. S. Jaywant, B. C. Wilson, M. Patterson, L. Lilge, T. Flotte, J. Woolsey, and C. McCulloch, "Temperature dependent changes in the optical absorption and scattering spectra of tissues: correlation with ultrastructure," *Proc. SPIE* **1882**, 218–229 (1993).
43. M. Hiraoka, M. Firbank, M. Essenpreis, M. Cope, S. R. Arridge, P. van der Zee, and D. T. Delpy, "A Monte Carlo investigation of optical pathlength in inhomogeneous tissue and its application to near-infrared spectroscopy," *Phys. Med. Biol.* **38**(12), 1859–1876 (1993).
44. M. Soto Thompson, S. Andersson-Engels, S. Svanberg, T. Johansson, S. Pålsson, N. Bendsoe, U. Stenram, A. Derjabo, J. Kapostins, J. Spigulis, and K. Svanberg, "Photodynamic therapy of basal cell carcinoma with multi-fibre contact light delivery," *J. Environ. Pathol. Toxicol. Oncol.* **25**(1–2), 411–424 (2006).
45. J. H. Woodhams, L. Kunz, S. G. Bown, and A. J. MacRobert, "Correlation of real-time haemoglobin oxygen saturation monitoring during photodynamic therapy with microvascular effects and tissue necrosis in normal rat liver," *Br. J. Cancer* **91**(4), 788–794 (2004).
46. Q. Peng, A. M. Soler, T. Warloe, J. M. Nesland, and K. E. Giercksky, "Selective distribution of porphyrins in skin thick basal cell carcinoma after topical application of methyl 5-aminolevulinate," *J. Photochem. Photobiol., B* **62**(3), 140–145 (2001).
47. L. O. Svaasand, P. Wyss, M. T. Wyss, Y. Tadir, B. J. Tromberg, and M. W. Berns, "Dosimetry model for photodynamic therapy with topically administered photosensitizers," *Lasers Surg. Med.* **18**, 139–149 (1996).
48. J. T. H. M. van den Akker, J. A. Holroyd, D. I. Vernon, H. J. C. M. Sterenborg, and S. B. Brown, "Comparative in vitro percutaneous penetration of 5-aminolevulinic acid and two of its esters through excised hairless mouse skin," *Lasers Surg. Med.* **33**(3), 173–181 (2003).
49. T. Svensson, J. Swartling, P. Taroni, A. Torricelli, P. Lindblom, C. Ingvar, and S. Andersson-Engels, "Characterization of normal breast tissue heterogeneity using time-resolved near-infrared spectroscopy," *Phys. Med. Biol.* **50**, 2559–2571 (2005).

Paper VI

Influence of treatment-induced changes in tissue absorption on treatment volume during interstitial photodynamic therapy of thick skin tumors

A. Johansson, N. Bendsoe, K. Svanberg, S. Svanberg,
S. Andersson-Engels.

Medical Laser Applications **21**, 261-270 (2006).

Available online at www.sciencedirect.com
ScienceDirect
Medical Laser Application 21 (2006) 261–270
Medical Laser Application
www.elsevier.de/mla

Influence of treatment-induced changes in tissue absorption on treatment volume during interstitial photodynamic therapy

Ann Johansson[a,*], Niels Bendsoe[b], Katarina Svanberg[c], Sune Svanberg[a], Stefan Andersson-Engels[a]

[a]*Lund University, Department of Physics, PO Box 118. SE-221 00 Lund, Sweden*
[b]*Lund University Hospital, Department of Dermatology and Venereology, PO Box 118, SE-221 00 Lund, Sweden*
[c]*Lund University Hospital, Department of Oncology, PO Box 118. SE-221 00 Lund, Sweden*

Received 2 July 2006; accepted 2 August 2006

Abstract

Interstitial photodynamic therapy on thick skin lesions has been shown to induce changes in tissue light transmission as a direct consequence of variations in total blood volume and oxygen saturation. A finite element method was used in order to simulate the fluence rate distribution and total light dose throughout the target tissue for two cases. The first case constitutes a pre-treatment model where the tissue optical properties are assumed constant during the entire treatment. The second situation takes into account observed changes in tissue light transmission, small deviations in fiber insertion depth and a few cases of almost complete loss of source fiber output power possibly as a result of blood accumulation in front of the fiber tip. The pre- and post-treatment models from six clinical treatments are compared in terms of simulated treatment volumes. We conclude that real-time monitoring of the delivered fluence is necessary in order to ascertain a pre-determined light dose to the target tissue. Finally, we speculate on how to also include the sensitizer fluorescence level and tissue oxygenation in the real-time treatment feedback.

Keywords: Interstitial photodynamic therapies; δ-aminolevulinic acid; Protoporphyrin IX; Dosimetry

Introduction

Photodynamic therapy (PDT) is a cancer treatment modality that has been used successfully in the treatment of thin and superficially situated non-melanoma skin malignancies [1]. PDT relies on a sensitizer being activated by light in the presence of oxygen, leading to the production of toxic singlet oxygen radicals. Tissue destruction results from apoptosis, necrosis and vascular damage caused by these radicals [2,3].

δ-aminolevulinic acid (ALA)-induced protoporphyrin IX (PPIX) has since long been in clinical practice for the treatment of various skin malignancies, e.g. actinic keratosis, an indication for which it also holds FDA approval. The clinical treatment procedure involves topical ALA administration and superficial irradiation. Most often, standardized light delivery conditions are used where the irradiance at the therapeutic wavelength is kept constant throughout the treatment and the illumination time is determined by the requirement to deliver a pre-determined incident light dose, expressed in J/cm^2. Such a simplified dose metric ignores parameters such as depth of the lesion, sensitizer concentration and

*Corresponding author. Tel.: +46 462223120 ; fax: +46 462224250.
E-mail address: Ann.Johansson@fysik.lth.se (A. Johansson).

1615-1615/$ - see front matter © 2006 Elsevier GmbH. All rights reserved.
doi:10.1016/j.mla.2006.08.002

tissue oxygenation status throughout the target tissue. Among other things, these simplifications might explain the highly variable PDT effect, where the recurrence rate [4] and necrotic volume [5] display large variations despite using a constant light dose.

Several research groups have worked along the lines of implementing an implicit dosimetry model, in which a single parameter is used as dose metric [6]. Boere et al. [7] have found a good correlation between the initial sensitizer decay rate and treatment effect. This connection can be explained by a singlet oxygen-mediated sensitizer photobleaching [8], where the treatment-induced oxygen radicals attack both the target tissue and the photosensitizer itself. In contrast to implicit dosimetry, explicit dosimetry relies on measuring all three dose parameters, i.e. the fluence rate, sensitizer concentration and tissue oxygenation, independently. To date, no clinical practice exists that relies on an explicit dosimetry model. This might partly be explained by the difficulties associated with trying to monitor each of the parameters involved, inherently requiring a lot of instrumentation. It is yet uncertain exactly how a PDT dose should be defined in order to exhibit the correct dependence on the light fluence rate, the sensitizer concentration and the tissue oxygenation.

In an effort to extend the possible indications for PDT to also include thick and deeply situated lesions, we have developed an instrument for interstitial PDT (IPDT), where optical fibers inserted into the tumor are used to deliver the therapeutic irradiation. An early version of the system allowed for monitoring of the therapeutic light flux during the treatment using the same fibers as for therapeutic light delivery [9]. A more recent instrument offers the possibility to also monitor sensitizer fluorescence and tissue oxygen saturation [10]. Initial clinical trials on thick skin tumors have utilized six bare-ended fibers for light delivery and treatment monitoring. Data collected during the first ten treatments indicated significant variations in tissue light transmission and rapid sensitizer photobleaching [11]. The treatment-induced increase in absorption was found to be consistent with an increase in tissue average blood content and tissue de-oxygenation.

In this paper, we investigate the actual PDT dose being delivered during the treatments performed and compare it to a pre-treatment model. According to clinical practice, the PDT dose is based on the light fluence only. The analysis is based on a subset of previously published data, see Refs. [10–12]. While earlier publications highlight instrument performance and real-time monitoring of the fluence rate, sensitizer fluorescence and tissue oxygenation during treatment, here we focus on comparing treatment volume as predicted by pre- and post-treatment models of the fluence distribution. The fluence rate distribution inside the target tissue is modeled using the finite element method and the diffusion approximation. The pre-treatment model, which was used to determine approximate irradiation times prior to each treatment session, assumes constant tissue optical properties. This model is contrasted to a simulation where the tissue light transmission is allowed to vary according to the data from the clinical treatments. The comparison reveals significant differences in treatment volume as predicted by the pre- and post-treatment models of the fluence distribution. These results indicate a need for individualized treatment monitoring in order to deliver the predetermined PDT dose to the entire target tissue.

Materials and methods

Patients and treatment procedure: Ten treatments utilizing IPDT combined with simultaneous monitoring of light fluence rate, sensitizer photobleaching and tissue oxygen saturation were performed on eight patients with thick non-melanoma skin lesions. The lesions were photosensitized with methyl-esterified aminolevulinic acid (ALA-ME, MEDAC GmbH, Hamburg, Germany) either topically or both topically and intra-tumorally. Six sterilized optical fibers, hereafter referred to as the patient fibers, were inserted into the tumor mass at predetermined positions and utilized for both therapeutic light delivery and treatment monitoring. Further details on patients and treatment procedure can be found in Ref. [11]. Here we present data only from six of the treatment sessions where full data sets exist, see Table 1. These patients were all diagnosed as nodular basal cell carcinomas. IPDT was performed as part of a combined treatment where patients also received topical Efudix cream containing Fluorouracil.

Instrumentation: The setup of the IPDT instrument is shown in Fig. 1 and a more detailed description is given elsewhere [10,11]. The instrument allows for therapeutic light delivery and treatment monitoring via six 400-μm diameter optical fibers. While in treatment mode, light from the therapeutic light unit, consisting of six diode lasers emitting at 635 nm, is guided into the distribution module and directed into the patient fibers.

Occasionally the therapeutic irradiation is interrupted in order to perform measurement sequences, during which light from each of the two diagnostic light sources is successively coupled into each of the six patient fibers. The term ''diagnostic'' is used here to describe the progression of the treatment and does not refer to diagnosis of the patient's status. Utilizing the first diagnostic light source, a diode laser with the same wavelength as the treatment lasers, the detected signals at 635 and 705 nm are used to monitor tissue absorption and sensitizer photobleaching, respectively. The second light source within the diagnostic light unit consists of a

Table 1

Treatment	Lesion size (mm)	Delivered energy per fiber (J)	ALA administration	Treatment result	ΔHb_{tot} (μM)	Functional fibers	Fiber output power (mW)
1	12 × 14 × 3	30	Topical	~10% response	+38	6 (6)	75
2	12 × 14 × 7	30	Topical	>50% response	±0	6 (6)	100
3	30 × 25 × 3	83	Topical	75% response	+29	6 (6)	75
4	20 × 20 × 1	23	Topical + it.	100% response	+11	6 (6)	75
5	20 × 20 × 5	34	Topical + it.	~10% response	+28	4 (6)	75
6	20 × 20 × 4	45	Topical + it.	>50% response	−18	6 (6)	75

it. – intra-tumoral ALA administration. ΔHb_{tot} denotes the change in total blood volume found during the treatment. Functional fibers denote the number of fibers that were not characterized by almost complete loss of signal. For details on these parameters, see the following section.

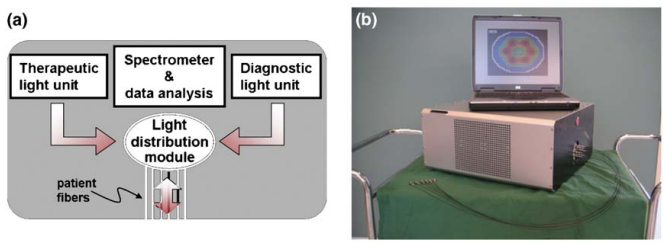

Fig. 1. (a) Schematic drawing of IPDT instrument. (b) Digital photograph of the instrument.

near-infrared LED covering the spectral range 760–810 nm and is used to measure the tissue optical density within this spectral interval. Based on the tissue absorbance, changes in oxy- and deoxy-hemoglobin concentration are calculated and the total blood content and oxygen saturation are monitored. The measurement sequences are performed prior to commencing therapeutic light delivery and at varying time intervals during the entire treatment and thereby give information on the temporal profile of the fluence rate, the PPIX fluorescence level and the tissue oxygenation. Refs. [10,11] give more details on instrument function and data analysis.

Pre-treatment model of the fluence distribution: A pre-treatment simulation of the fluence distribution was performed in order to predict the necessary treatment time. For this simulation, the tumor geometry was approximated with a flat disk with elliptical cross section where the radii and depth were assessed by visual inspection and palpation by an experienced oncologist. In order to give as homogenous fluence rate distribution within the tumor as possible, while sparing normal surrounding tissue, the fibers were evenly distributed along the periphery of an elliptical cross section at a radial position of approximately 7/10 of the tumor radius. The fiber insertion depth was equal to half the tumor thickness.

The finite element method (FEM) (Femlab® 3.1, Comsol AB, Stockholm, Sweden) was used to model the fluence rate distribution within the target tissue and normal tissue in close proximity to the lesion. The geometry consisted of the cylindrically shaped lesion within a semi-infinite homogeneous medium. The fluence rate, $\phi(\mathbf{r})$, was determined by solving the steady-state diffusion equation [13]:

$$\nabla^2\phi - \mu_{\mathrm{eff}}^2\phi = \sum_i S(r_i) \quad i = 1 \ldots 6 \tag{1}$$

where $\mu_{\mathrm{eff}} = \left[3\mu_a\left(\mu_a + \mu_s'\right)\right]^{1/2}$, μ_a and μ_s' are the effective attenuation, absorption and reduced scattering coefficients, respectively. In the pre-treatment model, these parameters were assumed constant and were set to 0.3 and 12 cm^{-1} for the absorption and reduced scattering coefficient, respectively [14]. The bare-ended fibers, constituting the source term, $\sum S(\mathbf{r}_i)$, were modeled as isotropic point sources positioned at a distance $1/\mu_s'$ in front of the actual fiber surfaces.

A Robin-type boundary condition (RBC) was used for the tissue–air interface when solving Eq. (1) [15]. The total fluence, expressed in J/cm^2, throughout the tumor volume was calculated by multiplying the fluence rate distribution, expressed in W/cm^2, with the irradiation time. The isodose surface at 50 J/cm^2 was set to represent the treatment volume [9]. The irradiation time was determined by the condition to deliver a fluence exceeding the threshold dose to every part of the lesion. Unfortunately, a different boundary condition was used at the time of using the pre-treatment model for determining the necessary treatment time. Therefore, despite using the same set of optical properties, the total treatment volume as predicted by the current pre-treatment model utilizing the RBC does not include the entire tumor volume for all treatment sessions.

Post-treatment model of the fluence distribution: The post-treatment model of the fluence distribution is based on in vivo clinical data. During each treatment session, the 635-nm light transmission was monitored between all possible source–detector fiber combinations. Thus, any treatment-induced changes in tissue light absorption within the treatment volume were tracked. We differentiate between two cases: on one hand, a moderate change in tissue light transmission (less than $\pm 50\%$) and on the other a rapid decrease of the transmission signal to less than 20% of the initial signal. The latter situation we believe is due to considerable blood pooling at the fiber tip and clearly prevents a sufficient light dose to reach the target tissue. In the post-treatment model, this situation is implemented by setting the output power of these fibers to zero starting at the time point of the detected signal loss.

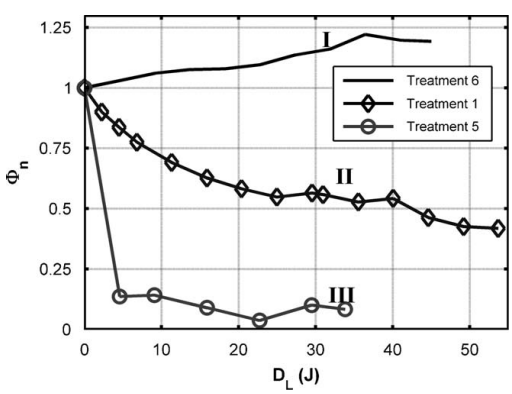

Fig. 2. Normalized light transmission between patient fibers as a function of the delivered energy. Curves I and III represents extreme measurements, while curve II is typical. The rapid signal reduction as illustrated by curve III is indicative of significant blood pooling in front of the fiber tip.

In the situation where the transmission changes are not as drastic, see Fig. 2, the transmission signals are assumed to vary solely due to changes in the total absorption coefficient in the entire probed treatment volume. The analysis relies on the assumption of diffuse light propagation and validity of the extrapolated boundary condition. The reduced scattering coefficient and the initial absorption coefficient are defined as above. Furthermore, assuming the absorption change is homogeneous within the region probed by a certain fiber pair, see Fig. 4(a), the following equation expresses the light transmission normalized with respect to the initial value in terms of the fiber positions and the tissue absorption and reduced scattering coefficients:

$$\frac{T(t)}{T(0)} = \frac{\mu_a(t)+\mu_s'}{\mu_a(0)+\mu_s'} \times \left[\frac{\exp\left(-\mu_{eff}(t)r_1\right)}{r_1} - \frac{\exp\left(-\mu_{eff}(t)r_2\right)}{r_2}\right] \times \left[\frac{\exp\left(-\mu_{eff}(0)r_1\right)}{r_1} - \frac{\exp\left(-\mu_{eff}(0)r_2\right)}{r_2}\right]^{-1} \quad (2)$$

Here r_1 expresses the source–detector fiber separation, $r_1 = \left[\rho^2 + (\Delta z)^2\right]^{1/2}$, where ρ denotes the radial inter-fiber separation and Δz is any possible fiber insertion depth difference found when withdrawing fibers at the completion of the treatment. The other distance, r_2, expresses the distance between detection fiber and the imaginary point source introduced to satisfy the extrapolated boundary condition. $r_2 = \left[\rho^2 + (z_{sf} + z_{df} + 2z_0 + 2z_b)^2\right]^{1/2}$, where z_{sf} and z_{df} denote the insertion depth of the source and detection fiber, respectively. Furthermore, $z_0 = 1/\mu_s'$ and $z_b = 2z_0$ [16].

When including transmission signals between all possible combinations of source–detector fibers, each measurement sequence results in 30 data points. Reciprocal signals, i.e. transmission signals both from fiber *X–Y* and from fiber *Y–X*, are then averaged reducing the number to 15. Eq. (2) is employed to solve for the time-dependent absorption coefficient, $\mu_a(t)$ for each source–detector configuration. The 15 transmission signals probe different tissue volumes and the resulting absorption coefficients represent a coarse average of the tissue absorption at 635 nm within these regions. In order to create a map of the spatially varying absorption coefficient, a Voronoi diagram is created utilizing Matlab's (Matlab®, The MathWorks Inc., Natick, MA) function "voronoi". Here, the midpoints between each source–detector fiber pair are used as generating points. The entire volume is then partitioned into 15 convex polygons such that each polygon contains exactly one generating point and every point in a given polygon is closer to its generating point than to any other. The absorption coefficient is assumed constant within each polygon and the same map is used

throughout the entire depth of the lesion. Based on measurement data, corresponding discretized maps of the absorption coefficient are created for each measurement sequence during the entire treatment session. These maps are then loaded into Femlab and a FEM simulation of the fluence rate distribution for each of the diagnostic time points is performed. The steady-state diffusion equation, source terms and boundary conditions as described in the previous section are used. Multiplying the modeled fluence rate distribution with the length of the following treatment sequence and adding the fluence delivered during each of the treatment sequences gives the total fluence for each treatment session. The pre- and post-treatment models are compared in terms of the fluence distribution and the tissue volume defined by the isodose surface at $50\,J/cm^2$ for each of the treatments listed in Table 1.

Results

Examples of measured temporal profiles of the light transmission between patient fibers are shown in Fig. 2. Each curve has been normalized to its initial value. Curve I was acquired during treatment 6 with a source–detector separation of 7 mm. This patient had previously undergone radiation therapy, perhaps leading to less vascularized target tissue. The edema resulting from the fiber insertion and the photodynamic effect might have caused a more transparent tissue. Curve II was measured utilizing fibers with a source–-detector separation of 8 mm. The fibers were placed in opposite quadrants of the target volume so that the detected light had probed the center of the lesion. The third curve illustrates the rapid signal decrease that could possibly be explained by significant blood accumulation in front of the fiber tip. Out of a total of 60 fiber insertions in 10 patients, this signal behavior could be identified in four cases [12], including two fibers during treatment 5, see Table 1.

Fig. 3(a) shows the average of the normalized light transmission between neighboring fibers during treatment 1. The relatively small standard deviations, illustrated by the error bars, indicate rather homogeneous absorption changes within the entire lesion. As published earlier, we have found a significant decrease in tissue light transmission in seven of nine completed treatments [10,11]. These transmission changes were found to agree with a change in the average tissue blood content and oxygenation status. The minor deviations in fiber insertion depth found upon withdrawing the patient fibers were calculated to influence the light transmission between neighboring fibers only $\pm 5\%$ for the set of initial optical properties used in the simulations. The blood volume and tissue oxygen saturation

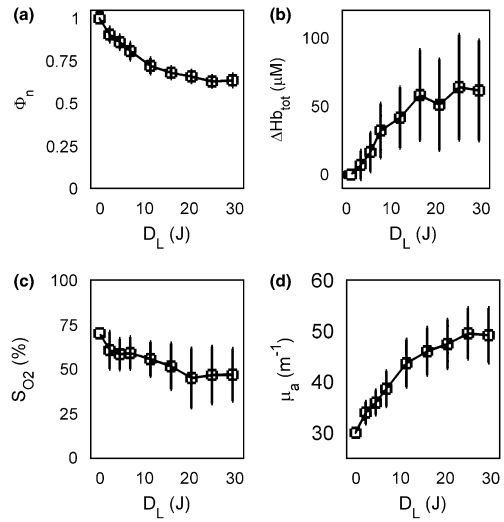

Fig. 3. (a) Normalized light transmission averaged over signals between neighboring fibers as a function of delivered energy during the treatment. (b) Average change in total hemoglobin content. (c) Average change in tissue oxygen saturation level. (d) Average increase in tissue absorption coefficient. Data is from treatment 1 and error bars denote standard deviations.

corresponding to the data in Fig. 3(a) are shown in Fig. 3(b) and (c), respectively. No evidence of hypoxic regions was found in any of the treatments. Fig. 3(d) shows the average tissue absorption increase where Eq. (2) and the data shown in Fig. 3(a) have been utilized. One should note that the data shown in this figure have been averaged over neighboring fibers only.

Fig. 4(a) shows the typical source configuration used in the treatments. Shaded areas indicate tissue areas probed by light transmitted from fiber 1. Transmission signals between neighboring fibers, such as fibers 1 and 2, mostly probe the outer volumes of the lesion. On the other hand, transmission signals between for example fibers 1 and 4 are used for calculating the tissue absorption coefficient within the tumor center. Fig. 4(b) shows the spatially varying absorption coefficient calculated utilizing all transmission signals at the end of treatment 1.

Dose volume histograms (DVHs) provide information on the fractional volume of the tissue of interest that receive a certain treatment dose and have been used in radiation treatment planning [17]. DVHs for the planned and actual fluence distribution, as determined by the pre- and post-treatment models, respectively, were compared in order to study the influence of the treatment-induced absorption changes and possible blood accumulation in front of the fiber tip on treatment volume. Fig. 5(a) and (b) show the fluence DVHs for

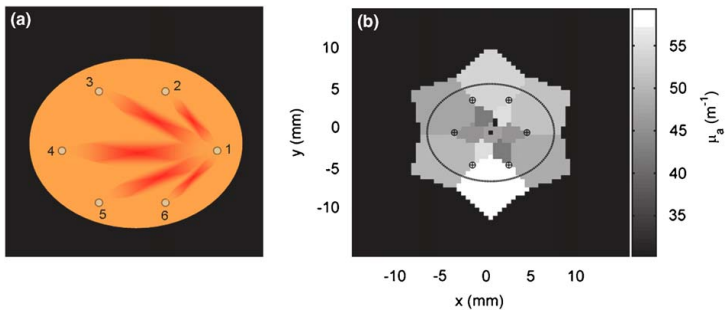

Fig. 4. (a) Fiber configuration used in treatment 1–6. Shaded regions indicate approximate areas probed by fiber 1. (b) Map of evaluated absorption coefficient as a function of position at the end of treatment 1. The tumor periphery and fiber positions are indicated.

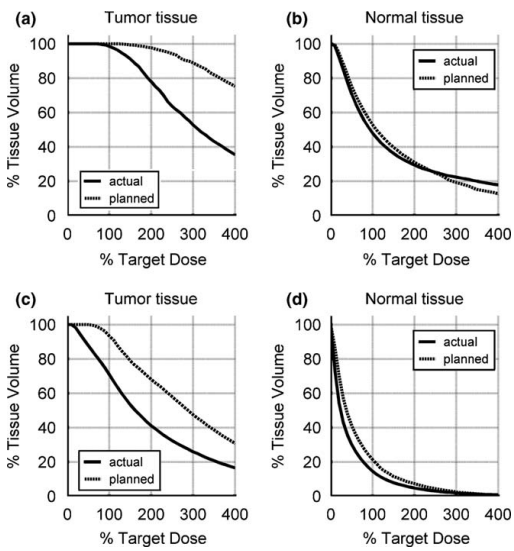

Fig. 5. Dose volume histograms for (a) target, and (b) normal tissue for treatment 1. (c) and (d) Corresponding data for treatment 5. In (a) and (c), the 100% target dose grid line can be used as a modeled estimate of the fraction of the tumor treated.

target and normal tissue for treatment 1. For this analysis, normal tissue was defined as non-target tissue voxels up to 3 mm outside the lesion. As can be seen, the pre-treatment model slightly overestimated the total irradiation time, leading to a minimum of approximately 150% of the threshold dose being delivered to the target tissue. The fluence DVH corresponding to the post-treatment model indicates a significantly lower fluence within the lesion. Fig. 5(c) and (d) illustrate the actual and planned fluence DVHs for lesion and normal tissue, respectively, for treatment 5. The loss of sufficient output energy from two fibers during this treatment clearly had a large impact on the treatment volume as displayed by the two curves in Fig. 5(c) For Fig. 5(a) and (c), the fraction of the target volume receiving a full light dose, i.e. corresponding to 100% target dose, can be seen as an indication of the treatment volume. Fig. 6(a) and (b) show the iso-surfaces at the threshold dose of 50 J/cm^2 for treatment 5 fluence model, respectively. Here it is obvious that large tissue volumes were undertreated.

As a summary of how the treatment-induced changes in tissue light transmission, possible blood accumulation at the source fiber surfaces and slight deviations in fiber insertion depth influenced the fluence distribution within the target tissue for treatments 1–6, Fig. 7 shows the ratio of the fluence DVHs for the post-treatment model to the pre-treatment model. Taking the fluence DVH ratio at the 100% threshold dose as an indication of how well the actual treatment targeted the planned treatment volume, a significant undertreatment is evident in three of the six treatments. Corresponding ratio for normal tissue varied within ± 0.2 except for treatment 5. As a result of one fiber depth increasing by 2 mm during the treatment, normal tissue received a significantly higher light dose than planned for this particular treatment.

Discussion

IPDT has been introduced with the aim to treat thick and/or deeply lying lesions. The use of several light delivery fibers makes it possible to target irregularly shaped lesions provided there is a careful light dosimetry. As shown in earlier work, the insertion of optical fibers and the therapeutic irradiation itself introduce changes in the tissue composition such as blood volume changes, tissue deoxygenation and edema [11]. These alterations affect the light distribution during the treatment and thereby the treatment volume.

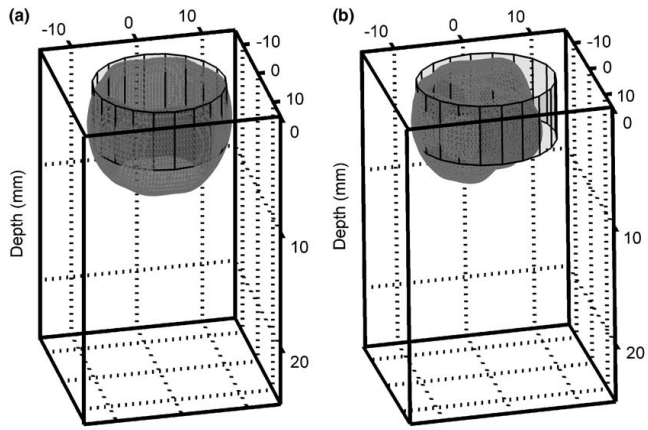

Fig. 6. (a) Isosurface at 50 J/cm^2 according to the pre-treatment model for treatment 5. (b) Corresponding isosurface from the post-treatment model taking into account increase in tissue absorption, loss of sufficient output power in two patient fibers and slightly altered fiber positions during the treatment.

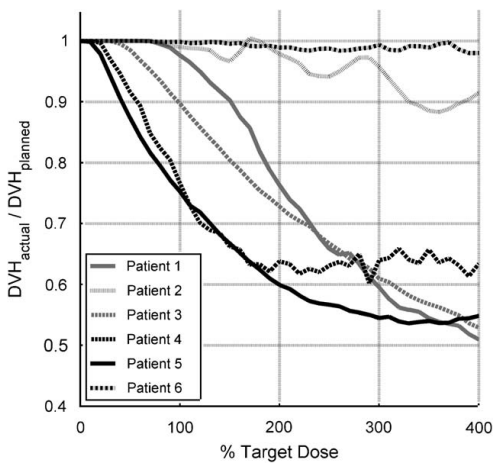

Fig. 7. Ratio of the actual to the planned fluence DVH curves for tumor tissue for treatments 1–6.

In this work, we compare the modeled treatment volumes as predicted by pre- and post-treatment fluence simulations. The pre-treatment model assumes constant optical properties and a set of near-optimal source fiber positions, whereas the post-treatment model takes into account any changes in tissue light transmission, blood accumulation in front of any source fiber that limits the delivered energy and possible deviations in fiber insertion depth. The DVHs for the fluence distribution resulting from the two models indicate varying degrees of undertreatment in three of the six treatments published here. With the source fiber configuration used in this work, volumes that receive a light dose just below the pre-determined threshold dose appear at or near the lesion periphery. Since tumors proliferate mainly from these regions, the limited fluence within these regions might have detrimental consequences for the long-term treatment outcome. Due to the low number of completed treatments, no correlation between predicted and actual treatment outcome was yet been attempted. The modeled fluence distribution revealed that surrounding tissue receiving high light doses were situated close to the tumor bed. Overtreating these regions might effectively prohibit tumor growth.

The aim with the instrument used in this study is to introduce real-time treatment feedback in order to ascertain a certain light dose to every part of the tumor despite treatment-induced changes in tissue light transmission. The present and previous studies reveal significant intra- and inter-patient variations in fluence rate distribution, indicating the need to monitor each individual treatment. Judging by the huge impact the loss of one or several source fibers has on the total treatment volume, it is especially important to avoid blood accumulation at the fiber emission surface. Situations where this occurs can perhaps be avoided by re-positioning the fiber or drainage through hollow catheters guiding the optical fibers. The execution time required for creating a three-dimensional map of the absorption coefficient and simulating the fluence rate distribution by FEM is on the order of one minute. In relation to the total treatment time, this rather short execution time allows for on-line treatment feedback in order to compensate for detected changes in light transmission.

We are presently extending our dosimetry model to also include the sensitizer concentration and tissue oxygenation. Future work needs to address in what way these signals should influence treatment parameters such as output power, irradiation time and irradiation fractionation. Following systemic administration of ALA, irradiation fractionation with dark intervals on the order of a couple of minutes has been shown to induce three times more necrosis than continuous therapeutic irradiation, an effect that has been explained by tissue reoxygenation during the dark periods [5]. When detecting hypoxic regions, halting the therapeutic irradiation in order to allow re-oxygenation of the tissue might thus improve treatment outcome. Since tissue reoxygenation has been demonstrated during dark intervals on the order of 5–45 s [18], the measurement sequences associated with the treatment monitoring might be sufficient to revoke possible hypoxia. Decreasing the individual fiber output power is another strategy for avoiding local hypoxia that has been shown to improve treatment efficacy [19,20]. Finally, the sensitizer fluorescence level can of course be used as an indication of its concentration. In addition, the initial rate of photobleaching can be used as an indicator of the oxygen concentration within the target tissue along the lines of implicit dosimetry according to Wilson et al. [6].

In conclusion, the comparison between treatment volumes predicted by pre- and post-treatment simulations of the fluence distribution reveal significant differences. The treatment-induced variations in tissue absorption prevented a sufficient light dose from being deposited to the peripheral regions of the lesion in 50% of the cases reported on here. We conclude that real-time treatment supervision and feedback is essential in order to fully ascertain the predetermined light dose. We further speculate on how the light dosimetry model can be extended to also include other parameters under supervision, such as the sensitizer fluorescence level and the tissue oxygen saturation.

Acknowledgements

The authors would like to acknowledge Thomas Johansson and Marcelo Soto Thompson for technical support and SpectraCure AB for financial support.

Zusammenfassung

Der Einfluss therapieinduzierter Veränderungen der Gewebeabsorption auf das Behandlungsvolumen während der interstitiellen photodynamischen Therapie

Bei der interstitiellen photodynamischen Therapie dicker Hautläsionen hat sich herausgestellt, dass Veränderungen in der Gewebelichttransmission erzeugt werden, was eine unmittelbare Folge der Schwankungen des Gesamtblutvolumens und der Sauerstoffsättigung ist. Zur Simulation der Energiedichte- und der Gesamtlichtdosisverteilung im Zielgewebe wurde in zwei Fällen eine Finite-Elemente-Methode angewandt. Im ersten Fall wird ein Modell des Zustandes vor der Behandlung festgelegt, bei dem die gewebeoptischen Eigenschaften während der gesamten Therapie als konstant angenommen werden. Bei der zweiten Simulation werden beobachtete Veränderungen der Gewebelichttransmission, geringe Abweichungen der Fasereinführungstiefe und vereinzelte Fälle von nahezu vollständigem Ausgangsleistungsverlust der Faser, möglicherweise verursacht durch vor der Faserspitze angesammeltes Blut, berücksichtigt. Die Modelle mit dem Gewebezustand vor und nach der Behandlung aus sechs klinischen Therapien werden in Bezug auf die simulierten Behandlungsvolumen verglichen. Wir kommen zu dem Schluss, dass zur Sicherstellung einer im Voraus festgelegten Lichtdosis im Zielgewebe ein Echtzeitmonitoring der abgegebenen Energiedichte erforderlich ist. Schließlich überlegen wir, wie auch das Fluoreszenzniveau des Photosensibilisators und der Sauerstoffgehalt des Gewebes in das Echtzeitbehandlungsfeedback einbezogen werden könnten.

Schlüsselwörter: Interstitielle photodynamische Therapie; δ-Aminolävulinsäure; Protoporphyrin IX; Dosimetrie

Resúmen

Influencia de los cambios de absorción del tejido inducidos por tratamiento con terapia intersticial fotodinámica en el volumen del tratamiento

Se ha demostrado que la terapia fotodinámica intersticial de lesiones cutáneas gruesas provoca cambios en la transmisión de la luz del tejido como consecuencia directa de variaciones en el volumen total de sangre y la saturación de oxígeno. Para simular la distribución de la velocidad de fluencia y la dosis total de luz a través del tejido blanco, se utilizó el Método de Elementos Finitos en dos casos. El primero, constituye un modelo de pre-tratamiento en el que se asume que las propiedades ópticas del tejido son constantes durante todo el tratamiento. En el segundo, se tienen en cuenta los cambios observados en la transmisión de luz del tejido, pequeñas desviaciones en la profundidad de inserción de la fibra y algunos casos en los que se produjo una pérdida completa de salida de potencia de la fibra, probablemente como resultado de la acumulación de sangre en la punta de la misma. Los modelos de pre- y pos- tratamiento de 6 casos clínicos fueron comparados en términos de volúmenes de tratamiento. Hemos concluido que el monitoreo en tiempo real de la fluencia aplicada es necesario a fin de establecer una

dosis predeterminada sobre el tejido blanco. Y finalmente hemos considerado cómo podría integrarse la determinación del nivel de fluorescencia del sensibilizador y de la oxigenación del tejido durante el seguimiento en tiempo real del tratamiento.

Palabras claves: Terapia fotodinámica intersticial; ácido δ-aminolevulínico; Protoporfirina IX; Dosimetría

References

[1] Peng Q, Warloe T, Berg K, Moan J, Kongshaug M, et al. 5-aminolevulinic acid-based photodynamic therapy: clinical research and future challenges. Cancer 1997;79: 2282–308.
[2] Noodt BB, Berg K, Stokke T, Peng Q, Nesland JM. Apoptosis and necrosis induced with light and 5-aminolaevulinic acid-derived protoporphyrin IX. Br J Cancer 1996;74:22–9.
[3] Roberts DJH, Cairnduff F, Driver I, Dixon B, Brown SB. Tumor vascular shutdown following photodynamic therapy based on polyhematoporphyrinor 5-aminolevulinic acid. Int J Oncol 1994;5:763–8.
[4] Calzavara-Pinton PG. Repetitive photodynamic therapy with topical δ-aminolaevulinic acid as an appropriate approach to the routine treatment of superficial non-melanoma skin tumours. J Photochem Photobiol B: Biol 1995;29:53–7.
[5] Curnow A, Haller JC, Bown SG. Oxygen monitoring during 5-aminolaevulinic acid induced photodynamic therapy in normal rat colon. Comparison of continuous and fractionated light regimes. J Photochem Photobiol B: Biol 2000;58:149–55.
[6] Wilson BC, Patterson MS, Lilge L. Implicit and explicit dosimetry in photodynamic therapy: a new paradigm. Laser Med Sci 1997;12:182–99.
[7] Boere IA, Robinson DJ, de Bruijn HS, van den Boogert J, Tilanus HW, Sterenborg HJCM, et al. Monitoring in situ dosimetry and protoporphyrin IX fluorescence photobleaching in the normal rat esophagus during 5-aminolevulinic acid photodynamic therapy. Photochem Photobiol 2003;78:271–2.
[8] Ericson MB, Grapengiesser S, Gudmundson F, Wennberg AM, Larko O, Moan J, et al. A spectroscopic study of the photobleaching of protoporphyrin IX in solution. Laser Med Sci 2003;18:56–62.
[9] Johansson T, Soto Thompson M, Stenberg M, af Klinteberg C, Andersson-Engels S, Svanberg S, et al. Feasibility study of a novel system for combined light dosimetry and interstitial photodynamic treatment of massive tumors. Appl Opt 2002;41:1462–8.
[10] Soto Thompson M, Johansson A, Johansson T, Andersson-Engels S, Bendsoe N, Svanberg K, et al. Clinical

system for interstitial photodynamic therapy with combined on-line dosimetry measurements. Appl Opt 2005; 44:4023–31.

[11] Johansson A, Johansson T, Soto Thompson M, Bendsoe N, Svanberg K, Svanberg S, et al. In vivo measurement of parameters of dosimetric importance during photodynamic therapy of thick skin tumors. J Biomed Opt 2006;11.

[12] Johansson A, Soto Thompson M, Johansson T, Bendsoe N, Svanberg K, Svanberg S, et al. System for integrated interstitial photodynamic therapy and dosimetric monitoring. SPIE 2005;5689:130–40.

[13] Case KM, Zweifel PF. Linear transport theory. Reading, MA: Addison-Wesley Publishing Co.; 1967.

[14] Fishkin JB, Coquoz O, Anderson ER, Brenner M, Tromberg BJ. Frequency-domain photon migration measurements of normal and malignant tissue optical properties in a human subject. Appl Opt 1997;36: 10–20.

[15] Schweiger M, Arridge SR, Hiraoka M, Delpy DT. The finite-element method for the propagation of light in scattering media – boundary and source conditions. Med Phys 1995;22:1779–92.

[16] Haskell RC, Svaasand LO, Tsay T-T, Feng T-C, McAdams MS, Tromberg BJ. Boundary conditions for the diffusion equation in radiative transfer. J Opt Soc Am A 1994;11:2727–41.

[17] Chen GTY. Dose volume histograms in treatment planning. Int J Radiat Oncol Biol Phys 1988;14:1319–20.

[18] Foster TH, Murant RS, Bryant RG, Knox RS, Gibson SL, Hilf R. Oxygen consumption and diffusion effects in photodynamic therapy. Radiat Res 1991;126:296–303.

[19] Woodhams JH, Kunz L, Bown SG, MacRobert AJ. Correlation of real-time haemoglobin oxygen saturation monitoring during photodynamic therapy with microvascular effects and tissue necrosis in normal rat liver. Br J Cancer 2004;91:788–94.

[20] Tsutsui H, MacRobert AJ, Curnow A, Rogowska A, Buonaccorsi G, Kato H, et al. Optimisation of illumination for photodynamic therapy with mTHPC on normal colon and a transplantable tumour in rats. Laser Med Sci 2002;17:101–9.

Paper VII

Pre-treatment dosimetry for interstitial photodynamic therapy

A. Johansson, J. Hjelm, A. Eriksson, S. Andersson-Engels.

Therapeutic Laser Applications and Laser-Tissue Interactions II, Ed. H. van den Bergh, A. Vogel, Proc. SPIE **5863**, 58630S (2005).

Pre-treatment dosimetry for interstitial photodynamic therapy

A. Johansson*, J. Hjelm, A. Eriksson, S. Andersson-Engels
Department of Physics, Lund Institute of Technology, PO Box 118, SE-221 00 Lund, Sweden

ABSTRACT

A genetic algorithm for optimal placement of optical fibers in arbitrary geometries for interstitial photodynamic therapy has been developed. Based on calculated fiber positions, the diffuse light distribution is simulated by solving the diffusion equation by means of the finite element method and the treatment time is calculated. Utilizing an instrument for interstitial photodynamic therapy that is capable of both delivering the therapeutic irradiation and measuring parameters of relevance to treatment monitoring, knowledge has been gained on temporal variations of tissue light absorption, sensitizer photobleaching and tissue oxygenation status. We speculate on how variations in these three parameters can be implemented in a crude pre-treatment dosimetry model for photodynamic therapy.

Keywords: Photodynamic Therapy, Interstitial, Dosimetry, Fluence rate, Sensitizer Photobleaching, Tissue Oxygenation

1. INTRODUCTION

In the search for new treatment modalities for cancer treatment, photodynamic therapy (PDT) has shown promising results in terms of selectivity and efficacy[1]. PDT relies on the presence of a photosensitizing agent, which once activated by light of the appropriate wavelength generates cytotoxic species, mostly singlet oxygen and other oxygen radicals. Tissue necrosis is caused by a combination of immediate tumor cell death and apoptosis induced by these radicals and indirect death due to damage to the vascular system[2]. Since the tissue following PDT often shows distinct boundaries between necrotic and unaffected regions, the concept of a threshold dose has been introduced [3]. Tissue destruction can only be induced once a minimum amount of toxic photoproducts, for example singlet oxygen molecules, has been formed. The amount of radicals created depends on the local sensitizer concentration, the number of photons absorbed by the sensitizer and the oxygen access. These three parameters can be used to define a photodynamic dose.

At the Department of Physics, Lund, Sweden an instrument for interstitial PDT has been developed that allows for treatment monitoring by measuring the local fluence rate, the sensitizer fluorescence and the tissue oxygen saturation throughout the treatment session[4]. Several optical fibers are used both for delivering the therapeutic irradiation and for collecting the signals relevant for treatment supervision. So far ten treatment sessions on thick non-melanoma skin tumors have been performed at the Oncology Clinic, Lund, Sweden. These treatments have provided us with important information on how tissue absorbance and oxygenation change during treatment sessions as well as the temporal profile of the sensitizer fluorescence signal[5]. This knowledge can help in forming a pre-treatment dosimetry model based on an explicit dosimetry concept according to Wilson *et al.* [6].

PDT has been applied in numerous clinical situations without any thorough pre-treatment dosimetry. In the case of superficial skin lesions, the photodynamic dose is often only defined based on the delivered light and drug doses in a standardized fashion without much concern of inter-patient variations in sensitizer accumulation and tissue oxygenation. Other factors of relevance in treatment planning are the tumor extension in three dimensions and the positioning of the optical fibers used for light delivery. Taking interstitial PDT on the prostate as an example, the proximity of sensitive tissue such as the rectum and the urethra puts additional requirements on optimal fiber positioning and an accurate model for the light distribution within the gland, possibly also including local tissue inhomogeneities, is highly important. In this work we propose a genetic algorithm for calculation of near-optimal fiber positions in arbitrary geometries. The resulting fiber coordinates are used as input parameters for modeling the fluence rate distribution within the prostate. The model relies on the finite element method (FEM) for solving the diffusion equation and therefore works in arbitrary geometries. Based on the knowledge gained during the interstitial PDT sessions, we speculate on how

* Ann.Johansson@fysik.lth.se, phone +46 46 2223120; fax +46 46 2224250; http://www-atom.fysik.lth.se/

to also include the sensitizer photobleaching and the tissue oxygenation status in a crude pre-treatment PDT dosimetry model.

2. MATERIALS AND METHODS

2.1. INSTRUMENTATION

The lay-out of the IPDT instrument is shown in Figure 1 and a more detailed description is given elsewhere[4]. The therapeutic light unit consists of diode lasers emitting at 635 nm, matching the absorption peak of the sensitizer used, protoporphyrin IX (PpIX). A maximum of six bare-end optical fibers are used to deliver the therapeutic light into the tumor mass.

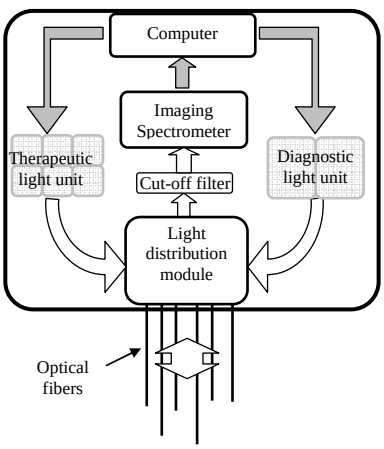

Figure 1 The overall instrument lay-out. Shaded arrows indicate data flow, whereas unshaded arrows represent light paths.

Throughout the treatment session, the therapeutic irradiation is repeatedly interrupted in order to perform measurements of parameters of importance for a successful treatment. While in measurement mode, light from the diagnostic unit is coupled into the same optical fibers as used for delivery of the therapeutic irradiation via the light distribution module. The parameters that are monitored during the treatment session are the light penetration in between optical fibers, tracking possible treatment induced increase in tissue absorption, the sensitizer fluorescence signal and changes in tissue oxygen saturation level. The term “diagnostic” has been introduced with the interpretation of treatment progression supervision and does not refer to diagnosis of the patient’s status.

2.2. MATHEMATICAL DESCRIPTION

The proposed algorithm is based on a genetic programming scheme, where the optimization process mimics the concept of evolution in the nature, see Figure 2[7].

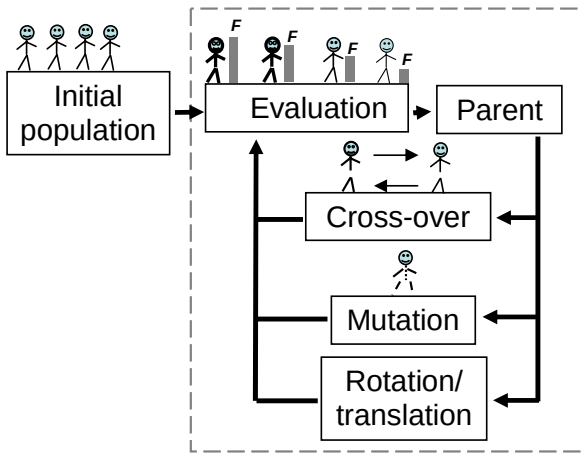

Figure 2 Lay-out of the algorithm showing data flow and steps taken during the iterative optimisation process.

The algorithm is initiated by creating a start population consisting of a certain number of individuals. Each individual consists of a specific set of fiber configurations and for the initial population each individual is given random start coordinates. In the next step, the reproduction stage indicated by the dashed rectangle in Figure 2, each individual is first evaluated according to its fitness value, *F*. A certain fraction of the most fit individuals are chosen as parents for the next generation. The higher the fitness value, the better the proposed coordinates and the greater the probability of that individual surviving for the next generation. The most common way is simply to let the survival probability be proportional to the fitness value.
In the next step, a younger population is created by performing various alterations on the previous generation. An operation referred to as cross-over can be seen as mating between two parents. This step is implemented by splitting each individual's set of fiber coordinates in two halves and merging the first part from one parent with the second part from the other parent. Cross-over opens up the possibilities for one set of promising characteristics from one parent to be combined with the advantages of the other parent. The equivalence of the concept of mutation in nature's evolution is performed by including a small probability for randomly changing parts of the set of fiber coordinates. This step prevents premature convergence of the algorithm. The cross-over and mutation operations are included in order to allow for exploration of new regions in the search space. In addition, there is also a certain probability that each parent is exposed to some geometrical operation. In our work we have included the possibility of rotation and translation of fiber coordinates. In order to guarantee the survival of the most fit individual, an elitist algorithm has been used. This means that the survival of the best solution at a specific time point is guaranteed by letting that individual pass onto the generation unaltered.

The new population, also referred to as the children, thus created, is used as starting point for another reproduction stage and the creation of the next generation is initiated. The process of reproduction, cross-over and mutation is repeated until the fitness value can no longer be improved between consecutive generations.

The maybe most important parameter is the fitness function, according to which individuals are ranked. The fitness value is used to direct the search and should reflect the characteristics of a good solution. The fitness function, also referred to as the objective function, used in this work is given according to Eq. (1);

$$F = \sum_{i=1}^{M} w_i \phi_i + \sum_{j=1}^{N} \omega_j \phi_j \ , \qquad (1)$$

where ϕ denotes the fluence rate, ω is a weighting factor characteristic of each specific tissue type and *M* and *N* are the number of tumor and surrounding tissue voxels to be included in the fitness function. The product $M \cdot N$ is usually less than the total number of voxels in order to speed up the execution.

The calculations are carried out under the assumption of diffuse light propagation, where the bare-end optical fibers used for delivering the therapeutic irradiation are modeled as isotropic point sources. The fluence rate, $\phi(\mathbf{r})$, is described by the analytical solution to the steady-state diffusion equation in a homogenous medium[8];

$$\phi_i = \sum_s \frac{P_s \mu_{eff}^2}{4\pi\mu_a r} \exp\left(-\mu_{eff}|r|\right), \qquad (2)$$

where $\mu_{eff} = [\,3\mu_a(\mu_a + \mu_s')\,]^{1/2}$, μ_a and μ_s' are the effective attenuation, absorption and reduced scattering coefficients, respectively. The summation is carried out over all light sources, characterized by output power P_s. The parameter *r* denotes the distance between each individual light source and the voxel of interest.

By having certain weights, ω_i, for different regions, one can easily incorporate tissue types of varying sensitivity. When treating the prostate for example, the urethra and the rectum would constitute regions of higher sensitivity and their respective weights should reflect the risk of delivering too high light doses to these volumes. If giving negative weights to sensitive tissue and positive weights to the target volume, the final output of the genetic algorithm is the individual with the highest fitness value. The inclusion of voxel weights allows for more details in tumor characteristics to influence the fiber positioning. If, for example, the central parts of the tumor are necrotic this region should be given a weight reflecting the smaller need for receiving high light doses. There is also a possibility to let the inhomogeneous sensitizer accumulation and the tissue oxygenation status influence the different weights.

Different solutions proposed by the genetic algorithm have been rated based on their fitness values and significant differences were tested using a Student t-test at significance level $P \leq 0.01$.

Once the optimal fiber positions are found, an approximation of the fluence rate distribution within the tissue volume of interest is calculated by solving the diffusion equation,

$$\nabla^2\phi(\mathbf{r}) - \mu_{\text{eff}}^2\phi(\mathbf{r}) = \sum_i S(\mathbf{r}_i), \qquad (3)$$

by means of the finite element method. The source term, $\sum S(\mathbf{r}_i)$ is modeled as isotropic point sources, denoted by the index *i*. In the case of superficial lesions, the extrapolated boundary condition is used when solving Eq. (3)[9]. Based on the calculated fluence rate distribution, the sensitizer concentration and the oxygen access, the local rate of singlet oxygen production, which is related to the PDT dose, can be predicted according to the following formula:

$$\frac{\partial D(r,t)}{\partial t} = \varepsilon \cdot \phi(r,t) \cdot [PS(r,t)] \cdot [O_2(r,t)] \qquad (4)$$

In Eq. (4), [*PS*] and [O_2] denote the sensitizer and oxygen concentrations, respectively. ε is a scalar constant taking into account quantum efficiencies in the excitation of the sensitizer molecules and the singlet oxygen production. Treatment induced changes in tissue absorption, sensitizer concentration and tissue oxygen saturation level are indicated by the time dependence and possible spatial variations are also indicated by the inclusion of the parameter *r*. Integrating Eq. (4) over time and putting it in relation to some predefined threshold for the PDT dose, D_{th} (J/cm^3), considered sufficient for inducing tissue necrosis, leads to an estimate of the necessary treatment time;

$$t = \frac{D_{th}}{\int_{t'} \frac{\partial D}{\partial t'}} \tag{5}$$

3. RESULTS

3.1. Fiber positioning

The genetic algorithm was tested on the prostate geometry shown in Figure 3.a. As can be seen, the prostate gland has a slightly irregular shape and the urethra, running through the central part on the gland, and the rectum at the posterior part of the gland, are included in the prostate model. The prostate gland had a volume of approximately 40 ml and the absorption and reduced scattering coefficient were set to 0.30 and 14 cm^{-1}, respectively[10].

The genetic algorithm proved to be significantly better than manual placement of six fibers in this irregularly shaped three-dimensional geometry when comparing the fitness values according to Eq. (1) of the proposed solutions. The average fitness value for the genetic algorithm was found to be 0.0284, which was significantly better than the average of six manual placements of -0.0303. It should be noted that the absolute value of the fitness function is influenced by the number of voxels used to describe the geometry, the weights given to each tissue type and the optical parameters used and it is therefore not possible to compare fitness values between different geometries.

Figure 3.b shows the resulting solution given by the genetic algorithm for the case of six optical fibers. As can be seen, the fibers are positioned around the sensitive tissue, in this case the urethra and the rectum, in such a way as to provide as homogenous fluence rate distribution throughout the prostate gland as possible.

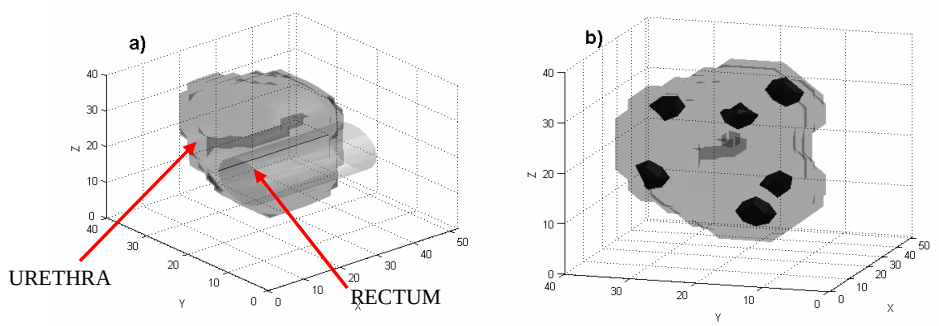

Figure 3 a) A three dimensional view of a prostate geometry with urethra and rectum included as sensitive tissue. b) Resulting fiber positions. The rectum is not displayed for clarity.

Figure 4 shows a cross section perpendicular to the direction of the urethra through the central part of the gland. The rectum and the urethra are indicated in the figure and as can be seen these parts are spared from too high light doses. Figure 5.a-c show histograms of the fluence rate distribution in tumor, rectum and urethra for the fiber positioning illustrated in Figure 3.b. As can be seen, the sensitive tissue regions receive a much lower light dose as compared to the tumor. These results were obtained with the weights for the urethra as sensitive tissue set rather low, i.e. representing tissue with relatively low risks associated with high light doses. The corresponding histograms of the fluence rate distribution in the case of a highly sensitive urethra are shown in Figure 5.d-f. In Figure 5, the weights for the urethra were changed from -1, in a-c, to -3, in d-f.

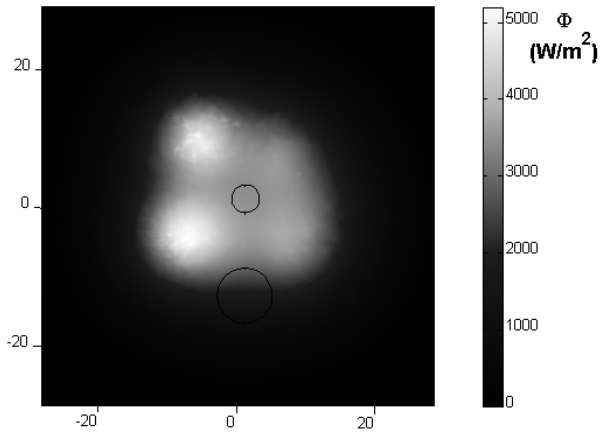

Figure 4 Fluence rate distribution through the central part of the prostate gland. The position of the rectum and the urethra are indicated in the cross section.

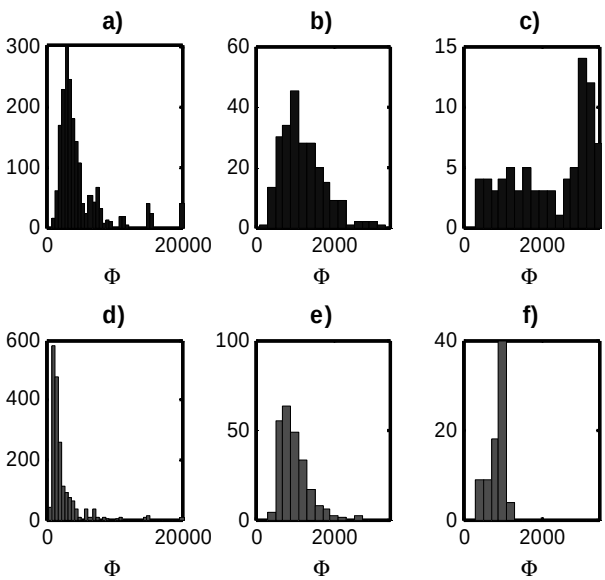

Figure 5 The fluence rate distribution using six treatment fibers for different weights on the sensitive tissue. The upper row shows histograms for the fluence rate distribution in a) prostate gland, b) rectum and c) urethra for a low-sensitive urethra. The lower row shows corresponding histograms for a high-sensitive urethra.

3.2. Treatment-induced changes

Measured temporal profiles of the light transmission, PpIX fluorescence level and tissue oxygen saturation in between patient fibers are shown in Figure 6.a-c. Figure 6.a illustrates how the treatment-induced increase in tissue absorption influences the light transmission between optical fibers during one of the treatment sessions performed. In rare cases the

light transmission at the treatment wavelength decreased to 30% of the initial transmission as measured prior to delivery of the therapeutic irradiation. This increase in tissue optical density severely limits the light distribution throughout the prostate and can prevent an efficient treatment. Figure 6.b shows the sensitizer fluorescence signal, reflecting the decrease in PpIX concentration as a result of photobleaching. Finally, part c illustrates the average tissue oxygen saturation level during the same treatment session.

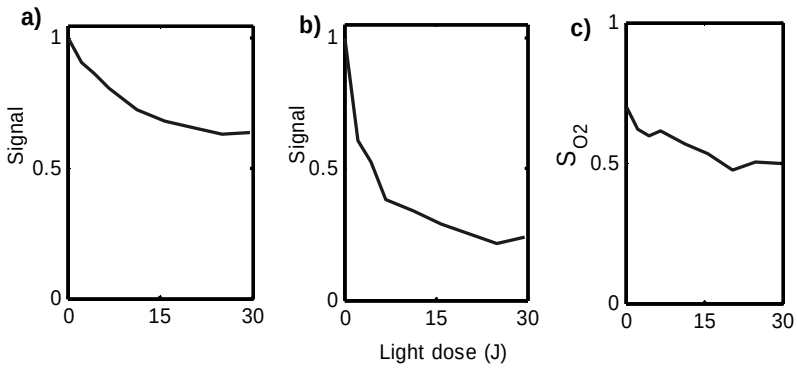

Figure 6 a) Average 635 nm-light transmission between optical fibers during one treatment session. b) Average PpIX fluorescence signal at 705 nm. c) Tissue oxygen saturation level during the same treatment. All signals have been normalized to their respective initial values.

Figure 7 shows the delivered PDT dose in a cross section of the prostate for three different situations. Figure 7.a illustrates the treatment dose after 100 seconds of irradiation if assuming constant parameters, i.e. no variation in light transmission, sensitizer concentration or tissue oxygen saturation. The delivered PDT dose in this case has simply been obtained by multiplying the fluence rate as shown in Figure 4 by the treatment time. In Figure 7.b, a tissue absorption varying according to Figure 6.a has been taken into account when evaluating the PDT dose according to Eq. (4). The increase in μ_a influences only the term $\phi(r,t)$ in Eq. (4), whereas the other two parameters were kept constant in calculating the delivered PDT dose. The increase in tissue absorption clearly limits the treatment volume.

Finally, Figure 7.c shows the delivered PDT dose when assuming temporal profiles of the light transmission, the sensitizer concentration and tissue oxygen saturation according to Figure 6.a-c, respectively. Now all parameters in Eq. (4) except the scalar ε displayed time variations, and from the figure it is clear that sensitizer photobleaching and tissue de-oxygenation further limits the delivered PDT dose. One should note that no spatial variations of the parameters in Eq. (4) have been included in the analysis of the delivered PDT dose.

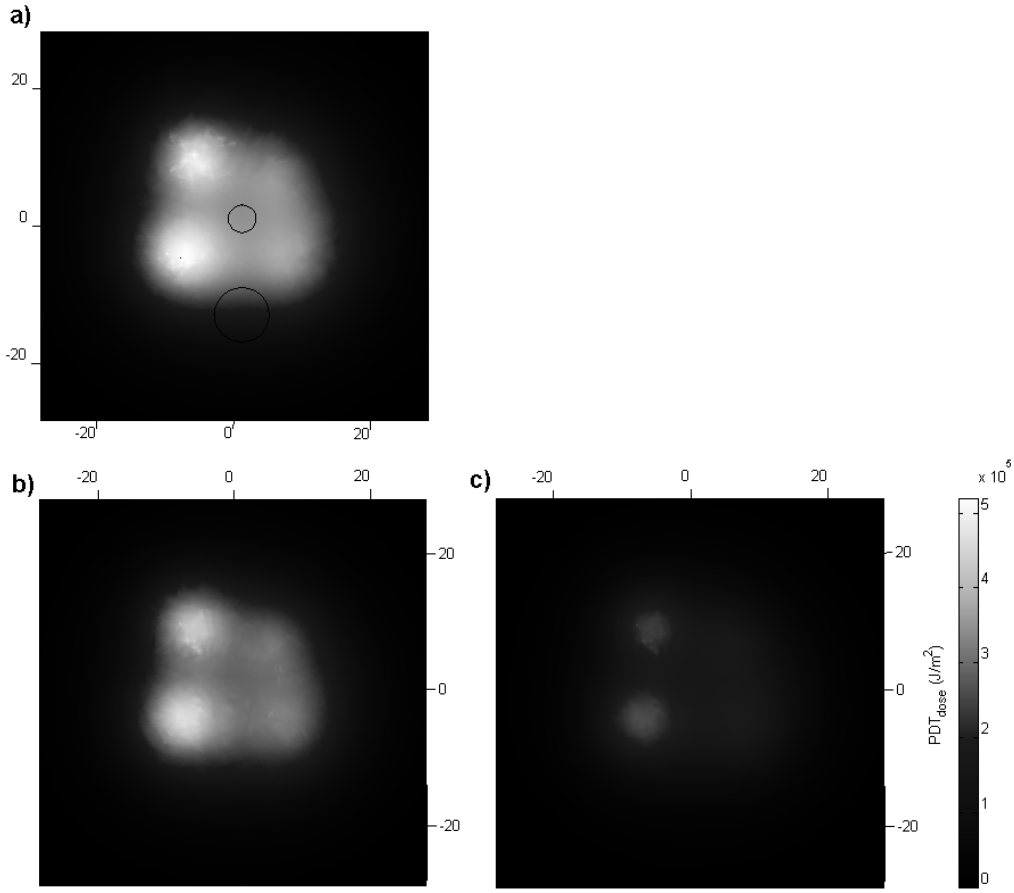

Figure 7 a) Cross section through the central part of the prostate gland showing the PDT dose after 100 s irradiation assuming constant optical properties, sensitizer concentration and oxygenation. b) Corresponding PDT dose assuming varying tissue absorption coefficient. c) PDT dose after 100 s irradiation when taking into account the variation of the tissue absorption coefficient, sensitizer concentration and tissue oxygen saturation according to Figure 6.

4. CONCLUSIONS

An algorithm for optimization of fiber positioning in connection with interstitial photodynamic therapy has been implemented based on a genetic computation scheme. The program relies on the knowledge of the tumor geometry, including regions of sensitive tissue, and is supposed to execute while the patient is under anesthesia. This has put additional requirements on short computation times, which are now on the order of 5 minutes. The algorithm can be used for an arbitrary number of optical fibers and arbitrary three dimensional geometries. In the present implementation all fibers have equal output powers, but future work includes improving the algorithm to also optimize the individual fiber output power.

The ability to incorporate sensitive tissue has been implemented by giving different tissue regions different weights, whose magnitudes describe the relative importance of giving each individual tissue region a sufficient light dose or the risk connected with over-treating a specific tissue type. Substantial work is still required in order to correlate the absolute magnitude of these weights to each organ, for example the urethra, the rectum or the urethral sphincter muscle. A further possibility that is opened up by including weights. is that the weights can used to reflect any pre-treatment knowledge of spatially varying sensitizer accumulation or tissue oxygenation. Central tumor regions, that are already necrotic, can be given a lower weight, as can any regions characterized by a higher sensitizer concentration, in order to reflect the lowered importance for a high light dose.

The amount of detail included in genetic algorithm can be adjusted and so far the resolution in the proposed fiber positions is set to 1 mm, matching the precision in fiber positioning *in vivo* reported[11]. Modeling of the light distribution throughout the gland and surrounding tissue at this stage can only give a crude approximation of the PDT dose and treatment time, since the actual fiber positions will deviate from the proposed configuration and temporal changes of light transmission and sensitizer and oxygen concentrations are not taken into account.

Ultrasound or MR can be used to monitor the actual fiber positions, which are then used as input parameters for the FEM calculations when modeling the fluence rate distribution and the PDT dose. Knowledge of the light distribution forms the basis for predicting treatment times but it is essential to also include the sensitizer and oxygen concentrations when calculating the delivered PDT dose. From Figure 7 it is clear that significant changes in treatment volume are introduced when we also consider treatment-induced variations in light transmission, sensitizer concentration and tissue oxygen saturation in the dose model.

Several definitions of the PDT dose have been proposed. Early work stated a PDT dose based on light and sensitizer dose only[12]. More recent results indicate that the total light dose delivered and sensitizer concentration are not sufficient to describe treatment response, and the importance of oxygen for the photodynamic reaction has been emphasized[13]. For example, a high rate of light delivery is believed to induce oxygen depletion and thereby reduced treatment efficiency[14]. In addition, de-oxygenated tissue has been shown to limit the light penetration and thereby the treatment volume[15]. Based on the importance of all three parameters, activating light, sensitizer and oxygen, Wilson *et al.* introduced the concept of explicit dosimetry for PDT[6]. In an explicit dosimetry model one would need exact knowledge of all three parameters in order to determine the PDT dose. This is in contrast to the implicit dosimetry model, introduced by the same authors, where a single parameter is used to describe the treatment dose. This parameter should depend on all other variables of importance to the treatment outcome and should also reflect their respective interdependencies. Several authors have proposed using the sensitizer photobleaching kinetics as such an implicit dose metric[16]. The instrument described in section 2.1 works along the lines of explicit PDT dosimetry for monitoring the treatment progress[5]. From the ten first treatment sessions we have gained experience on treatment-induced variations of the tissue absorption, the PpIX photobleaching and the average tissue oxygen saturation. These results tell us that not only are the variations in the parameters used for the explicit dosimetry large, but they are also significantly different from patient to patient. Based on the treatment sessions performed so far, there seems to be some interdependence between the absorption increase and initial rate of the sensitizer photobleaching, where a higher rate of photobleaching correlates with less pronounced overall increase in tissue absorption[5]. In addition, the treatment-induced changes in tissue optical density in the wavelength interval 760-800 nm are consistent with variations in tissue oxygenation and blood volume. Though, it seems difficult to predict exactly how much for example the light transmission will change based on measurements performed prior to the therapeutic irradiation. This conclusion might of course change as more patients are included in the study, but so far we find it essential to monitor all parameters of dosimetric importance during each individual treatment session. The inter-patient variations also imply that it is difficult to model the entire treatment session in advance and thereby get an estimate of the necessary irradiation time and other treatment parameters, such as fiber output power and irradiation fractionation. In a clinical situation it would be necessary to iterate measurement sequences and modeling of the PDT dose throughout the entire treatment session.

It should be noted that no spatial variations have been included in the analysis of the delivered PDT dose. Data from the treatment sessions showed that the change in tissue absorption coefficient was rather homogeneous throughout the entire tumor volume. The rapidly decreasing PpIX fluorescence level mostly reflects the photobleaching occurring close to the fiber tips where the fluence rate is very high. Further away from the light sources, the sensitizer bleaching is less and the

PpIX concentration stays high for longer time periods. This spatial variation of the sensitizer concentration should be taken into account when evaluating the delivered PDT dose throughout the gland.

The tissue oxygen saturation displays only a slight variation with the treatment time as shown in Figure 6.c. One reason might that PpIX-mediated PDT does in fact not result in as serious oxygen depletion as other sensitizers, for example Foscan and Photofrin, do[17]. Another plausible explanation is that the highest rate of oxygen consumption occurs close to the light delivering fibers where the fluence rate is highest. The signals that are involved in measuring and evaluating the tissue oxygen saturation level have traveled several millimeters in the tissue and therefore represent an average of the tissue in between the patient fibers. It is expected that this signal, probing large volumes far away from the light sources, does not display any major imprint of oxygen depletion[18].

When determining the treatment time, the concept of a threshold dose is important. Ultimately the threshold dose should express how many singlet oxygen molecules are necessary to induce tissue necrosis and it therefore depends among many other parameters on the local fluence rate and sensitizer concentration and the conversion efficiency between activated sensitizer molecule and singlet oxygen. The pronounced vascular effects associated with many sensitizers further complicate the situation since certain tissue regions might experience severe damage as a result of vascular shutdown instead of for example high local sensitizer concentration. Much work is still required in order to define an appropriate PDT dose based on some set of parameters and a threshold dose. The maybe most desirable characteristic of an implicit dosimetry model is that modeling and monitoring of one single parameter is sufficient. Future work involves correlating our explicit dosimetry with for example the sensitizer kinetics.

ACKNOWLEDGEMENTS

This project was financially supported by the Swedish Foundation for Strategic Research and also by Karolinska Development AB, Stockholm and Lund University Development AB through SpectraCure AB.

REFERENCES

1. Q. Peng, T. Warloe, K. Berg, J. Moan, M. Kongshaug, K.-E. Giercksky, and J. M. Nesland, "5-aminolevulinic acid-based photodynamic therapy: Clinical research and future challenges," Cancer **79**, 2282-2308 (1997).
2. Q. Peng, K. Berg, J. Moan, M. Kongshaug, and J. M. Nesland, "5-aminolevulinic acid-based photodynamic therapy: Principles and experimental research," Photochem. Photobiol. **65**, 235-251 (1997).
3. J. C. van Gemert, M. C. Berenbaum, and G. H. M. Gijsbers, "Wavelength and light-dose dependence in tumour phototherapy with haematoporphyrin derivative," Br. J. Cancer **52**, 43-49 (1985).
4. M. Soto Thompson, A. Johansson, T. Johansson, S. Andersson-Engels, N. Bendsoe, K. Svanberg, and S. Svanberg, "Clinical system for interstitial photodynamic therapy with combined on-line dosimetry measurements," Appl. Opt. (to be published).
5. A. Johansson, T. Johansson, M. Soto Thompson, N. Bendsoe, K. Svanberg, S. Svanberg, and S. Andersson-Engels, are preparing a manuscript to be called "In vivo measurement of parameters of dosimetric importance during photodynamic therapy of thick skin tumors."
6. B. C. Wilson, M. S. Patterson, and L. Lilge, "Implicit and explicit dosimetry in photodynamic therapy: a new paradigm," Lasers Med. Sci. **12**, 182-199 (1997).
7. D. E. Goldberg, *A Gentle Introduction to Genetic Algorithms*, (Addison-Wesley publishing company, Inc, 1989).
8. K. M. Case and P. F. Zweifel, *Linear Transport Theory*, (Addison-Wesley Publishing Co., Reading, MA, 1967).
9. A. J. Welch and M. J. C. van Gemert, *Optical-Thermal Response of Laser-Irradiated Tissue*, (Plenum Press, New York, NY, 1995).
10. T. C. Zhu, E. Glatstein, S. M. Hahn, A. Dimofte, J. C. Finlay, D. Stripp, T. Busch, J. Miles, R. Whittington, S. B. Malkowicz, and Z. Tochner, "Optical Properties of Human Prostate at 732 nm Measured In Vivo during Motexafin Lutetium-Mediated Photodynamic Therapy," Photochem Photobiol (2004).
11. L. K. Lee, C. Whitehurst, M. L. Pantelides, and J. V. Moore, "An interstitial light assembly for photodynamic therapy in prostatic carcinoma," Br. J. Urol. **84**, 821-826 (1999).

12. W. R. Potter, T. S. Mang, and T. J. Dougherty, "The theory of photodynamic therapy dosimetry: consequences of photodestruction of sensitizer," Photochem. Photobiol. **46**, 97-101 (1987).
13. T. H. Foster, D. F. Hartley, M. G. Nichols, and R. Hilf, "Fluence rate effects in photodynamic therapy of multicell tumor spheroids," Cancer Res. **53**, 1249-1254 (1993).
14. D. J. Robinson, H. S. de Bruijn, N. van der Veen, M. R. Stringer, S. B. Brown, and W. M. Star, "Fluorescence photobleaching of ALA-induced protoporphyrin IX during photodynamic therapy of normal hairless mouse skin: The effect of light dose and irradiance and the resulting biological effect," Photochem. Photobiol. **67**, 140-149 (1998).
15. M. Soumya and T. H. Foster, "Carbogen breathing significantly enhances the penetration of red light in murine tumours *in vivo*," Phys. Med. Biol. **49**, 1891-1904 (2004).
16. I. A. Boere, D. J. Robinson, H. S. de Bruijn, J. van den Boogert, H. W. Tilanus, H. J. C. M. Sterenborg, and R. W. F. de Bruin, "Monitoring in situ dosimetry and protoporphyrin IX fluorescence photobleaching in the normal rat esophagus during 5-aminolevulinic acid photodynamic therapy," Photochem. Photobiol. **78**, 271-2 (2003).
17. I. Wang, S. Andersson-Engels, G. E. Nilsson, K. Wårdell, and K. Svanberg, "Superficial blood flow following photodynamic therapy of malignant skin tumours measured by laser Doppler perfusion imaging," Br. J. Dermatol. **136**, 184-189 (1997).
18. A. Curnow, J. C. Haller, and S. G. Bown, "Oxygen monitoring during 5-aminolaevulinic acid induced photodynamic therapy in normal rat colon. Comparison of continuos and fractionated light regimes.," J. Photochem. Photobiol. B. **58**, 149-155 (2000).

Paper VIII

Realtime light dosimetry software tools for interstitial photodynamic therapy of the human prostate

A. Johansson, J. Axelsson, J. Swartling, S. Andersson-Engels.
Medical Physics, in press (2007).

Realtime light dosimetry software tools for interstitial photodynamic therapy of the human prostate

Ann Johansson,* Johan Axelsson, and Stefan Andersson-Engels
Lund University, Department of Physics, PO Box 118, SE-221 00 Lund, Sweden

Johannes Swartling
SpectraCure AB, Ole Römers väg 16, SE-223 70 Lund, Sweden
(Dated: September 1, 2007)

Photodynamic therapy (PDT) for the treatment of prostate cancer has been demonstrated to be a safe treatment option capable of inducing tissue destruction and decreasing prostate specific antigen (PSA) levels. However, prostate-PDT results in large intra- and inter-patient variations in treatment response, possibly due to biological variations in tissue composition and short-term response to the therapeutic irradiation. Within our group, an instrument for interstitial PDT on prostate tissue has been developed that combines therapeutic light delivery and monitoring of light transmission via numerous bare-ended optical fibers. Here, we present algorithms that utilize data on the light distribution within the target tissue to provide realtime treatment feedback based on a light dose threshold model for PDT. This realtime dosimetry module is implemented to individualize the light dose and compensate for any treatment-induced variations in light attenuation. More specifically, based on the light transmission signals between treatment fibers, spatially resolved spectroscopy is utilized to assess the effective attenuation coefficient of the tissue. These data constitute input to a Block-Cimmino optimization algorithm, employed to calculate individual fiber irradiation times provided the requirement to deliver a pre-determined light dose to the target tissue while sparing surrounding, sensitive organs. By repeatedly monitoring the light transmission signals during the entire treatment session, optical properties and individual fiber irradiation times are updated in realtime. The functionality of the algorithms is tested on diffuse light distribution data simulated by means of the finite element method (FEM). The feasibility of utilizing spatially resolved spectroscopy within heterogeneous media such as the prostate gland is discussed. Furthermore, we demonstrate the ability of the Block-Cimmino algorithm to discriminate between target tissue and organs at risk (OAR). Finally, the realtime dosimetry module is evaluated for treatment scenarios displaying spatially and temporally varying light attenuation levels within the target tissue. We conclude that the realtime dosimetry module makes it possible to deliver a certain light dose to the target tissue despite spatial and temporal variations of the target tissue optical properties at the therapeutic wavelength.

PACS numbers: 87.54.Fj, 42.62.Be, 87.53.Tf, 87.53.Bn or 87.58.Sp

I. INTRODUCTION

Photodynamic therapy (PDT) is a cancer treatment modality in which the extent of tissue damage depends among other parameters on the light dose, the tissue oxygenation and the sensitizer concentration.[1,2] For PDT, clinical treatment protocols often rely on a simplified light dose threshold model where it is assumed that only tissue regions exposed to a light dose exceeding a pre-defined threshold are unreversibly damaged.[3,4] The model holds the advantage that the total light dose is one of the parameters that can be most easily varied during a treatment session, although predicting the exact distribution of the delivered fluence requires knowledge of the optical properties of the target tissue prior to and during the PDT treatment.

Recently, several groups have investigated interstitial PDT (IPDT) as an alternative to radical prostatectomy, external and internal radiation therapy for the treatment of localized prostate cancer. For example, Bown *et al.*[5–7] have used the photosensitizer Temoporfin (mTHPC, meso-tetra(hydroxyphenyl)chlorin) for treating secondary and primary prostate cancer. Light delivery resulted in significant treatment-induced necrosis and decreasing prostate-specific antigen (PSA) levels. In general, complications were minor,[6] but PSA eventually started to increase again with tumor recurrences in 13 out of the 14 secondary cancer patients.[5] Weersink *et al.*[8,9] have reported on IPDT for recurrent prostate cancer using the vascular-targeted photosensitizer Tookad (WST09). Here, lesion formation was observed to primarily depend on the total light dose for the maximum drug dose (2 mg/kg). Furthermore, Hahn *et al.*[10] have utilized the photosensitizer motexafin lutetium (MLu) for the treatment of recurrent prostate carcinoma. Aminolevulinic acid (ALA)-PDT has been investigated by Sroka *et al.*,[11] resulting in decreasing PSA levels and no evidence of incontinence or dysuria following PDT. Among many others, the cited references indicate that IPDT is a relatively safe treatment modality capable of inducing significant tissue necrosis within the prostate.

Ideally, by careful light dosimetry one might target the entire prostate while sparing sensitive surrounding organs to minimize recurrences and treatment-related

complications. However, giving initial evidence for the complexities associated with prostate-PDT dosimetry, many PDT-trials on prostate tissue report on large intra- and inter-patient variations in treatment-induced necrotic volumes despite delivering similar drug and light doses.[6,8,10] These effects might partly be explained by inter- and intra-patient variations of the tissue optical properties, directly influencing the light distribution within the prostate,[8,12,13] as well as any treatment-induced variations in tissue composition, such as changing blood volume and tissue oxygenation status.[14] Many authors acknowledge the need for more accurate and individualized realtime dosimetry, both for PDT on prostate tissue[5,9,10,15] and in more general terms.[16,17] There are numerous reports on prostate *in vivo* spectroscopic measurements of parameters related to the PDT effect, e.g. light[8,18] and sensitizer[18,19] distribution and tissue oxygenation[18] as well as blood flow and volume.[20] Such studies hold great potential in increasing the understanding of the processes associated with PDT on prostate tissue and in extending clinical prostate-PDT to also incorporate individualized treatment dosimetry and realtime treatment feedback.

Here, we report on algorithms constituting a realtime dosimetry module for IPDT on prostate tissue with treatment feedback based on a light dose threshold model. Previously, we have observed significant treatment-induced changes in tissue optical properties during IPDT of thick skin tumors,[14,21] emphasizing the need for treatment feedback to compensate the influence of varying light transmission on the deposited light dose within the target tissue.[22] Our most recent IPDT instrumentation therefore incorporates realtime monitoring of the light transmission signals between patient fibers in order to evaluate the effective attenuation coefficient at the therapeutic wavelength. These data together with information on the tissue geometry are used as input for a Block-Cimmino optimization algorithm, predicting individual fiber irradiation times. By iterating measurements, calculation of the effective attenuation and the Block-Cimmino optimization procedure, the irradiation times for each source fiber can thus be continuously updated throughout the treatment session. This realtime dosimetry module is also referred to as Interactive DOsimetry by Sequential Evaluation (IDOSE). In this work, the finite element method (FEM) is utilized to simulate light transmission signals within a realistic prostate model for temporally and spatially varying optical properties. Based on the simulated data set, we test the ability of the algorithm to track an increase in the effective attenuation coefficient within the prostate. Furthermore, via tissue importance weighting within the Block-Cimmino algorithm we evaluate the possibility to discriminate between target tissue and organs at risk (OAR) in terms of the deposited light dose. Finally, the dose volume histograms (DVHs) of the light dose delivered during an IPDT treatment with a simulated absorption increase are compared with and without treatment feedback. In this way, we demonstrate the feasibility of an IPDT dosimetry model that ascertains a certain predetermined light dose within the target tissue irrespective of any treatment-induced changes in tissue absorption.

II. METHODS AND ALGORITHMS

A. Treatment procedure

The IDOSE module has been developed for an intended clinical trial utilizing Temoporfin-mediated IPDT for the treatment of primary prostate cancer. In this trial, Temoporfin will be administered intravenously 96 hours prior to light delivery at a dose of 0.15 mg/kg b.w. The IPDT treatment procedure as outlined in Figure 1.a incorporates pre-treatment and treatment tasks where a graphical user interface guides the physician through each step.

At first, a transrectal ultrasound investigation is performed to assess the geometry of target tissue as well as nearby OAR, step (1). Within a set of 6 to 10 ultrasound images, the physician delineates the extent of the prostatic gland, urethra, rectum, upper and lower sphincters and the cavernous nerve bundles. These tissue contours are then patched into a three-dimensional voxel representation of the geometry containing all organs, step (2). An iterative random-search algorithm, similar to a simulated annealing type algorithm, is employed to find near-optimal source fiber positions for each specific prostate geometry, step (3), as has been described previously.[23]. Briefly, for every iteration each fiber is moved a limited length in a random direction, where the movement is restricted to prostate voxels and one source fiber per voxel. The maximum step size is decreased gradually from three to one voxel to ensure convergence. Following a fiber movement, a fitness function value is computed. By optimizing this value, the fluence rate within the prostate is maximized whereas the light distribution within the OAR is minimized. A new set of fiber positions is accepted only if the fiber movement leads to a higher fitness function value. Typical execution times are on the order of 45 to 60 minutes. Figure 1.b illustrates a sample three-dimensional geometry, with 1 mm voxel side length, including the target tissue, i.e. the prostate, the OAR, consisting of the urethra, rectum, and normal, surrounding tissue as well as the source fiber positions. This geometry, representing the "test" geometry used in this work, was created based on eight ultrasound images from a patient with a glandular volume of approximately 27 cm^3. Patient fiber positions were calculated by the random-search algorithm. In this study, the upper and lower sphincters are not included in the geometry model. Utilizing hollow steel needles, the optical fibers, also referred to as patient fibers, are guided into position, step (4), with the transperineal approach and transrectal ultrasound guidance. Within this fourth step, the physician is given the opportunity to update the final fiber

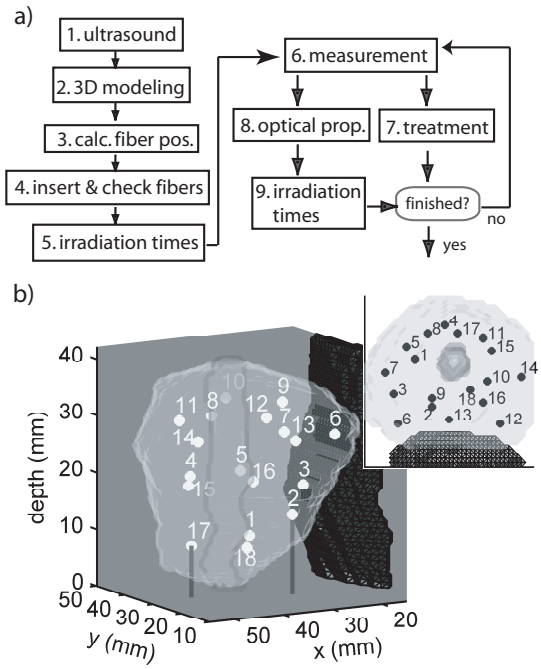

FIG. 1: a) Flow chart illustrating the entire treatment procedure. In the pre-treatment planning, transrectal ultrasound, step (1), is utilized to create a three-dimensional voxel representation of the target geometry, step (2). Source fiber positions are calculated, step (3), fibers are inserted, step (4), and their individual irradiation times are predicted, step (5). During the treatment session, dosimetric measurements, step (6), and calculations, steps (8) and (9), repeatedly interrupt the therapeutic irradiation, step (7). Steps (6) and (8) aim at monitoring and calculating the effective attenuation coefficient, μ_{eff}, respectively. This coefficient is then used to recalculate individual fiber irradiation times, t_i, thus updating the dose plan. The treatment session finishes once the remaining irradiation times as predicted by step (9) equal zero. b) This test geometry was reconstructed from a set of 8 ultrasound images and incorporates prostate, rectum, urethra and normal surrounding tissue. The source fiber locations, calculated in step (3), are also displayed, indicating the increasing depths, i.e. as measured from the prostate apex, for fibers 1 to 9, whereas fibers 10 to 18 are positioned with decreasing depths. Fibers are inserted transperitoneally, as indicated for sources 2 and 17. The inset is the geometry as viewed from the prostate base.

positions as these might deviate slightly from the set of positions calculated by the random-search optimization algorithm. The geometry model, the actual fiber positions and a set of default tissue optical properties,[13] see also Table I, are used as input for the Block-Cimmino optimization algorithm to predict irradiation times for all source fibers, step (5).

The IPDT session involves iterating measurement, step (6), and treatment, step (7), sequences. Measurements are performed prior to and at varying time intervals after the start of therapeutic light delivery. Immediately following a measurement sequence, delivery of therapeutic irradiation, step (7), runs in parallel to evaluating the measurement data to assess the effective attenuation coefficient within the prostate gland, step (8). The Block-Cimmino algorithm, step (9), is then executed in order to update the irradiation times. Steps (6) to (9) are iterated until the remaining treatment time as predicted by the Block-Cimmino algorithm equals zero. The implemented scheme, where steps (8) and (9) constitute the realtime IDOSE module, will be described in Section II C.

B. Hardware

The instrument used during the clinical trial employs up to 18 bare-ended 400-μm diameter optical fibers for delivery of therapeutic light around 652 nm, matching one of the absorption bands of the photosensitizer Temoporfin. By means of internal optical beamsplitters, which have been described in greater detail in Ref. 21, the instrument can switch between treatment and measurement mode. In treatment mode, the output from individual 652 nm-diode lasers is coupled into each of the patient fibers. Pre-treatment calibration guarantees 0.15 W output power per fiber. In measurement mode, output from the diagnostic light unit, consisting of a 652 nm-diode laser and a broadbanded near-infrared (NIR) LED, is sequentially coupled into each of the patient fibers. For each light source and patient fiber, the N neighboring fibers collect the transmitted light. N can in principle range between 1 and 17 but in this study we let $N = 6$. Six spectrometers are used to detect and disperse the transmission signals between 630 and 840 nm. From the collected spectra, the 652 nm-light transmission is used to analyze the tissue effective attenuation coefficient (μ_{eff}), see further Section II C 1. Furthermore, the instrument is capable of monitoring the sensitizer fluorescence following excitation at 652 nm and the tissue NIR absorbance by the transmission signals around 720 nm and between 740 and 820 nm, respectively. However, these parameters, related to Temoporfin distribution and tissue oxygenation, are not included in the feedback scheme as the current dose metric is based on the light dose only.

Within homogenous tissue phantoms, containing water, Pelikan Fount India Ink (Hannover, Germany) and Intralipid (Fresenius Kabi, Uppsala, Sweden) to give $\mu_a \in [0.4, 0.7]$ cm^{-1} and $\mu_s' \in [7.4, 11.0]$ cm^{-1}, μ_{eff} could be determined with an accuracy of $\pm 10\%$. This accuracy is in agreement with previously reported results.[24,25] A more detailed analysis of system performance and initial clinical data will be part of a future publication.

C. IDOSE

1. Optical properties

As the measurement sequences are executed during the therapeutic session it is of ample importance that the scheme used to evaluate the tissue optical properties from the light transmission signals is fast and requires limited computational cost. All measurements are performed in steady-state with source-detector separations on the order of 9 to 25 mm where diffuse light propagation can be assumed. As no absolute fluence rate measurements are performed, there is no possibility to separately assess the absorption and reduced scattering coefficients. Instead, the evaluation scheme aims to quantify the effective attenuation coefficient, $\mu_{\text{eff}} = \sqrt{3\mu_{\text{a}}(\mu_{\text{a}} + \mu'_{\text{s}})}$. For each patient fiber, only six detection fibers are used, thus restricting the probed tissue volume to regions close to the source fiber. Within each of the 18 partially overlapping sub-geometries, the tissue is assumed homogeneous and characterized by a fiber-specific $\mu_{\text{eff(i)}}$. The fiber positions are sorted so that fibers 1 to 9 are located within the left lateral lobe of the gland at increasing distance from the prostate apex. Fibers 10 to 18 are sorted in decreasing order from the apex but within the right lateral lobe. For each source fiber *i* the *N* neighbors used for light transmission measurements are *i-N/2,...,i+N/2*. In this way, probing light transmitted through the urethra is minimized.

By modeling the interstitially positioned source fibers as isotropic point sources, the Green's solution to the diffusion equation can be used to describe the fluence rate;

$$\phi_{\text{ij}} = \frac{P\,\mu^2_{\text{eff(i)}}}{4\pi\mu_{\text{a}}|r_{\text{j}} - r_{\text{i}}|} \exp\left(-\mu_{\text{eff(i)}}|r_{\text{j}} - r_{\text{i}}|\right) \quad i = 1,..,18 \quad j = 1,..,N \qquad (1)$$

Here, ϕ_{ij} denotes the fluence rate at a location r_{j} due to a point source at r_{i} and P is the fiber output power. By the isotropy assumption we thus ignore the contribution of the radiant flux, **j**, to the detected signal.[26] However, for the range of source-detector separations and optical properties encountered in *in vivo* prostate tissue, the fluence rate term typically exceeds the flux term by a factor 15-20.

Both ϕ_{ij} and ϕ_{ji} are measured and hence $2N$ measurements can be used to assess the fiber-specific $\mu_{\text{eff(i)}}$. Ideally, the logarithm of the fluence rate multiplied by the source-detector separation, $|r_{\text{j}} - r_{\text{i}}|$, is a first order polynomial with respect to $|r_{\text{j}} - r_{\text{i}}|$, where the slope yields μ_{eff} according to Eq. (2). The linear fit is performed for each source fiber, resulting in 18 different coefficients, $\mu_{\text{eff(i)}}$.

$$ln(\phi_{\text{ij}}|r_{\text{j}} - r_{\text{i}}|) = ln\left(\frac{P\,\mu^2_{\text{eff}(i)}}{4\pi\mu_{\text{a}}}\right) - \mu_{\text{eff(i)}}|r_{\text{j}} - r_{\text{i}}| \qquad (2)$$

TABLE I: Input parameters for the module evaluating target tissue optical properties. SNR threshold and r-range control what transmission signals are utilized for the linear fit and all evaluated $\mu_{\text{eff(i)}}$ are checked to lie within the μ_{eff} range, otherwise they are set to μ_{eff} default.

Parameter	Value
SNR threshold	3
r-range	8 mm
μ_{eff} range	1-8 cm^{-1}
μ_{eff} default[a]	3.7 cm^{-1}

[a]See Ref. 13, where $\mu_{\text{a}} = 0.5\ \text{cm}^{-1}$ and $\mu'_{\text{s}} = 8.7\ \text{cm}^{-1}$.

To reject non-valid measurements, for example caused by blood pooling at any fiber tip, only transmission signals with a sufficient signal-to-noise-ratio (SNR) are utilized. Here, the SNR is defined as the light transmission summed between 648 and 656 nm divided by the standard deviation (SD) of detector dark noise. Also, the source-detector separations must span a sufficiently large distance to allow a robust linear fit and validity of Eq. (2). In the current implementation, the algorithm used for evaluating $\mu_{\text{eff(i)}}$ thus requires specifying a SNR-threshold as well as a minimum range for $|r_{\text{j}} - r_{\text{i}}|$. If the number of valid measurements is less than six for a particular source fiber, due to either noise rejection or too limited source-detector distances, the transmission signals from two source fibers are combined and incorporated into the linear fit. This effectively expands the volume of the analyzed sub-geometry. If the number of valid measurements within the expanded sub-geometry is still less than six, further addition of sub-geometries is performed. The maximum number of included sub-geometries is 18, for which case the whole tissue geometry is analyzed as one unit. In the data post-processing, the evaluated effective attenuation coefficients are checked to be within a pre-defined range, otherwise all $\mu_{\text{eff(i)}}$ are set to a default value. Table I lists specific parameters that are used within this software module.

2. Irradiation times

The Cimmino optimization algorithm has previously been used for external radiotherapy treatment planning[27] and also very recently for determining light diffuser positions, lengths and strengths in prostate IPDT treatment planning.[28] Here we employ the Block-Cimmino optimization algorithm[29] for the inverse problem of finding individual irradiation times, t_{i}, for I isotropic point sources within a specific tissue geometry with certain optical properties. The optimization conditions can be expressed as the requirement to deliver a light dose exceeding a pre-determined threshold dose to the target tissue, i.e. the prostate glandular tissue, while minimizing the dose to the OAR, here defined as the urethra, rectum and normal, surrounding tissue. As already mentioned, the

PDT dose is based on the fluence, i.e. the fluence rate, ϕ, multiplied by the irradiation time, t. This simplification effectively means assuming homogenous photosensitiser distribution, as might be better justified at the long drug-light interval used in our clinical study, as well as ignoring effects of treatment-induced tissue hypoxia. The optimization problem is thus formulated as satisfying the following system of inequalities for the fluence in all tissue voxels;

$$L_\mathrm{j} \leq \langle \phi_\mathrm{j}, t \rangle = \sum_i \phi_\mathrm{ij} t_\mathrm{i} \leq U_\mathrm{j} \quad j = 1, 2, .., J$$
$$t_\mathrm{i} \geq 0 \quad i = 1, 2, .., 18 \qquad (3)$$

Here, J is the number of tissue voxels and L_j and U_j represent tissue type specific lower and upper threshold doses, respectively. Table II lists the thresholds used in this study. These threshold levels were found reasonable from the clinical work previously published by Bown *et al.*[6] No upper dose limit was imposed on prostate tissue as might be motivated by the presence of sensitizer photobleaching, the lack of hyperthermic effects associated with interstitial light delivery in prostate tissue[30] and the occurrence of only relatively minor treatment-related complications.[5,6] ϕ_ij is given by Eq. (1), where each source fiber is characterized by a specific $\mu_{\mathrm{eff(i)}}$ as described in Section II C 1. A fiber output power of 0.15 W is assumed for all fibers. In calculating the fluence rate distribution, we separate the absorption and reduced scattering coefficients by letting $\mu_\mathrm{s}' = 8.7$ cm^{-1} and determine $\mu_{\mathrm{a(i)}}$ from $\mu_{\mathrm{eff(i)}}$.

The current implementation uses the block-action scheme as outlined by Censor *et al.*,[29] where each voxel is ascribed a block corresponding to its tissue type, differentiating between prostate, urethra, rectum and normal tissue. The algorithm is based on an iterative scheme, starting from an arbitrary point in I-dimensional space. Non-violated constraints do not affect the new solution, whereas voxels experiencing light doses outside the specified range bring the successive iteration closer to the optimal solution defined by Eq. (3). This procedure is described mathematically in Eqs. (4) and (5).

$$\hat{t}^{k+1} = t^k + \lambda_\mathrm{k} \sum_{\mathrm{j} \in B_s} \alpha_\mathrm{j} s_\mathrm{j}(t^k) \phi_\mathrm{ij}$$
$$t^{k+1} = \begin{cases} \hat{t}^{k+1} & \text{if } \hat{t}_\mathrm{j}^{k+1} \geq 0 \\ 0 & \text{if } \hat{t}_\mathrm{j}^{k+1} < 0 \end{cases} \qquad (4)$$

where

$$s_\mathrm{j}(y) = \begin{cases} 0 & \text{if } L_\mathrm{j} \leq \langle \phi_\mathrm{j}, y \rangle \leq U_\mathrm{j} \\ \frac{U_\mathrm{j} - \langle \phi_\mathrm{j}, y \rangle}{\|\phi_\mathrm{j}\|^2} & \text{if } U_\mathrm{j} < \langle \phi_\mathrm{j}, y \rangle \\ -\frac{\langle \phi_\mathrm{j}, y \rangle - L_\mathrm{j}}{\|\phi_\mathrm{j}\|^2} & \text{if } \langle \phi_\mathrm{j}, y \rangle < L_\mathrm{j} \end{cases} \qquad (5)$$

The iterations are stopped either when the solution has converged or when a stipulated maximum number of iterations, here set to 50, has been reached. To improve initial convergence, the relaxation parameter λ_k is set to 20, but this parameter is successively decreased in case oscillations occur between iterations. Each tissue type, i.e. block B_s, is given a certain weight, α_j, which reflects the punishment associated with delivering a light dose outside the allowed interval. The sum of these tissue weights is normalized. In order not to let normal tissue voxels far away from the prostate influence the iterates in Eq. (4), only a certain number of the normal tissue voxels experiencing the highest light doses are included. This number is calculated as the number of voxels on the surface of a sphere with the same volume as the prostate gland. The explicit α_j values used in this study are given in Table II.

TABLE II: Input parameters for the Block-Cimmino optimization algorithm. L_j and U_j denote lower and upper light dose thresholds (J/cm^2), respectively, and α_j are the tissue importance weights.

Parameter	Prostate	Rectum	Urethra	Normal
L_j (J)	5	0	0	0
U_j (J)	∞	5	5	5
α_j	10	5^a	0.1	1e-8

[a]Varied between 1e-4 and 500, see Figure 4.

Except for the first time the Block-Cimmino algorithm executes, the fraction of the entire treatment session already completed during the previous treatment sequence(s) is subtracted from the newly calculated irradiation times. The output thus constitutes the remaining irradiation times based on the current set of $\mu_{\mathrm{eff(i)}}$. When all $\mu_{\mathrm{eff(i)}}$ display no pronounced variation, for example change by less than 10%, as compared to the previous measurement sequence, or, in the case of the first measurement sequence, relative to the pre-treatment plan, which utilizes the default value of μ_eff given in Table I, the Block-Cimmino algorithm is not executed. Instead, remaining fiber irradiation times are calculated by simply subtracting the duration of the previous treatment sequence.

Although the Cimmino algorithm does not allow for straightforward implementation of DVH constraints,[31] here we use the resulting DVHs to check the light dose distribution. In general, DVHs provide information on the tissue fractional volume that receives a certain treatment dose. For all results, the DVH doses equal the fluence, i.e. $\sum_i \phi_\mathrm{ij} t_\mathrm{i}$, where t_i are calculated by the Block-Cimmino algorithm and ϕ_ij are modeled by means of the FEM, see Section II D. The importance weights, α_j, are empirically adjusted to reflect the sensitivity of the different OAR and to discriminate these organs from the target tissue. In this paper, we aim at delivering a light dose exceeding our pre-defined threshold in 90% of the target tissue, whereas a maximum of 25% of the voxels representing the rectum is allowed this light dose. No dose restrictions are imposed on normal tissue and urethra.

D. Modeling the light distribution

To provide realistic input for the realtime dosimetry module, the FEM (Multiphysics 3.3®, Comsol AB, Stockholm, Sweden) is used to model the fluence rate distribution, ϕ_{ij}, within the geometry illustrated in Figure 1.b. As the PDT dose is based on the fluence only, photosensitizer and oxygen distributions are not modeled. The target and risk organs are surrounded by a tissue block, representing normal tissue. With a side-length of 60 mm this block is sufficiently large for boundary effects not to influence the solution. The fluence rate is determined by solving the steady-state diffusion equation;

$$-\nabla \cdot (D_j \nabla \phi_{ij}) + \mu_{a(j)} \phi_{ij} = S(r_i) \qquad i = 1, .., 18. \quad (6)$$

Here, the diffusion coefficient $D_j = [3(\mu_{a(j)} + \mu'_{s(j)})]^{-1}$ and the bare-ended fibers, constituting the 18 source terms $S(r_i)$, are modeled as isotropic point sources with 0.15 W output power. The partial current boundary condition is implemented at the boundaries;[32]

$$\hat{n} \cdot D_j \nabla \phi_{ij} + \frac{1}{2}\Big[\frac{1 - R_{eff}}{1 + R_{eff}}\Big]\phi_{ij} = 0. \quad (7)$$

For all boundaries, R_{eff}=1, except for the prostate-urethra interface where R_{eff}=0.493 to model an air-filled urethra. Eq. (6) is solved 18 times, i.e. with one source fiber active at a time, resulting in the fluence rate distribution due to each of the 18 sources. For each solution, the fluence rate at the positions of the six neighboring fibers is assessed as a means to quantify the light transmission between patient fibers. Here, we chose to match format of the simulated data, consisting of single numbers representing $\phi(r_{ij})$ at the treatment wavelength, to the data format used in the clinical setting, i.e. spectrally resolved transmission data between 630 and 840 nm. Thus, each transmission number resulting from a FEM simulation is set to represent the peak transmission signal at 652 nm and a full transmission spectrum is constructed by fitting a Gaussian function with a HWHM of 2 nm centered at this wavelength. Furthermore, white Gaussian noise with SD=0.1% of the maximum transmission signal is added to each spectrum between 630 and 840 nm to represent detector dark noise.

The FEM simulation process is performed for five levels of light absorption within the prostate. Table III lists the optical properties used in the simulations. For each simulation, spatial variations of the prostate tissue optical properties are modeled by adding white Gaussian noise with a SD of 10 and 5% to the absorption and reduced scattering coefficients, respectively. These noise data are generated for every fifth voxel within the geometry model and is linearly interpolated to voxels in between. In this way we try to correctly model spatial variations of the optical properties typically found in prostate tissue.[18] In Eqs. (6) and (7) this spatial dependency is indicated by the subscript j. The possibilities of incorporating well defined and spatially varying absorption and scattering coefficients as well as tissue heterogeneities were the main motivations for choosing FEM simulated data on light transmission levels instead of experimental data within tissue phantoms.

TABLE III: Optical properties used for the five FEM simulations of the fluence rate. All units are in [cm^{-1}].

	Prostate	Rectum	Urethra	Normal
μ_a	0.3,0.4,0.5,0.6,0.7	0.3	air-filled	0.3
μ'_s	8.7	8	air-filled	8
μ_{eff}	2.8,3.3,3.7,4.1,4.4	2.7	air-filled	2.7

III. RESULTS

A. Optical properties

We used light transmission data simulated by the FEM as input for the software module developed for evaluating the effective attenuation coefficients. Figure 2.a shows the individual $\mu_{eff(i)}$ evaluated from the modeled data set, and in Figure 2.b the data have been averaged for the 18 source fibers for each absorption level. The average μ_{eff} (solid line) illustrates an underestimation as compared to the prostate-μ_{eff} used in the simulations (dashed line), also referred to as the true μ_{eff}. The error bars denote ±1SD. μ_{eff} was not underestimated when evaluating simulated data for a totally homogeneous medium. It was also observed that for the geometry and range of tissue optical properties used in this work, varying the SNR-threshold between 1 and 10 had negligible influence on the average μ_{eff}.

A sensitivity analysis was performed to investigate the influence of the heterogeneous geometry, i.e. the lower attenuation levels within urethra and normal, surrounding tissues, on the transmission measurements. Considering absorbing heterogeneities, the change in the fluence rate at position r_j from a point source at r_i, i.e. ϕ_{ij}, due to an absorption change in a voxel at r_k, $\Delta\mu_{a(k)}$, is given by;[33]

$$\Delta ln(\phi_{ij}) = \mathbf{J}_{ijk} \Delta\mu_{a(k)} = -\frac{G_{ik} G_{kj}}{G_{ij}} \Delta\mu_{a(k)} \quad (8)$$

Here G_{ik} is the Green's solution to the diffusion equation for the fluence rate in voxel k due an isotropic point source at r_i, see also Eq. (1). G_{kj} and G_{ij} are defined analogously. $\mathbf{J}$ is the Jacobian, which was calculated on the FEM-mesh for all source-detector pairs. To quantify to what extent the transmission signals probe the target tissue and the different OAR, a fiber- and tissue type-specific Jacobian was evaluated;

$$\tilde{\mathbf{J}}_{i,B_s} = \sum_{k \in B_s} \sum_{j=1}^{6} \mathbf{J}_{ijk} \qquad i = 1, .., 18 \quad (9)$$

B_s represents any of the tissue types included in the geometry and index j relates to the six neighboring detec-

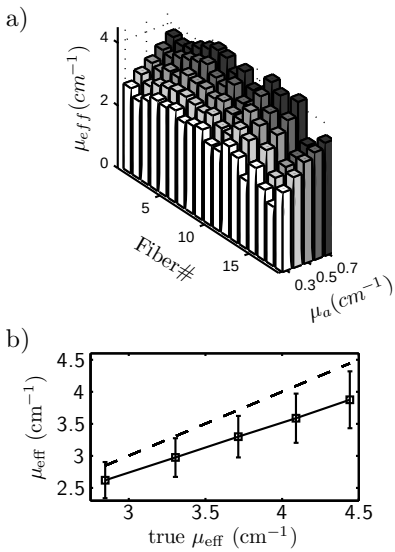

FIG. 2: a) The evaluated $\mu_{\text{eff(i)}}$ for different levels of absorption within the prostate. The FEM was utilized to provide data on light transmission signals within a realistic prostate geometry. Here, μ_s'=8.7 cm^{-1} within the prostate for all simulations. b) Evaluated μ_{eff} (solid) averaged over all fibers as a function of the true μ_{eff} (dashed). Error bars denote ±1SD.

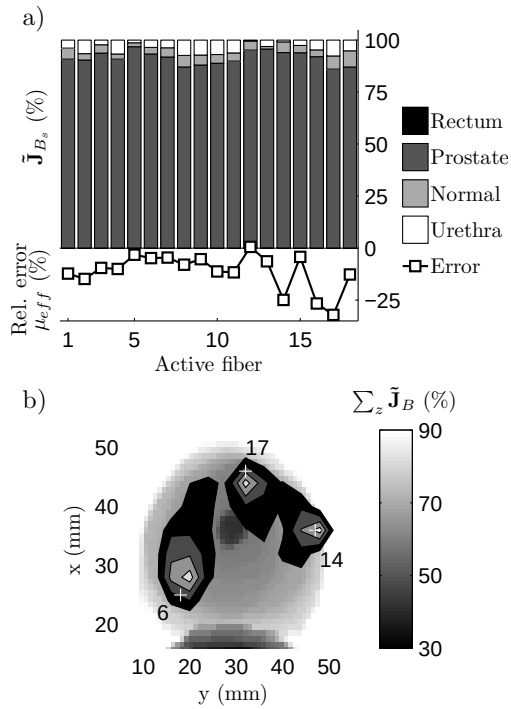

FIG. 3: To quantify to what extent the heterogeneous tissue structure influences the transmission signals, the Jacobian according to Eq. (9) was studied utilizing FEM-simulated data for μ_{eff}=3.7 cm^{-1}. a) The fiber- and tissue type-specific Jacobian, normalized for each source fiber, together with the relative error of the evaluated $\mu_{\text{eff(i)}}$. The influence of rectum was negligible. b) Isosurfaces of $\tilde{\mathbf{J}}$ summed in z-direction for fibers 6, 14 and 17. Fiber 6 is associated with a small relative μ_{eff}-error as it detects transmitted light that mostly probes prostate tissue. Fibers 14 and 17 probe larger fractions of the urethra and normal, surrounding tissue, respectively, resulting in a pronounced underestimation of the effective attenuation coefficient.

tion fibers. Figure 3.a is a bar plot displaying $\tilde{\mathbf{J}}_{\text{i,B}_s}$ normalized with respect to the total sum of the Jacobian for each patient fiber. The relative error between the true and evaluated $\mu_{\text{eff(i)}}$ is also included in the graph. For most source fibers, a large error of the evaluated $\mu_{\text{eff(i)}}$ corresponded to high $\tilde{\mathbf{J}}_{\text{urethra}}$ and/or $\tilde{\mathbf{J}}_{\text{normal}}$. Figure 3.b displays $\tilde{\mathbf{J}}_{\text{B}_s}$ summed along the prostate depth dimension for the monitoring sub-geometries corresponding to fibers 6, 14 and 17. Here, fiber 6 probed mostly prostate tissue and correspondingly was associated with a small relative μ_{eff}-error. On the other hand, fibers 14 and 17 also detected light transmitted via normal, surrounding tissue and urethra, leading to worse μ_{eff}-estimations. From Figure 3.a it can be observed that fiber 12 was associated with a much smaller error than fiber 14 despite having similar $\tilde{\mathbf{J}}_{\text{urethra}}$. However, a more detailed analysis showed that for fiber 14 it was the transmission to only one detection fiber that probed the urethra, whereas for fiber 12 the transmission to all six detection fibers probed the urethra to an equal but small extent. The linear fit performed to extract $\mu_{\text{eff(i)}}$ was therefore characterized by a better goodness for fiber 12 than for 14. To summarize, the underestimation of the effective attenuation coefficient could be explained by the presence of the air-filled urethra and the lower overall attenuation within the remaining organs, especially influencing light transmission between fibers close to either the urethra or the periphery of the prostatic gland.

B. Irradiation times

The possibility of imposing varying sensitivity on the OAR was investigated by studying the predicted irradiation times and delivered light doses after changing the importance weight on the rectum. As an example, Figure 4.a shows the DVHs of the delivered light dose for

α_j(rectum)=0.01. The weights on the remaining organs remained fixed at values given in Table II. For all calculations, $\mu_{eff(i)}$=3.7 cm^{-1} within the target tissue. The dashed lines are used to illustrate that approximately 43% of the rectum was exposed to the threshold light dose for this set of importance weights. The corresponding number, hereafter referred to as the treatment fraction, was 98% for prostate tissue indicating that almost the entire gland was targeted. The α_j(rectum) was varied between 1e-4 and 500 and the treatment fractions for each tissue type are plotted in Figure 4.b. For α_j(rectum)>1 the rectum was better discriminated from the target tissue and the treatment fraction of the prostate gland was still sufficiently large. In Figure 4.c, the individual fiber irradiation times for α_j(rectum)=1e-4 (white bars) and 500 (black bars) are shown. From this plot, it is interesting to observe that for higher sensitivity on the rectum, the irradiation times of source fibers close to this organ, i.e. fibers 2, 6, 12, 13 and 16, were decreased, whereas for source fibers positioned at the greatest distance from the rectum, i.e. fibers 1, 4, 5, 8, 11, 15, 17 and 18 that are positioned within the anterior part of the gland, were prolonged. These effects can be explained by the relatively high α_j on the prostate, directing the Block-Cimmino optimization algorithm towards a solution that theoretically will treat as large fraction of the target tissue as possible. For the case of the highest α_j(rectum), the source fiber positions were most likely not optimal and thus fibers distant from the rectum were forced to deliver a much larger light dose. This helps explain the drastic increase of the total delivered light energy, defined as the sum of all fiber irradiation times multiplied by the 0.15 W output power, from 865 (at α_j(rectum)=1e-4) to 1350 J (at α_j(rectum)=500). From Figure 4.c it can be seen that the total treatment time, as determined by the maximum irradiation time, was not greatly influenced by the varying importance weight. In general, we have observed that for a certain μ_{eff}, the total treatment time is primarily determined by the geometry, i.e. the size of the target tissue as well as the source positions. Due to the rapid decay of the fluence rate with distance from an isotropic point source, the total treatment time increases dramatically with the glandular volume. For the remainder of the results, α_j(rectum) is set to 5.

Figures 5.a and b illustrate the consequences on DVHs and irradiation times of increasing the absorption coefficient within the prostate. Here, μ_a=0.3 (dotted), 0.5 (dash-dotted) or 0.7 (solid) cm^{-1} whereas μ_s'=8.7 cm^{-1}. Thus, $\mu_{eff(i)}$=2.8, 3.7 or 4.4 cm^{-1} were used as input for the Block-Cimmino optimization algorithm for all source fibers. Three observations are worth mentioning; firstly, the DVHs in Figure 5.a indicate some overtreatment of the rectum; secondly, higher μ_{eff} within the prostate results in a larger treatment fraction of the target tissue; and thirdly, whereas the total light energy increased from 420 (at μ_a=0.3 cm^{-1}) to 1065 J (at μ_a=0.7 cm^{-1}), the total treatment time, as determined by the maximum irradiation time, was only increased by 90 s. These effects can all be explained by the rapid decrease of the fluence rate with distance from a point source, the assumption of an infinite, homogeneous medium inherent in the current implementation of the Block-Cimmino optimization algorithm and the ability of the optimization algorithm to converge to a close approximation of the least-intensity feasible solution.[34] Firstly, the Block-Cimmino algorithm underestimated the light propagation within the OAR due to the lower absorption and scattering levels of these organs used in the FEM model. The overtreatment was thus more pronounced the larger the difference of μ_{eff} between target tissue and OAR. Secondly, the increased treatment fraction of the target tissue for the higher absorption levels is due to the more rapid decay of the fluence rate with r for increasing μ_{eff}. From the expression $\frac{\partial\phi}{\partial r} \propto \frac{\partial}{\partial r}\left[\frac{1}{r}\exp(-\mu_{eff}r)\right]$, derived from Eq. (1), it is evident that the transition zone between treated, i.e. light doses above the threshold, and untreated, i.e. light doses below the threshold, regions becomes more narrow the higher the effective attenuation coefficient. Thus, under the assumption of an infinite, homogeneous medium inherent in the optimization algorithm it is theoretically easier to discriminate between target tissue and OAR for higher μ_{eff} levels. Finally, from the perspective of optimizing the treatment volume in relation to the total treatment time it is more "cost-effective" to distribute the higher light doses required among all patient fibers. This means that for increasing absorption, the relative increase in individual irradiation times was largest for fibers characterized by initially short irradiation times, located close to the rectum, than for fibers characterized by the longest irradiation times, positioned in the peripheral regions of the prostate gland but further away from the rectum. One should observe that an absorption increase inevitably introduces a spatial shift of the treated tissue volume as glandular regions closer to the OAR are favored instead of the prostate periphery. In conclusion, the Block-Cimmino algorithm achieved better targeting of the prostate gland at the expense of overtreating the OAR for higher μ_a.

C. IDOSE module

The performance of the IDOSE module, i.e steps (8) and (9) in Figure 1.a, was evaluated on treatment scenarios displaying both temporally invariant and varying target tissue optical properties. As in Section III A, light transmission signals obtained from the FEM simulations were utilized as input for the module evaluating the target tissue optical properties.

Figure 6.a shows the total delivered light energy predicted by the IDOSE module (square markers) as a function of the prostate μ_{eff} assuming this coefficient would remain constant throughout the entire treatment session. The total light energy calculated by the Block-Cimmino optimization algorithm when utilizing the true μ_{eff} as input are also shown (diamond markers). Firstly, the graph

illustrates a dramatic increase in light energy, and thus total irradiation times, with higher overall absorption. Secondly, the underestimation of μ_{eff}, as already shown in Figure 2, decreased the demand on total light energy. This effect was more pronounced for the higher μ_{eff}-levels. Figure 6.b compares the DVHs of the delivered light dose for a true μ_{eff}=3.7 cm^{-1}. Dashed and solid lines correspond to true and evaluated μ_{eff}, respectively, indicating a lower treatment fraction of the prostate resulting from underestimating the light attenuation coefficient. On the other hand, the treatment fractions of the remaining organs were rather insensitive to the error associated with the μ_{eff}-evaluation. The influence on the treatment fraction of the prostate caused by underestimating the light attenuation can be decreased by increasing the target tissue importance weight (data not shown).

The IDOSE module was also tested on a treatment scenario displaying temporally varying μ_{eff}. The time-dependent μ_{eff} is indicated by the solid line in Figure 7.a. Such a situation might correspond to a treatment-induced tissue deoxygenation combined with an increased blood volume that gradually levels as the blood flow is limited by the vascular effects of the PDT treatment. A similar absorption increase has been observed during *in vivo* IPDT on massive skin tumors.[14] In the graph, the dashed line represents the default effective attenuation coefficient upon which the pre-treatment plan, i.e. steps (3) and (5) in Figure 1.a, was based. Furthermore, shaded areas indicate treatment sequences and squares denote measurement sequences performed after 0, 1, 2, 3, 4, 5, 7, 9 and 11 min of therapeutic irradiation. The three μ_{eff}-levels in Figure 7.a correspond to the three sets of optical properties in Table III with the highest absorption coefficient. Data on light transmission were thus acquired from the three sets of FEM-simulations performed for these absorption levels and used as input for the algorithm evaluating $\mu_{\text{eff}(i)}$. Hence, transmission data were identical for monitoring sequences 3 and 4 as well as for sequences 5-9. Following each measurement sequence, $\mu_{\text{eff}(i)}$ were evaluated from FEM modeled light transmission signals and used as input for the Block-Cimmino algorithm, updating individual fiber irradiation times. Figure 7.b compares the resulting DVHs of the delivered light dose for the cases of no treatment feedback, i.e. irradiation times as calculated based on the first measurement sequence, (dashed lines) and with treatment feedback (solid lines) based on continuous measurements and $\mu_{\text{eff(i)}}$-evaluation. The treatment fraction of the target tissue was larger for the case of treatment feedback (∼96%) as compared to no treatment feedback (∼86%). Finally, Figure 7.c shows the fiber irradiation times without (white bars) and with (black bars) treatment feedback. The treatment feedback quite naturally increases the total delivered light dose as compared to a treatment situation without any treatment feedback. However, only source fibers 2, 4, 13, 14, 16 and 17, characterized by initially short irradiation times, are forced to emit higher light doses. The irradiation times of all other treatment fibers remain constant or even decrease slightly. These effects are explained by on the one hand the tendency of the Cimmino optimization algorithm to yield an approximation of the least-intensity feasible solution and on the other the possibility to better discriminate between target and sensitive tissue for higher light attenuation. These factors, already discussed in relation to Figures 5 and 6, force the optimization algorithm to target prostate regions closer to the urethra and rectum, as the OAR are more easily discriminated due to the higher absorption levels. In conclusion, for this temporal behavior of the effective attenuation coefficient the feedback enables a larger treatment fraction without prolonging the overall treatment time by introducing a spatial shift of the treatment volumes.

D. Robustness and error analysis

Here, we discuss the influence of deviating fiber positions, due to a limited accuracy when guiding patient fibers into position, and varying scattering levels, i.e. $\mu_s' \neq$8.7 cm^{-1}, on the resulting prostate treatment fraction. As described in Section II C 2, μ_a is solved for from μ_{eff} assuming a constant scattering coefficient. Deviations in calculated fluence rate distribution thus occur whenever the reduced scattering coefficient deviates from the assumed value.

To quantify these errors, homogeneous optical properties were assumed within the geometry shown in Figure 1.b and Eq. (1) was used for calculating the fluence rate distribution. The fiber positions were slightly altered in all three dimensions, where the deviations were independent and sampled from a normal distribution of zero mean and 2 mm SD. The data were simulated using $\mu_a \in [0.36, 0.61]$ cm^{-1} and $\mu_s' \in [6.8, 10.06]$ cm^{-1}.[13] As described for the IDOSE module, $\mu_{\text{eff(i)}}$ were solved for from the fluence rate distribution and the DVHs were calculated from the irradiation times shown in Figure 7.c (white bars). This procedure was repeated 100 times for each set of absorption and reduced scattering levels. The resulting prostate treatment fractions were compared to those calculated utilizing true fiber positions and μ_s'=8.7 cm^{-1}. Treatment fraction deviations, $\Delta DVH_{100\%}$, were quantified by Eq. (10).

$$\Delta DVH_{100\%} = \frac{DVH_{100\%}^{\text{true}} - DVH_{100\%}^{\text{IDOSE}}}{DVH_{100\%}^{true}} \times 100 \quad (10)$$

where superscript *true* refers to actual, shifted fiber positions, and true optical properties whereas *IDOSE* refers to fiber positions and optical properties assumed by the IDOSE model.

After introducing the spatial shifts of the fiber positions, the evaluated $\mu_{\text{eff(i)}}$ were on average overestimated by +5% (data not shown). For all r, $|\ \frac{\partial \phi}{\partial r}\ |_{\Delta r>0} > |\ \frac{\partial \phi}{\partial r}\ |_{\Delta r<0}$, where Δr is the fiber position shift. This dif-

ference is larger at small r, leading to a steeper slope in Eq. (2) and apparently increasing the effective attenuation coefficient.

Figure 8 illustrates the treatment fraction deviations for shifted fiber positions and varying tissue optical properties. Erroneous fiber positioning leads to lowered treatment fractions as shown by the solid curves. The errors are on the average -1% and -6% for the lowest and highest absorption coefficient, respectively, leading to an undertreatment of the prostate gland. This undertreatment is caused by combination of non-optimal fiber positions and falsely predicted optical properties. For shifted fiber positions, the assumption of a constant μ_s' has a minor impact on the delivered light dose as shown by the flat appearance of the solid curves over the range of optical properties presented here. Considering the treatment fractions retrieved using true fiber positions, i.e. the dashed curves in Figure 8, the errors are within $\pm 1\%$ and $\pm 3\%$ for the lowest and highest absorption coefficient, respectively.

IV. DISCUSSION

As IPDT on tissue has been shown to cause changes in light transmission and there exists a large biological variability of the prostate tissue composition, light doses required to treat the entire prostate gland are likely to vary between patients. This has raised increasing interest in individualizing treatment parameters, such as the delivered light dose,[15] and introducing realtime treatment feedback.[17] Here, we have presented a treatment procedure for IPDT on prostate tissue incorporating realtime treatment monitoring and feedback based on a light dose threshold model. Algorithms have been implemented that utilize light transmission signals between patient fibers in order to assess the effective attenuation coefficient within the target tissue. These coefficients are utilized as input for a Block-Cimmino optimization algorithm, thus updating individual fiber irradiation times. By iterating measurement sequences during the entire treatment session, we aim at individualizing the delivered light dose and compensate for any treatment-induced alterations of the light attenuation within the target tissue. To evaluate the performance of the realtime dosimetry module, the FEM was utilized to model the diffuse light distribution within a realistic prostate model. The model geometry included an air-filled urethra, lower levels of absorption and scattering within tissue surrounding the prostate as well as local variation in the prostate tissue optical properties. Due to the difficulties of fabricating a tissue phantom with such characteristics, we chose to evaluate the realtime dosimetry module on simulated light transmission data. In addition, the use of the FEM was essential in evaluating the true DVHs from the predicted irradiation times in each treatment scenario.

As was demonstrated in Figure 2, the μ_{eff}-increase could be tracked but it was consistently underestimated. This effect was explained by the fact that the transmission signals for some source-detector fiber configurations also probed the urethra, which was modeled as air-filled, and/or the normal, surrounding tissue, characterized by lower levels of absorption and scattering. The method of spatially-resolved spectroscopy tends to average the effect of any heterogeneity throughout the entire tissue volume probed by the transmitted light. Although the measurement configuration was determined by the desire to avoid probing the urethra, this heterogeneity had pronounced influence on the evaluated attenuation coefficients. One important conclusion to be drawn from these results is that the prostate gland is small enough to allow surrounding organs to influence the diffuse light distribution. When relying on spatially resolved spectroscopy and diffuse light propagation for assessing the target tissue optical properties, one should be aware of these effects. The evaluation method presented herein is *subdomain-based* where neighboring subdomains probe greatly overlapping tissue regions. The possibilities of improving spatial resolution and incorporating spatial priors constitute advantages of *voxel-based* methods, such as diffuse optical tomography (DOT). The sensitivity analysis presented in Section III A constitutes a first step towards a future *voxel-based* method for reconstructing the tissue optical properties.

From the DVHs in Figure 6.b, it was evident that the underestimation of μ_{eff} caused a slight undertreatment of the prostate. However, when in the clinical situation the treatment of the entire prostate gland is deemed essential, an undertreatment can be reduced by increasing the importance weight of the target tissue. The presence of other tissue heterogeneities, such as calcifications and local blood accumulation, constitutes a further challenge to the algorithm assessing $\mu_{\text{eff(i)}}$. Due to the strong absorption by hemoglobin, light transmission signals to and from occluded fibers will be characterized by poor SNR. The SNR-threshold for including a transmission signal can be adjusted to exclude fibers with large amounts of blood in front of the fiber tips. When ignoring data from one fiber, the current algorithm instead includes more distant fibers for evaluating $\mu_{\text{eff(i)}}$, thereby averaging the level of light attenuation over larger volumes and making the procedure less sensitive to the presence of a few local heterogeneities. Extended simulations and *in vivo* clinical data are required to optimize the SNR-threshold.

The Block-Cimmino optimization algorithm was used to solve for individual fiber irradiation times provided the requirement to deliver a pre-determined light dose to the target tissue while sparing surrounding, sensitive organs. The importance weights, α_j, were adjusted to reflect the relative sensitivity of the OAR. As was seen in Figure 4.b, increasing the importance weight of the rectum lowered the light doses within this organ. In this study, the urethra was not considered a particularly sensitive organ due to the transient periods of catheterization reported by others.[6] In contrast to Altschuler *et al.*[28], who investigated the use of the Cimmino optimization algorithm for PDT pre-treatment planning, we observed pro-

nounced effects on the deposited dose distribution when varying the tissue importance weights. However, that study is different from this work in that diffusing fibers and spatially homogeneous optical properties were used. A simplification of the present implementation is the assumption of an infinite, homogeneous medium inherent in the optimization problem as formulated in Eqs. (3) and (1). As already discussed, the presence of tissue heterogeneities makes this assumption erroneous. However, the shorter calculation times achievable when utilizing the analytical expression for ϕ_{ij} as compared to for example a FEM-based model are most important for the realtime feedback scheme outlined here.

The influence on DVHs and irradiation times of varying the effective attenuation coefficient was studied in Figure 5. Despite more than doubling the absorption coefficient, the treatment fraction of the prostate remained relatively constant, indicating a certain robustness of the Block-Cimmino algorithm. However, the higher the absorption within the prostate, the larger the treatment fraction of the OAR. This overtreatment was due to the assumption of an infinite, homogeneous medium, thus underestimating the light propagation within the organs surrounding the target tissue. As already discussed in Section III B, for an infinitely large and homogeneous medium it is theoretically easier to discriminate between target tissue and OAR the higher the μ_{eff}. Although no clinical data exist to justify the lower μ_{eff} within the surrounding tissue used in our model, the current geometry was employed to exploit the capabilities and shortcomings of our dosimetry module.

The concept of realtime treatment feedback was tested by executing the algorithms constituting the realtime dosimetry module on a simulated treatment session with temporally varying absorption. Here, the effective attenuation coefficient was increased above the levels usually observed within *in vivo* prostate tissue[13] as the treatment progressed. For the case of no treatment feedback a pronounced undertreatment of the target tissue was noted. On the other hand, after enabling the realtime feedback, individual fiber irradiation times were adjusted so as to deliver a light dose exceeding the threshold dose to more than 95% of the target tissue voxels. Thus, the ability of the IDOSE module to detect and compensate changes to the effective attenuation coefficient occurring during the IPDT procedure was shown. As indicated by the treatment flow chart in Figure 1.a, updating irradiation times are done in parallel to a treatment sequence. This procedure was implemented in order to limit total treatment times but also means the update lags one cycle as compared to the measurement sequences. Therefore, a slight overtreatment of some tissue regions might occur in the unlikely event that there is a drastic reduction of the light attenuation at the end of a treatment session.

The error analysis presented in Section III D, although performed within a homogenous medium, shows relatively little influence of deviating source fiber positions and varying μ_s' on the total prostate treatment fraction. For the model geometry, range of tissue optical properties and fiber positioning inaccuracy investigated here, it seems tissue heterogeneities, such as the urethra, and varying μ_a within the prostate have a comparatively larger impact on the targeted tissue volume. Thus, it appears worthwhile investigating realtime feedback for ascertaining delivery of predefined PDT doses.

The software modules described in this work are implemented on a clinically adapted system for IPDT on prostate tissue. As the instrumentation also monitors the Temoporfin fluorescence and the tissue absorbance within the NIR wavelength region, the clinical treatment sessions will provide information on the feasibility of including also the photosensitizer distribution and the target tissue oxygen saturation level in the PDT dose metric. For example, fluorescence and NIR transmission signals could be combined with low-resolution DOT to map the spatial distribution of the sensitizer and tissue oxygenation levels. These parameters could then be weighted into the Block-Cimmino algorithm, for example increasing the demand on therapeutic light for regions with a lower photosensitizer concentration and pausing the treatment within hypoxic tissue volumes. However, note that such a mapping of the sensitizer distribution is of limited spatial resolution and does not allow us to study its diffusion out of the tissue vasculature as outlined in Ref. 35. A more detailed instrumental description and initial clinical results will be presented in the near future.

In conclusion, we have presented algorithms that constitute a realtime dosimetry module for IPDT on the whole prostate tissue. Implemented on an 18-fiber IPDT instrument, the dosimetry software includes monitoring of the light attenuation during the treatment procedure and updating individual fiber irradiation times. Thus, the delivered light dose can be adjusted to take into account patient-specific and treatment-induced variations in tissue light transmission. Utilizing data on light distribution simulated by the FEM within a realistic prostate model we have shown that increasing levels of light attenuation can be tracked. The Block-Cimmino algorithm was shown to predict irradiation times such that sufficiently large prostate volumes were targeted irrespective of the tissue optical properties. Finally, by continuously monitoring the tissue light transmission and updating irradiation times during a simulated treatment session, an undertreatment, evident for the case of no treatment feedback, could be avoided.

V. ACKNOWLEDGEMENTS

The authors highly appreciate the support by Dr. Katarina Svanberg and Prof. Sune Svanberg. SpectraCure AB (Lund, Sweden) is gratefully acknowledged for financial and technical support.

* Electronic address: ann.johansson@fysik.lth.se; URL: http://www-atom.fysik.lth.se/

[1] B. Wilson, M. Patterson and L. Lilge, "Implicit and explicit dosimetry in photodynamic therapy: A new paradigm," Lasers Med. Sci. **12**(3), 182–199 (1997).

[2] B. Henderson, T. Busch and J. Snyder, "Fluence rate as a modulator of PDT mechanisms," Lasers Surg. Med. **38**(5), 489–493 (2006).

[3] M. Patterson, B. Wilson and R. Graff, "In vivo tests of the concept of photodynamic threshold dose in normal rat liver photosensitized by aluminum chlorosulphonated phthalocyanine," Photochem. Photobiol. **51**(3), 343–349 (1990).

[4] T. Farrell, B. Wilson, M. Patterson and M. Olivo, "Comparison of the in vivo photodynamic threshold dose of Photofrin, mono- and tetrasulfonated aluminum phthalocyanine using a rat liver model," Photochem. Photobiol. **68**(3), 394–399 (1998).

[5] T. Nathan, D. Whitelaw, S. Chang, W. Lees, P. Ripley, H. Payne, L. Jones, M. Parkinson, M. Emberton, A. Gillams, A. Mundy and S. Bown, "Photodynamic therapy for prostate cancer recurrence after radiotherapy: A phase I study," J. Urol. **168**(4), 1427–1432 (2002).

[6] C. Moore, T. Nathan, W. Lees, C. Mosse, A. Freeman, M. Emberton and S. Bown, "Photodynamic therapy using meso tetra hydroxy phenyl chlorin (mTHPC) in early prostate cancer," Lasers Surg. Med. **38**(5), 356–363 (2006).

[7] C. Moore, I. Hoh, S. Bown and M. Emberton, "Does photodynamic therapy have the necessary attributes to become a future treatment for organ-confined prostate cancer?" BJU Int. **96**(6), 754–758 (2005).

[8] R. Weersink, A. Bogaards, M. Gertner, S. Davidson, K. Zhang, G. Netchev, J. Trachtenberg and B. Wilson, "Techniques for delivery and monitoring of TOOKAD (WST09)-mediated photodynamic therapy of the prostate: Clinical experience and practicalities," J. Photochem. Photobiol. B **79**(3), 211–222 (2005).

[9] J. Pinthus, A. Bogaards, R. Weersink, B. Wilson and J. Trachtenberg, "Photodynamic therapy for urological malignancies: Past to current approaches," J. Urol. **175**(4), 1201–1207 (2006).

[10] K. Du, R. Mick, T. Busch, T. Zhu, J. Finlay, G. Yu, A. Yodh, S. Malkowicz, D. Smith, R. Whittington, D. Stripp and S. Hahn, "Preliminary results of interstitial motexafin lutetium-mediated PDT for prostate cancer," Lasers Surg. Med. **38**(5), 427–434 (2006).

[11] D. Zaak, R. Sroka, M. Höppner, W. Khoder, O. Reich, S. Tritschler, R. Muschter, R. Knüchel and A. Hofstetter, "Photodynamic therapy by means of 5-ALA induced PPIX in human prostate cancer - preliminary results," Med. Laser Appl. **18**, 91–95 (2003).

[12] T. Zhu, A. Dimofte, J. Finlay, D. Stripp, T. Busch, J. Miles, R. Whittington, S. Malkowicz, Z. Tochner, E. Glatstein and S. Hahn, "Optical properties of human prostate at 732 nm measured in vivo during motexafin lutetium-mediated photodynamic therapy," Photochem. Photobiol. **81**(1), 96–105 (2005).

[13] T. Svensson, M. Einarsdottir, K. Svanberg and S. Andersson-Engels, "In vivo optical characterization of human prostate tissue using near-infrared time-resolved spectroscopy," J. Biomed. Opt. **12**(1), 014022–1–014022–10 (2006).

[14] A. Johansson, T. Johansson, M. Soto Thompson, N. Bendsoe, K. Svanberg, S. Svanberg and S. Andersson-Engels, "In vivo measurement of parameters of dosimetric importance during photodynamic therapy of thick skin tumors," J. Biomed. Opt. **11**(3) (2006).

[15] A. Rendon, R. Weersink and L. Lilge, "Towards conformal light delivery using tailored cylindrical diffusers: attainable light dose distributions," Phys. Med. Biol. **51**(23), 5967–5975 (2006).

[16] B. Pogue, C. Sheng, X. Zhou, P. Hoopes and T. Hasan, "Photosensitizer dosimetry controlled PDT: is there proof that improved tools improve treatment outcome?" Proc. SPIE **6427**, 20 (2007).

[17] R. van Veen, D. Robinson, P. Siersema and H. Sterenborg, "The importance of in situ dosimetry during photodynamic therapy of Barrett's esophagus," Gastrointest. Endosc. **64**(5), 786–788 (2006).

[18] T. Zhu, J. Finlay and S. Hahn, "Determination of the distribution of light, optical properties, drug concentration, and tissue oxygenation in-vivo in human prostate during motexafin lutetium-mediated photodynamic therapy," J. Photochem. Photobiol. B **79**(3), 231–241 (2005).

[19] J. Finlay, T. Zhu, A. Dimofte, D. Stripp, S. Malkowcz, T. Busch and S. Hahn, "Interstitial fluorescence spectroscopy in the human prostate during motexafin lutetium-mediated photodynamic therapy," Photochem. Photobiol. **82**(5), 1270–1278 (2006).

[20] G. Yu, T. Durduran, C. Zhou, T. Zhu, J. Finlay, T. Busch, S. Malkowicz, S. Hahn and A. Yodh, "Real-time in situ monitoring of human prostate photodynamic therapy with diffuse light," Photochem. Photobiol. **82**(5), 1279–1284 (2006).

[21] M. Soto Thompson, A. Johansson, T. Johansson, S. Andersson-Engels, N. Bendsoe, K. Svanberg and S. Svanberg, "Clinical system for interstitial photodynamic therapy with combined on-line dosimetry measurements," Appl. Opt. **44**(19), 4023–4031 (2005).

[22] A. Johansson, N. Bendsoe, K. Svanberg, S. Svanberg and S. Andersson-Engels, "Influence of treatment-induced changes in tissue absorption on treatment volume during interstitial photodynamic therapy," Med. Laser Appl. **21**, 261–270 (2006).

[23] A. Johansson, J. Axelsson, J. Swartling, T. Johansson, S. Pålsson, J. Stensson, M. Einarsdottir, K. Svanberg, N. Bendsoe, K. Kälkner, S. Nilsson, S. Svanberg and S. Andersson-Engels, "Interstitial photodynamic therapy for primary prostate cancer incorporating realtime treatment dosimetry," Proc. SPIE **6427** (2007).

[24] M. Nichols, E. Hull and T. Foster, "Design and testing of a white-light, steady-state diffuse reflectance spectrometer for determination of optical properties of highly scattering systems," Appl. Opt. **36**(1), 93–104 (1997).

[25] T. Farrell, M. Patterson and B. Wilson, "A diffusion theory model of spatially resolved, steady-state diffuse reflectance for noninvasive determination of tissue optical properties in vivo," Med. Phys. **19**(4), 879–888 (1992).

[26] V. Venugopalan, J. You and B. Tromberg, "Radiative transport in the diffusion approximation: An extension for highly absorbing media and small source-detector separations," Phys. Rev. E **58**(2), 2395–2407 (1998).

[27] Y. Xiao, J. Galvin, M. Hossain and R. Valicenti, "An opti-

mized forward-planning technique for intensity modulated radiation therapy," Med. Phys. **27**(9), 2093–2099 (2000).

[28] M. Altschuler, T. Zhu, J. Li and S. Hahn, "Optimized interstitial PDT prostate treatment planning with the Cimmino feasibility algorithm," Med. Phys. **32**(12), 3524–3536 (2005).

[29] Y. Censor, M. Altschuler and W. Powlis, "On the use of Cimmino simultaneous projections method for computing a solution of the inverse problem in radiation-therapy treatment planning," Inverse Probl. **4**(3), 607–623 (1988).

[30] S. Chang, G. Buonaccorsi, A. MacRobert and S. Bown, "Interstitial and transurethral photodynamic therapy of the canine prostate using meso-tetra-(m-hydroxyphenyl) chlorin," Int. J. Cancer **67**(4), 555–562 (1996).

[31] G. Bednarz, D. Michalski, C. Houser, M. Huq, Y. Xiao, P. Anne and J. Galvin, "The use of mixed-integer programming for inverse treatment planning with pre-defined field segments," Phys. Med. Biol. **47**(13), 2235–2245 (2002).

[32] R. Haskell, L. Svaasand, T.-T. Tsay, T.-C. Feng, M. McAdams and B. Tromberg, "Boundary conditions for the diffusion equation in radiative transfer," JOSA A **11**(10), 2727–2741 (1994).

[33] S. Arridge and J. Hebden, "Optical imaging in medicine: II. Modelling and reconstruction," Phys. Med. Biol. **42**(5), 841–853 (1997).

[34] Y. Xiao, D. Michalski, J. Galvin and Y. Censor, "The least-intensity feasible solution for aperture-based inverse planning in radiation therapy," Ann. Operations Research **119**(1-4), 183–203 (2003).

[35] S. Mitra, E. Maugain, L. Bolotine, F. Guillemin and T. Foster, "Temporally and spatially heterogeneous distribution of mTHPC in a murine tumor observed by two-color confocal fluorescence imaging and spectroscopy in a whole-mount model," Photochem. Photobiol. **81**(5), 1123–1130 (2005).

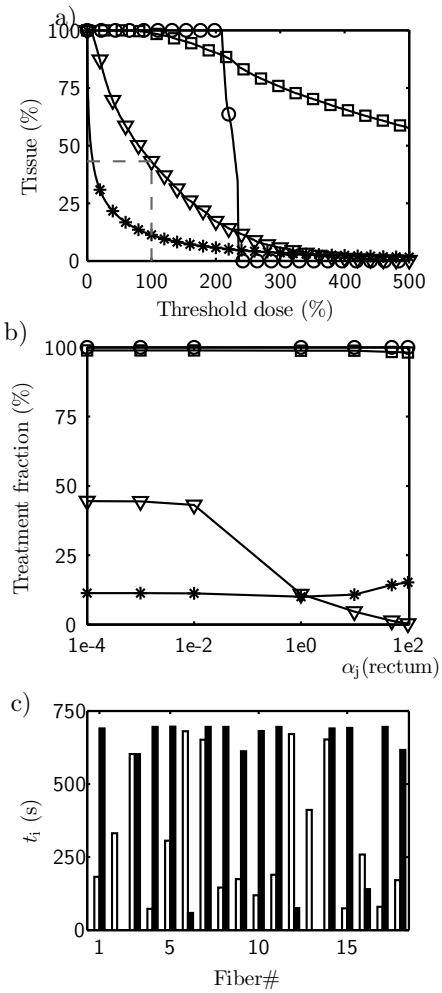

FIG. 4: a) DVHs of the delivered light dose for an importance weight on the rectum, α_j(rectum), of 1e-2. □ prostate, ○ urethra, ∇ rectum, ∗ normal tissue. The dashed lines indicate that approximately 43% (treatment fraction) of the rectum was exposed to the threshold light dose, i.e. 5 J/cm^2. b) Treatment fractions for each tissue type for varying α_j(rectum). c) Irradiation times for each source fiber for α_j(rectum) =1e-4 (white) and 500 (black). Here, $\mu_{eff(i)}$=3.7 cm^{-1}.

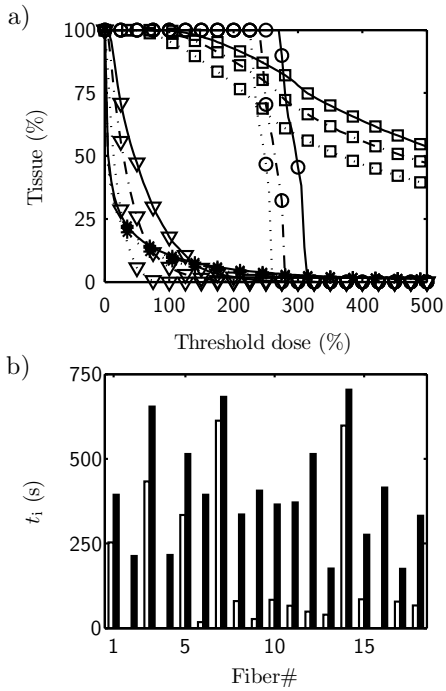

FIG. 5: a) DVHs of the delivered light dose for varying absorption within the prostate gland. $\mu_a = 0.3$ (dotted), 0.5 (dash-dot) and 0.7 cm^{-1} (solid) within the prostate. $\square$ prostate, $\circ$ urethra, ∇ rectum, $*$ normal tissue. b) Irradiation times for each source fiber for $\mu_a = 0.3$ (white) and 0.7 cm^{-1} (black).

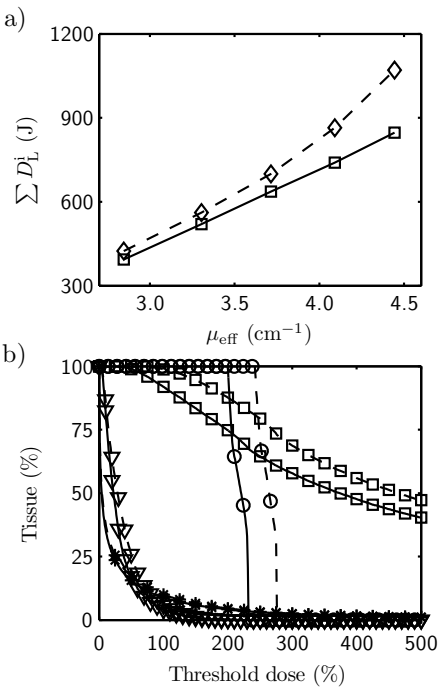

FIG. 6: a) The total light energy, $\sum D_L^i$, for different levels of light attenuation within the prostate. ◊ true μ_{eff}, □ evaluated $\mu_{eff(i)}$. b) DVHs of the delivered light dose for evaluated (solid) and true (dashed) effective attenuation coefficients where the true μ_{eff}=3.7 cm^{-1}. □ prostate, ○ urethra, ∇ rectum, ∗ normal tissue.

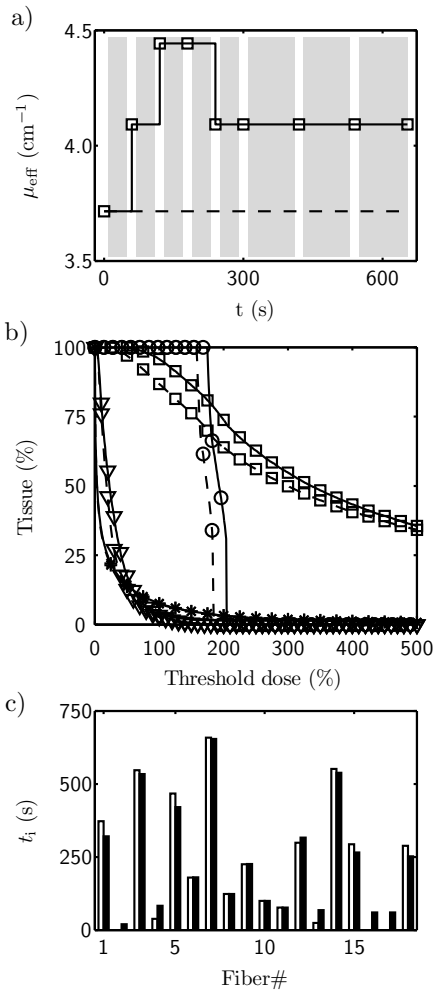

FIG. 7: a) μ_{eff} (solid) during the simulated treatment session compared to the default effective attenuation coefficient used for the pre-treatment plan (dashed). Shaded areas indicate treatment sequences, whereas square markers denote measurement sequences. b) DVHs of the delivered light dose without (dashed) and with (solid) treatment feedback. $\square$ prostate, $\circ$ urethra, ∇ rectum, $*$ normal tissue. c) Irradiation times for each source fiber without (white) and with (black) feedback.

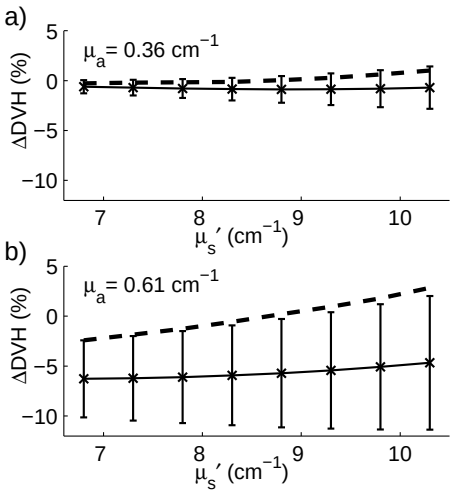

FIG. 8: The deviations in prostate treatment fraction due to erroneous fiber positioning and presumed constant scattering levels. The errors are shown relative the true $\mu_s\prime$ for a) $\mu_a = 0.36\ cm^{-1}$ and b) $\mu_a = 0.61\ cm^{-1}$. $(- -)$: true fiber positions, and $(*)$: average after randomizing fiber positions. The errorbars represent $\pm$1SD of the 100 simulations.